Dielectric Leaky Wave Antennas for Future Terahertz Systems

by

YAO KAI

A thesis submitted to
the University of Birmingham
for the degree of
DOCTOR OF PHILOSOPHY

Terahertz Sensing Laboratory
Department of Electronic, Electrical and System Engineering
College of Engineering and Physical Sciences
University of Birmingham
December 2023

ABSTRACT

This thesis endeavours to enhance the performance of terahertz antennas for communication and sensing applications. In pursuit of this objective, the thesis presents the design of two integrated dielectric leaky wave antennas (LWAs) operating in the sub-terahertz band. It includes the design of a H-band Dirac leaky wave antenna (DLWA) constructed from micromachined silicon, which is suitable for beam scanning applications. Additionally, the research encompasses a H-band direct laser written polymer Fabry-Perot cavity antenna (FPCA), designed for stable beam pointing applications.

In this thesis, the proposed DLWA represents the first instance of a sub-terahertz band all-dielectric DLWA featuring a closed bandgap. The all-dielectric unit cell exploits accidental degeneracy (i.e. frequency-balancing) to achieve suppression of the open stopband at broadside radiation. Through dispersion analysis of the unit cell, the radiation aperture is tapered with a Taylor amplitude distribution to achieve a sidelobe level (SLL) less than -30 dB at the center frequency while keeps the open stopband suppressed. The DLWA proposed in this thesis exhibits a fan-beam radiation pattern, low sidelobe levels (SLLs), and high aperture efficiency across the entire WR-3 frequency band. To mitigate Ohmic losses and enhance total efficiency, the antenna was fabricated using through-hole deep reactive ion etching (DRIE) on a high resistivity silicon wafer. The fabricated prototype of the DLWA has been measured, providing further validation for the proposed design.

Additionally, for the first time, an all-dielectric direct laser written FPCA operating at

WR-3 band is proposed. Leaky wave analysis and transvers resonance method is used for the unit cell design. For a wider working bandwidth, the resonance unit cell of the FPCA’s partial reflective dielectric surface is tapered. Additionally, the total quality factor of the FPCA's resonance cavity is carefully adjusted to optimize gain while minimizing dielectric losses attributed to the photoresin. A standard UG-387/U flange shim is fabricated to integrate the FPCA with open-ended waveguide and evaluate the performance of the FPCA. After the measurement of the fabricated prototype of the FPCA, it was confirmed that the innovative design eliminates the need for additional iris and matching metal layers. This achievement leads to good impedance matching and a high 3 dB gain bandwidth product (GBWP), surpassing the performance of similar antennas reported in previous publications.

Finally, this thesis discusses the remaining issues and future work plans for the two antenna designs proposed.

ACKNOWLEDGMENTS

I would like to express my sincere gratitude to my supervisor, Dr Stephen Hanham, who has been a constant source of guidance and support throughout my Ph.D. study. He has always encouraged me to pursue my research interests, challenged me to improve my skills, and provided me with valuable feedback and suggestions. Without him, I could not have completed the study and achieved my academic goals. He is not only a great mentor, but also a role model and a friend. I am truly honoured and lucky to have him as my supervisor.

To my beloved parents, your unwavering support and care have been my constant source of strength and inspiration. Your sacrifices and belief in my abilities have made all the difference. I am eternally grateful for your love and encouragement.

I would like to express my gratitude to Dr. Mira Naftaly at the National Physical Laboratory, U.K., for her contributions to measuring the NTD silicon properties using THz-TDS. Special thanks to Dr. Milan Salek for his insightful suggestions on the design of the antenna fixture, and to the team at the UoB Physics Workshop for their expert fabrication. I am also deeply thankful to Dr. Miguel Navarro-Cía for his measurement of the Nanoscribe photoresin properties using THz-TDS. Furthermore, I extend my sincere appreciation to Prof. Stefan Dimov and Vahid Nasrollahi for their exceptional laser machining work in the fabrication of the silicon shim used for the FPCA antenna design. I also acknowledge the invaluable assistance from the Nanoscribe support team in the fabrication process.

I am thankful for the assistance provided by the BEAR support team. The

computations described in this thesis were performed using the University of Birmingham's BlueBEAR HPC service and Baskerville Tier 2 HPC.

Finally, my heartfelt thanks to the School of Engineering for their financial support.

Table of Contents

List of Figures

List of Tables

List of Symbols and Abbreviations

SLL	Side Lobe Level
DLWA	Dirac Leaky-Wave Antenna
DRIE	Deep Reactive Ion Etching
FPCA	Fabry Perot Cavity Antenna
FSPL	Free-space Path Loss
LOS	Line-of-sight
EIRP	Effective Isotropic Radiated Power
CNC	Computer Numerical Control
OSB	Open Stopband
HRS	High-resistivity Silicon
DSW	Dielectric Slab Waveguide
2PP	Two-photon Polymerization
PRDS	Partially Reflective Dielectric Surfaces
1D	One-dimensional
T-matrix	Transfer Matrix
MPM	Matrix Pencil Method
TRM	Transverse Resonance Method
2D	Two-dimensional
CRLH	Composite Right/Left-handed
MMTMM	Multimodal T-matrix Method
CST MWS	CST Microwave Studio

PRS	Partially Reflective Surface
DBWP	Directivity Bandwidth Product
Q-factor	Quality-factor
GBWP	Gain Bandwidth Product
GRIN	Gradient Index
TLM	Transmission Line Model
TRE	Transverse Resonance Equation
AM	Additive Manufacturing
FDM	Fused Deposition Modelling
SLA	Stereolithography
JM	Jet Modelling
SLS	Selective Laser Sintering
PLA	Polylactic Acid
MJM	Multi Jet Modelling
MJP	Multi Jet Printing
SLM	Selective Laser Melting
EBM	Electron Beam Melting
DMLM	Direct Metal Laser Melting
DMLS	Direct Metal Laser Sintering
TPA	Two-photon Absorption
DiLL	Dip-in Laser Lithography
THz-TDS	Terahertz Time-domain Spectroscopy
PBCs	Periodic Boundary Conditions
OBCs	Open Boundaries Conditions

DIL	Dielectric Image Line
TRL	Through-Reflect-Line
NSGA-II	Non-dominated Sorting Genetic Algorithm II
CAD	Computer-aided Design
PGMEA	Propylene Glycol Methyl Ether Acetate
IPA	Isopropanol

List of Publications

Conference Papers

Kai Yao and Stephen M. Hanham, “A Terahertz All-dielectric EBG Resonator Antenna”, AP-S/URSI 2021.

Kai Yao, Ali M. Mohammed, Vahid Nasrollahi, Stefan Dimov, Miguel Navarro-Cía, and Stephen M. Hanham, “A H-band Direct Laser Written Leaky-wave Fed GRIN Lens Antenna”, AP-S/URSI 2024.

Chapter 1

Introduction

The terahertz frequency band, generally accepted as the frequency range from 100 GHz to 10 THz, occupies a unique position between the microwave and infrared bands in the electromagnetic spectrum [1]. In recent years, the terahertz band has emerged as a pivotal frontier in technological advancement, attracting significant attention in various research and application domains. Its potential has been explored in fields such as imaging, where it offers non-destructive inspection capabilities with applications ranging from security screening to medical diagnostics [2-5]. In spectroscopy, the terahertz band enables the detection and analysis of chemical and biological substances with unprecedented precision, which has implications for environmental monitoring, food contamination testing and pharmaceuticals [6-8]. Furthermore, the promise it holds for communication systems is immense, especially in the development of high-speed wireless networks, which could revolutionize data transmission by offering significantly higher speeds and capacities compared to current technologies [9-13].

Terahertz imaging systems provide higher spatial resolution than imaging systems operating in lower-frequency bands, due to their shorter operating wavelengths and therefore smaller diffraction-limited spot size [14]. Compared with imaging systems operating in the optical and infrared bands, terahertz imaging systems offer certain

advantages such as higher penetration depth through clothes and common packaging materials [14], making them more suitable for non-destructive inspection [15].

Terahertz imaging can be categorized into two distinct types: active imaging and passive imaging [16]. In terahertz active imaging systems, terahertz waves are emitted from a source, often via an antenna, then propagate through or scatter off the object being imaged. The attenuated terahertz radiation that is then received is processed and interpreted for the reconstruction of the image [17]. To achieve enhanced imaging resolution, an antenna with high directivity is often essential. Moreover, in order to mitigate shadowing or interference effects in single-frequency imaging systems, the object is typically illuminated at different frequencies. Consequently, an antenna with a moderate bandwidth becomes necessary [15].

Terahertz active imaging systems offer advantages in biomedical imaging due to their non-ionizing nature, unlike higher frequency waves such as X-rays, which can be harmful. Due to their lower photon energy, terahertz waves are safer for the human body. In biomedical research, this has led to their increasing application in skin cancer screening [18, 19], and breast cancer diagnosis [3, 20, 21]. Their capability to provide high-resolution imaging of cancerous tissues offers invaluable insights for medical professionals, establishing them as a promising tool in medical diagnostics.

Blackbody radiation emitted by the human body compared with other materials such as metals, show distinct contrast in the terahertz band due to minor temperature or emissivity differences. This characteristic allows passive detection and imaging of terahertz radiation to identify concealed contraband [22]. Consequently, beyond its medical applications, terahertz imaging has also gained significance in airport security screening, enabling rapid and reliable detection of concealed weapons [4]. The passive

terahertz imaging security inspection system, developed by Thruvision [23-25], for example, has been successfully deployed in several European airports, demonstrating the capacity to process up to 1,800 passengers per hour.

Terahertz spectroscopy uncovers distinctive absorption peaks in a range of substances, thereby underscoring its viability for substance identification. This method proves particularly efficacious, given that many polar molecules display specific terahertz energy absorption patterns that are indicative of their intermolecular activities [8]. In order to precisely capture the responses across a wideband spectrum, wideband terahertz antennas are essential for terahertz spectroscopy applications. Utilizing a comprehensive spectral fingerprint database, a foremost application of terahertz waves is the discernment of different compound compositions, capitalizing on these unique spectral properties for precise analysis. Consequently, an emerging area of application for the terahertz band lies in the detection of contamination in food and water. By utilizing terahertz non-destructive detection technology, it is possible to identify microbial pollutants in water and food [26], thereby addressing increasing concerns about food safety amid environmental pollution challenges. Furthermore, terahertz spectroscopy enables the precise identification of various gas components in mixed gases [27]. In pharmaceutical applications, terahertz spectroscopy serves diverse functions, including the differentiation and quantification of polymorphs and hydrates, solid state analysis, and real-time assessment of tablet coatings, both in quantification and dissolution [8].

In the era of digital transformation, the demand for effective information transmission has significantly increased, necessitating advancements in technology and communication strategies. Building upon Shannon's information theory, it is

understood that communication systems can be enhanced by expanding the bandwidth utilized within the spectrum. This expansion allows for greater data throughput by accommodating more frequencies for transmission, although it is important to consider factors like signal-to-noise ratio and modulation techniques for optimal performance [28]. To meet this demand, 5G+ technologies are evolving and leveraging the millimetre-wave spectrum. In order to further expand the spectral capacity, the IEEE introduced the 802.15.3d standard in 2017 to include the terahertz band for 6G wireless communication [9]. Building on this momentum, at the World Radio Conference 2019, a bandwidth of 160 GHz within the range of 275 GHz to 460 GHz was allocated for wireless communication by land mobile and fixed services [29].

However, in the terahertz frequency range, electromagnetic wave transmission attenuation presents a significant challenge for widespread practical deployment. The predominant cause of this attenuation is the free-space path loss (FSPL). As the waves propagate, their energy spreads over a larger area due to diffraction, leading to further loss at the receiver. The FSPL is determined by the equation [30]:

$$\mathrm{FSPL} = 20\log_{10}\left(\frac{4\pi d}{\lambda}\right) \tag{1.1}$$

In this context, d designates the propagation distance of the electromagnetic wave in free-space, while λ denotes its wavelength. As inferred from 1.1, an increase in the frequency of the electromagnetic wave, for a given distance, results in a corresponding increase in FSPL. Consequently, in the terahertz frequency band, the FSPL during electromagnetic wave transmission is greater than that of the millimetre wave frequency band.

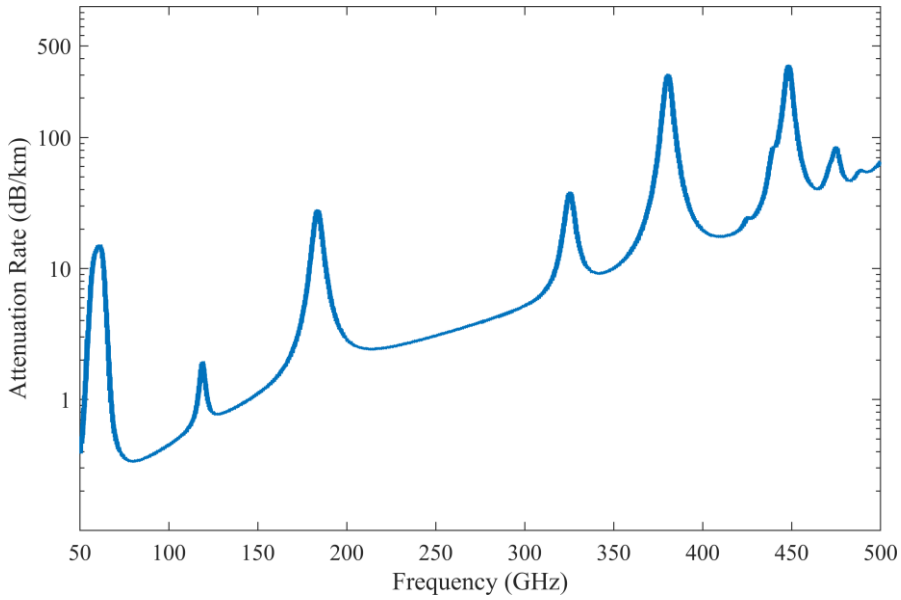

Figure 1.1. Frequency-dependent atmospheric attenuation rate in standard atmospheric condition, data from [31].

In addition to FSPL, atmospheric molecules, including water vapor and oxygen, contribute to the attenuation of electromagnetic wave propagation [30-33]. Figure 1.1 shows the attenuation characteristics of electromagnetic waves in the millimeter wave and sub-THz bands for each kilometer of propagation under standard atmospheric conditions. The data, taken from [31], corresponds to a temperature of 288.15 K, air pressure of 1013.25 hPa, and 50.0% relative humidity. Elevated humidity levels exacerbate this attenuation; as a consequence, attenuation markedly increases during rainfall relative to clear atmospheric conditions.

When accounting for both FSPL and atmospheric attenuation, the total electromagnetic wave attenuation per kilometre can be observed in Figure 1.2. It is essential to emphasize that this data pertains solely to line-of-sight (LOS) transmission and excludes obstructions that may cause blockage and extra propagation losses. This high attenuation of terahertz waves is often viewed as a drawback. However, it provides an opportunity for secure communication at the physical layer to prevent

eavesdropping as well as spectrum re-use. By adjusting the communication frequency, one can manage the attenuation and limit the range of the communication beam, reducing eavesdropping risks [32, 34].

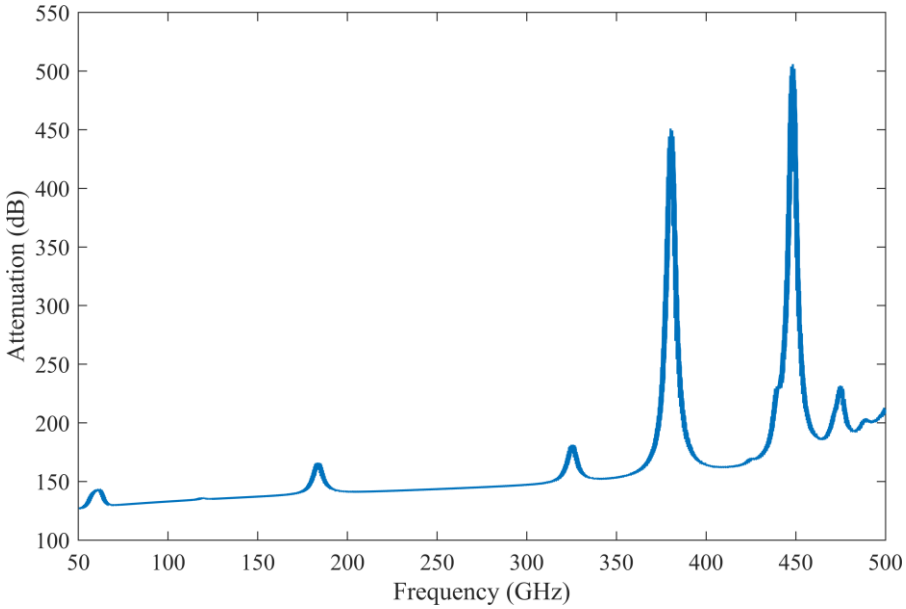

Figure 1.2. Total electromagnetic wave attenuation at a distance of 1 km due to FSPL and atmospheric attenuation for LOS transmission, excluding obstructions.

In the realm of 5G communication systems and beyond, the implementation of Massive MIMO and beamforming through large-scale antenna arrays has emerged as a pivotal solution. This approach is key to achieving higher antenna gain and effectively counteracting signal transmission attenuation [35, 36]. Such technology also ensures adequate compensation for the additional losses arising from feeding and power distribution structure. Nevertheless, challenges persist within the terahertz band, where the integration of any waveguide feed structure invariably leads to escalated energy losses and a consequent reduction in the effective isotropic radiated power (EIRP).

To overcome this issue and minimize the attenuation caused by the supplementary feed structure in terahertz band systems, a promising strategy entails the integration

of the antenna directly with the chip. The tight integration not only addresses the aforementioned challenge but also holds particular relevance for applications requiring components that are both lightweight and low profile [37, 38]. Examples of such applications include communication user terminals, wherein the antenna must not only maintain a low-profile design but also exhibit high levels of integration with the system.

The fabrication accuracy is also a significant challenge for antennas in the terahertz band, because terahertz band electromagnetic waves have shorter wavelengths than those in the microwave band. The tolerance of Computer Numerical Control (CNC) machines varies depending on the specific machine and the material being machined, with typical accuracy ranging between 10 μm and 130 μm [39-41]. However, at terahertz frequencies, where wavelengths are at the sub-millimetre level, fabrication tolerances become more pronounced. This limitation leads to the need for new antenna fabrication methodologies which have (sub-) tens of micron level accuracy such as optical lithography, deep reactive ion etching and direct laser writing of structures.

1.1. Motivation and Summary of Contribution

As discussed in the previous section, the challenges and requirements for antenna design in terahertz applications can be categorized based on the specific application. For terahertz imaging application, the key requirements are:

- Achieving higher spatial resolution through the utilization of high-gain antennas.
- Mitigating shadowing or interference effects by employing antennas with moderate bandwidth.

In the context of terahertz spectroscopy application, the primary requirement is:

- Capturing the responses across a wideband spectrum with wideband antennas.

For terahertz communication application, the essential requirements are:

- Enabling high data rates through the use of wideband antennas.
- Achieving high gain to compensate for high path loss and achieve a high signal-to-noise ratio (SNR).

Across all the aforementioned terahertz applications, the following common requirements are listed:

- Ensuring tight integration to minimize the loss and a low-profile antenna design.
- Maintaining precision throughout the antenna's fabrication process.

As a summary, to address the challenges and meet the requirements of future terahertz antenna applications, the key design considerations are high gain, wideband capabilities, low loss and a low-profile design. Additionally, maintaining precision throughout the antenna fabrication process and ensuring tight integration with the terahertz system are crucial factors.

This thesis introduces and thoroughly examines two innovative antenna designs optimized for terahertz band applications: (1) H-band Dirac leaky wave antenna (DLWA) based on micromachined silicon and (2) H-band direct laser written polymer Fabry-Perot cavity antenna (FPCA). Each of these antenna designs offers unique advantages in overcoming the inherent difficulties of terahertz transmission, catering to specific application needs including frequency beam scanning or consistent beam pointing.

1.1.1. A H-band DLWA Based on Micromachined Silicon

In the terahertz frequency range, leaky wave antennas (LWAs) are gaining prominence, especially in situations that demand beam scanning with frequency.

Previously, LWAs have been effectively used in the millimetre-wave band for various applications, such as wireless communication systems [42, 43], radar [44, 45], imaging [46], and location applications [47] due to their ability to produce a frequency-scannable narrow beam without requiring a complex feeding network. Unlike waveguide horn antennas, LWAs offer a feeding structure on the same plane as the circuit board, leading to a more compact and streamlined design. A more detailed exploration of the fundamentals of LWA is presented in Section 2.1 of this thesis.

A challenge to LWA's adoption at higher terahertz frequencies is that the commonly employed waveguiding technologies, such as coplanar waveguide [48], substrate integrated waveguide [49, 50] and metal rectangular waveguide [51] exhibit increasing Ohmic loss resulting in reduced antenna efficiency.

Another challenge in the design of LWAs is the open stopband (OSB) that can occur in periodic LWAs when radiating close to broadside which can result in a degradation in the realized gain and antenna efficiency, and an increased VSWR [52, 53]. However, in some cases these solutions do not completely close the stopband and the effects are still apparent in terms of a reduced return loss near broadside.

In Chapter 3 of this thesis, to address the challenges in designing LWA for the terahertz frequency band, a novel periodic Dirac LWA (DLWA) is proposed, built on a high-resistivity silicon (HRS) dielectric slab waveguide (DSW). The contributions of this work are summarized as follows:

1. The design of an all-dielectric DLWA unit cell, based on a low-loss silicon waveguide.
2. Overcoming the unit cell's OSB problem through dispersion analysis.
3. A curve fitting method is proposed to accurately predict the physical dimensions

of the unit cell at each coordinate, which facilitates the tapering of the DLWA's radiation aperture.

1.1.2. A H-band Direct Laser Written Polymer FPCA

The lens antenna is a popular antenna choice for terahertz applications that require an antenna radiation pattern with a frequency-stable mainlobe angle. They benefit from moderate-to-high gain, low complexity, and relatively straightforward fabrication. Lens antennas can be made from various low-loss materials, such as polymers [54, 55] and HRS [56-58], amongst others.

However, lens antennas fabricated utilizing HRS through the DRIE process tend to be bulky, weighty, and expensive [59-61]. Moreover, the terahertz band antennas necessitate exacting fabrication tolerances, resulting in elevated costs for the CNC fabrication process in comparison to lower frequency bands.

An emerging fabrication technique is 3D printing using the two-photon polymerization (2PP) of a photoresin. It offers sub-micrometre resolution, precise shape accuracy, rapid prototyping, and the ability to create versatile and complex 3D designs. Furthermore, it is more cost-effective than HRS, making it a potential solution for terahertz antenna design. Details regarding the 2PP 3D printing process are presented in Section 2.5 of this thesis.

One significant challenge associated with employing 2PP 3D printing for lens antennas operating in the terahertz band is the substantial dielectric loss exhibited by the 2PP photo resin, thereby impacting the overall performance of the lens antenna. One solution to address this high dielectric loss could be to reduce the infill factor within the antenna structure, while still maintaining the wave reshaping feature. This

approach is shown to lead to a viable solution.

A FPCA fabricated via direct laser writing, which meets the aforementioned criteria, is introduced in Chapter 4 of this thesis. Typically, the simplest FPCA design consists of a primary source, a metal ground, a partially reflective dielectric surface (PRDS), and an air gap between the metal ground and the PRDS. The resonator formed by the PRDS and the metal ground reshapes the wavefront of the primary source, resulting in higher gain. The presence of an air gap between the PRDS of the FPCA leads to a diminution in dielectric loss, in comparison to that observed in a homogenous dielectric layer. Additionally, the fabrication of the PRDS with sub-wavelength air perforations further contributes to the reduction of dielectric loss. More details of the fundamentals of FPCA design are presented in Section 2.3 of this thesis.

This work presents several novel contributions to the PRDS based 3D printing FPCA in the WR-3 band. Key achievements include:

1. A new methodology is introduced to optimize the FPCA's quality factor, significantly reducing dielectric losses associated with the 2PP photo resin.
2. Higher 3 dB GBWP and minimized SLLs are achieved through optimizing the PRDS unit cells.
3. The optimized FPCA achieves low return loss without the need for conventional matching structures, through its integration with a silicon shim.

1.2. Outline of thesis

The remainder of this thesis is structured as follows. In Chapter 2, the foundational theories relevant to the antenna designs proposed in this thesis are presented. Firstly, the operating principles and implementation mechanisms of LWAs is discussed. This

is followed by an analysis and discussion on the selection of correct excitation modes for LWA radiation, incorporating methods to address the OSB issue. This discussion then leads to the introduction and realization of the Dirac Leaky Wave Antenna (DLWA). Additionally, an analysis of methodologies for calculating the leakage rate of a 1D periodic LWA unit cell, with the objective of achieving a reduced SLL through tapering of the radiation aperture of the DLWA is presented. Following this, the fundamental working principles of the FPCA are elucidated. To facilitate the design and analysis of the PRDS within the FPCA, the transverse resonance method is introduced. After that, an overview of prevalent 3D printing technologies utilized in antenna fabrication, including the 2PP 3D print technology is presented.

In Chapter 4, a novel design for a DLWA operating in the H-band is presented. The DLWA designs consists of a 2D array of unit cells which permits the analysis of the antenna properties based on the unit cell characteristics. The unit cell that forms the DLWA's radiation aperture is analysed using several computational electromagnetic techniques, with adjustments made to its dimensional parameters to mitigate the open stop band effect. Following this, the leakage rate of the unit cell is accurately calculated, and curve fitting techniques are applied. This helps establish a relationship between the unit cell's dimensions and its leakage rate, which is crucial for constructing a DLWA with a tapered aperture. Additionally, the chapter covers the design considerations for the DLWA’s overall structure, examining the tapered dielectric waveguide, the termination structure, the fixture, and the silver film reflector in detail. Then, the design of DLWA proposed in this thesis is verified by the measurements of the DLWA prototype, alongside an analysis and discussion on how errors in the fabrication process influence the DLWA’s performance.

In Chapter 5, details on the design of a novel 2PP 3D printed all-dielectric FPCA are presented. Initially, considerations on the unit cell design and the optimization of the PRDS that constitute the FPCA are discussed. This primarily involves using the effective medium method to model the unit cell, conducting dispersion analysis, and optimizing the Q-factor of the unit cell to reduce dielectric loss caused by the IP-Q photo resin. Following this, the overall design of the FPCA is discussed, including the implementation process for impedance matching between the FPCA and the open-ended waveguide. Additionally, the design of the PRDS is revisited, with a particular emphasis on performing transverse permittivity gradient tapering and further optimizing the FPCA. Next, the optimization and considerations necessary to solve the problem caused by the overhanging feature during the 2PP 3D printing process of the FPCA is presented. Finally, the measurement results of the FPCA are analysed and discussed to verify the design of FPCA.

In Chapter 4, the conclusions of this thesis are presented, along with descriptions of future work.

1.3. Summary

In this chapter, the background of the research addressed by this thesis is explained, including the challenges and requirements for antenna design in terahertz applications. Following this, the contributions of the two dielectric LWAs proposed in this thesis are outlined. Finally, the structure of the entire thesis is summarized.

Reference

[1] R. Xu *et al.*, "A Review of Broadband Low-Cost and High-Gain Low-Terahertz Antennas for Wireless Communications Applications," *IEEE Access,* vol. 8, pp.

57615-57629, 2020.
[2] E. Castro-Camus, M. Koch, and D. M. Mittleman, "Recent Advances in Terahertz Imaging: 1999 to 2021," *Appl. Phys. B,* vol. 128, no. 1, p. 12, 2021/12/30 2021.
[3] N. Vohra *et al.*, "Terahertz Imaging of Breast Cancer Using Human and Animal Models," in *2021 IEEE Conference on Antenna Measurements and Applications (CAMA)*, 15-17 Nov. 2021 2021, pp. 368-371.
[4] P. Hillger, J. Grzyb, R. Jain, and U. R. Pfeiffer, "Terahertz Imaging and Sensing Applications with Silicon-Based Technologies," *IEEE Trans. Terahertz Sci. Technol.,* pp. 1-1, 2018.
[5] L. Cheng, Y. Ji, C. Li, X. Liu, and G. Fang, "Improved Ssd Network for Fast Concealed Object Detection and Recognition in Passive Terahertz Security Images," *Sci. Rep.,* vol. 12, no. 1, p. 12082, 2022.
[6] A. Ren, A. Zahid, D. Fan, M. A. Imran, A. Alomainy, and Q. H. Abbasi, "Establishing a Novel Technique for the Detection of Water Contamination Using Terahertz Waves," in *2019 IEEE MTT-S International Wireless Symposium (IWS)*, 19-22 May 2019 2019, pp. 1-3.
[7] N. Shimizu *et al.*, "Comparison of Gas Content in Smoke Measured with a Continuous-Wave Terahertz Spectrometer and Fourier Transform Infrared Spectrometer," in *2011 International Conference on Infrared, Millimeter, and Terahertz Waves*, 2-7 Oct. 2011 2011, pp. 1-2.
[8] S. K. Mathanker, P. R. Weckler, and N. Wang, "Terahertz (Thz) Applications in Food and Agriculture: A Review," *Trans. ASABE,* vol. 56, no. 3, pp. 1213-1226, 2013.
[9] V. Petrov, T. Kürner, and A. I. Hosako, "Ieee 802.15.3d: First Standardization Efforts for Sub-Terahertz Band Communications Towards 6g," *IEEE Commun. Mag.,* vol. 58, no. 11, pp. 28-33, 2020.
[10] B. Aqlan, M. Himdi, H. Vettikalladi, and L. Le-Coq, "A 300-Ghz Low-Cost High-Gain Fully Metallic Fabry–Perot Cavity Antenna for 6g Terahertz Wireless Communications," *Sci. Rep.,* vol. 11, no. 1, pp. 1-9, 2021.
[11] L. Cen and G. Y. Li, "Indoor Terahertz Communications: How Many Antenna Arrays Are Needed?," *IEEE Trans. Wireless Commun.,* vol. 14, no. 6, pp. 1-1, 2015.
[12] P. Kysti, K. Rikkinen, M. Berg, M. E. Leinonen, and A. Prssinen, "Thz Radio Communication: Link Budget Analysis toward 6g," *IEEE Commun. Mag.,* vol. 58, no. 11, pp. 22-27, 2020.
[13] H. Sarieddeen, N. Saeed, T. Y. Al-Naffouri, and M. S. Alouini, "Next Generation Terahertz Communications: A Rendezvous of Sensing, Imaging, and Localization," *IEEE Commun. Mag.,* vol. 58, no. 5, pp. 69-75, 2020.
[14] P. Mukherjee and B. Gupta, "Terahertz (Thz) Frequency Sources and Antennas-a Brief Review," *Int. J. Infrared Millimeter Waves,* vol. 29, pp. 1091-1102, 2008.
[15] I. Malhotra, K. R. Jha, and G. Singh, "Terahertz Antenna Technology for Imaging Applications: A Technical Review," *Int. J. Microwave Wireless Technolog.,* vol. 10, no. 3, pp. 271-290, 2018.
[16] E. N. Grossman, J. Gordon, D. Novotny, and R. Chamberlin, "Terahertz Active and Passive Imaging," in *The 8th European Conference on Antennas and Propagation (EuCAP 2014)*, 2014: IEEE, pp. 2221-2225.
[17] D. Mittleman, "Terahertz Imaging," in *Sensing with Terahertz Radiation*:

Springer, 2003, pp. 117-153.
[18] I. Mohammad *et al.*, "Photonic Non-Invasive Mmw and Thz Imaging for Non-Melanoma Skin Cancer Detection," in *2022 Fifth International Workshop on Mobile Terahertz Systems (IWMTS)*, 4-6 July 2022 2022, pp. 1-5.
[19] A. Balakin *et al.*, "Terahertz Image Processing for the Skin Cancer Diagnostic," in *2014 39th International Conference on Infrared, Millimeter, and Terahertz waves (IRMMW-THz)*, 14-19 Sept. 2014 2014, pp. 1-1.
[20] T. C. Bowman, Y. Wu, A. Walter, J. M. Gauch, M. El-Shenawee, and L. Campbell, "Time of Flight Thz Imaging of 3d Ex-Vivo Breast Cancer Tumor Tissues," in *2015 40th International Conference on Infrared, Millimeter, and Terahertz waves (IRMMW-THz)*, 23-28 Aug. 2015 2015, pp. 1-2.
[21] A. Al-Ibadi *et al.*, "Thz Spectroscopy and Imaging for Breast Cancer Detection in the 300–500 Ghz Range," in *2017 42nd International Conference on Infrared, Millimeter, and Terahertz Waves (IRMMW-THz)*, 27 Aug.-1 Sept. 2017 2017, pp. 1-1.
[22] M. Kowalski and M. Kastek, "Comparative Studies of Passive Imaging in Terahertz and Mid-Wavelength Infrared Ranges for Object Detection," *IEEE Trans. Inf. Forensics Secur.,* vol. 11, no. 9, pp. 2028-2035, 2016.
[23] Thruvision. "Next Deploys 1,800 People-Per-Hour 'Game Changing' Screening Solution." https://thruvision.com/next-deploys-1800-people-per-hour-game-changing-screening-solution/ (accessed March 29th, 2024).
[24] S. R. Kasjoo, M. Mokhar, N. Zakaria, and N. Juhari, "A Brief Overview of Detectors Used for Terahertz Imaging Systems," in *AIP conference proceedings*, 2020, vol. 2203, no. 1: AIP Publishing.
[25] M. Shur, "Recent Developments in Terahertz Sensing Technology," *Micro-and Nanotechnology Sensors, Systems, and Applications VIII,* vol. 9836, pp. 494-501, 2016.
[26] A. Ren *et al.*, "State-of-the-Art in Terahertz Sensing for Food and Water Security – a Comprehensive Review," *Trends Food Sci. Technol.,* 2019.
[27] K. Komatsu, T. Iwamoto, H. Ito, and H. Saitoh, "Thz Gas Sensing Using Terahertz Time-Domain Spectroscopy with Ceramic Architecture," *ACS Omega,* vol. 7, no. 35, pp. 30768-30772, 2022.
[28] S. Verdú, "Spectral Efficiency in the Wideband Regime," *IEEE Trans. Inf. Theory,* vol. 48, no. 6, pp. 1319-1343, 2002.
[29] T. Kürner and A. Hirata, "On the Impact of the Results of Wrc 2019 on Thz Communications," in *2020 Third International Workshop on Mobile Terahertz Systems (IWMTS)*, 1-2 July 2020 2020, pp. 1-3.
[30] T. Ismail, E. Leitgeb, and T. Plank, "Free Space Optic and Mmwave Communications: Technologies, Challenges and Applications," *IEICE Trans. Commun.,* vol. E99B, no. 6, pp. 1243-1254, 2016.
[31] Z. K. Weng *et al.*, "Millimeter-Wave and Terahertz Fixed Wireless Link Budget Evaluation for Extreme Weather Conditions," *IEEE Access,* vol. 9, pp. 163476-163491, 2021.
[32] J. M. Jornet, E. W. Knightly, and D. M. Mittleman, "Wireless Communications Sensing and Security above 100 Ghz," *Nat. Commun.,* vol. 14, no. 1, 2023.
[33] F. Al-Ogaili and R. M. Shubair, "Millimeter-Wave Mobile Communications for 5g: Challenges and Opportunities," in *2016 IEEE International Symposium on Antennas and Propagation (APSURSI), 26 June-1 July 2016*, Piscataway, NJ,

USA, 2016: IEEE, in 2016 IEEE International Symposium on Antennas and Propagation (APSURSI), pp. 1003-4.

[34] Z. Fang, H. Guerboukha, R. Shrestha, M. Hornbuckle, Y. Amarasinghe, and D. M. Mittleman, "Secure Communication Channels Using Atmosphere-Limited Line-of-Sight Terahertz Links," *IEEE Trans. Terahertz Sci. Technol.,* vol. 12, no. 4, pp. 363-369, 2022.

[35] F. Al-Ogaili and R. M. Shubair, "Millimeter-Wave Mobile Communications for 5g: Challenges and Opportunities," in *2016 IEEE International Symposium on Antennas and Propagation (APSURSI)*, 26 June-1 July 2016 2016, pp. 1003-1004.

[36] H. J. Song and N. Lee, "Terahertz Communications: Challenges in the Next Decade," *IEEE Trans. Terahertz Sci. Technol.,* vol. 12, no. 2, pp. 105-117, 2022.

[37] T. Zwick, F. Boes, B. Göttel, A. Bhutani, and M. Pauli, "Pea-Sized Mmw Transceivers," *IEEE Microwave Mag.,* vol. 18, no. 6, pp. 79-89, 2017.

[38] R. Correia, T. Varum, J. N. Matos, A. Oliveira, and N. B. Carvalho, "User Terminal Segments for Low-Earth Orbit Satellite Constellations: Commercial Systems and Innovative Research Ideas," *IEEE Microwave Mag.,* vol. 23, no. 10, pp. 47-58, 2022.

[39] A. Ohadi and G. V. Eleftheriades, "Slotted Waveguide Frequency-Scanned Slow-Wave Antenna with Reduced Sensitivity of the Closed Stopband at Millimeter-Wave Frequencies," *IEEE Access,* vol. 10, pp. 27783-27793, 2022.

[40] I. Santosa, S. Siswiyanti, and M. N. Alif, "Analisa Kualitas Hasil Produk Pada Pengerjaan Pocketing Dengan Mesin Cnc Frais 3 Axis," *JTT (Jurnal Teknologi Terapan),* vol. 7, no. 2, pp. 145-152, 2021.

[41] J. Lee, J. Song, Y. C. Lee, and J. T. Kim, "Development of a Huge Hybrid 3d-Printer Based on Fused Deposition Modeling (Fdm) Incorporated with Computer Numerical Control (Cnc) Machining for Industrial Applications," *High Temp. Mater. Processes (London),* vol. 41, no. 1, pp. 123-131, 2022.

[42] D. B. Montero, M. A. Campo, and N. Llombat, "Broadband Low-Permittivity Elliptical Lens Fed by a Leaky-Wave Antenna for Communications Applications," in *2018 43rd International Conference on Infrared, Millimeter, and Terahertz Waves (IRMMW-THz)*, 9-14 Sept. 2018 2018, pp. 1-2.

[43] G. B. Wu, Q. L. Zhang, K. F. Chan, B. J. Chen, and C. H. Chan, "Amplitude-Modulated (Am) Leaky-Wave Antennas," *IEEE Trans. Antennas Propag.,* pp. 1-1, 2020.

[44] K. Murano *et al.*, "Demonstration of Short-Range Terahertz Radar Using High-Gain Leaky-Wave Antenna," in *2016 41st International Conference on Infrared, Millimeter, and Terahertz waves (IRMMW-THz)*, 25-30 Sept. 2016 2016, pp. 1-2.

[45] Kosuke *et al.*, "Low-Profile Terahertz Radar Based on Broadband Leaky-Wave Beam Steering," *IEEE Trans. Terahertz Sci. Technol.,* 2017.

[46] K. K. Mutai, H. Sato, and Q. Chen, "Active Millimeter Wave Imaging Using Leaky-Wave Focusing Antenna," *IEEE Trans. Antennas Propag.,* vol. 70, no. 5, pp. 3789-3798, 2021.

[47] M. Steeg, A. A. Assad, and A. Stohr, "Simultaneous Doa Estimation and Ranging of Multiple Objects Using an Fmcw Radar with 60 Ghz Leaky-Wave Antennas," in *2018 43rd International Conference on Infrared, Millimeter, and Terahertz Waves (IRMMW-THz2018)*, 2018.

[48] L. Cao, A.-S. Grimault-Jacquin, and F. Aniel, "Comparison and Optimization of Dispersion, and Losses of Planar Waveguides on Benzocyclobutene (Bcb) at Thz Frequencies: Coplanar Waveguide (Cpw), Microstrip, Stripline and Slotline," *Progress In Electromagnetics Research B,* vol. 56, pp. 161-183, 2013.

[49] W. Che, D. Wang, K. Deng, and Y. Chow, "Leakage and Ohmic Losses Investigation in Substrate-Integrated Waveguide," *Radio Sci.,* vol. 42, no. 05, pp. 1-8, 2007.

[50] N. Ranjkesh and M. Shahabadi, "Loss Mechanisms in Siw and Msiw," *Progress In Electromagnetics Research B,* vol. 4, pp. 299-309, 2008.

[51] K. Singh, A. Bandyopadhyay, and A. Sengupta. "Low-Loss Metallic Waveguide for Terahertz Applications." https://www.comsol.fr/paper/download/579301/singh_paper.pdf (accessed October,15th, 2023).

[52] D. R. Jackson, C. Caloz, and T. Itoh, "Leaky-Wave Antennas," *Proc. IEEE,* vol. 100, no. 7, pp. 2194-2206, 2012.

[53] D. R. Jackson and A. A. Oliner, "Leaky-Wave Antennas," in *Modern Antenna Handbook*, 2008, pp. 325-367.

[54] K. Konstantinidis *et al.*, "A Thz Dielectric Lens Antenna," in *2016 IEEE International Symposium on Antennas and Propagation (APSURSI)*, 2016: IEEE, pp. 1493-1494.

[55] K. Konstantinidis *et al.*, "Low-Thz Dielectric Lens Antenna with Integrated Waveguide Feed," *IEEE Trans. Terahertz Sci. Technol.,* vol. 7, no. 5, pp. 572-581, 2017.

[56] N. Llombart, G. Chattopadhyay, A. Skalare, and I. Mehdi, "Novel Terahertz Antenna Based on a Silicon Lens Fed by a Leaky Wave Enhanced Waveguide," *IEEE Trans. Antennas Propag.,* vol. 59, no. 6, pp. 2160-2168, 2011.

[57] M. Alonso-delPino, C. Jung-Kubiak, T. Reck, N. Llombart, and G. Chattopadhyay, "Beam Scanning of Silicon Lens Antennas Using Integrated Piezomotors at Submillimeter Wavelengths," *IEEE Trans. Terahertz Sci. Technol.,* vol. 9, no. 1, pp. 47-54, 2019.

[58] N. Llombart and G. Chattopadhyay, "Extended Hemispherical Silicon Lens Excited by a Leaky Wave Waveguide Feed," in *Proceedings of the Fourth European Conference on Antennas and Propagation*, 12-16 April 2010 2010, pp. 1-4.

[59] Q. Yu *et al.*, "All-Dielectric Meta-Lens Designed for Photoconductive Terahertz Antennas," *IEEE Photonics J.,* vol. 9, no. 4, pp. 1-9, 2017.

[60] E. Erfani, M. Niroo-Jazi, and S. Tatu, "A High-Gain Broadband Gradient Refractive Index Metasurface Lens Antenna," *IEEE Trans. Antennas Propag.,* vol. 64, no. 5, pp. 1968-1973, 2016.

[61] S. Zhu, "Silicon-Based High Gain Terahertz Metasurface Antennas Working at 1 Thz," in *2021 IEEE International Workshop on Electromagnetics: Applications and Student Innovation Competition (iWEM)*, 2021: IEEE, pp. 1-2.

Chapter 2

Theoretical Background

This chapter presents the theoretical background for the two principal types of antennas studied in this thesis: the leaky wave antenna (LWA) and Fabry-Perot cavity antenna (FPCA). It also describes the methodologies by which they are commonly analysed, and this will be later utilised in Chapters 3 and 4 for the design of the respective antennas.

Section 2.1 provides an overview of LWA theory, including its working principles, selection of the appropriate eigenmodes to suppress the open stop band (OSB), and the basics of the design of a Dirac leaky wave antenna (DLWA). Section 2.2 presents the methods of dispersion analysis applicable to a one-dimensional (1D) periodic LWA unit cell. This includes the three techniques: (1) the transfer matrix (T-matrix) method; (2) the Matrix Pencil Method (MPM); and (3) the complex Eigenmode Solver method. These methods serve as tools for the design and performance prediction of the periodic LWA. Section 2.3 delves into the FPCA, elucidating its working principles, limitations, and related optimization methods from the perspective of LWA theory. Subsequently, Section 2.4 introduces the transverse resonance method (TRM), a method for dispersion analysis used in this thesis to aid the FPCA's design. Finally, Section 2.5 summarises 3D printing as a fabrication technique for antennas in the millimetre-wave and terahertz band.

2.1. LWA Theory

In this section, the basic theory of the LWA is summarized. Additionally, the working principle of 1D periodic LWA is introduced. Traditional designs of 1D periodic LWAs often suffer from the OSB problem, which leads to a degradation in the antenna's performance, primarily affecting gain and return loss, when the beam of the LWA is frequency scanned through the broadside direction. Various methods for suppressing an OSB have been presented in the literature and these will be discussed in Section 2.1.2. Furthermore, the fundamental theory behind the design of DLWAs involves closing the bandgap—a range in the frequency spectrum where no eigenmodes exist—to achieve broadside radiation. This is presented in Section 2.1.3.

2.1.1. Fundamentals on Leaky Wave Antenna

As the name suggests, the "leaky-wave antenna" operates on the principle of energy leakage from a wave traveling in or along a guiding structure. The leaked energy interferes in the far-field to produce the radiation pattern for the antenna.

The LWA can be divided into two categories based on the mechanism that generates the leaky wave radiation. One category is the fast wave LWA, and the other is the slow wave LWA [1, 2]. In cases where a fast wave is excited by the wave launcher, the propagation constant of the fast wave will be smaller than the wave number of free space and the wave will directly radiate if the guiding structure is open, forming a fast wave LWA.

In the other case, when a slow wave is excited by the wave launcher and propagates inside or along the guiding structure, no leaky wave will be excited unless additional perturbation to the structure is introduced [1]. This phenomenon can be elucidated by

examining the interaction between Bloch modes and spatial modes within photonic crystals. The guiding structure, similar to a photonic crystal, exhibits a periodic architecture that affects the propagation of electromagnetic waves. When the slow wave navigates through this periodicity, it interacts with the structure's repeating elements. This interaction gives rise to Bloch modes, which are wave patterns formed due to the periodicity of the structure [3]. Concurrently, this interaction also stimulates specific spatial modes. Spatial modes describe the electromagnetic field distribution within localized areas of the guiding structure. Essentially, they are manifestations of Bloch modes in the spatial domain. At least one of these spatial modes is instrumental in contributing to the far-field pattern, enabling the structure to function as a slow wave LWA. The generation of a leaky wave, in this context, is attributed to the periodic modulation of the guiding structure, hence, this type of slow wave LWA is often referred to as a periodic LWA [2].

Besides the wave launcher serving as the source for a LWA, an impedance matching termination is usually added at the end of the LWA. This ensures that the remaining energy inside the LWA is absorbed, thereby minimizing reflections. Without such absorption, reflections at the open end of the LWA could cause additional leaky wave radiation and contribute to side lobes in the radiation pattern.

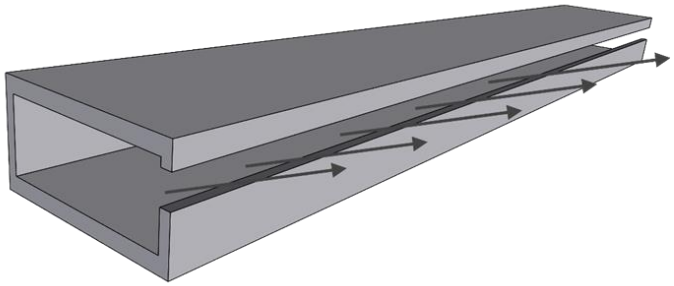

Figure 2.1. Example of a 1D uniform fast wave LWA: metal rectangular waveguide with a long slit in the sidewall.

LWAs can also be classified based on the dimensions of their guiding structures. If the radiation aperture of the LWA is maintained sufficiently narrow in the transverse direction, and the guided wave is attenuated only in the longitudinal direction, then the structure can be categorized as a 1D LWA. For example, as illustrated in Figure 2.1, a metal rectangular waveguide with a long slit in the longitudinal direction can form a 1D LWA. On the other hand, when the leaky wave propagates and decays in both transverse directions, a two-dimensional (2D) LWA is formed. If the leaky wave is travelling inside a resonant cavity, then this can also be referred to as a FPCA. More details regarding the FPCA will be presented in Section 2.3.

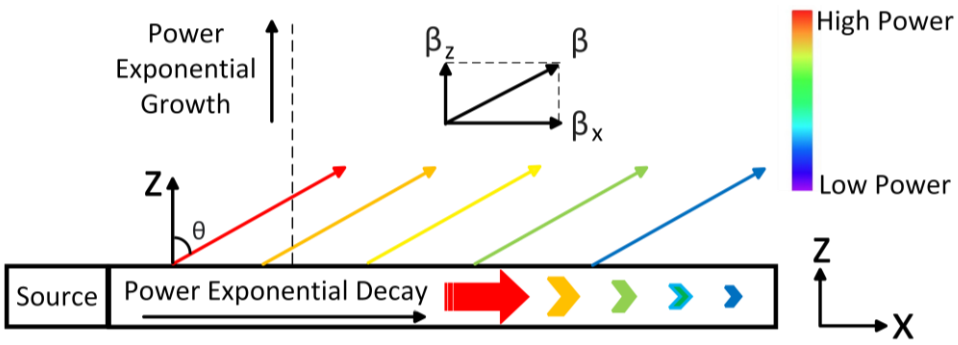

Figure 2.2. Power flow of a leaky wave propagating in the $+x$ direction. The power in the leaky wave decays exponentially along the $+x$ direction, while showing exponential growth along the dashed line in the $+z$ direction. The size and colour of the arrow represent the power amplitude.

As illustrated in Figure 2.2, the power flow of the leaky wave mode possesses both $+x$ and $+z$ components. For simplicity, the guiding structure is assumed to be infinite in the y direction, and propagation of the leaky mode in the y direction is not considered here. Consequently, the electric field propagate above the guiding structure (in the air) can be represented as follows:

$$E(x,z) = Ae^{-jk_x x}e^{-jk_z z} \tag{2.1}$$

where A is the amplitude of the electric field, while k_x and k_z represent the complex

wave numbers that determine the propagation characteristics of the leaky wave traveling in the $+x$ direction and $+z$ directions, respectively.

For more detailed evaluation, the complex wave number k_x and k_z can be represented as follows:

$$k_x = \beta_x - j\alpha_x \tag{2.2}$$

$$k_z = \beta_z - j\alpha_z \tag{2.3}$$

$$k_x = \sqrt{k_o^2 - k_z^2} \tag{2.4}$$

where k_o represent the wave number of free space, β is the phase constant, α is the leakage rate or attenuation constant, β_x and α_x are the components of the phase constant and leakage rate, respectively, specific to the x direction. Similarly, β_z and α_z are the z directional phase constant and leakage rate, respectively. Substituting (2.2) and (2.3) into (2.4) yields the following:

$$\beta_x\alpha_x = -\beta_z\alpha_z \tag{2.5}$$

Equation (2.5) elucidates the working principle of LWA [1], and helps explain why leaky waves are often being considered "improper" or "non-spectral" [1]. As shown in Figure 2.2, the power flow of the forward leaky wave mode possesses both $+x$ and $+z$ components, indicating that $\beta_x > 0$, $\beta_z > 0$ and $\alpha_x > 0$. From (2.5) it is determined that $\alpha_z < 0$. This suggests that the power of the leaky wave exponentially increases along the $+z$ direction, following the dashed line shown in in Figure 2.2. However, such an implication that power could infinitely increase with height is physically implausible. In reality, the exponential increase in power does not occur because the guiding structure, as illustrated in Figure 2.2, cannot be infinitely long. As a result, although leaky waves are often considered "improper" or "non-spectral" [1], they still adhere to the laws of physics.

The radiation angle and beamwidth of LWAs is determined by the phase constant β and attenuation constant α, respectively [4]. As demonstrated in Figure 2.2, the radiation angle θ, with respect to z-axis, can be calculated as follows [1]:

$$\theta = \tan^{-1}\left(\frac{\beta_x}{\beta_z}\right) \tag{2.6}$$

If α_x is sufficiently small, the radiation angle can also be approximated by the following [5]:

$$\theta = \cos^{-1}\left(\frac{\beta_x}{k_o}\right) \tag{2.7}$$

Equation (2.7) suggests that for broadside radiation where $\theta = 0°$ that β_x must be equal to zero, indicating that it is approaching the cut-off frequency when the beam is almost pointed at the broadside. As a result, 1D uniform LWAs cannot achieve broadside radiation during frequency scanning.

While feeding the 1D uniform LWA from both sides or in the centre may attain broadside radiation, it may still suffer from a narrowband due to beam scanning caused by dispersion.

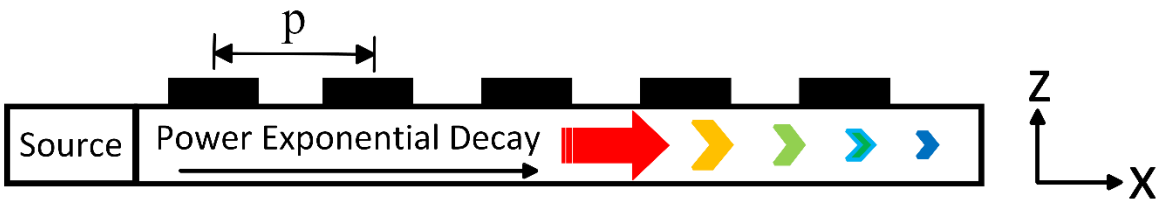

Figure 2.3. 1D Periodic LWA, the guiding structure is modulated in the direction of guided propagation.

Equation (2.7) suggests that a 1D uniform LWA supports only forward propagation of the leaky wave, as shown in Figure 2.2. This is because as the frequency increases from the cut-off to higher frequencies, the beam scanning angle θ correspondingly increases from the broadside direction to larger angles. As a result, the leaky wave

mode can only radiate towards the front hemisphere.

As for the slow wave LWAs, when the guiding structure undergoes periodic modulation, as depicted in Figure 2.3, infinite number of Bloch modes are generated due to periodic modulation [1]. Consequently, the modal field transforms from the initial state (2.1) to the following:

$$\sum_{n=-\infty}^{+\infty} A_n e^{-jk_{xn}x} e^{-jk_{zn}z} \tag{2.8}$$

where k_{xn}, the wavenumber of n^{th} Bloch mode change in the x direction, can be expanded as:

$$k_{xn} = k_{x0} + \frac{2\pi n}{p} \tag{2.9}$$

where p represents the periodicity of the modulation, as shown in Figure 2.3. Due to the periodicity in k_x, only $-\frac{\pi}{p} < k_x \leq \frac{\pi}{p}$ need to be considered, and this region containing the unique values of k_x is called the Brillouin zone [3].

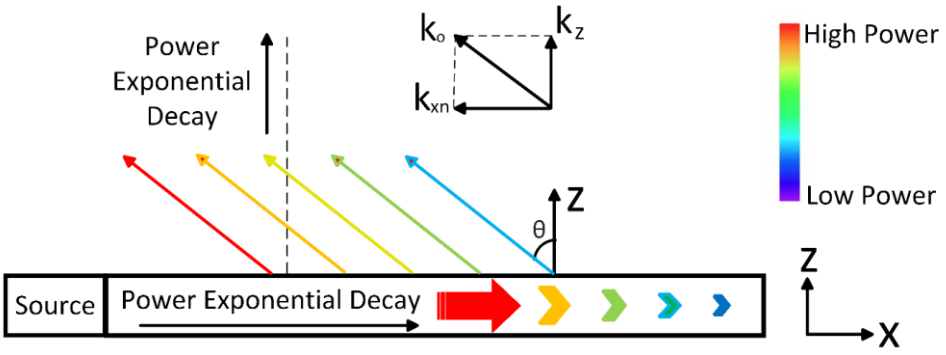

Figure 2.4. The backward radiating leaky wave becomes "proper," as its power decays exponentially in the +z direction. The size and colour of the arrow represent the power level.

If the wavenumber of the n^{th} Bloch mode satisfies the following condition:

$$-k_o < k_{xn} < 0 \tag{2.10}$$

the n^{th} Bloch mode is identified as a fast wave and contributes to backward radiation. Consequently, the periodicity of the modulation can be chosen such that the 1D periodic LWA supports both forward and backward beam scanning.

In the case of a backward radiating leaky wave, when $-k_o < k_{xn} < 0$, as illustrated in Figure 2.4, the leaky wave is considered "proper". This is because from (2.5), it can be determined that $\alpha_{zn} > 0$, which means the power decreases exponentially away from the guiding structure in the z direction.

The 3 dB power beamwidth of a LWA can be approximated by the following [5, 6]:

$$BW = 2\csc(\theta)\frac{\alpha_x}{k_o} \approx \frac{2\alpha_x}{\beta_x} \tag{2.11}$$

Equation (2.10) indicates that when the attenuation constant α_x is sufficiently low, it forms a long radiation aperture, consequently leading to higher gain and a narrower beamwidth. On the other hand, a high attenuation constant α_x implies rapid energy decay within the guiding structure. This phenomenon results in a shorter radiation aperture, leading to lower gain and a broader beam width.

If all unit cells of the 1D periodic LWA have the same leakage rate, the radiation efficiency can be calculated using the following formula:

$$\eta_r = 1 - e^{-2\alpha L} \tag{2.12}$$

where α represents the leakage rate, and L denotes the length of the open guiding structure. This equation considers only the energy loss due to radiation, assumes all energy leakage contributes to the antenna radiation pattern and ignores material losses.

The leakage rate of 1D periodic LWA unit cell can be calculated by stimulate N cascaded unit cells in a full wave electromagnetic simulation. The leakage rate α can then be determined by transmission coefficient S_{21} using the following equation:

$$\alpha = \frac{-In|S_{21}|}{Np} \tag{2.13}$$

It is important to note that this method does not consider the dielectric and ohmic losses.

In reality, the radiation efficiency η_r cannot reach $100\,\%$, because not all energy excited by the source is radiated in a finite length structure, and at the end of the guiding structure a portion of the energy remains. Reflection at this endpoint (called the termination) can contribute to unwanted radiation, possibly increasing the sidelobe level. If the remaining energy inside the LWA is still quite high, a matched load is usually mounted at the termination. An alternative solution involves reducing the energy at the end of the LWA to a sufficiently low level by ensuring most of the energy is radiated during the forward propagation. In a typical LWA design, an antenna length is chosen to ensure that more than 90% of the energy is radiated, which means less than -10 dB power remains at the end of the LWA [1].

In practice, the radiation aperture of a LWA is usually tapered to achieve a specific SLL. For instance, the radiation amplitude along the guiding structure at a specific frequency f_c is tapered using a Taylor distribution. To achieve this, the leakage rate $\alpha(x)$ of each unit cell as a function of the coordinate x can be calculated using the following formula [1]:

$$\alpha(x) = \frac{\frac{1}{2}A^2(x)}{\frac{1}{e_r}\int_0^L A^2(x)dx - \int_0^x A^2(x)dx} \tag{2.14}$$

where $A(x)$ denotes the desired Taylor distribution, L represents the length of radiation aperture and e_r is the radiation efficiency. Typically, a radiation efficiency of 0.9 is chosen to achieve a high total efficiency and prevent an impractically high leakage rate

of unit cells near the end of the LWA.

Given that $\alpha(x)$, the leakage rate of each unit cell, is a function of the operating frequency, the field distribution on the tapered aperture may change, and the SLL performance could gradually worsen as the frequency deviates from the centre frequency, f_c.

Moreover, it is important to note that when adjusting each unit cell for leakage rate manipulation, it becomes necessary to ensure that all unit cells have an equal propagation constant at the preset operating frequency, f_c. This is to ensure that all unit cells radiate at the same angle. Otherwise, radiation deviating from the intended direction may contribute to shoulders or sidelobes in the radiation pattern [1].

2.1.2. Eigenmode Selection and Open Stopband Suppression

In this thesis, an all-dielectric LWA is proposed, and the eigenmodes of the LWA unit cell are excited by a tapered dielectric slab waveguide. The efficiency of the LWA design significantly relies on the selection of these eigenmodes. More specifically, those eigenmodes that demonstrate effective coupling with the propagating mode inside the taper are preferred.

An overlap integral of the field distributions can be used to calculate mode coupling efficiency. The corresponding formula is as follows [7]:

$$\eta = \left| \mathrm{Re}\left[\frac{(\int \boldsymbol{E_1} \times \boldsymbol{H_n^*} \cdot d\boldsymbol{S})(\int \boldsymbol{E_n} \times \boldsymbol{H_1^*} \cdot d\boldsymbol{S})}{\int \boldsymbol{E_1} \times \boldsymbol{H_1^*} \cdot d\boldsymbol{S}} \right] \frac{1}{\mathrm{Re}(\int \boldsymbol{E_n} \times \boldsymbol{H_n^*} \cdot d\boldsymbol{S})} \right| \quad (2.15)$$

where $\boldsymbol{E_1}$ and $\boldsymbol{H_1}$ represent the electric and magnetic field of the mode propagating inside the taper, respectively. $\boldsymbol{E_n}$ and $\boldsymbol{H_n}$ represent the electric and magnetic field of

the n^{th} eigenmode of the unit cell, respectively.

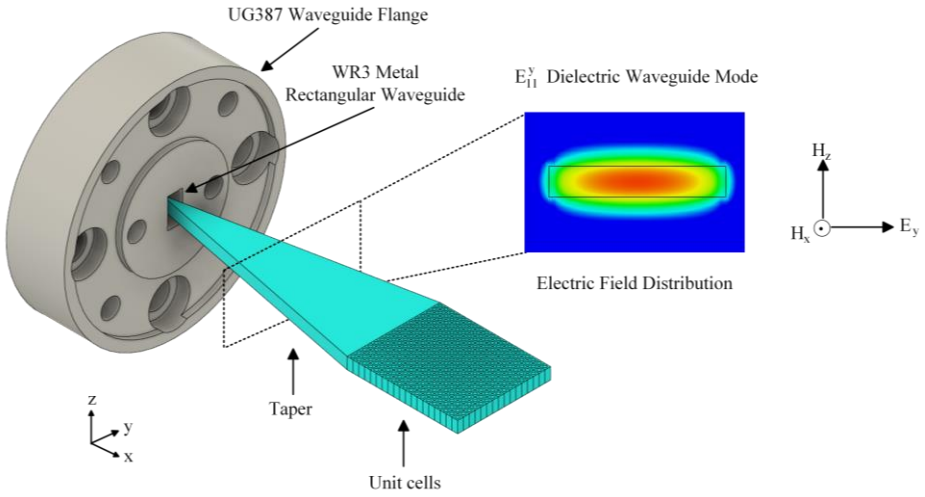

Figure 2.5. The unit cells are excited by the taper, and the E_{11}^{y} dielectric waveguide mode is coupled to the eigenmodes of the unit cell.

As shown in Figure 2.5, the taper is partially inserted inside the metal rectangular waveguide, and the E_{11}^{y} dielectric slab waveguide mode propagate along the taper is excited by the TE_{10} metal rectangular waveguide mode. The dominant field components of E_{11}^{y} dielectric waveguide mode are $\mathrm{E_y}$, $\mathrm{H_z}$ and $\mathrm{H_x}$. For brevity, only the E_{11}^{y} mode case is illustrated in Figure 2.5.

To ensure that 1D periodic LWAs can achieve backward and forward radiation, the eigenmodes of the unit cell must satisfy the following selection criteria: first, the phase fronts of the two chosen eigenmodes should be perpendicular to the propagation direction of the leaky wave. Additionally, if TE (TM) modes are chosen to implement leaky wave radiation, the main electric (magnetic) field component directions of the two eigenmodes need to be consistent to ensure the spatial field matching between the feeding structure and the eigenmodes, so that both selected modes can be excited simultaneously. These are the most fundamental mode selection and optimization rules

in the process of implementing the 1D periodic LWA unit cell design. The all-dielectric LWA proposed in this thesis is based on the selection criteria.

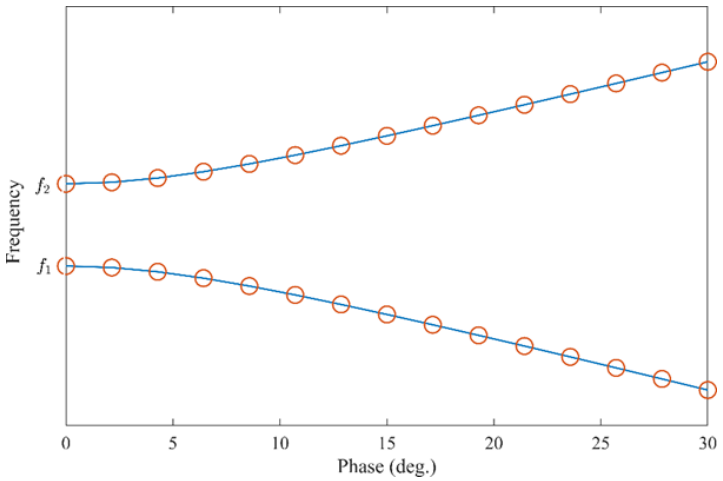

Figure 2.6. Dispersion diagram for the unit cell of an example 1D periodic LWA exhibiting a bandgap between the first two modes.

Beam pointing precisely in the broadside direction presents a challenge for traditional 1D periodic LWAs, a problem caused by the OSB. The stopband is typically situated within the frequency range where the 1D periodic LWA transitions from a backward radiating mode (negative phase constant) to a forward radiating mode (positive phase constant). To further analyse these modes as the frequency changes, the dispersion diagram is commonly used.

A dispersion diagram represents the relationship between wave vector and frequency for the eigenmodes within the unit cell. The horizontal axis typically displays the wave vector, indicating the direction and phase change of the eigenmode, while the vertical axis shows the corresponding frequency. In the dispersion diagram, each point represents an eigenmode that exists with the specific wave vector and corresponding eigenfrequency.

Figure 2.6 shows the dispersion diagram for the unit cell of an example periodic LWA. In this example, it can be seen that there are two modes which contribute to the

frequency scanning of the beam. The first mode corresponds to radiation in the backward direction while the second mode corresponds to the radiation in the forward direction. It can be observed in the dispersion diagram that a bandgap exists between the two modes at a 0-degree phase change between unit cells which corresponds to broadside radiation. Theoretically, no radiation occurs within the bandgap over the frequency range f_1 to f_2. Within this stopband, the antenna radiates very inefficiently or not at all. This issue arises because no eigenmode exists within the stopband, leading to most of the energy decaying and reflecting [1].

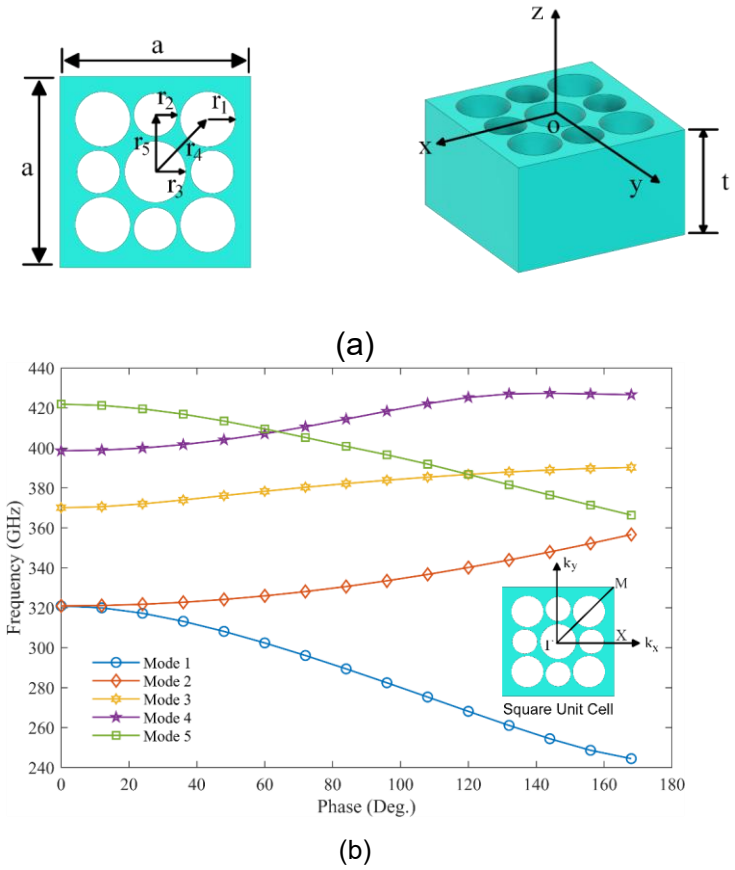

Figure 2.7. An example of an all-dielectric unit cell and the dispersion diagram of the unit cell. (a) The unit cell is formed by the perforation of circular holes in the dielectric block. (b) Dispersion diagram of the unit cell.

The bandgap's existence can also be attributed to mode coupling between two space

harmonics traveling in opposite directions [1].As a result, cancelling this mode coupling could close the bandgap, which means two eigenmodes of the unit cell must be degenerate and orthogonal to each other at the broadside radiation frequency.

Mode degeneracy can take two forms: deterministic degeneracy and accidental degeneracy. Deterministic degeneracy emerges due to the symmetry of the unit cell whereas accidental degeneracy arises due to an appropriately designed unit cell structure which depends on its exact geometry and permittivity of its constituents [8, 9].

As illustrated in Figure 2.7(a), an all-dielectric unit cell is proposed as an example to explain the unit cell design process. Periodic boundary conditions are set in $\pm x$ and $\pm y$ directions, and in $\pm z$ directions the boundary condition are set to be open to allow radiation from the unit cell. The “General (Lossy)” Eigenmode Solver method is utilized for the determination of the eigenfrequency and Q-factor of the eigenmodes. The permittivity of the unit cell is 11.7. The other structural parameters are as follows: $a = 0.5\ \mathrm{mm}, r_1 = 0.07\ \mathrm{mm},\ r_2 = 0.06\ \mathrm{mm}, r_3 = 0.08\ \mathrm{mm},\ r_4 = 0.19\ \mathrm{mm},\ r_5 = 0.15\ \mathrm{mm},\ t = 0.5\ \mathrm{mm}$.

As shown in Figure 2.7(b), although the bandgap between Mode 1 and Mode 2 appears to be closed, this "closed bandgap" is not actually helpful for achieving broadside radiation in a 1D periodic LWA because the mode degeneration between Mode 1 and Mode 2 is a result of the symmetry of the unit cell, which forms a deterministic degeneration, not an accidental degeneration. Further optimization of the unit cell is required to close the bandgap between Mode 1 and Mode 4.

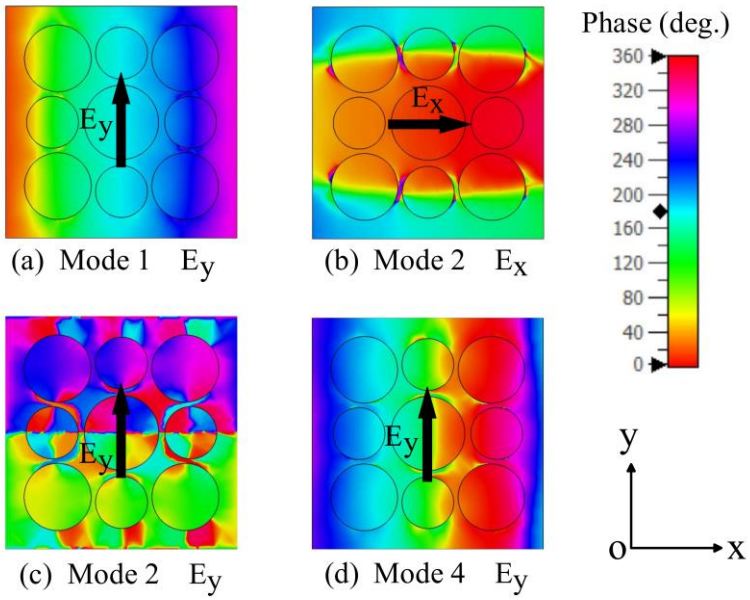

Figure 2.8: Plot of the electric field phase for several unit cell eigenmodes when $k_x = \frac{7}{18}\pi \; and \; k_y = 0$ as an example for mode profile inspection. (a) Phase of the y-component of the electric field for Mode 1. (b) Phase of the x-component of the electric field for Mode 2. (c) Phase of the y-component of the electric field for Mode 2. (d) Phase of the y-component of the electric field for Mode 4.

To maximise the coupling between the exciting dielectric slab E_{11}^{y} mode propagating in the antenna taper (as shown in Figure 2.5) and the radiating Bloch mode, we would like the two modes to have similar field characteristics.

In Figure 2.8, the spatial distributions of the phase across the unit cell for the specific electric field components of the eigenmodes are plotted. As illustrated in Figure 2.8(a), the phase front of $\mathrm{E_y}$ for eigenmode 1 is parallel to the y-axis and perpendicular to the propagation direction along the x-axis, and closely match the exciting dielectric slab E_{11}^{y} mode. As a result, Mode 1 can be chosen as the backward radiation leaky wave mode. Given that Mode 1 has been selected, the electric field component of the second eigenmode should also be parallel to the y-axis.

Mode 2 has a positive group velocity and appears capable of achieving forward

radiation as shown in Figure 2.7(b). However, as illustrated in Figure 2.8(c), the phase front of E_y for Mode 2 is not perpendicular to the x-axis, unlike Mode 1, which is shown in Figure 2.8(a). As a result, Mode 2 cannot be used as the second eigenmode and achieve beam scanning from the backward to forward direction.

As illustrated in Figure 2.8(d), E_y for Mode 4 is parallel to the y-axis and perpendicular to the phase increment direction on the x-axis. Consequently, Mode 4 meets the eigenmode selection criteria, and can be selected with Mode 1 to achieve beam scanning from backward to forward direction.

After identifying the two eigenmodes that can be used for the 1D periodic LWA design, further optimization of the physical dimensions of the unit cell is required to close the bandgap between the two selected eigenmodes. In fact, during the process of optimizing the unit cell, calculating and optimizing the leakage rate of the selected mode is also necessary. This will be described later in Chapter 4.

To date, various methods have been devised to suppress the open stopband and realize continuous beam scanning. In 1963, A. A. Oliner explained the connection between the symmetries in the periodic structure and mode-coupling [10]. According to Oliner, the glide and screw symmetry can be used to avoid certain pairs of mode-coupling and close the bandgap, but this kind of approach may not be useful for 1D periodic LWA design, because the degenerate modes protected by the symmetry are deterministic, as discussed above.

A double-strip grating leaky-wave antenna was proposed in 1993 by M. Guglielmi *and* D. R. Jackson [4]. This method places two metal strips within each unit cell to achieve a nearly closed bandgap. The notion that a bandgap cannot be entirely closed by incorporating an additional unit within a unit is discussed in [4]. A negligible stop band

still exist and the bandgap can be seen to be partially closed. In 2009, Simone Paulotto *et al* proposed another method to eliminate the open stopband [11]. A quarter-wave transformer or matching stub is used in this method to ensure the Bloch-wave impedance is real and non-zero at the broadside. Another paper proposed a similar method by introducing a π-network inside the unit cell to match the impedance [12].

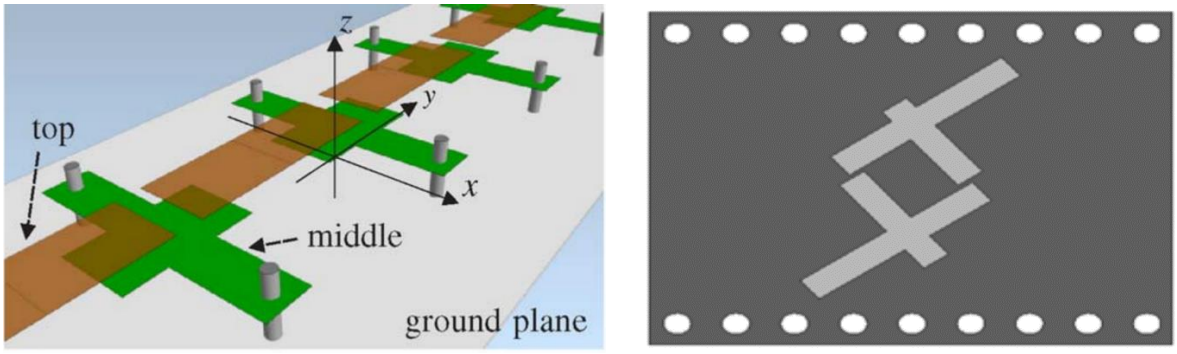

(a) (b)

Figure 2.9. LWA unit cells utilize transversal asymmetry to close the bandgap. (a) Unit cells of a PCB LWA, figure reproduced from [13]. (b) Unit cell of a LWA based on substrate-integrated waveguide, figure reproduced from [14].

An alternative approach to completely suppress the open stopband is proposed in [15], by using two non-identical elements within the unit cell. Tuning the distance between the elements and the dimension of one element will close the bandgap. Similarly, as shown in Figure 2.9, in the paper [13, 14], transversal asymmetry is introduced in the design of the unit cell to close the bandgap.

Another commonly used method to close the bandgap and achieve broadside radiation is to introduce Left-handed (LH) elements based on the transmission-line model [16-21]. For LWA based on the composite right/left-handed (CRLH) microstrip structure [18], the unit cell can be simplified as an equivalent-circuit model, which can be used to guide the optimization process and ensure that the unit cell achieves a closed bandgap design [22].

The methods to close the bandgap discussed above can be generalised into one singular strategy: the introduction of additional structure to the unit cell to ensure that the energy of the oppositely propagating waves cancel out at the broadside radiation frequency. This allows for the maintenance of in-phase excitation without significant reflection accumulation caused by each unit cell.

When considering the design of the additional structure, it is important to note that the energy diminishes as it travels through the LWA. As a result, the amplitude of the reflected wave differs from that of the wave traveling in the opposite direction. This difference in wave amplitudes implies that the physical dimensions of the introduced structure should not be identical to those of the original perturbation structure. This ensures that the counter-propagating waves are able to effectively cancel each other out. From another perspective, the newly introduced structure also imparts asymmetry to the unit cell, disrupting the deterministic degeneracy. The bandgap subsequently closes through the process of tuning the physical dimensions and inducing accidental degeneracy.

2.1.3. Dirac Leaky Wave Antenna (DLWA)

The Dirac cone, named after physicist Paul Dirac, signifies the linear dispersion relation near a Dirac point in materials like graphene [23-25]. This cone-shaped energy-momentum relationship is critical for understanding the electronic properties of materials, as it suggests high electron mobility and unique conductivity [26]. Represented in band structure diagrams, the Dirac cone highlights the fundamental quantum mechanical behaviors central to modern materials science applications.

Dirac dispersion properties have also been realized in photonic crystals [27-29] for

photons rather than fermions. In photonic crystals, at the Brillouin zone centre, the Γ point, a Dirac cone can be formed by the accidental degeneracy [28, 30]. With proper design, such photonic crystals can exhibit an effective zero refractive index at the Dirac frequency. On the other hand, Dirac cones at Brillouin zone boundaries are related to pseudo-diffusive transmission and other exotic propagation effects [31-33] but do not correspond to zero-refractive-index behaviour [30].

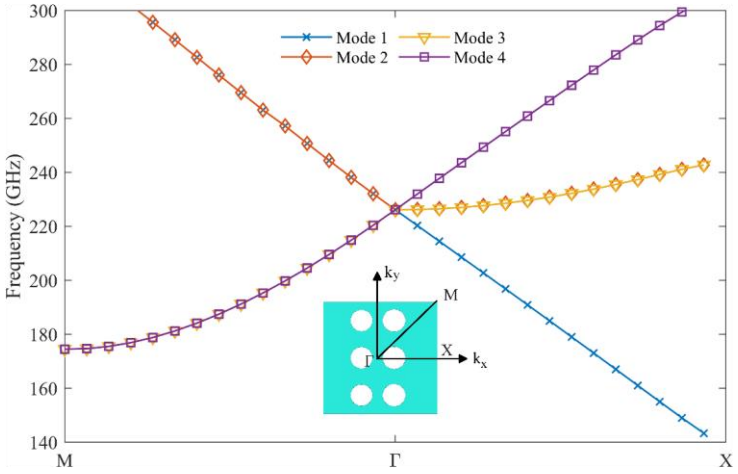

Figure 2.10: Dispersion diagram of the 2D photonic crystal shown in the inset. A Dirac dispersion characteristic can be observed for four modes which are degenerate at the Γ point, which is the center of the Brillouin zone.

As shown in Figure 2.10, four modes accidentally degenerate at the Γ point and forms a Dirac cone. The accidental degeneration occurs following the optimization of the unit cell structure. Detailed information on the physical dimensions and the process of optimizing the unit cell, shown in the inset of Figure 2.10, will be presented later in Section 3.3. Comparing this dispersion diagram with that illustrated in Figure 2.7(b), it can be seen that the bandgap between Mode 1 and Mode 4 is completely closed. In addition, the dispersion diagram exhibits linear dispersion in the zone between the Γ point and the X point. This is advantageous for beam-scanning in a LWA as the scan rate is constant with frequency. The dispersion diagram also implies that the mode

possessing the wave vector along the ΓX direction can possibly be employed for the design of 1D periodic LWAs.

Moreover, the form of the Dirac cone can be leveraged to suppress the open stopband. At the Γ point, the phase changes of the Bloch modes in all directions equal to $2\pi n$, where n can be any integer. This allows for the design of 1D periodic LWA capable of continuous beam scanning from backward to forward direction, which also covers the broadside direction [22]. Such a LWA can also be referred to as a DLWA [22, 34-36].

An additional critical aspect in the design process of the DLWA involves computing the leakage rate of the unit cell. As explained in Section 2.1.1, the maintenance of an appropriate leakage rate, neither excessively high nor low, within the working bandwidth is essential for the proper functioning of the DLWA. Furthermore, achieving the intended design of the radiation aperture necessitates an accurate calculation of this unit cell leakage rate.

Further elaboration on the methodologies for computing the phase constant and the leakage rate of the unit cell will be presented in the next section.

2.2. Dispersion Analysis Methods for LWAs

This section introduces three methods for performing dispersion analysis on 1D periodic LWA unit cell. The first method introduced is based on the T-matrix. In this method, a full-wave solver is used to calculate the T-matrix of an N-unit-cell structure, taking into account the mutual coupling of nearby unit cells. The dispersion properties can then be extract through the eigenvalue of the T-matrix of one unit cell. Following the method base on the T-matrix, the MPM for dispersion analysis is discussed. The

MPM is utilized to analyse and extract the dispersion properties by decomposing the sampled field data into a summation of decaying exponential functions. It operates by formulating a matrix from the sampled data, and then, through eigenvalue decomposition, yields the desired parameters. This method is particularly effective in the presence of noise and offers superior resolution. Finally, the dispersive analysis method based on using a complex eigenmode solver is introduced. This method not only supports periodic boundary conditions that consider the coupling between adjacent unit cells, but also supports open boundary conditions to account for the leaky wave mode radiation. This method directly provides the eigenfrequency of each eigenmode with a specific propagation constant, and the leakage rate can be calculated using the Q-factor, and the group velocity of the eigenmode. In this thesis, the eigenmode solver is employed to evaluate the design of the unit cell of DLWA, with the MPM and T-matrix method used as benchmarks for verification of the results.

2.2.1. Transfer Matrix Method

The T-matrix method extracts the propagation constant and leakage rate of the leaky wave mode from the T-matrix of one unit cell, which can be obtained through full wave electromagnetic simulation.

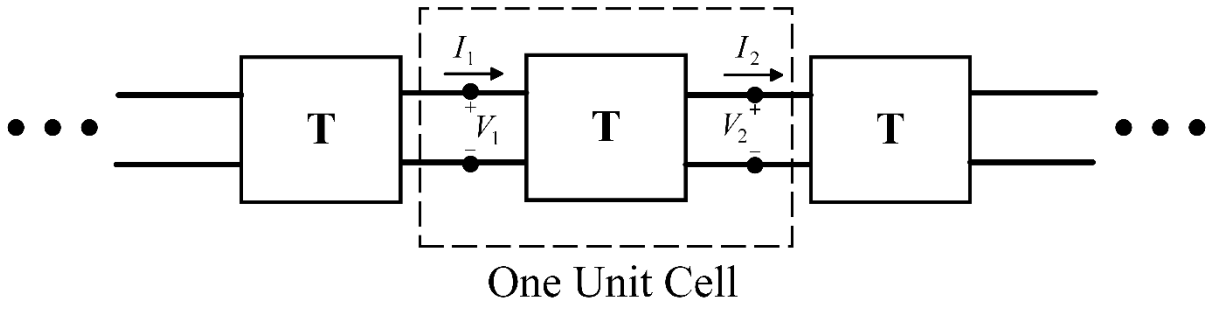

Figure 2.11: Equivalent T-matrix network of 1D periodic LWA unit cells cascaded together which is equivalent to having periodic boundary conditions in the simulation.

As depicted in Figure 2.11, the cascade of 1D periodic LWA unit cells can be characterized using an equivalent T-matrix network. The analysis begins with a simplified assumption: the periodic structure is built upon the background waveguide structure and only one single waveguide mode is under consideration. This structure allows the waveguide mode to excite the leaky wave mode [37]. Consequently, each 2-port unit cell can be represented by the T-matrix. We define the effective voltages V and currents I as shown in Figure 2.11. This formulation leads us to the following eigenvalue problem [37-40]:

$$[\boldsymbol{T}]\begin{bmatrix}V_1\\I_1\end{bmatrix} = \lambda\begin{bmatrix}V_1\\I_1\end{bmatrix} = e^{-jkp}\begin{bmatrix}V_1\\I_1\end{bmatrix} = \begin{bmatrix}V_2\\I_2\end{bmatrix} \tag{2.16}$$

where $k = \beta + j\alpha$ is the complex wavenumber of the leaky wave mode, p represent the periodicity of the unit cell, and $\lambda = e^{-jkp}$ is the eigenvalue of the T-matrix of the LWA unit cell. The two eigenvalues of the T-matrix of the unit cell corresponding to the wavenumbers of two oppositely propagating eigenmodes. The propagation constant β and leakage rate α of the unit cell can be expressed as follows [37]:

$$\beta_n = \frac{-\text{angle}(\lambda)}{p} - \frac{2\pi m}{p} \tag{2.17}$$

$$\alpha_n = \frac{\text{In}|\lambda|}{p} \tag{2.18}$$

where $angle$ is the function which returns the angle of the complex eigenvalue in the complex plane in the range of $(-\pi, \pi]$ and the value of m is an arbitrary integer, implying different possible Bloch modes for the propagation of the leaky wave within the unit cell.

It is important to note that typically, the full-wave simulation of a single unit cell is insufficient for accurately extracting the dispersive property of the leaky wave Bloch

mode. The limitation arises due to the requirement of considering the coupling between adjacent unit cells in the direction of periodicity. To adequately account for this mode coupling, we typically need to extract the T-matrix of N identical cascaded unit-cells through full-wave simulation [37, 39]. This approach ensures that the intricate interplay between nearby unit cells is factored into the final analysis.

After the full wave simulation of N unit-cells, T^N, the Nth power of the T-matrix for a single unit cell can be obtained. To proceed with the calculation of the leakage rate for a single unit cell, the following formula is used [37]:

$$\alpha = \frac{\mathrm{In}\left|\sqrt[N]{\lambda_N}\right|}{p} \tag{2.19}$$

where λ_N represents the eigenvalue of T^N, and the N^{th} root of it can be straightforwardly calculated.

However, when it comes to calculation of the propagation constant from the T-matrix, it is necessary to identify the correct N^{th} root of the eigenvalue from the T-matrix of N unit-cells [37]. To facilitate this identification, an additional full wave simulation for M-unit-cells needs to be conducted. This step involves comparing the N^{th} root values of λ_N and the M^{th} root values of λ_M to identify the correct root value $\lambda_{M,N}$, which is the common root value found in both sets. Consequently, the propagation constant of the Bloch mode can be calculated using the following formula [37]:

$$\beta_{M,N} = \frac{-\mathrm{angle}\left(\lambda_{M,N}\right)}{p} - \frac{2\pi m}{p} \tag{2.20}$$

where m is an integer that determines the chosen branch cut of the propagation constant.

The selection of the correct N^{th} root of the eigenvalue T^N may also be facilitated by the propagation constant of the background waveguide. However, the accuracy of this

method may be compromised if the periodic perturbations become overly intense [37].

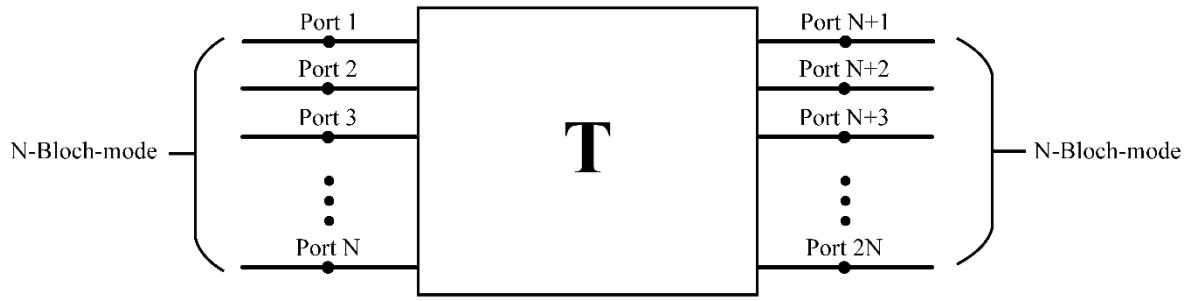

Figure 2.12: Equivalent network of the unit cell with $2N$-port. The unit cell is characterized by the $2N \times 2N$ T-matrix.

In a more general scenario, when considering the dispersive property of N Bloch modes of the unit cell, it is appropriate to employ the multimodal T-matrix method (MMTMM) as a tool for analysis. [40-42]. The eigenvalue problem can still be expressed using equation (2.16). However, in this case, the T-matrix transforms into a $2N \times 2N$ matrix, which corresponds to the equivalent $2N$-port network of the unit cell [39, 40], as illustrated in Figure 2.12.

To extract the wavenumber of N Bloch modes, a zero-searching method is employed to solve the following equations [39, 40]:

$$det(T - \Lambda) = 0 \tag{2.21}$$

$$\mathbf{\Lambda} = \begin{bmatrix} e^{-jkp} & 0 & \cdots & 0 & 0 \\ 0 & e^{-jkp} & & 0 & 0 \\ \vdots & & \ddots & & \vdots \\ 0 & 0 & & e^{-jkp} & 0 \\ 0 & 0 & \cdots & 0 & e^{-jkp} \end{bmatrix} \tag{2.22}$$

where $\mathbf{\Lambda}$ is a $2N \times 2N$ diagonal matrix. At each discrete frequency point, the complex wavenumber $k = \beta + j\alpha$ is determined through a zero-searching process in the complex plane [39]. During the search process, the wavenumber k that fulfils condition (2.21) will be located, allowing for the determination of the dispersive properties of the unit cell.

2.2.2. Matrix Pencil Method

The MPM is an eigen-based technique employed for approximating a function as a sum of complex exponentials, particularly used to extract the poles and residues of these signals from a finite set of sampled data points [43].

The application of the MPM has various uses, including identifying and extracting the parameters of exponential signals buried in noise [43-45], estimating the angle of arrival of signals [46], and reducing the number of elements in an antenna array [47].

The MPM can also be employed to estimate both the leakage rate and the propagation constant of the modes that propagate within the guiding structure of the LWA. This can be achieved by analysing a component of the sampled field data obtained either from full-wave simulation or measurement.

Assuming propagation of the leaky mode within the LWA in the x direction, the sampled complex electric field component can be formulated as:

$$E_n = E(x = np) = \sum_{i=1}^{M} R_i Z_i = \sum_{i=1}^{M} R_i e^{-jk_i np}, n = 1,2\ldots, N \tag{2.23}$$

where E_n represents the n^{th} sample of the complex electric field data, M stands for the number of mode components, $k_i = \beta_i + j\alpha_i$ denotes the complex wavenumber of the leaky wave mode of index i, $Z_i = e^{-jk_i np}$ denotes the phase factor of i^{th} mode components, p the perturbation period, and R_i represents the complex amplitude of the i^{th} mode component.

A matrix $\boldsymbol{D}$ can be formed by the sampled data E_n as follows:

$$\boldsymbol{D} = \begin{bmatrix} E_1 & E_2 & \cdots & E_{L+1} \\ E_2 & E_3 & \cdots & E_{L+2} \\ \vdots & \vdots & & \vdots \\ E_{N-L} & E_{N-L+1} & \cdots & E_N \end{bmatrix} \tag{2.24}$$

where L denotes the pencil parameter. The value of L is typically chosen to fall within the range $\frac{N}{3}$ to $\frac{N}{2}$. This range is chosen to minimise the noise influence that arises from the sampled data [43].

The singular values of the matrix $\boldsymbol{D}$ can then be derived by implementing a singular value decomposition (SVD) on $\boldsymbol{D}$. This process can be expressed as follows [43]:

$$\boldsymbol{D} = \boldsymbol{USV}^{\mathrm{H}} \tag{2.25}$$

where the superscript H denotes the conjugate transpose, $\boldsymbol{U}$ and $\boldsymbol{V}$ are unitary matrices, and $\boldsymbol{S}$ is a diagonal matrix, denoted as $\boldsymbol{S} = diag([S_1, S_2, S_3, \cdots, S_N])$. Each diagonal element S_i corresponds to a singular value associated with matrix $\boldsymbol{D}$.

To extract the M mode components from the sampled data and minimize the influence of the noise, $\boldsymbol{V}$ is reconstructed with the right-singular vectors that corresponds to the largest M singular values:

$$\boldsymbol{V}' = [v_1, v_2, \cdots, v_M] \tag{2.26}$$

where $\boldsymbol{V}'$ denotes the reconstructed $\boldsymbol{V}$ matrix. Two additional matrices, denoted as $\boldsymbol{V_1'}$ and $\boldsymbol{V_2'}$, can be derived from $\boldsymbol{V}'$. Specifically, $\boldsymbol{V_1'}$ is obtained by removing the last row of $\boldsymbol{V}'$, while $\boldsymbol{V_2'}$ is obtained by eliminating the first row of $\boldsymbol{V}'$ [48].

Then with the reconstructed matrix $\boldsymbol{V_1'}$ and $\boldsymbol{V_2'}$, it is possible to have:

$$\boldsymbol{D_1} = \boldsymbol{US'}(\boldsymbol{V_1'})^{\boldsymbol{H}} \tag{2.27}$$

$$\boldsymbol{D_2} = \boldsymbol{US'}(\boldsymbol{V_2'})^{\boldsymbol{H}} \tag{2.28}$$

where $\boldsymbol{S'}$ denotes a diagonal matrix, wherein the diagonal entries represent the M largest singular values [43].

Finally, the phase factors Z_i can be obtained by solving the following generalized eigenvalue problem [48]:

$$\boldsymbol{D_1} b = Z \boldsymbol{D_2} b \tag{2.29}$$

where b represents the corresponding eigenvectors. The complex wavenumber for the dominant M mode components can then be calculated with:

$$k_i = \frac{ln\, Z_i}{p} = \beta_i + j\alpha_i, i = 1,2, \cdots M \tag{2.30}$$

Once the complex wavenumbers have been calculated, the complex amplitude of the dominant M mode components can be derived. This is accomplished by setting up and solving a least-squares problem, which is formulated based on the reconstruction of (2.23). For this reconstruction, the solved phase factors Z_i are utilised [43].

2.2.3. Complex Eigenmode Solver

The eigenmode solver within CST Microwave Studio (CST MWS) has recently been enhanced through the implementation of the so called *General Lossy Method*. This update makes the utilization of open boundary conditions possible in the context of eigenproblem solutions. Consequently, it facilitates the analysis of radiation associated with the periodic LWA unit cell.

The solution from the eigenmode solver is a complex angular eigenfrequency ω_c, dependent on the wavenumber k. The Q-factor of the unit cell is derived from the imaginary part of ω_c, corresponding to the radiative loss of the unit cell. This relationship can be expressed mathematically as follows [49]:

$$\omega_c = \omega_c(k) = \omega_r + j\omega_i = \omega\left(1 + j\frac{1}{2Q}\right) \tag{2.31}$$

where $\omega_r = \omega$ is the real part of the complex angular eigenfrequency, and ω_i is the imaginary part of the complex angular eigenfrequency.

However, the eigenmode solver of the CST MWS does not directly provide the

leakage rate α. Consequently, post-processing is required to calculate the leakage rate α for the unit cell. Through a Taylor expansion of $\omega_c(k)$ in the complex plane, the wavenumber $k(\omega) = \beta + j\alpha$ can be expanded as a function of ω as follows [50]

$$k(\omega) = \beta + j\omega_i \frac{d\beta}{d\omega}. \tag{2.32}$$

Then the leakage rate of the unit cell can be related to the complex frequency ω_c by:

$$\alpha = \frac{2\omega_i}{V_g} \tag{2.33}$$

where $V_g = \frac{d\omega}{d\beta}$ is the group velocity. The leakage rate α of the unit cell can be expressed from (2.32) and (2.33) as:

$$\alpha = \frac{\pi f}{V_g Q} \tag{2.34}$$

where $f = \omega/2\pi$ is the eigenfrequency provided by the eigenmode solver. The group velocity is obtained from the numerical derivative of the dispersion curve.

2.3. Fabry Perot Cavity Antenna Theory

A FPCA is a type of antenna that utilizes a resonant cavity to reshape the radiation pattern of its primary source. It is recognized for its high gain and low-profile attributes [51]. Various studies indicate its potential in mobile communications [52-55], WiBro and WLAN applications [56-58], among others [59-61]. As illustrated in Figure 2.13, for most designs of FPCA, the key components include the primary source, metal ground or high impedance surface, and the Partially Reflective Surface (PRS). Radiation waves emitted from the primary source undergo multiple reflections within the resonant cavity formed by both the PRS and the metal ground. This repeated reflection process reshapes the wavefront and allows for the energy to be spread over a wide transverse

area, yielding a radiation pattern gain that exceeds that of the primary source.

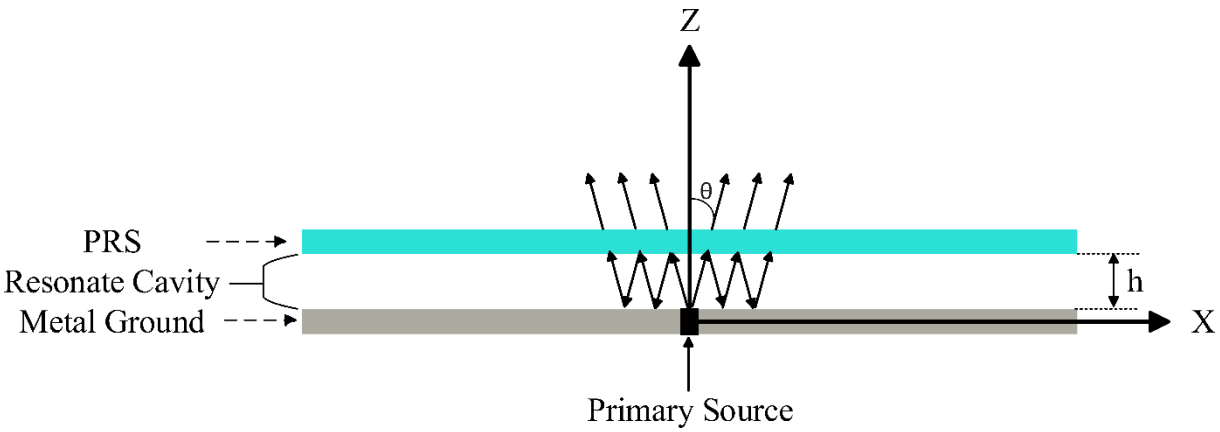

Figure 2.13: Schematic of the FPCA showing the operating principles: a primary source is coupled to a resonant cavity defined by the PRS and metal ground. The antenna radiates by way of the resonant cavity leaking energy through the PRS.

The primary source can manifest as either a singular radiating element or a radiating antenna array. Potential radiating elements encompass the coaxial antenna, loop antenna, orthogonal (90°) coaxial antenna, and the slotted waveguide antenna [51].

As shown in Figure 2.13, from a ray optics perspective, when the radiation beam is pointing to broadside, the air resonant cavity's thickness h is given by:

$$\varphi_{PRS} + \varphi_{gnd} - \frac{4\pi}{\lambda_0} h = 2n\pi, \qquad n = 0, \pm 1, \pm 2 \ldots \tag{2.35}$$

where φ_{PRS} is the reflection phase of the PRS, $\varphi_{gnd} = -\pi$ is the reflection phase of the metal ground, and λ_0 is the working wavelength in free space. This ensures consistent phase distribution in the radiation aperture, leading to higher radiation directivity. In the case when the reflection phase of PRS is close to the metal ground, the resonant cavity's thickness will be about $0.5\lambda_0$ [51].

PRS can be realized using various configurations, including dielectric substrates [62], metallic meshes [63], or periodic metal patches on dielectric substrates [64]. A

thorough analysis, characterization, and optimization of these PRS configurations can improve the overall performance of the FPCA.

The enhancement in directivity, resulting from the use of PRS, can be determined using the equation:

$$D_{PRS} = 10\log_{10}\frac{1+R}{1-R},\ 0 < R < 1 \tag{2.36}$$

where R represents the reflection magnitude of the PRS. Equation (2.36) indicates that higher reflection magnitude from the PRS leads to an increase in antenna directivity. However, this assumes that the PRS and the metal ground are sufficiently large in the transverse direction, meaning that at the boundary of the PRS, the energy must have decayed to less than -10 dB relative to the primary source.

The Q-factor of the resonator formed by the PRS and metal ground can be calculated with the following equation:

$$\mathrm{Q} = \frac{-\pi}{\ln(\mathrm{R})} \tag{2.37}$$

Equation (2.37) implies that higher reflection magnitude will lead to a high Q-factor. As a result, high directivity of the FPCA is accompanied by strong resonance within its cavity, implying a narrow bandwidth for the FPCA.

Typically, the fractional bandwidth of a FPCA is a few percent, this bandwidth is inversely proportional to the antenna's directivity. As a result, the product of the gain and fractional bandwidth is a valuable metric for evaluating the FPCA's performance.

In this thesis, the 3 dB gain bandwidth product (GBWP) is defined as follows:

$$GBWP = \left(\frac{BW}{f_c}\right) \times 100 \times 10^{G/10} \tag{2.38}$$

where BW signifies the 3 dB gain bandwidth, f_c denotes the center frequency of the BW, and G represents the antenna gain in decibels.

As discussed in Section 2.1.1, from a LWA perspective, the FPCA is fundamentally a 2D LWA. The radiative energy originating from the primary source undergoes a progressive attenuation during its radial propagation. In the terahertz band, the commonly used primary sources are the open-ended waveguide or modified waveguide fed slot for impedance matching, which will launch both TE and TM cylindrical leaky wave modes inside the cavity. Although various high-order modes are launched, the far-field radiation pattern of the FPCA is primarily determined by the 0^{th} and 1^{st} order leaky wave modes [65, 66].

The far-field radiation pattern of FPCA corresponding to the TE mode in spherical coordinates (r, θ, φ) is [1]:

$$E_\theta(r, \theta, \varphi) = R(r)\, cos\, \theta\, cos\, \varphi\, C(\theta) \tag{2.39}$$

$$E_\varphi(r, \theta, \varphi) = -R(r)\, sin\, \varphi\, P_1(\theta) \tag{2.40}$$

In the spherical coordinates, r represents the radial distance, θ is the polar angle, and φ is the azimuthal angle. The far-field radiation pattern for the TM mode is [1]:

$$E_\theta(r, \theta, \varphi) = R(r)\, cos\, \theta\, cos\, \varphi\, P_1(\theta) \tag{2.41}$$

$$E_\varphi(r, \theta, \varphi) = -R(r)\, sin\, \varphi\, C(\theta) \tag{2.42}$$

In both cases,

$$R(r) = -\frac{j\omega\mu_0}{4\pi r} e^{-jk_o r} \tag{2.43}$$

$$P_1(\theta) = \frac{2j}{k_\rho} - \frac{4jk_\rho}{k_\rho^2 - k_o^2\, sin^2\, \theta} \tag{2.44}$$

$$C(\theta) = \frac{-2j}{k_\rho} \tag{2.45}$$

where $k_\rho = \sqrt{{k_x}^2 + {k_y}^2} = k_o(\beta - j\alpha)$ represents the transverse complex wavenumber of the cylindrical leaky waves, k_o represents the free space wavenumber,

β denotes the normalized phase constant and α represents the normalised leakage rate. Consequently, the radiation pattern can be ascertained by analysing the k_ρ^{TE} and k_ρ^{TM} values of both the 0th and 1st order leaky wave modes [65]. The TRM can be used to perform a dispersion analysis of the leaky waves propagating inside the resonant cavity. This topic will be discussed in the next section.

As illustrated in Figure 2.13, the beam pointing angle, denoted as θ is shown. When the leakage rate of the cylindrical leaky wave undergoes weak attenuation, the beam pointing angle θ can be determined by the following relationship:

$$\theta = \sin^{-1}\frac{k_\rho}{k_o} \tag{2.46}$$

Consequently, for the FPCA, beam scanning is feasible by adjusting the frequency. When the radiation angles for both TE (H-plane) and TM (E-plane) modes are close to zero, the two symmetric beams coalesce to form a broadside pencil beam.

To point a pencil beam towards the broadside, nearly degenerate TE and TM cylindrical leaky wave modes must be excited, satisfying the following conditions [1]:

$$k_\rho^{TE} \approx k_\rho^{TM} \tag{2.47}$$

$$\beta_{TE} \leq \alpha_{TE} \tag{2.48}$$

$$\beta_{TM} \leq \alpha_{TM} \tag{2.49}$$

It is noteworthy that as the frequency increases and the phase constant β exceeds the leakage rate α, the pencil beam will then split, resulting in a conical radiation pattern. In this context, $\beta_{TE} \approx \alpha_{TE} \approx \beta_{TM} \approx \alpha_{TM}$ delineates the beam splitting condition for the FPCA [1].

The directivity bandwidth product (DBWP) of a simplified FPCA design as shown in Figure 2.13 is given by [67]:

$$D \times FBW \approx \frac{2.47}{\varepsilon_r} \tag{2.50}$$

where FBW denotes the fractional bandwidth of the FPCA, and ε_r is the permittivity of the material that fills the resonant cavity. As a result, low permittivity dielectric materials are preferred to achieve a higher directivity-bandwidth product. The bandwidth limitation in maintaining the directivity of the FPCA arises from its inherent resonance characteristics. At both the lower and upper bounds of the 3 dB directivity bandwidth, the pencil beam bifurcates into two conical beams, leading to a reduction in directivity.

In the existing literature, researchers have proposed various optimization techniques to address these constraints and enhance the GBWP or the DBWP. One technique to enhance the 3 dB gain bandwidth of a FPCA involves optimizing the unit cell of the PRS. As elucidated in [68], the unit cell exhibits a reflection phase curve versus frequency with a positive slope. This leads to the presence of multiple resonant points that satisfy the broadside radiation condition, subsequently broadening the operational bandwidth.

Furthermore, a tapered PRS with gradient index (GRIN), can also facilitate broadside radiation resonance over an expanded bandwidth. In [69, 70], a PRS, featuring a radial gradient in permittivity is utilized to compensate the phase front across the aperture, thus attaining a greater 3 dB GBWP [71]. This tapered PRS can also be achieved by manipulating the effective permittivity of the unit cell. This manipulation can be achieved by altering the air filling rate, obviating the need for material modifications during PRS fabrication. In Chapter 4, a terahertz band FPCA, 3D-printed with all-dielectric PRS, is proposed. This design adopts the aforementioned method to achieve a broader 3 dB GBWP.

Besides optimizing the design of the PRS, a broader GBWP can also be attained by

optimising the shape of the resonant cavity. Several techniques can be employed, including integrating the resonant cavity with a spherically modified geometry [72], incorporating a conical horn [73], or introducing a trapezoid shape at the edge of the metal ground [71]. These adjustments can gradually modify the reflective phase, thereby achieving a wider bandwidth resonance.

2.4. Transverse Resonance Method

In this section, the fundamental principles of the TRM are presented. Throughout this thesis, TRM is employed for modal analysis of leaky wave modes in FPCA resonant cavities. The TRM models the resonant cavity, PRS, and metal ground as an equivalent transmission line model (TLM). This modelling approach gives rise to the Transverse Resonance Equation (TRE) and a dispersion analysis of modes propagating within the resonant cavity can be conducted by numerically solving the transcendental TRE.

The versatility of the TRM extends beyond the aforementioned application. While it effectively analyses LW modes in open resonant cavities, it can also evaluate resonant modes within closed waveguide structures, given that these have a uniform cross-sectional profile [74].

As illustrated in Figure 2.14, the cross-section of the simplified FPCA model comprises a PRS and a metal ground. The reference plane, as delineated in Figure 2.14, is selected at the interface between the PRS and the air cavity, specifically for the TRM analysis.

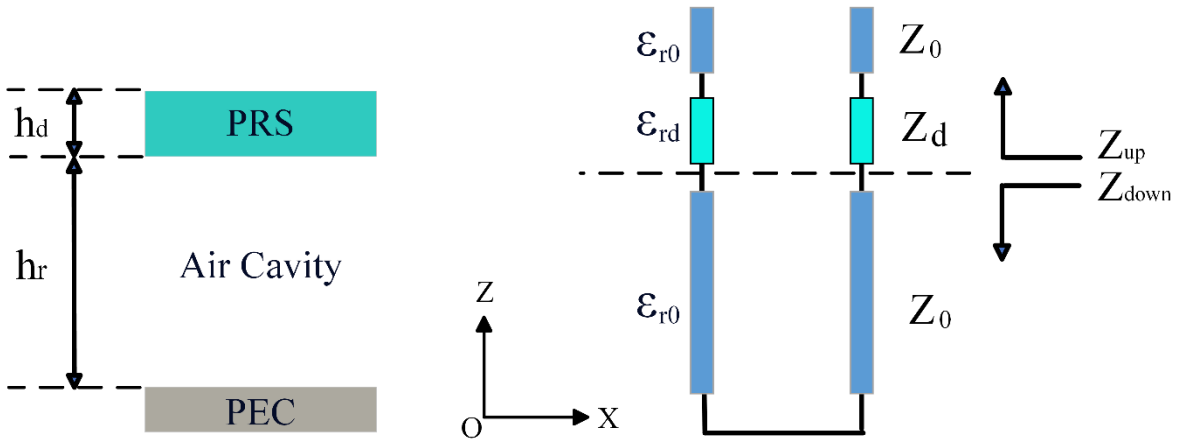

Figure 2.14: Cross-section of the air cavity formed by PRS and PEC reflective ground and corresponding TLM for TRM analysis.

The characteristic impedance with TLM is given by:

$$Z_0 = 120\pi \tag{2.51}$$

$$Z_d = \frac{Z_0}{\sqrt{\varepsilon_{rd}}} \tag{2.52}$$

For modes that propagate within the air cavity, it is assumed there is no variation in the Y direction, the Z component of the wavenumber can be defined by the following equation:

$$k_{z_0} = \sqrt{{k_0}^2 - {k_x}^2} \tag{2.53}$$

$$k_{z_d} = \sqrt{{k_d}^2 - {k_x}^2} \tag{2.54}$$

Here, k_{z_0} denotes the Z component of the wavenumber corresponding to the resonant modes in the air cavity. Meanwhile, k_{z_d} signifies the Z component of the wavenumber for the resonant modes within the PRS.

The characteristic impedance encountered by both TE and TM resonant modes is intrinsically related to the wavenumber. This relationship can be articulated as follows:

$$Z_0^{TE} = \frac{k_0}{k_{z_0}} Z_0 \tag{2.55}$$

$$Z_d^{TE} = \frac{k_d}{k_{z_d}} Z_d \tag{2.56}$$

$$Z_0^{TM} = \frac{k_{z_0}}{k_0} Z_0 \tag{2.57}$$

$$Z_d^{TM} = \frac{k_{z_d}}{k_d} Z_d \tag{2.58}$$

For both TE and TM modes, the input impedance above the reference plane can be expressed as:

$$Z_{up} = Z_d^{TE/TM} \left(\frac{Z_0^{TE/TM} + jZ_d^{TE/TM} \tan(k_{z_d} h_d)}{Z_d^{TE/TM} + jZ_0^{TE/TM} \tan(k_{z_d} h_d)} \right) \tag{2.59}$$

For both TE and TM modes, the input impedance beneath the reference plane can be represented as:

$$Z_{down}^{TE/TM} = jZ_0^{TE/TM} \tan(k_{z_0} h_r) \tag{2.60}$$

In scenarios where the leaky wave radiation beam's orientation is near the broadside direction, k_{z_d} can be approximated by k_{z_0}. Finally, the TRE can be formulated as:

$$Z_{up} = -Z_{down} \tag{2.61}$$

Upon formulation of the TRE, the numerical complex root-finding technique can be employed to determine the wavenumber of the resonance modes.

2.5. Fundamentals of 3D Printed Antenna

Additive manufacturing (AM), commonly referred to as 3D printing, offers enhanced flexibility in fabricating antennas with intricate geometries, and is often considered advantageous in terms of being both environmentally friendly and cost-efficient due to

less waste and more efficient use of material. Furthermore, 3D printing of antennas offers a rapid method for validating a proof of concept in antenna design. This is crucial for researchers engaged in antenna design and verification. In this section, an overview of the commonly used 3D printing technologies for antenna fabrication is provided. This background information is used to inform the FPCA antenna design presented in Chapter 4.

The four predominant AM processes most utilized in antenna design are fused deposition modelling (FDM), stereolithography (SLA), jet modelling (JM), and selective laser sintering (SLS) [75]. Each of these additive manufacturing processes possesses unique attributes. Specifically, FDM is recognized for its cost-effectiveness and adaptability [76], whereas SLA is distinguished by its enhanced resolution and precision [77].

2.5.1. Fused Deposition Modelling (FDM)

Fused Deposition Modelling (FDM) offers a significant cost advantage over other 3D printing techniques [77]. This is largely attributed to contributions from open-source communities and commercial ventures, resulting in competitively priced FDM-based printers [78]. Furthermore, thermoplastic filaments, integral to the FDM process, are cost-effective consumables. In the FDM printing process, continuous filaments of thermoplastic polymers are mechanically fed to the extrusion nozzle, where they are melted. Guided by a precision stepper motor, the nozzle follows a pre-programmed path on a horizontal plane to print a two-dimensional layer. Subsequently, it ascends vertically (or the model descends) and initiates the deposition of the succeeding layer. This sequence continues until the entire object is fabricated [75-78].

While FDM boasts rapid print cycles, the layer-by-layer deposition can introduce mechanical vulnerabilities within the printed assembly [77]. Commercial FDM systems typically achieve resolutions between 100-300 microns. Through meticulous system optimization, resolutions between 50 and 70 microns can be achieved. However, achieving sub-100 micron resolution necessitates significant modifications beyond standard commercial FDM capabilities [79]. Consequently, FDM printed structures typically display a coarse surface finish. However, this can be ameliorated through techniques such as mechanical sanding or chemical etching to improve the surface texture. Furthermore, a conductive layer can be applied to the printed structure using a metallization process, such as electroplating process, conductive spray coating, enabling the fabrication of antennas requiring conductive surface [75, 76].

Over the years, FDM 3D printing techniques have been employed in the manufacture of various antennas. Nevertheless, the inherent limitations in the print resolution of the FDM process restrict the operational frequency range of antennas fabricated using this method. In [80], Yao *et al.* present the design and fabrication of Ka band pyramidal horn antennas operating at 28 GHz using FDM 3D printing. The antennas are based on a standard gain horn designed for 20 dBi gain. Two metallization techniques are explored, copper tape and conductive copper paint applied to the 3D printed plastic substrate. This work demonstrates the feasibility of fabricating millimetre-wave antennas using low cost FDM 3D printing and metallization. Similarly, in [81], a lightweight X-band waveguide horn antenna using FDM 3D printing and conductive spray coating is proposed.

In addition, the simple FDM printing process enables rapid prototyping of GRIN lens antennas. Through the control of the dielectric filling ratio within individual unit cells, it

becomes feasible to achieve precise modulation of the effective permittivity. In [82], Kim et al. propose a lightweight 3D-printed GRIN lens antenna for millimetre-wave applications. The lens is fabricated using FDM with polylactic acid (PLA) filament. The GRIN profile is achieved using hollow honeycomb unit cells. The lightweight fractal lens fed by a Yagi antenna demonstrates stable gain performance from 24 to 32 GHz.

2.5.2. Stereolithography (SLA)

SLA was invented in 1986 and is among the earliest 3D printing technologies developed [77]. During the printing process, a UV light source is directionally projected onto the surface of a UV-curable resin or monomer solution. The resin or monomer solution, upon exposure to the UV light within the targeted area, undergoes a polymerization chain reaction, resulting in its transformation into a polymer which then solidifies. By precisely controlling the area and scanning path of the UV exposure, the shape of each solidified layer post-printing can be controlled. Subsequently, by adjusting the depth at which the solidified structure is submerged inside the resin, the thickness of the subsequent layer is determined. The combination of a thin layer thickness and a high-resolution laser ensures a smooth surface finish in SLA-printed parts [75, 83].

After the printing process is completed, it is essential to remove any uncured resin from the printed structure. However, the liquid resins require cautious handling due to toxicity. Additionally, for certain printed structures, it may be necessary to continue exposing them to a UV light source or apply heat until they are fully cured to enhance their mechanical strength [77]. By introducing ceramic or silica particles into a photosensitive resin or a monomer solution, it becomes feasible to achieve the SLA

printing of structures made from ceramic or silica composite materials [84-86]. SLA can achieve resolutions as precise as 10 microns, while most prints can achieve up to 25 microns resolution [75, 87].

In the typical design process of composite photosensitive resins, their potential application in antenna manufacturing has often been overlooked. As a result, prior to the design of a 3D printed antenna, it becomes necessary to characterize the electromagnetic properties in-house, specifically focusing on parameters such as permittivity and loss tangent.

The effectiveness of SLA in fabricating complex antenna structures for millimetre-wave frequencies is evidenced by various studies. Tak *et al.* [88] introduced a 3D printed W-band slotted waveguide array antenna, monolithically fabricated using SLA with an acrylate-based photopolymer resin. It was metallized with silver via a jet spraying process, demonstrating a gain of 22.5 dBi and a sidelobe level of -13.5 dB at 78.7 GHz. In [89], Lomakin et al. present the design, fabrication and measurement of a 3D printed 77 GHz helical antenna using SLA. In [90], Palomares-Caballero *et al.* present the design and fabrication of a multilayer aperture antenna array operating at 70 GHz based on glide-symmetric holey gap-waveguide technology and split E-plane waveguides. The array is fabricated using high-precision SLA with subsequent copper plating, demonstrating the potential of SLA for low-cost, lightweight manufacturing of multilayer antennas at millimetre-wave frequencies.

2.5.3. Jet Modelling (JM)

Jet Modelling (JM), Multi Jet Modelling (MJM) or Multi Jet Printing (MJP), is an AM technique that uses inkjet printhead to jet photopolymer materials in a layer-by-layer

manner to build 3D objects. The printheads selectively deposit droplets of liquid photopolymer and wax-based support material onto a build platform. The photopolymer immediately cures and solidifies due to UV light exposure. MJP allows for high accuracy and detailed resolution down to 16 microns layer thickness. Parts can be printed with complex geometries without the need for support structure [75, 91-93]. Once the full 3D geometry is complete, the wax support material is melted and drained away in a post-processing step, leaving only the hardened photopolymer part. MJP enables the fabrication of intricate shapes with fine details not achievable through traditional fabrication processes. The rapid solidification of the photopolymer layers produces minimal internal stresses, avoiding warpage distortion issues faced in other additive methods involving material cooling. MJP is suited for prototyping and low-volume manufacturing of end-use polymer parts, with applications ranging from design validation to tooling patterns and functional end products. MJP offers several advantages including high resolution, multi-material capabilities, reduced material waste, and low temperature operation. However, the MJP process is currently limited to photocurable polymers, which have inferior mechanical strength compared to traditional materials and require post-processing, such as UV post-curing, to achieve a finer surface finish [91, 92].

The advanced design of JM printers allows the integration of multiple nozzles, potentially numbering in the hundreds, into one printhead. Such a configuration provides increased flexibility, enabling instantaneous material changes during the printing stage [75]. Consequently, it becomes possible to adjust the permittivity in specific areas of a 3D-printed antenna during its fabrication process.

In [94], three lenses were fabricated using a MJM 3D printer with a proprietary plastic

material, VisiJet. The study indicates that MJM is a viable rapid fabrication technique for terahertz lens antennas. Nonetheless, optimization of lens designs and material selection is essential to reduce dielectric losses.

2.5.4. Selective Laser Sintering (SLS)

Selective Laser Sintering (SLS) is a type of 3D printing technique within the Power Bed Fusion category, which also includes Selective Laser Melting (SLM), Electron Beam Melting (EBM), Direct Metal Laser Melting (DMLM) and Direct Metal Laser Sintering (DMLS) [83], but the most commonly used methods among them for antenna fabrication is SLS [75].

SLS employs a meticulous process wherein a carefully prepared powder, spanning a variety of materials like polymers, metals, or alloys, is spread on a build platform. A high-energy laser selectively sinters the powder within the focused area, causing molecular-level fusion without fully melting the particles. After sintering one area, the laser moves to the next specified point, progressively completing the 2D layer. Once this layer is finished, a roller evenly spreads another layer of powder over the build platform. The laser then continues the sintering process for this new layer, sintering the powder in the defined areas. This layer-by-layer approach is repeated until the entire three-dimensional structure is precisely fabricated [95]. The mechanism empowers the production of parts characterized by uniform density and notable mechanical properties, albeit often necessitating post-processing due to surface roughness considerations [77].

In [96], Ferrando-Rocher et al. demonstrated a dual-band antenna array for K and Ka bands using SLS metal 3D printing. While SLS exhibited minor inefficiencies due to

surface roughness compared to CNC, it provided comparable performance in a reduced time for antenna sample fabrication. Consequently, despite its precision and surface finish challenges, SLS offers a promising method for producing flat panel antennas at microwave frequencies.

2.5.5. Two-photon Polymerization (2PP)

The concept of 3D printing through 2PP was first proposed by Göppert-Mayer in 1931 [97, 98]. As shown in Figure 2.15(a), during the printing process, the photosensitive material solidifies only at the focal volume of the laser pulse illumination due to the simultaneous absorption of two photons when the energy exceeds a certain threshold, leading to a polymerization reaction. This process is termed as Two-Photon Absorption (TPA) [99]. The volume where energy exceeds the threshold are referred to as polymerization voxels. In areas outside the focal volume, even though they are within the beam of laser illumination, the photosensitive material remains unsolidified because the energy does not exceed the TPA threshold [98].

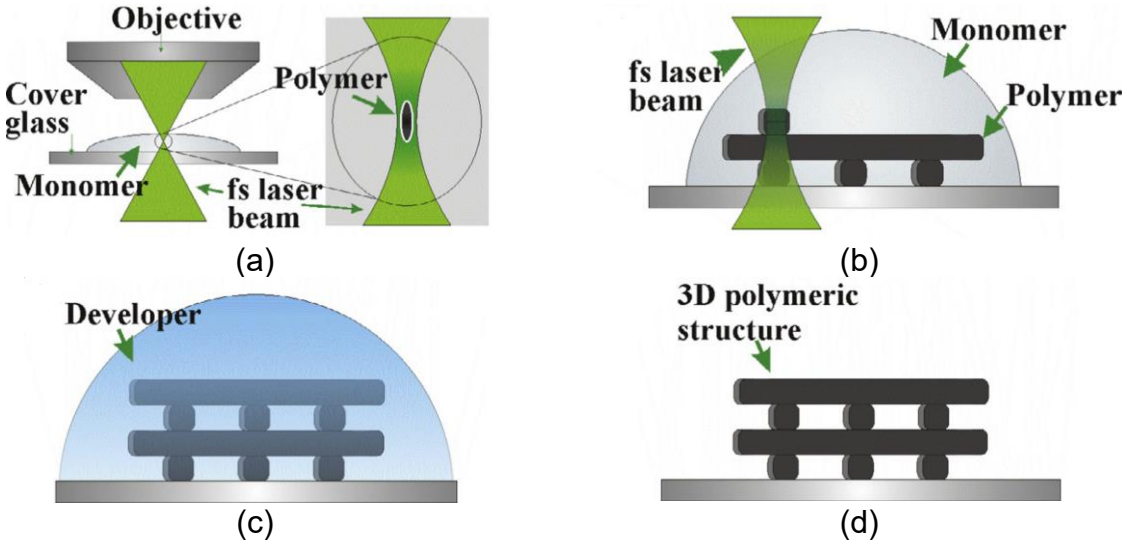

Figure 2.15. 2PP 3D print process. (a). laser beam focusing within the voxel. (b). 3D printing process. (c). Developing after fabrication. (d). Structure after 3D printing. The figures are reproduced from [100].

As shown in Figure 2.16, utilizing precise control over the scanner and translational stages, the laser's focal point is systematically shifted within the 2PP photosensitive material. This allows for the selective solidification of designated regions, culminating in the 3D printing of the complete structural design [101], as shown in Figure 2.15(b). Following the printing process, the printed structure should be extracted from the printer and immersed in the solvent developer to eliminate any residual photosensitive material on its surface [98], as shown in Figure 2.15(c).

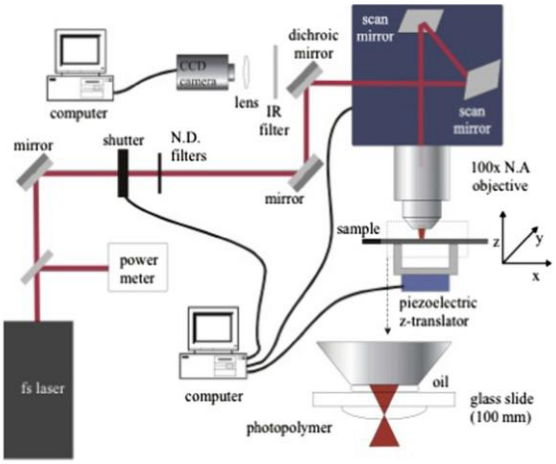

Figure 2.16. Typical setup of a DLW machine. The figure is reproduced from [100].

By changing lenses of the laser source, one can modify the focal volume size, offering flexibility in changing the polymerization voxel size before the printing phase. This, in turn, allows for precise control of print resolution. 2PP can achieve a 3D printing resolution as fine as 100 nm [98, 101]. However, this precision comes at the cost of reduced printing speed. To expedite the printing process for larger structures, adjusting the lens for a larger voxel size can reduce the printing resolution, thereby increasing the printing speed. Enhancing the printing speed presents a multifaceted challenge in engineering. Key parameters, such as printing resolution, laser scanning speed, stage movement speed, size of block splitting and print sequencing, play pivotal roles.

Additionally, a careful consideration must be given to balance the speed with the desired print quality.

2PP is also referred to as direct laser writing (DLW), femtosecond laser writing, dip-in laser lithography (DiLL), multiphoton SLA, or 3D laser lithography [98]. The main distinctions between 2PP and SLA lie in the type of light source they use and the corresponding photo-curable materials. During the print process, 2PP doesn't employ UV light source; rather, it uses near-infrared femtosecond laser source [101]. Additionally, the printing material for 2PP is a photosensitive substance that is tailored to support the TPA within the focal volume illuminated by the laser source, differing from those materials that solidify immediately under UV light exposure. but UV light curing of the post printing structure is still possible.

Currently, owing to the limitations in resolution of 3D printing technologies, most 3D printed antennas are limited to the lower frequency bands. The fabrication of 3D-printed antennas for the terahertz band demands exceptionally high resolution. As a result, only a limited number of 3D print FPCA operating in the terahertz band have been proposed and characterized [102-104]. The 2PP 3D printing technique, renowned for its high-resolution capabilities, offers a promising approach to fabricate antennas with intricate details tailored for terahertz band operation. In this study, the 2PP process is utilized to fabricate a terahertz band FPCA. A comprehensive discussion on this topic, including design considerations and performance evaluations, will be provided in Chapter 5 of this thesis.

2.6. Summary

In this chapter, the theoretical background necessary for understanding the proposed

two LWAs is provided. It begins with an in-depth discussion of LWAs, covering fundamentals, eigenmode selection, open stopband suppression, and the concept of the DLWA, which provides detailed knowledge related to the DLWA proposed in Chapter 4. Following this, various dispersion analysis methods used in Chapter 4 for accurate LWA unit cell design are examined, including the transfer matrix method, MPM, and the complex eigenmode solver. This chapter also explores FPCA theory and the TRM as the basic knowledge for the FPCA proposed in Chapter 5. Additionally, it delves into the fundamentals of 3D printed antennas, discussing different manufacturing techniques such as FDM, SLA, JM, SLS as the background and comparing these with the 2PP technique. The subsequent chapter will conduct a literature review of DLWA and terahertz FPCA, where the research gaps will be further identified and discussed.

Reference

[1] C. A. Balanis, *Modern Antenna Handbook*. John Wiley & Sons, 2011.

[2] D. Headland, Y. Monnai, D. Abbott, C. Fumeaux, and W. Withayachumnankul, "Tutorial: Terahertz Beamforming, from Concepts to Realizations," *APL Photonics,* vol. 3, no. 5, 2018.

[3] J. D. Joannopoulos, S. G. Johnson, and J. N. Winn, *Photonic Crystals:Molding the Flow of Light*. Photonic crystals:molding the flow of light, 1995.

[4] Guglielmi, M., Jackson, and R. D., "Broadside Radiation from Periodic Leaky-Wave Antennas," *Antennas and Propagation, IEEE Transactions on,* vol. 41, no. 1, pp. 31-37, 1993.

[5] F. Monticone and A. Alu, "Leaky-Wave Theory, Techniques, and Applications: From Microwaves to Visible Frequencies," *Proc. IEEE,* vol. 103, no. 5, pp. 793-821, 2015.

[6] S. F. Mahmoud and Y. M. Antar, "Leaky Wave Antennas: Theory and Design," in *2013 30th National Radio Science Conference (NRSC)*, 2013: IEEE, pp. 1-8.

[7] A. W. Snyder and J. D. Love, *Optical Waveguide Theory*. Chapman and hall London, 1983.

[8] Z.-Q. Ma, *Group Theory for Physicists*. World Scientific, 2007.

[9] A. Zee, *Group Theory in a Nutshell for Physicists*. Princeton University Press,

2016.
[10] A. Oliner, "Radiating Periodic Structures: Analysis in Terms of K Vs. B Diagrams," *Short course on microwave field and network techniques,* vol. 4, 1963.
[11] S. Paulotto, P. Baccarelli, F. Frezza, and D. R. Jackson, "A Novel Technique for Open-Stopband Suppression in 1-D Periodic Printed Leaky-Wave Antennas," *IEEE Trans. Antennas Propag.,* vol. 57, no. 7, pp. 1894-1906, 2009.
[12] P. Ba Ccarelli, S. Paulotto, and D. R. Jackson, "A Π-Matching Network to Eliminate the Open-Stopband in 1-D Periodic Leaky-Wave Antennas," *IEEE,* 2012.
[13] S. Otto, A. Al-Bassam, A. Rennings, K. Solbach, and C. Caloz, "Transversal Asymmetry in Periodic Leaky-Wave Antennas for Bloch Impedance and Radiation Efficiency Equalization through Broadside," *IEEE Trans. Antennas Propag.,* vol. 62, no. 10, pp. 5037-5054, 2014.
[14] R. Agrawal, P. Belwal, and S. Gupta, "Asymmetric Substrate Integrated Waveguide Leaky Wave Antenna with Open Stop Band Suppression and Radiation Efficiency Equalization through Broadside," *Radioengineering,* vol. 27, no. 2, pp. 409-416, 2018.
[15] J. Liu, W. Zhou, and Y. Long, "A Simple Technique for Open-Stopband Suppression in Periodic Leaky-Wave Antennas Using Two Non-Identical Elements Per Unit Cell," *IEEE Trans. Antennas Propag.,* pp. 1-1, 2018.
[16] C. Caloz, T. Itoh, and A. Rennings, "Crlh Metamaterial Leaky-Wave and Resonant Antennas," *IEEE Antennas Propag. Mag.,* vol. 50, no. 5, pp. 25-39, 2008.
[17] S. Paulotto, P. Baccarelli, F. Frezza, and D. R. Jackson, "Full-Wave Modal Dispersion Analysis and Broadside Optimization for a Class of Microstrip Crlh Leaky-Wave Antennas," *IEEE Trans. Microwave Theory Tech.,* vol. 56, pp. 2826-2837, 2008.
[18] S. Lim, C. Caloz, and T. Itoh, "Metamaterial-Based Electronically Controlled Transmission-Line Structure as a Novel Leaky-Wave Antenna with Tunable Radiation Angle and Beamwidth," *IEEE Trans. Microwave Theory Tech.,* vol. 52, no. 12, pp. 2678-2690, 2004.
[19] Casares-Miranda, P. Francisco, Camacho-Peñalosa, Carlos, Caloz, and Christophe, "High-Gain Active Composite Right/Left-Handed Leaky-Wave Antenna," *IEEE Trans. Antennas Propag.,* 2006.
[20] Y. Shang, H. Yu, L. Peng, L. Yuan, and Y. Chang, "A 280ghz Cmos on-Chip Composite Right/Left Handed Transmission Line Based Leaky Wave Antenna with Broadside Radiation," in *2014 IEEE MTT-S International Microwave Symposium (IMS2014)*, 1-6 June 2014 2014, pp. 1-3.
[21] D. D. Yuan and T. Itoh, "Composite Right/Left-Handed Substrate Integrated Waveguide Leaky-Wave Antennas," in *2009 European Microwave Conference (EuMC)*, 2009.
[22] M. Memarian and G. V. Eleftheriades, "Dirac Leaky-Wave Antennas for Continuous Beam Scanning from Photonic Crystals," *Nat. Commun.,* vol. 6, no. 1, p. 5855, 2015/01/05 2015.
[23] A. C. Neto, F. Guinea, N. M. Peres, K. S. Novoselov, and A. K. Geim, "The Electronic Properties of Graphene," *Rev. Mod. Phys.,* vol. 81, no. 1, p. 109, 2009.

[24] S. D. Sarma, S. Adam, E. Hwang, and E. Rossi, "Electronic Transport in Two-Dimensional Graphene," *Rev. Mod. Phys.,* vol. 83, no. 2, p. 407, 2011.
[25] D. R. Cooper *et al.*, "Experimental Review of Graphene," *International Scholarly Research Notices,* vol. 2012, 2012.
[26] P. A. M. Dirac, "The Quantum Theory of the Electron," *Proceedings of the Royal Society of London. Series A, Containing Papers of a Mathematical and Physical Character,* vol. 117, no. 778, pp. 610-624, 1928.
[27] R. Sepkhanov, Y. B. Bazaliy, and C. Beenakker, "Extremal Transmission at the Dirac Point of a Photonic Band Structure," *Physical Review A,* vol. 75, no. 6, p. 063813, 2007.
[28] X. Huang, Y. Lai, Z. H. Hang, H. Zheng, and C. T. Chan, "Dirac Cones Induced by Accidental Degeneracy in Photonic Crystals and Zero-Refractive-Index Materials," *Nat. Mater.,* vol. 10, no. 8, pp. 582-586, 2011.
[29] W.-Y. He and C. T. Chan, "The Emergence of Dirac Points in Photonic Crystals with Mirror Symmetry," *Sci. Rep.,* vol. 5, no. 1, p. 8186, 2015.
[30] C. T. Chan, Z. Hang, and X. Huang, "Dirac Dispersion in Two-Dimensional Photonic Crystals," *Adv. OptoElectron.,* 2012.
[31] S. Raghu and F. D. M. Haldane, "Analogs of Quantum-Hall-Effect Edge States in Photonic Crystals," *Physical Review A,* vol. 78, no. 3, p. 033834, 2008.
[32] F. D. M. Haldane and S. Raghu, "Possible Realization of Directional Optical Waveguides in Photonic Crystals with Broken Time-Reversal Symmetry," *Phys. Rev. Lett.,* vol. 100, no. 1, p. 013904, 2008.
[33] G. J. Tang, X. T. He, F. L. Shi, J. W. Liu, X. D. Chen, and J. W. Dong, "Topological Photonic Crystals: Physics, Designs, and Applications," *Laser and Photonics Reviews,* vol. 16, no. 4, p. 2100300, 2022.
[34] S. Rezaee and M. Memarian, "Dirac Leaky Wave Antennas," in *2018 Fifth International Conference on Millimeter-Wave and Terahertz Technologies (MMWaTT)*, 18-20 Dec. 2018 2018, pp. 1-5.
[35] S. Rezaee, M. Memarian, and G. V. Eleftheriades, "Dirac Leaky Wave Antenna for Millimetre-Wave Applications," *IET Microwaves, Antennas & Propagation,* vol. 14, no. 9, pp. 874-883, 2020.
[36] S. Rezaee, M. Memarian, and M. Ahmadian, "Parallel-Plates-Based Dirac Leaky Wave Antennas," *IET Microwaves, Antennas & Propagation,* vol. 15, no. 15, pp. 1877-1890, 2021.
[37] G. Valerio, S. Paulotto, P. Baccarelli, P. Burghignoli, and A. Galli, "Accurate Bloch Analysis of 1-D Periodic Lines through the Simulation of Truncated Structures," *IEEE Trans. Antennas Propag.,* vol. 59, no. 6, pp. 2188-2195, 2011.
[38] M. Bagheriasl, O. Quevedo-Teruel, and G. Valerio, "Bloch Analysis of Artificial Lines and Surfaces Exhibiting Glide Symmetry," *IEEE Trans. Microwave Theory Tech.,* vol. 67, no. 7, pp. 2618-2628, 2019.
[39] Q. Chen, F. Mesa, X. Yin, and O. Quevedo-Teruel, "Accurate Characterization and Design Guidelines of Glide-Symmetric Holey Ebg," *IEEE Trans. Microwave Theory Tech.,* vol. 68, no. 12, pp. 4984-4994, 2020.
[40] F. Giusti, Q. Chen, F. Mesa, M. Albani, and O. Quevedo-Teruel, "Efficient Bloch Analysis of General Periodic Structures with a Linearized Multimodal Transfer-Matrix Approach," *IEEE Trans. Antennas Propag.,* vol. 70, no. 7, pp. 5555-5562, 2022.
[41] P. Castillo-Tapia, K. Van Gassen, Q. Chen, F. Mesa, Z. Sipus, and O. Quevedo-

Teruel, "Dispersion Analysis of Twist-Symmetric Dielectric Waveguides," in *Photonics*, 2021, vol. 8, no. 6: MDPI, p. 206.

[42] F. Giusti, F. Mesa, Q. Chen, G. Valerio, and O. Quevedo-Teruel, "Multimodal Transfer Matrix Method Applied to 3-D Periodic Structures," in *2021 International Symposium on Antennas and Propagation (ISAP)*, 2021: IEEE, pp. 1-2.

[43] T. K. Sarkar and O. Pereira, "Using the Matrix Pencil Method to Estimate the Parameters of a Sum of Complex Exponentials," *IEEE Antennas Propag. Mag.,* vol. 37, no. 1, pp. 48-55, 1995.

[44] Y. Hua and T. K. Sarkar, "Matrix Pencil Method for Estimating Parameters of Exponentially Damped/Undamped Sinusoids in Noise," *IEEE Trans. Acoust. Speech Signal Process.,* vol. 38, no. 5, pp. 814-824, 1990.

[45] L. L. Grant and M. L. Crow, "Comparison of Matrix Pencil and Prony Methods for Power System Modal Analysis of Noisy Signals," in *2011 North American power symposium*, 2011: IEEE, pp. 1-7.

[46] N. Yilmazer, R. Fernandez-Recio, and T. K. Sarkar, "Matrix Pencil Method for Simultaneously Estimating Azimuth and Elevation Angles of Arrival Along with the Frequency of the Incoming Signals," *Digital Signal Process.,* vol. 16, no. 6, pp. 796-816, 2006.

[47] Y. Liu, Z. Nie, and Q. H. Liu, "Reducing the Number of Elements in a Linear Antenna Array by the Matrix Pencil Method," *IEEE Trans. Antennas Propag.,* vol. 56, no. 9, pp. 2955-2962, 2008.

[48] B. Salarieh and H. De Silva, "Review and Comparison of Frequency-Domain Curve-Fitting Techniques: Vector Fitting, Frequency-Partitioning Fitting, Matrix Pencil Method and Loewner Matrix," *Electr. Power Syst. Res.,* vol. 196, p. 107254, 2021.

[49] "User Manual Version 2022," *CST Computer Simulation Technology GmbH, Darmstadt, Germany,* 2022.

[50] "How Do I Compute the Effective Index of an Eigenmode of a Lossy Waveguide." https://meep.readthedocs.io/en/latest/FAQ/#how-do-i-compute-the-effective-index-of-an-eigenmode-of-a-lossy-waveguide (accessed Aug 3,2023.

[51] P. Burghignoli, W. Fuscaldo, and A. Galli, "Fabry–Perot Cavity Antennas: The Leaky-Wave Perspective [Electromagnetic Perspectives]," *IEEE Antennas Propag. Mag.,* vol. 63, no. 4, pp. 116-145, 2021.

[52] A. Goudarzi, M. M. Honari, and R. Mirzavand, "A Millimeter-Wave Fabry–Pérot Cavity Antenna with Unidirectional Beam Scanning Capability for 5g Applications," *IEEE Trans. Antennas Propag.,* vol. 70, no. 3, pp. 1787-1796, 2021.

[53] Q.-Y. Guo and H. Wong, "Wideband and High-Gain Fabry–Pérot Cavity Antenna with Switched Beams for Millimeter-Wave Applications," *IEEE Trans. Antennas Propag.,* vol. 67, no. 7, pp. 4339-4347, 2019.

[54] B. Aqlan, M. Himdi, H. Vettikalladi, and L. Le-Coq, "A 300-Ghz Low-Cost High-Gain Fully Metallic Fabry–Perot Cavity Antenna for 6g Terahertz Wireless Communications," *Sci. Rep.,* vol. 11, no. 1, p. 7703, 2021.

[55] S. Dey and S. Dey, "Ebg Superstrate Loaded Circularly Polarized Fabry-Perot Cavity Antenna at Sub-6 Ghz for Satellite and 5g Cellular Communications," in *2020 International Symposium on Antennas and Propagation (APSYM)*, 2020:

IEEE, pp. 101-104.
[56] M. L. Abdelghani, H. Attia, and T. A. Denidni, "Dual-and Wideband Fabry–Pérot Resonator Antenna for Wlan Applications," *IEEE Antennas Wirel. Propag. Lett.,* vol. 16, pp. 473-476, 2016.
[57] J. Ju, D. Kim, and J. Choi, "Fabry-Perot Cavity Antenna with Lateral Metallic Walls for Wibro Base Station Applications," *Electron. Lett.,* vol. 45, no. 3, pp. 141-142, 2009.
[58] R. Lian, Z. Tang, and Y. Yin, "Design of a Broadband Polarization-Reconfigurable Fabry–Perot Resonator Antenna," *IEEE Antennas Wirel. Propag. Lett.,* vol. 17, no. 1, pp. 122-125, 2017.
[59] S. A. Muhammad, R. Sauleau, and H. Legay, "Small-Size Shielded Metallic Stacked Fabry–Perot Cavity Antennas with Large Bandwidth for Space Applications," *IEEE Trans. Antennas Propag.,* vol. 60, no. 2, pp. 792-802, 2011.
[60] W. Cao, X. Lv, Q. Wang, Y. Zhao, and X. Yang, "Wideband Circularly Polarized Fabry–Pérot Resonator Antenna in Ku-Band," *IEEE Antennas Wirel. Propag. Lett.,* vol. 18, no. 4, pp. 586-590, 2019.
[61] Z. M. Razi and P. Rezaei, "Fabry Perot Cavity Antenna Based on Capacitive Loaded Strips Superstrate for X-Band Satellite Communication," *ARS JOURNAL,* vol. 2, no. 1, 2013.
[62] Zhao and Oliner, "Simple Cad Model for a Dielectric Leaky-Wave Antenna," *IEEE Antennas Wirel. Propag. Lett.,* vol. 3, pp. 243-245, 2004.
[63] A. Hosseini, F. De Flaviis, and F. Capolino, "Design Formulas for Planar Fabry–Pérot Cavity Antennas Formed by Thick Partially Reflective Surfaces," *IEEE Trans. Antennas Propag.,* vol. 64, no. 12, pp. 5487-5491, 2016.
[64] S. Fang, L. Zhang, Y. Guan, Z. Weng, and X. Wen, "A Wideband Fabry–Perot Cavity Antenna with Single-Layer Partially Reflective Surface," *IEEE Antennas Wirel. Propag. Lett.,* vol. 22, no. 2, pp. 412-416, 2022.
[65] A. Ip and D. R. Jackson, "Radiation from Cylindrical Leaky Waves," *IEEE Trans. Antennas Propag.,* vol. 38, no. 4, pp. 482-488, 1990.
[66] N. Llombart, G. Chattopadhyay, A. Skalare, and I. Mehdi, "Novel Terahertz Antenna Based on a Silicon Lens Fed by a Leaky Wave Enhanced Waveguide," *IEEE Trans. Antennas Propag.,* vol. 59, no. 6, pp. 2160-2168, 2011.
[67] P. Burghignoli, W. Fuscaldo, and A. Galli, "Fabry–Pérot Cavity Antennas: The Leaky-Wave Perspective [Electromagnetic Perspectives]," *IEEE Antennas Propag. Mag.,* vol. 63, no. 4, pp. 116-145, 2021.
[68] N. Wang, J. Li, G. Wei, L. Talbi, Q. Zeng, and J. Xu, "Wideband Fabry–Perot Resonator Antenna with Two Layers of Dielectric Superstrates," *IEEE Antennas Wirel. Propag. Lett.,* vol. 14, pp. 229-232, 2014.
[69] R. M. Hashmi and K. P. Esselle, "Distribution Profiles for Transverse Permittivity Gradient Superstrates in Extremely Wideband Resonant Cavity Antennas," in *2016 IEEE International Symposium on Antennas and Propagation (APSURSI)*, 2016: IEEE, pp. 1847-1848.
[70] R. M. Hashmi, K. P. Esselle, and S. G. Hay, "Achieving High Directivity-Bandwidth through Flat Grin Superstrates in Fabry-Perot Cavity Antennas," in *2014 IEEE Antennas and Propagation Society International Symposium (APSURSI)*, 2014: IEEE, pp. 1748-1749.
[71] L.-Y. Ji, P.-Y. Qin, and Y. J. Guo, "Wideband Fabry-Perot Cavity Antenna with a Shaped Ground Plane," *IEEE Access,* vol. 6, pp. 2291-2297, 2017.

[72] F. Wu and K. M. Luk, "Wideband High-Gain Open Resonator Antenna Using a Spherically Modified, Second-Order Cavity," *IEEE Trans. Antennas Propag.,* vol. 65, no. 4, pp. 2112-2116, 2017.
[73] Y. Ge, Z. Sun, Z. Chen, and Y.-Y. Chen, "A High-Gain Wideband Low-Profile Fabry–Pérot Resonator Antenna with a Conical Short Horn," *IEEE Antennas Wirel. Propag. Lett.,* vol. 15, pp. 1889-1892, 2016.
[74] D. M. Pozar, *Microwave Engineering*. Microwave engineering, 2004.
[75] I. Munina, I. Grigoriev, G. O'donnell, and D. Trimble, "A Review of 3d Printed Gradient Refractive Index Lens Antennas," *IEEE Access,* 2023.
[76] J. S. Chohan, R. Singh, K. S. Boparai, R. Penna, and F. Fraternali, "Dimensional Accuracy Analysis of Coupled Fused Deposition Modeling and Vapour Smoothing Operations for Biomedical Applications," *Composites, Part B,* vol. 117, pp. 138-149, 2017.
[77] T. D. Ngo, A. Kashani, G. Imbalzano, K. T. Nguyen, and D. Hui, "Additive Manufacturing (3d Printing): A Review of Materials, Methods, Applications and Challenges," *Composites, Part B,* vol. 143, pp. 172-196, 2018.
[78] V. G. Gokhare, D. Raut, and D. Shinde, "A Review Paper on 3d-Printing Aspects and Various Processes Used in the 3d-Printing," *Int. J. Eng. Res. Technol,* vol. 6, no. 06, pp. 953-958, 2017.
[79] R. F. Quero, G. D. da Silveira, J. A. F. da Silva, and D. P. de Jesus, "Understanding and Improving Fdm 3d Printing to Fabricate High-Resolution and Optically Transparent Microfluidic Devices," *Lab Chip,* vol. 21, no. 19, pp. 3715-3729, 2021.
[80] H. Yao, S. Sharma, R. Henderson, S. Ashrafi, and D. MacFarlane, "Ka Band 3d Printed Horn Antennas," in *2017 Texas Symposium on Wireless and Microwave Circuits and Systems (WMCS)*, 2017: IEEE, pp. 1-4.
[81] J. Tak, D. G. Kang, and J. Choi, "A Lightweight Waveguide Horn Antenna Made Via 3 D Printing and Conductive Spray Coating," *Microwave Opt. Technol. Lett.,* vol. 59, no. 3, pp. 727-729, 2017.
[82] Y. Kim, D. A. Pham, R. Phon, and S. Lim, "Lightweight 3d-Printed Fractal Gradient-Index Lens Antenna with Stable Gain Performance," *Fractal and Fractional,* vol. 6, no. 10, p. 551, 2022.
[83] A. Jandyal, I. Chaturvedi, I. Wazir, A. Raina, and M. I. U. Haq, "3d Printing–a Review of Processes, Materials and Applications in Industry 4.0," *Sustainable Oper. Comput.,* vol. 3, pp. 33-42, 2022.
[84] J. S. Yun, T.-W. Park, Y. H. Jeong, and J. H. Cho, "Development of Ceramic-Reinforced Photopolymers for Sla 3d Printing Technology," *Appl. Phys. A,* vol. 122, pp. 1-6, 2016.
[85] Y. Y. Wang *et al.*, "Fabrication of Dense Silica Ceramics through a Stereo Lithography-Based Additive Manufacturing," *Solid State Phenomena,* vol. 281, pp. 456-462, 2018.
[86] A. C. Tilendo and B. B. Pajarito, "Reinforcement of Stereolithography Resin with Silica-Based Fillers," in *Materials Science Forum*, 2017, vol. 890: Trans Tech Publ, pp. 74-77.
[87] J. Wang, A. Goyanes, S. Gaisford, and A. W. Basit, "Stereolithographic (Sla) 3d Printing of Oral Modified-Release Dosage Forms," *Int. J. Pharm.,* vol. 503, no. 1-2, pp. 207-212, 2016.
[88] J. Tak, A. Kantemur, Y. Sharma, and H. Xin, "A 3-D-Printed W-Band Slotted

Waveguide Array Antenna Optimized Using Machine Learning," *IEEE Antennas Wirel. Propag. Lett.,* vol. 17, no. 11, pp. 2008-2012, 2018.

[89] K. Lomakin, M. Sippel, I. Ullmann, K. Helmreich, and G. Gold, "3d Printed Helix Antenna for 77ghz," in *2020 14th European Conference on Antennas and Propagation (EuCAP)*, 2020: IEEE, pp. 1-4.

[90] A. Palomares-Caballero, A. Alex-Amor, J. Valenzuela-Valdés, and P. Padilla, "Millimeter-Wave 3-D-Printed Antenna Array Based on Gap-Waveguide Technology and Split E-Plane Waveguide," *IEEE Trans. Antennas Propag.,* vol. 69, no. 1, pp. 164-172, 2020.

[91] M. Mieloszyk, A. Andrearczyk, K. Majewska, M. Jurek, and W. Ostachowicz, "Polymeric Structure with Embedded Fiber Bragg Grating Sensor Manufactured Using Multi-Jet Printing Method," *Measurement,* vol. 166, p. 108229, 2020.

[92] R. Chand, V. S. Sharma, R. Trehan, M. K. Gupta, and M. Sarikaya, "Investigating the Dimensional Accuracy and Surface Roughness for 3d Printed Parts Using a Multi-Jet Printer," *J. Mater. Eng. Perform.,* vol. 32, no. 3, pp. 1145-1159, 2023.

[93] M. Layani, X. Wang, and S. Magdassi, "Novel Materials for 3d Printing by Photopolymerization," *Adv. Mater.,* vol. 30, no. 41, p. 1706344, 2018.

[94] A. Squires, E. Constable, and R. Lewis, "3d Printed Terahertz Diffraction Gratings and Lenses," *Journal of infrared, millimeter, and terahertz waves,* vol. 36, pp. 72-80, 2015.

[95] A. Awad, F. Fina, A. Goyanes, S. Gaisford, and A. W. Basit, "3d Printing: Principles and Pharmaceutical Applications of Selective Laser Sintering," *Int. J. Pharm.,* vol. 586, p. 119594, 2020.

[96] M. Ferrando-Rocher, J. I. Herranz-Herruzo, A. Valero-Nogueira, and B. Bernardo-Clemente, "Selective Laser Sintering Manufacturing as a Low Cost Alternative for Flat-Panel Antennas in Millimeter-Wave Bands," *IEEE Access,* vol. 9, pp. 45721-45729, 2021.

[97] M. Göppert-Mayer, "Über Elementarakte Mit Zwei Quantensprüngen," *Ann. Phys.,* vol. 401, no. 3, pp. 273-294, 1931.

[98] Z. Faraji Rad, P. D. Prewett, and G. J. Davies, "High-Resolution Two-Photon Polymerization: The Most Versatile Technique for the Fabrication of Microneedle Arrays," *Microsystems and nanoengineering,* vol. 7, no. 1, p. 71, 2021.

[99] M. T. Raimondi, S. M. Eaton, M. M. Nava, M. Laganà, G. Cerullo, and R. Osellame, "Two-Photon Laser Polymerization: From Fundamentals to Biomedical Application in Tissue Engineering and Regenerative Medicine," *Journal of applied biomaterials and functional materials,* vol. 10, no. 1, pp. 56-66, 2012.

[100] A. Selimis, V. Mironov, and M. Farsari, "Direct Laser Writing: Principles and Materials for Scaffold 3d Printing," *Microelectron. Eng.,* vol. 132, pp. 83-89, 2015.

[101] A. Ostendorf and B. N. Chichkov, "Two-Photon Polymerization: A New Approach to Micromachining," *Photonics spectra,* vol. 40, no. 10, p. 72, 2006.

[102] C. Gu *et al.*, "A D-Band 3d-Printed Antenna," *IEEE Trans. Terahertz Sci. Technol.,* vol. 10, no. 5, pp. 433-442, 2020.

[103] B. Aqlan, M. Himdi, H. Vettikalladi, and L. Le-Coq, "A 300-Ghz Low-Cost High-Gain Fully Metallic Fabry–Perot Cavity Antenna for 6g Terahertz Wireless Communications," *Sci. Rep.,* vol. 11, no. 1, pp. 1-9, 2021.

[104] K. Konstantinidis, A. P. Feresidis, Y. Tian, X. Shang, and M. J. Lancaster, "Micromachined Terahertz Fabry–Perot Cavity Highly Directive Antennas," *IET Microwaves Antennas Propag.,* vol. 9, no. 13, pp. 1436-1443, 2015.

Chapter 3

Literature Review

3.1. Introduction

In Chapter 2, the theoretical background of Dirac leaky wave antenna (DLWA) and Fabry-Perot cavity antenna (FPCA) was discussed. This chapter conducts a further literature review, summarizing the published works related to DLWAs and terahertz FPCAs. Additionally, this chapter evaluates the strengths and limitations of previous research, identifying gaps in the literature that this thesis aims to address. In Section 3.2, a literature review of the published work of DLWAs is presented. In Section 3.3, a literature review of terahertz FPCAs is introduced. A summary of this chapter is presented in Section 3.4

3.2. Review of DLWAs

As discussed in Section 2.1.3, a DLWA is a type of leaky wave antenna (LWA) whose leaky mode exhibits Dirac-type dispersion without a bandgap at broadside. Consequently, it avoids the issues of reduced radiation at broadside and fluctuations in gain and efficiency.

In [1], a DLWA formed by a photonic crystal that utilizes high permittivity dielectric rods inside a top-perforated PEC waveguide is proposed. This DLWA unit cell achieves an accidental degeneracy of TM Bloch eigenmodes by carefully tuning its geometrical

dimensions. As shown in Figure 3.1(a), the top-perforated slots are used to leak the energy outside of the metal waveguide.

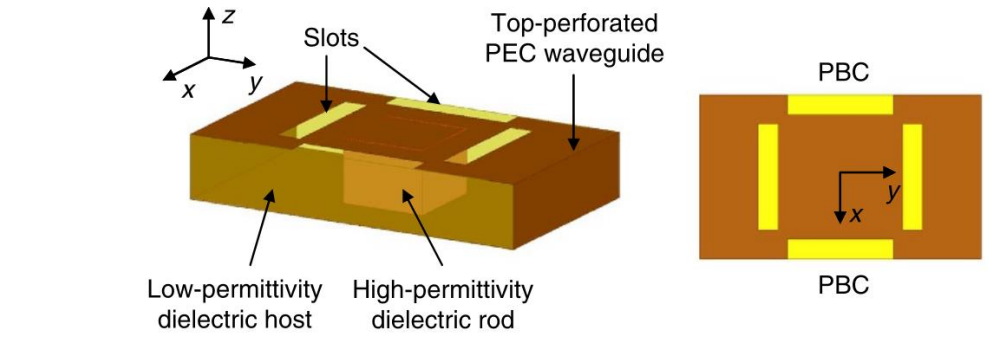

(a)

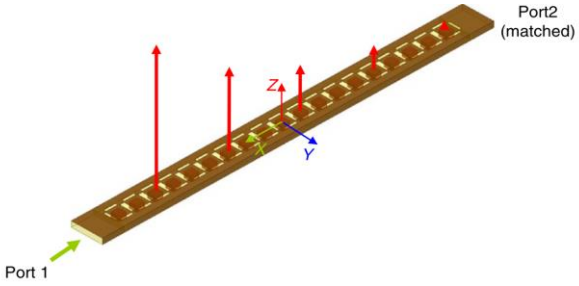

(b)

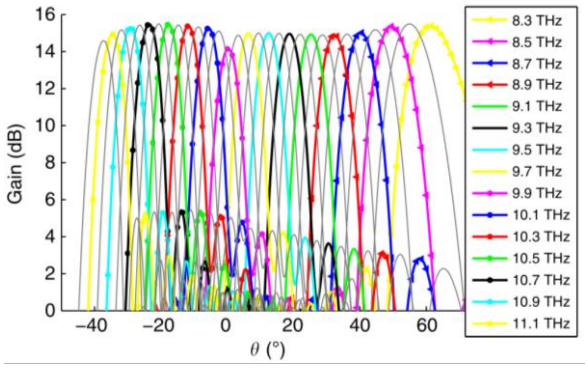

(c)

Figure 3.1. DLWA formed by top-perforated PEC waveguide unit cells. (a) The unit cell design. (b) DLWA formed by 19 cascaded photonic crystal unit cells. (c) The radiation pattern of the DLWA. The figures are reproduced from [1].

The DLWA achieves a scanning range from +61 degrees to -37 degrees over frequencies from 8.3 THz to 11.12 THz, with continuous beam scanning from backward to forward direction by suppressing the open stop band, as depicted in Figure 3.1(c). A decrease in gain can be seen in Figure 3.1(c) when the beam scans over the broadside direction. It is worth noting that [1] provides only simulation results; no measured results are presented for the proposed DLWA design.

In addition to metal waveguides, the DLWA unit cell can also be adapted for other waveguide structures. In [2], a DLWA unit cell utilizing a ridge gap waveguide (RGW)

filled with silicon dioxide is introduced. As illustrated in Figure 3.2(a) and Figure 3.2(b), a silicon rod is placed inside the RGW to modulate the guided mode. The design of the RGW unit cell employs the method akin to that in [1], where a rod with higher permittivity is positioned inside the waveguide to facilitate the mode degeneration of leaky eigenmodes.

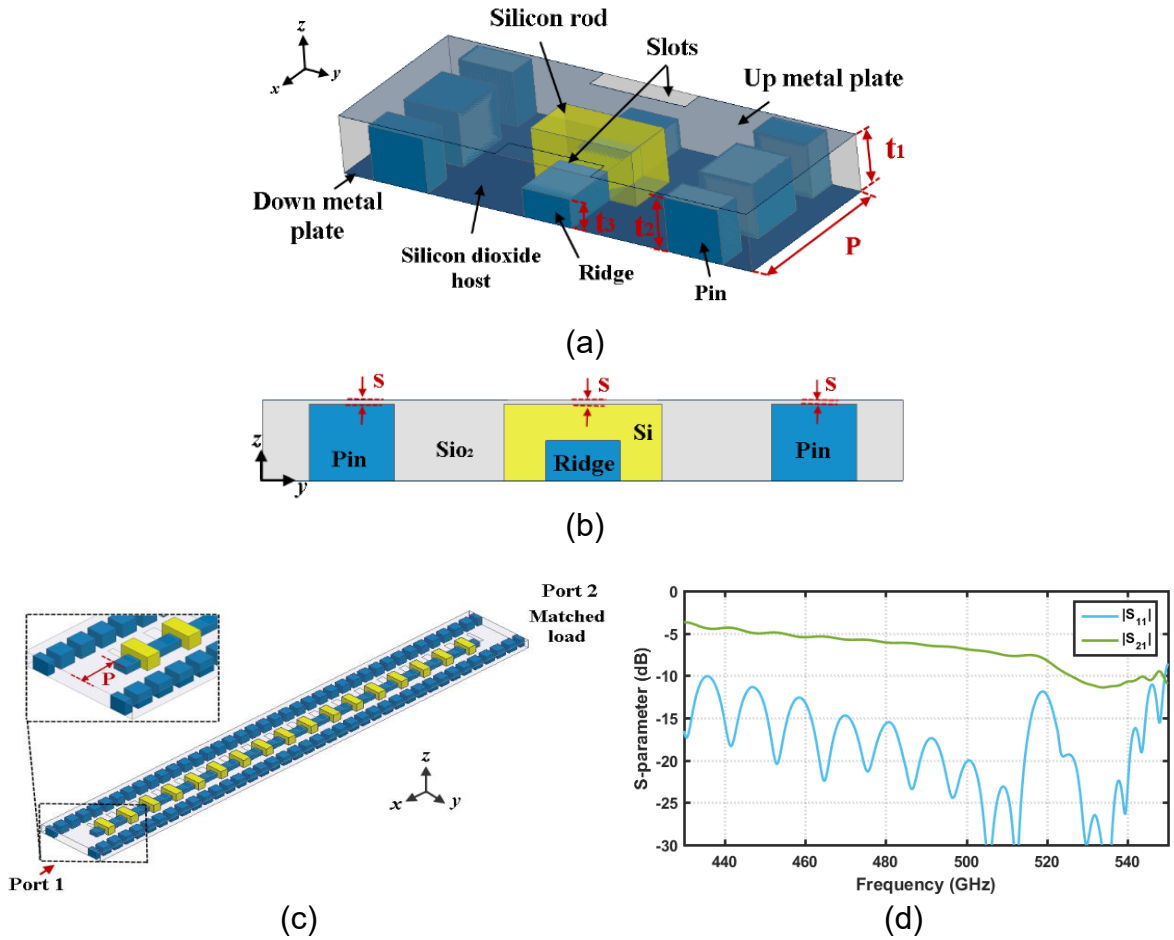

Figure 3.2. A DLWA formed by RGW unit cells. (a) Perspective view of the RGW unit cell. (b) Side view of the RGW unit cell. (c) DLWA formed by cascaded 17 RGW unit cells. (d) Simulated S_{11} of the RGW DLWA. The figures are reproduced from [2].

As shown in Figure 3.2(d), at the broadside frequency of approximately 520 GHz, the simulated S_{11} of the RGW DLWA peaks at -12 dB. This is attributed to the cumulative energy reflection from the 17-unit cells, which is a result of the partially open bandgap. The simulation results indicate that the RGW DLWA can achieve beam scanning from

-30 degrees to +55 degrees by varying the frequency from 430 GHz to 550 GHz. So far, only simulated results have been reported in [2].

In [3], a Ku band DLWA based on parallel plate waveguide (PPW) is introduced. The unit cell is formed by cutting slots on the top layer of PPW, as shown in Figure 3.3(a). A prototype of the 1D PPW DLWA, illustrated in Figure 3.3(b), is fabricated in [3], employing Rogers RO4003 as the dielectric substrate. The 1D PPW DLWA shows a 2 to 4 degrees beam pointing angle deviation between simulation and prototype measurement due to fabrication error.

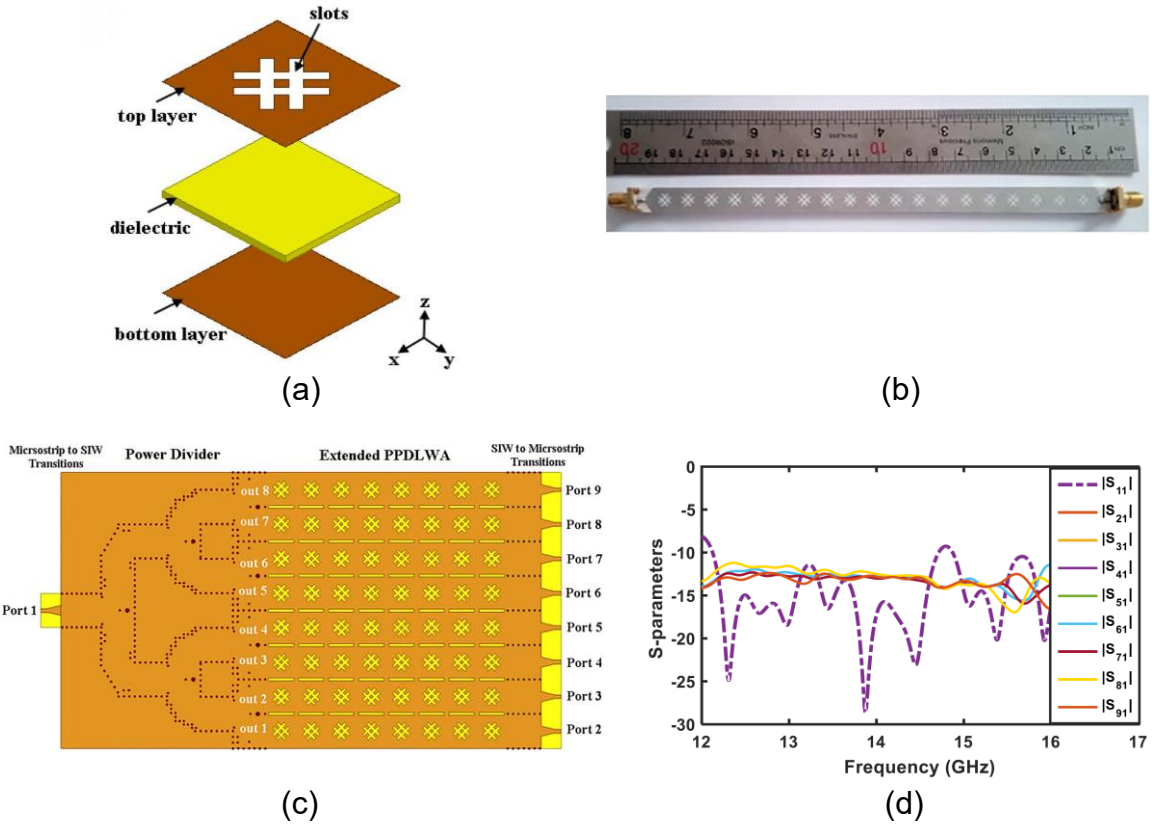

Figure 3.3. DLWA based on PPW. (a) Design of the unit cell. (b) Prototype of 1D PPW DLWA. (c) Top view of 2D PPW DLWA design. (d) Simulated S-parameters of the 2D PPW DLWA. The figures are reproduced from [3].

In [3]. a 2D DLWA design is also proposed. The extended PPW DLWA is formed by 8×8 unit cells. A substrate integrated waveguide (SIW) based power divider is used to

split the power and excite the 2D unit cells to achieve a pencil beam radiation pattern. It is worth noting that, the simulated S_{11} of the 2D PPW DLWA peaks at -9.25 dB when measured at the Dirac frequency, indicating that there remains a partially open bandgap. Compared to the 1D PPW DLWA design, the higher reflection level is directly correlated with the greater number of 64 unit cells. Only simulated results of 2D PPW DLWA are provide in [3].

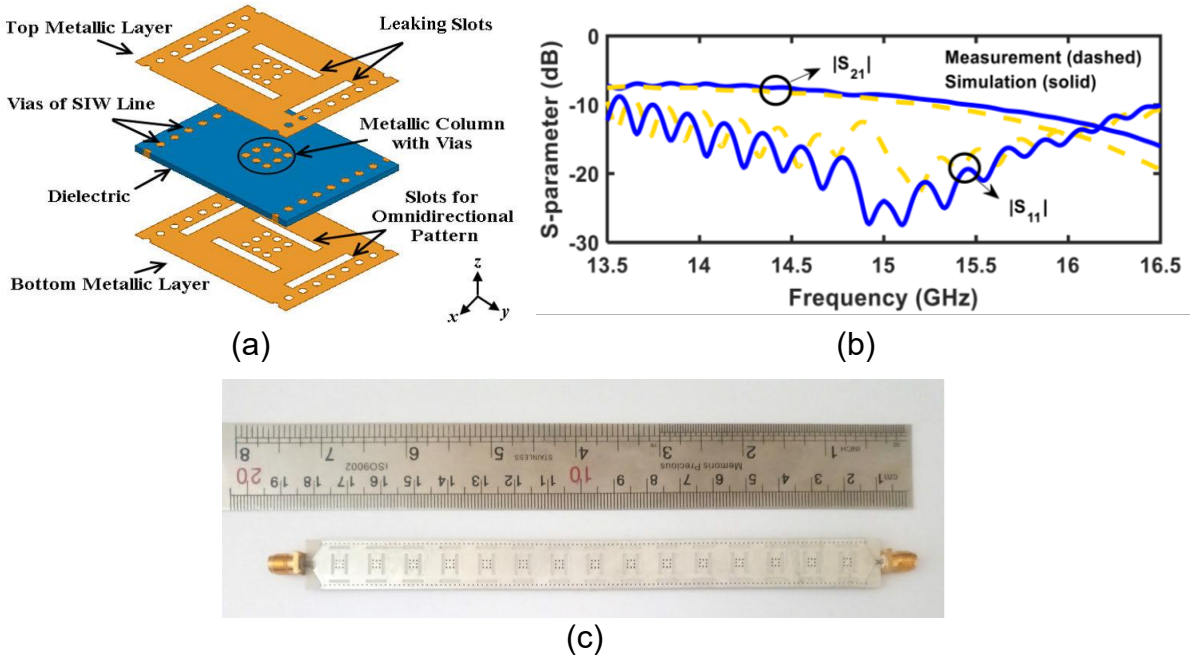

Figure 3.4. A SIW based DLWA. (a) Design of the SIW unit cell. (b) S_{11} of the SIW DLWA. (c) Prototype of the SIW DLWA. The figures are reproduced from [4].

In addition to the PPW, the SIW can also be used for the DLWA unit cell design. In [4], a DLWA formed by SIW with perforated metallic via holes and leakage slots is introduced. As depicted in Figure 3.4(a), energy leaks from both sides of the unit cell, leading to an omnidirectional fan beam radiation pattern in the complete DLWA design. A prototype of the SIW DLWA, consisting of 15 cascaded unit cells, is illustrated in Figure 3.4(c) and was fabricated and tested as reported in [4]. Figure 3.4(b) shows that the measured S_{11} of the prototype peaks at -12 dB at the Dirac (broadside) frequency,

although the simulated S_{11} indicates that good matching has been achieved. Another DLWA based on SIW is introduced in [5], and it shows nearly the same performance, as listed in Table 3.1.

To avoid high losses in the dielectric and metal ground at submillimetre-wave and terahertz bands, a DLWA unit cell design based on the modulated Goubau line is introduced in [6]. As shown in Figure 3.5(b), the unit cell utilizes the transverse asymmetry of the line width to periodically module the Goubau line for suppression of the open stop band (OSB). This DLWA achieves continuous beam scanning from -13.1 degrees to 19.1 degrees when the frequency varies from 9 GHz to 13 GHz.

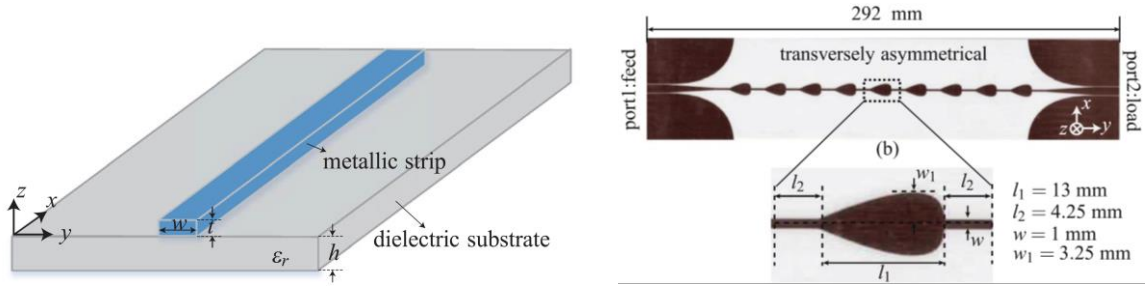

(a) (b)

Figure 3.5. DLWA based on the modulated Goubau line. (a) Design schematic of the Goubau line. (b) The prototype of the DLWA based on modulated Goubau line. The figures are reproduced from [6].

In summary, the waveguiding technologies have been proposed to form the unit cell of DLWAs including metal rectangular waveguide [1], ridge gap waveguide (RGW) [2], parallel plate waveguide (PPW) [3], substrate integrated waveguide (SIW) [4, 5], and Goubau line [6], as listed in Table 3.1.

It can be seen from Table 3.1 that the measured S_{11} of all existing designs of the DLWA shows a peak at the broadside frequency. The S_{11} peak value correlates with the number of unit cells in the DLWA. As listed in Table 3.1, similar S_{11} peak at the broadside frequency exist for all references except for [1]. Considering that the unit cell

number of this work is 100 in the longitudinale direction, more reflections will be accumulated than the DLWA design listed in Table 3.1 that has fewer unit cells. It is worth noting that, the return loss caused by the reflection at the broadside frequency is proportional to the size of the open bandgap. As the bandgap approaches zero, the strength of this reflection (called the “mirror strength”) linearly approaches zero [7]. As a result, an almost closed bandgap (caused by fabrication tolerances) will still allow radiation at broadside with reasonable efficiency and lower reflection.

As listed in Table 3.1, these works focused on the design of DLWA unit cells that can achieve a close bandgap. However, the SLLs are not optimized. Also, the listed 1D DLWAs consist of only a single row of unit cells, limiting aperture expansion to either elongating the antenna—unsuitable for compact designs—or complicating the feeding network, thus increasing design complexity.

Table 3.1. Comparison of DLWA between proposed design and other works

Ref.	Fabrication Technology	Unit Cells	Frequency (GHz)	Scan Range (Deg.)	Max Gain (dBi)	SLL (dB)	Broadside Radiation	Broadside S_{11} (dB)	S_{11} Peak at Broadside
[1]	Metal Waveguide	19	8300 - 11120	−37 to +61	14 to 16	−10	Yes	−40 (Sim.)	No
[8]	SIW	25	25 - 31	-19 to +18	16.5	N.A.	Yes	-14.2 (Mea.)	Yes
[5]	SIW	15	13.5-16.5	-30 to +30	10	-10	Yes	-12 (Mea.)	Yes
[4]	SIW	15	13.5-16.5	-30 to +30	12.5	N.A.	Yes	-12 (Mea.)	Yes
[2]	RGW	17	430 - 550	-30 to +55	16.1	-12.	Yes	-12 (Sim.)	Yes
[3]	PPW	19	12 - 17	-47 to +20	13	-10	Yes	-20 (Mea.)	Yes
[3]	PPW & SIW	8×8	12 - 16	-60 to +18	22.5	-10	Yes	-9.25 (Sim.)	Yes
[6]	Goubau Line	9	9 -13	-13.1 to 19.1	11	N.A.	Yes	-10 (Mea.)	Yes
This work	DRW	17×100	220 - 313	−32 to +40	29	−26 to −18	Yes	-15 (Sim.), −6.4 (Mea.)	Yes

Compared to existing works, the DLWA proposed in Chapter 4 is based on a high-resistivity silicon (HRS) dielectric rectangular waveguide (DRW). The novel DLWA unit cell design offers advantages including low loss at the terahertz band, a wider aperture size, and optimized SLL.

3.3. Review of Terahertz FPCAs

The fundamentals, including the background and theory of the FPCA, are discussed in Section 2.3. So far, only a few studies on FPCA operating in the terahertz band have been reported and demonstrated with measured results.

In [9], Chao Gu *et al.* presented a 3D-printed metal FPCA design, from which two prototypes were fabricated. Both prototypes have the same configuration, as illustrated in Figure 3.6. The first prototype, fabricated using DMLS, achieved a gain of 15.5 dBi at 135 GHz and a 3 dB bandwidth of 20 GHz.

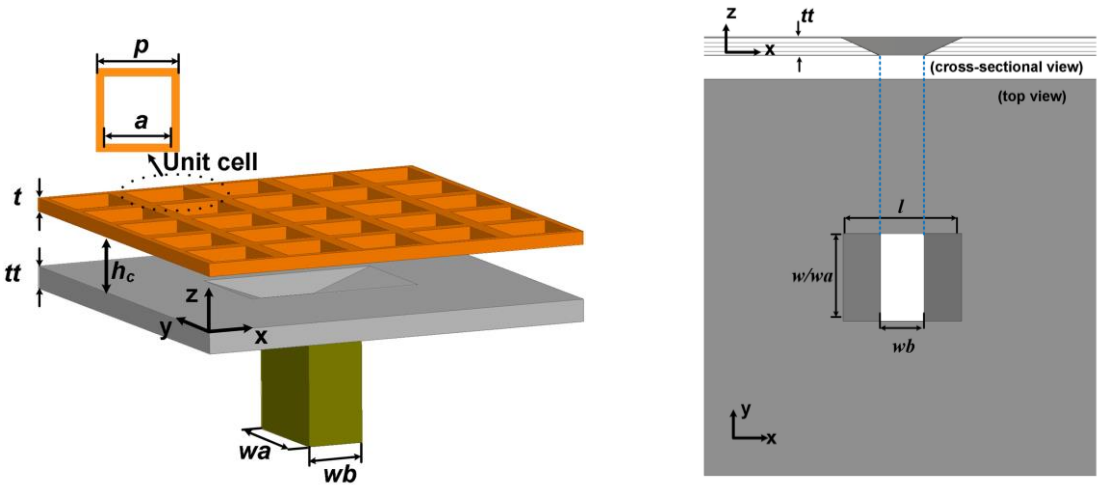

(a) (b)

Figure 3.6. An H-band 3D-printed FPCA. (a) Resonant cavity configuration with metal unit cell and metal ground. (b) Impedance matching layer for performance optimization. The figures are reproduced from [9].

The second prototype, which has the same design as shown in Figure 3.6, is fabricated through a polymer 3D printing process and subsequently metalized with copper via physical vapor deposition (PVD) and electroplating, attained a gain of 12.1 dBi at 151.25 GHz. Due to the partial metallization of the inner surface and cavity, the second prototype exhibits a gain reduction of around 4 dB compared to simulation. Additionally, to achieve a broader bandwidth, as shown in Figure 3.6(b), an impedance

matching layer was designed to gradually transition the impedance from the waveguide to the cavity input.

A fully metallic FPCA that operates at 300 GHz is reported by Aqlan *et al*. in [10], as shown in Figure 3.7. The fabrication of the FPCA employs laser-cutting of brass. This design achieves a gain of 17.7 dBi at 289 GHz and a 3 dB bandwidth of 22 GHz. A step-profiled horn antenna, in conjunction with two slots on the coupling layer, is used to couple energy from the open-ended waveguide to the resonant cavity. In the ground layer, as shown in Figure 3.7, a slot smaller than the inner dimensions of the open-ended waveguide is cut for impedance matching.

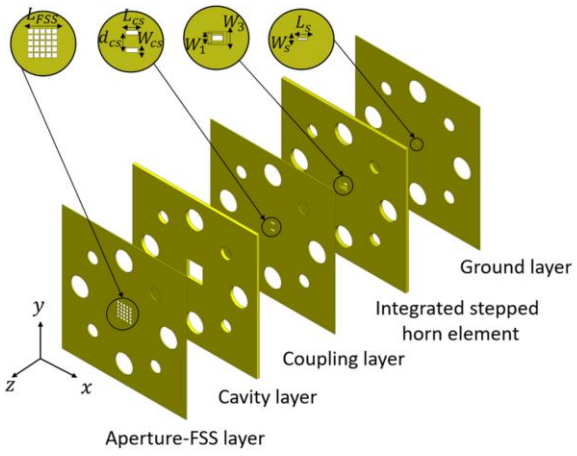

(a)

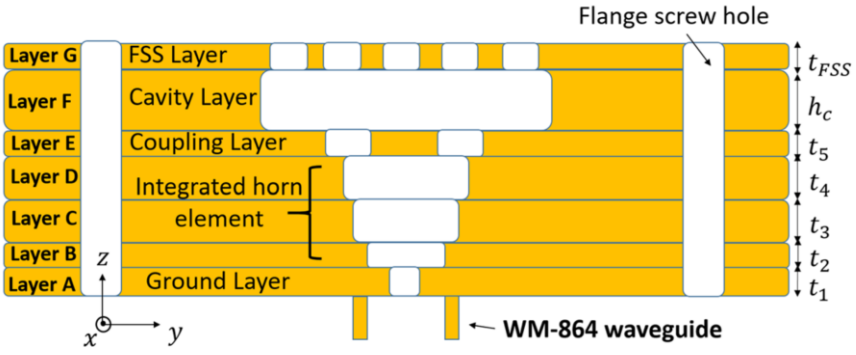

(b)

Figure 3.7. Configuration of each layer of a full metallic FPCA. (a) Design schematic of the FPCA. (b) Cross-section view of the metallic FPCA. The figures are reproduced from [10].

A high directivity, micromachined, reconfigurable FPCA is presented by Konstantinidis *et al.* in [11]. The complete structure, as shown in Figure 3.8, is composed of six silver-coated SU-8 layers. Testing of the prototype demonstrated a maximum gain of 19.1 dBi at 267 GHz, although the return loss at this band was 2 dB. A matched gain of 15.9 dBi was achieved at approximately 284 GHz. In a similar manner, a narrower slot in the ground plane was utilized to achieve impedance matching with the open-ended waveguide.

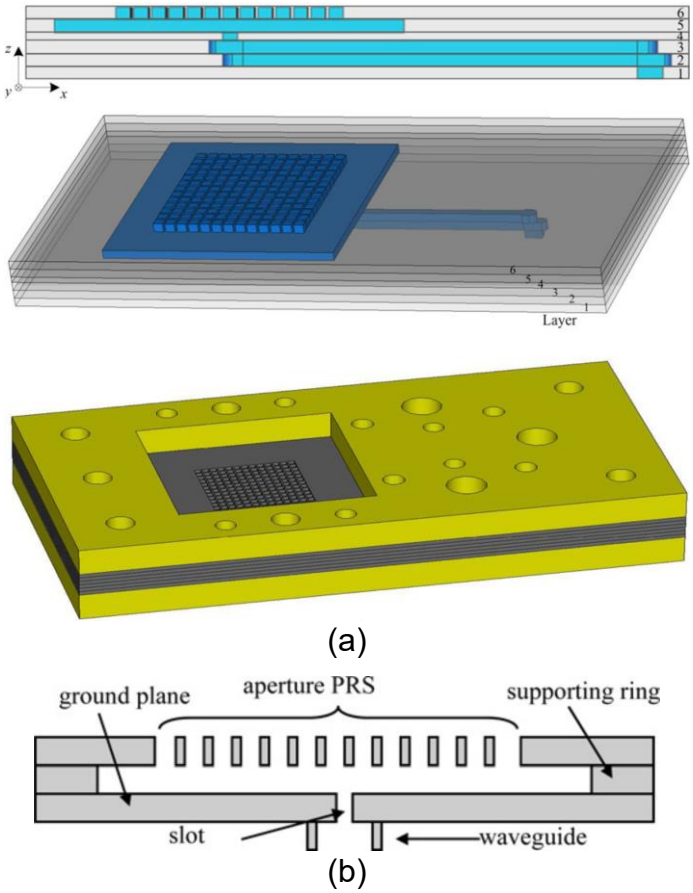

Figure 3.8. Diagrams of a micromachined H-band FPCA. The figures are reproduced from [11].

Typically, an FPCA that operates at the terahertz band is fed by an open-ended waveguide. To achieve wideband impedance matching, an extra matching structure is usually required to transform the impedance from the open-ended waveguide to the

resonance cavity input impedance. Additionally, the matching structure may also be used to avoid exciting unwanted modes, such as the TM_0 mode which has an undesirable radiation pattern [12-14]. The introduction of these matching structures introduces additional fabrication complexity, which may be undesirable at high frequencies.

As discussed above, and listed in Table 3.2, the referenced works employ different matching methods between the waveguide and the cavity, including an impedance matching layer, horn profiled step layer transitions, and slots on the coupling layer, to achieve broader bandwidth impedance matching.

Table 3.2. Comparison of key performance metrics of this work with other published terahertz FPCAs

Reference	Fabrication Process	Extra Matching Configuration	Centre Frequency (GHz)	3 dB Gain Bandwidth (GHz)	Gain (dBi)	3 dB GBWP	SLL (dB)
[9]	DLMS	Impedance Matching Layer	135	20	15.5	458	-13
[10]	Laser Cutting Brass	Step Profiled Horn Layers and 2 Slots on Coupling Layer	300	22	17.7	430	-15
[9]	Polymer 3D Printing, PVD, Electroplating	Impedance Matching Layer	151.25	31.1	12.1	332.5	-13
[11]	Micromachining	Feeding Slot	284	4.5	15.9	61.5	-20
This work	2PP Direct Laser Writing	WR3 Open-ended Waveguide Only	283.7	23.3	20.3	892	-14

Table 3.2 shows a comparison of the FPCA proposed in this thesis with other published works on terahertz FPCAs. Compared with other published terahertz FPCAs, the FPCA proposed in this thesis has the advantage of a higher 3 dB gain bandwidth product (GBWP) and low return loss without the need for conventional matching structures.

3.4. Summary

In this chapter, the literature review of DLWAs and terahertz FPCA were presented.

Details of these works including the design were discussed and their performance compared with the DLWA and FPCA designs proposed later in Chapter 4 and Chapter 5, respectively.

Reference

[1] M. Memarian and G. V. Eleftheriades, "Dirac Leaky-Wave Antennas for Continuous Beam Scanning from Photonic Crystals," *Nat. Commun.,* vol. 6, no. 1, p. 5855, 2015/01/05 2015.

[2] S. Rezaee and M. Memarian, "Rgw Based Leaky Wave Antenna for Terahertz Application," in *2020 28th Iranian Conference on Electrical Engineering (ICEE)*, 2020: IEEE, pp. 1-5.

[3] S. Rezaee, M. Memarian, and M. Ahmadian, "Parallel-Plates-Based Dirac Leaky Wave Antennas," *IET Microwaves, Antennas & Propagation,* vol. 15, no. 15, pp. 1877-1890, 2021.

[4] S. Rezaee, M. Memarian, and G. V. Eleftheriades, "Analytical Study of Dirac Type Dispersion in Simple Periodic Waveguide Structures for Leaky-Wave Applications," *IEEE Access,* vol. 10, pp. 25707-25717, 2022.

[5] S. Rezaee and M. Memarian, "Analytical Study of Open-Stopband Suppression in Leaky-Wave Antennas," *IEEE Antennas Wirel. Propag. Lett.,* vol. 19, no. 2, pp. 363-367, 2020.

[6] X.-L. Tang *et al.*, "Continuous Beam Steering through Broadside Using Asymmetrically Modulated Goubau Line Leaky-Wave Antennas," *Sci. Rep.,* vol. 7, no. 1, p. 11685, 2017.

[7] Q. Quan, P. B. Deotare, and M. Loncar, "Photonic Crystal Nanobeam Cavity Strongly Coupled to the Feeding Waveguide," *Appl. Phys. Lett.,* vol. 96, no. 20, 2010.

[8] S. Rezaee, M. Memarian, and G. V. Eleftheriades, "Dirac Leaky Wave Antenna for Millimetre-Wave Applications," *IET Microwaves, Antennas & Propagation,* vol. 14, no. 9, pp. 874-883, 2020.

[9] C. Gu *et al.*, "A D-Band 3d-Printed Antenna," *IEEE Trans. Terahertz Sci. Technol.,* vol. 10, no. 5, pp. 433-442, 2020.

[10] B. Aqlan, M. Himdi, H. Vettikalladi, and L. Le-Coq, "A 300-Ghz Low-Cost High-Gain Fully Metallic Fabry–Perot Cavity Antenna for 6g Terahertz Wireless Communications," *Sci. Rep.,* vol. 11, no. 1, pp. 1-9, 2021.

[11] K. Konstantinidis, A. P. Feresidis, Y. Tian, X. Shang, and M. J. Lancaster, "Micromachined Terahertz Fabry–Perot Cavity Highly Directive Antennas," *IET Microwaves Antennas Propag.,* vol. 9, no. 13, pp. 1436-1443, 2015.

[12] S. Bosma, N. Van Rooijen, M. Alonso-delPino, and N. Llombart, "A Wideband Leaky-Wave Lens Antenna with Annular Corrugations in the Ground Plane," *IEEE Antennas Wirel. Propag. Lett.,* vol. 21, no. 8, pp. 1649-1653, 2022.

[13] N. Llombart, G. Chattopadhyay, A. Skalare, and I. Mehdi, "Novel Terahertz Antenna Based on a Silicon Lens Fed by a Leaky Wave Enhanced Waveguide," *IEEE Trans. Antennas Propag.,* vol. 59, no. 6, pp. 2160-2168, 2011.

[14] M. A. Hickey, M. Qiu, and G. V. Eleftheriades, "A Reduced Surface-Wave Twin Arc-Slot Antenna for Millimeter-Wave Applications," *IEEE Microwave Wireless Compon. Lett.,* vol. 11, no. 11, pp. 459-461, 2001.

Chapter 4

A Terahertz All-dielectric Dirac Leaky Wave Antenna

4.1. Introduction

As discussed in Section 1.1.1 of the thesis, LWAs have been widely employed in various applications within the microwave band; however, adapting LWA designs for the terahertz band remains challenging. These challenges include developing waveguide solutions to minimize both dielectric and Ohmic loss, along with resolving the open stop band (OSB) issue that can reduce the gain and lead to high return loss at certain scan angles. Numerous studies have been conducted to tackle these challenges, aiming to develop a LWA design for future terahertz applications. Despite these efforts, as reviewed in Section 3.2, certain proposed solutions exhibit shortcomings: they do not effectively mitigate the stopband, leading to high return loss most commonly at the broadside radiation angle and high ohmic loss at terahertz band.

In this chapter, a periodic Dirac leaky wave antenna (DLWA) is introduced which uses an all-dielectric design (except for reflector and feeding waveguide) to achieve high efficiency across the H band. A design approach which attempts to use accidental mode degeneracy to overcome the common OSB problem is described.

The remainder of this chapter is organized as follows. Section 4.2 describes the design of the unit cell of the DLWA and the detailed method for achieving bandgap suppression. Section 4.3 presents the design and implementation methods of aperture tapered for the DLWA, aiming to achieve a reduced SLL. In Section 4.4, the design of the power feeding transition structure from the open-ended waveguide to the dielectric waveguide section of the DLWA and the design of its termination are discussed. Additionally, details of the complete DLWA design that incorporates the DLWA, supporting arms of suspended DLWA and an additional CNC-manufactured fixture are presented. Section 4.5 reports the fabrication process of the DLWA. Finally, Section 4.6 provides an overview of the measurement results of the DLWA, offering a comprehensive evaluation of the DLWA's overall performance and discussing potential future improvements.

4.2. Unit Cell Design and Bandgap Suppression

A dielectric slab waveguide (DSW) fabricated from high-resistivity silicon (HRS) is chosen as the starting point for the antenna design due to its low propagation loss compared to other terahertz waveguiding technologies [1]. HRS has the lowest loss tangent of all dielectrics in the terahertz band at room temperature [2]. In this work, terahertz time-domain spectroscopy (THz-TDS) is employed to characterize a 4-inch HRS wafer, which is utilized in the design of the DLWA. This measurement process was conducted by M. Naftaly at the National Physical Laboratory, U.K, and the results measured are consistent with those published in the literature for high resistivity silicon [3]. The absorption coefficient of the HRS wafer has been measured and is depicted in Figure 4.1. The absorption coefficient is a parameter that used to calculate the

electromagnetic energy that being absorbed by a material of known thickness. The energy absorbed can be calculated using the formula $P = 1 - e^{-2\alpha x}$, where α is the absorption coefficient and x represent the thickness of the material. As shown in Figure 4.1, within the spectrum range from 0 to 500 GHz, the HRS wafer exhibits an absorption coefficient near zero, indicating negligible dielectric loss at the WR-3 band.

This experimental data confirms the considerable advantage in selecting HRS for the DLWA fabrication. Figure 4.2 illustrates that, at a frequency of 300 GHz, the refractive index of the HRS utilized in the DLWA fabrication is 3.417, corresponding to a permittivity value of 11.67.

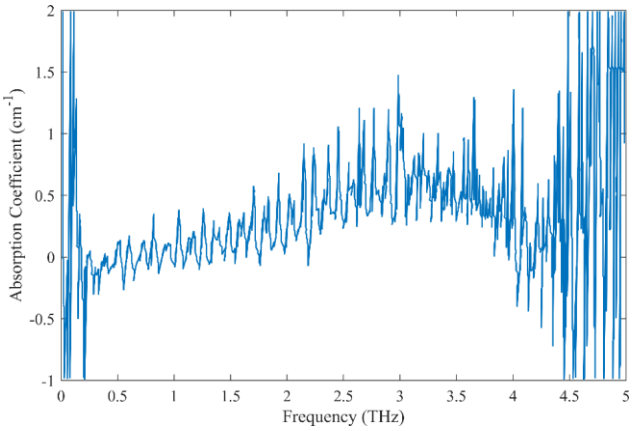

Figure 4.1. Absorption coefficient of the HRS employed in DLWA fabrication, characterized by THz time-domain spectroscopy.

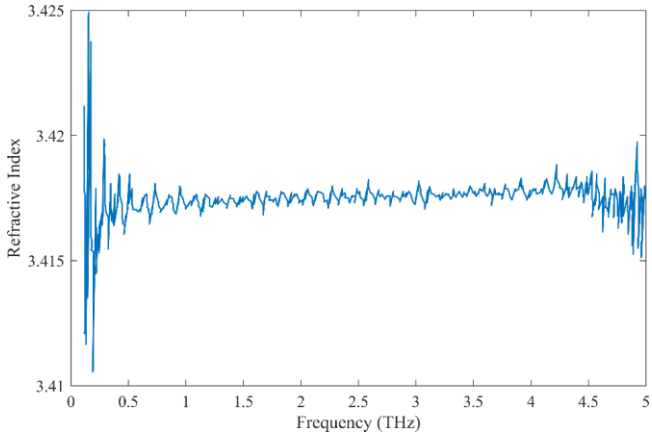

Figure 4.2. Refractive index of the HRS employed in DLWA fabrication, characterized by THz time-domain spectroscopy.

For the purposes of simulation in this Chapter, a permittivity and loss tangent of 11.67 and 5.18×10^{-5}, respectively, were used based on these terahertz time-domain spectroscopy measurements of the HRS wafers.

To enable the guided mode on the DSW to radiate, periodic perturbations are introduced in the form of sub-wavelength through-holes. This type of structure supports leaky Bloch modes which can be used to realize a frequency-scanning beam. The geometry of the unit cell constituting the periodic perturbations is chosen so that the desired Bloch mode is readily excited by the E_{11}^{y} mode on (unperturbed) DSW and the structure is compatible with the deep reactive ion etching (DRIE) fabrication process. The latter is achieved by choosing straight-walled vertical cylindrical holes passing through the HRS wafer.

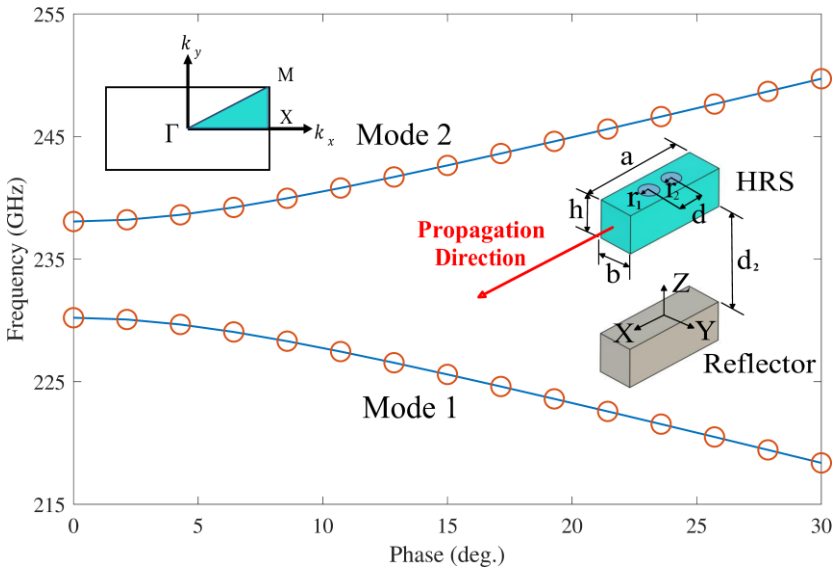

Figure 4.3. Dispersion diagram for a wave travelling in the $\Gamma \rightarrow X$ direction for the unoptimized unit cell design. Note that a sizeable stopband exists for this unit cell geometry at the Γ point. Unit cell parameters: $a = 0.5$ mm, $b = 0.167$ mm and silicon thickness $h = 0.28$ mm. The radii of two holes are $r_1 = 0.044$ mm, $r_2 = 0.042$ mm, and the distance between them is $d = 0.127$ mm.

The eigenmode solver in CST Microwave Studio 2021 was used to calculate the

dispersion properties of the leaky Bloch modes supported by the DSW with periodic perturbations. Tetrahedral meshing and the “general (lossy) eigenmode” solver method were employed which allows the accurate determination of an eigenmode’s Q-factor in open structures [4]. The inset in Figure 4.3 shows the initial unit cell design which consists of two cylindrical holes through an HRS wafer. This geometry will be later optimized to suppress the OSB. The unit cell is initially assumed to be infinitely periodic in both the x- and y-directions to simplify analysis and the finite extent of the structure in the *y*-direction will be considered later. Periodic boundary conditions (PBCs) are used in the $\pm x$ and $\pm y$ directions and open boundaries conditions (OBCs) are used in the $\pm z$ direction to allow for radiation.

The calculated dispersion diagram for the leaky Bloch modes travelling in the $\Gamma \rightarrow X$ direction ($k_y = 0$) is shown in Figure 4.3 as a function of the phase angle $k_x a$. It can be observed that a sizeable stopband exists between the two modes at the Γ point, meaning that this design will be unable to frequency scan the beam through broadside. The stopband may be suppressed by ensuring that the two eigenmodes at the Γ point have the same frequency and are therefore degenerate. This has been referred to as “frequency balancing” in LWA unit cell design [5]. Additionally, it is suggested in [6] that the Q-factor of both modes at the Γ point should be to tuned to nearly the same value for “Q-balancing” [6]. A LWA with both a frequency- and Q-balanced design will then be able to achieve a continuous beam scan through the broadside direction while maintaining a low VSWR [7].

As explained in Section 2.1.2, deterministic degeneracy emerges due to the symmetry of the unit cell whereas accidental degeneracy arises due to an appropriately designed unit cell structure which depends on its exact geometry and permittivity of its

constituents [8, 9]. Here, we attempt to optimize the unit cell so that the two leaky Bloch modes have a suppressed stopband at broadside through accidental degeneracy at the Γ point. Moreover, it is known that accidental degeneracy can lead to a linear or Dirac-like dispersion characteristic [10]. This is advantageous for beam-scanning in a LWA as the scan rate is constant with frequency.

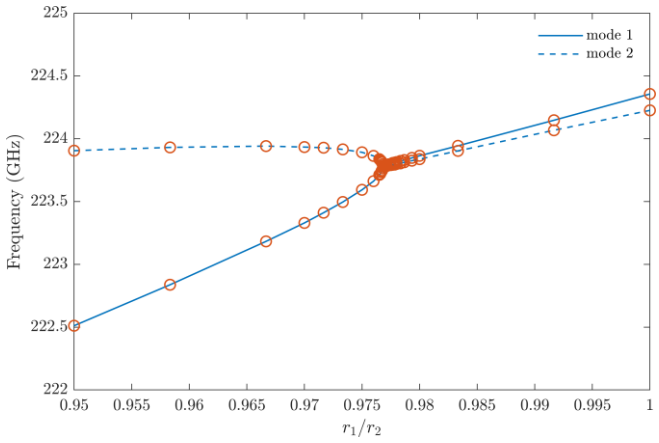

(a)

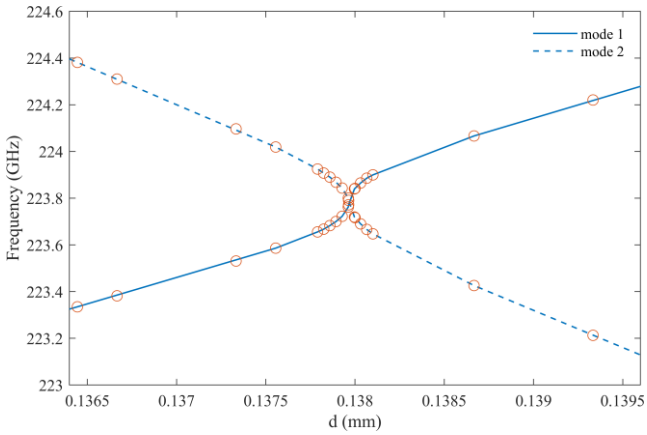

(b)

Figure 4.4. Parameter optimisation to close the OSB through (a) tuning r_1/r_2, and (b) tuning d. The red circles represent the simulated sample results, while the blue curve is obtained by connecting these points.

To realize the accidental degeneracy, two geometric parameters related to the cylindrical holes in the unit cell are tuned: r_1/r_2, the ratio of the radii of the two holes, and d, the distance between the two holes. Figure 4.4 shows the effect of changing

these parameters on the two eigenmode's frequencies at the Γ point. It can be seen that by choosing $r_1/r_2 = 0.976$ and $d = 0.138$ mm, the modes can be made degenerate at the Γ point of the Brillouin zone and the OSB closed.

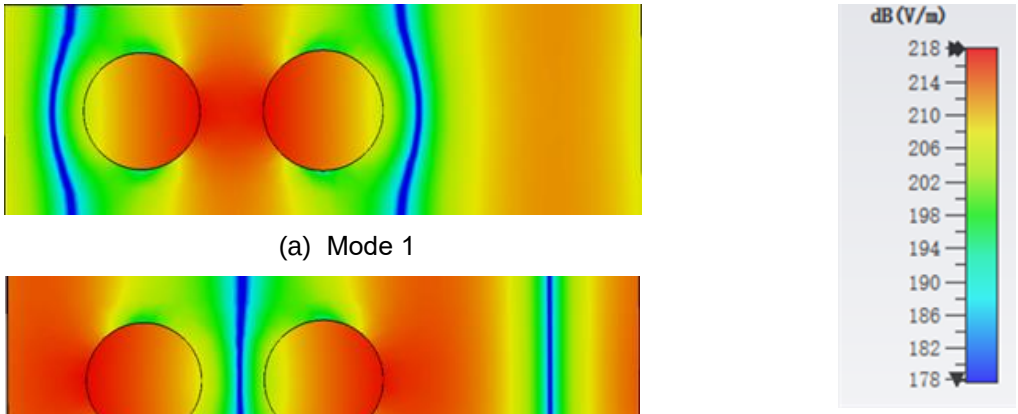

(a) Mode 1

(b) Mode 2

Figure 4.5. Plot of the electric field for the two degenerate modes at the Γ point. (a) Mode 1 and (b) Mode 2 at 223.78 GHz. Unit parameters: $r_1 = 0.041$ mm, $r_2 = 0.042$ mm, $d = 0.138$ mm, unit cell height = 0.28 mm.

To achieve Q-balance [7], we need to ensure they have the same Q-factor when the frequency corresponds to the broadside radiation direction. The Q-factors are directly accessible during the eigenmode simulations. After optimization, the Q-factor of mode 1 is 306, mode 2 is 302 and the difference in eigenmode frequencies is 5 MHz, which is sufficiently small that the OSB is suppressed, leading to a frequency- and Q-balanced design.

During the optimization process aimed at achieving both frequency- and Q-balance, two sets of geometric parameters that ensure frequency-balance are first identified. Subsequently, the Q-factors between the two sets of designs are compared, and the set with the smaller Q differences is selected as one sample for the next iteration. By repeating this process, the set of geometric parameters that achieves both frequency-

and Q-balance can gradually be identified.

Figure 4.5 shows the electric field of the two orthogonal eigenmodes at the Γ point of the Brillouin zone for the tuned unit cell. The Q-balancing process can be seen as controlling the electric field distribution inside the holes for both modes. A larger hole radius leads to an increased leakage rate for both modes and increasing the distance between the two holes leads to a decreased leakage rate for mode 1 but an increased leakage rate for mode 2. The advantage of having two holes in the unit cell with different radii means that there are more degrees of freedom for achieving the Q-balance condition than for a single hole. As discussed in Section 2.1.3, another viewpoint on the OSB suppression is that it results from the cancellation of energy reflection accumulation when an additional hole is added to the unit cell design that initially had only one hole.

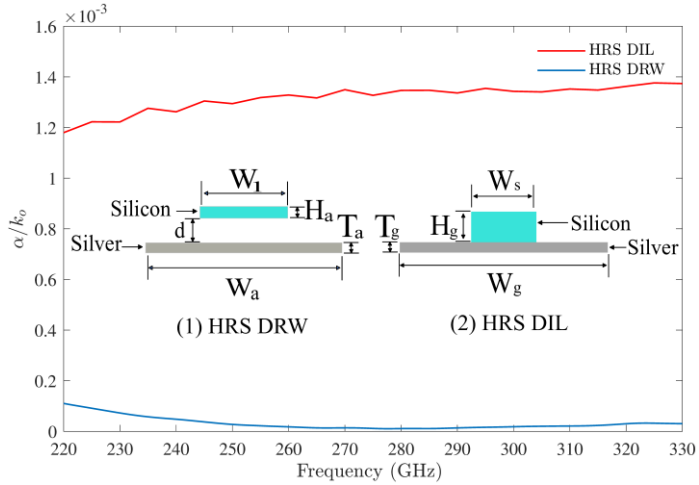

Figure 4.6. Normalized attenuation coefficient for typical HRS dielectric image line (DIL) (shown right inset) and HRS dielectric rectangular waveguide (shown left inset). Dimensions (mm): $W_a = 9, W_1 = 2.4, d = 0.5, H_a = 0.28,\ T_a = T_g = 0.001, W_g = 1.4, W_s = 0.32$ and $H_g = 0.16$.

It is worth noting that the mode degeneration achieved during the optimization of the unit cell is sensitive to the distance between the HRS and metal reflector ($d_2 = 0.5$

mm), as shown in Figure 4.3. As a result, this distance is kept the same for the DLWA.

The asymmetry introduced by the different hole radii can also be seen as a form of *transversal asymmetry* in the unit cell (asymmetric about $x = 0$). This form of asymmetry in metal-based periodic LWAs has previously been shown by Otto *et al* to solve the problem of radiation degradation at broadside by closing the OSB and maintaining radiation efficiency [11]. Here we have demonstrated the usefulness of this approach for a dielectric structure.

Another design consideration is the direction of radiation. The symmetry of the dielectric rectangular waveguide (DRW) with the vertical holes means that a leaky wave travelling in the x-direction will radiate equally on both sides ($\pm z$) of the HRS slab. To achieve single-beam radiation in the $+z$ direction only, a reflector is positioned underneath the HRS slab. Here, we have chosen a metal reflector instead of a dielectric mirror as a metal reflector will have less than 1% Ohmic losses at 300 GHz [12] and achieve a high efficiency. The metal reflector is positioned beneath the HRS DRW with a spacing of 0.5 mm, which is optimized at the broadside frequency. It is important to note that the unit cell including reflector is different to dielectric image line (DIL) wherein the metal reflector directly touches the bottom of the dielectric slab and large currents are present [13]. Figure 4.6 compares the propagation loss of a DRW with a 0.5 mm spaced silver ground plane ($\sigma = 5.28 \times 10^7$ S/m based on the Drude model [14]) and DIL (designed according to [15, 16]), both fabricated from HRS. It can be seen that the DRW structure achieves far lower propagation loss and is more suitable for higher frequencies in the terahertz band.

4.3. Radiation Aperture Tapering

In this section, the radiation amplitude is tapered in the x-direction to reduce the SLL of the antenna. Then the geometric parameters of the unit cell are related with the α needed at each x position through a curve fitting.

4.3.1. Leakage Rate Calculation

As discussed in Section 2.1.2, to achieve a desired amplitude distribution of a LWA with an effective aperture length of L, the leakage rate $\alpha(x)$ as a function of x position is given by (2.14). It is worth noting that the value of radiation efficiency e_r is set to be 0.9 in this work for a practical LWA design [17]. A Taylor 30 dB amplitude distribution is adopted to improve the SLL of the antenna. As $A(x)$ is a known discrete function of x, when the length of the antenna aperture and total efficiency is known, the distribution of α for each unit cell can be calculated.

We next need to relate the required α of each unit cell to its modified geometric parameters. Here, we choose to modify the two hole's radii and separation distance rather than the hole depth so that the fabrication method remains compatible with a single DRIE etch rather than requiring multiple etches to different depths as in a conventional grating antenna.

As discussed in Section 2.2.3, the eigenmode solver is again used to calculate the the leakage rate α of the unit cell, which can be expressed as:

$$\alpha = \frac{\pi f}{V_g Q}, \tag{4.1}$$

where $f = \omega/2\pi$ is the mode eigenfrequency provided by the eigenmode solver. The group velocity is obtained from the numerical derivative of the dispersion curve.

To validate the calculation of the unit cell leakage rate described above, two additional methods were trialled: the *S*-parameter extraction technique [18] and the matrix pencil method (MPM) [19]. For the S-parameter extraction technique, this involved simulating 16 uniform unit cells arranged lengthwise in the x-direction with PBCs in the y-direction and using the FEM method in CST Microwave Studio. It was found that this length of unit cells was sufficient to account for mode coupling between the unit cells. Here, the energy loss in the TE_1 mode was considered to be the result of radiation from the leaky wave.

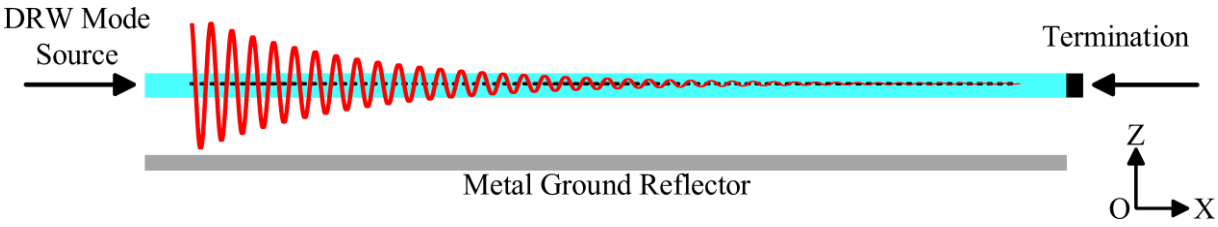

Figure 4.7. The cascaded 16-unit cell is excited by the DRW E_{11}^{y} mode source. The electric field is sampled along the indicated black dashed line, and the MPM is utilized to estimate the leakage rate of each Bloch mode.

The same structure and simulation result was used for the MPM calculation. As shown in Figure 4.7, the DRW mode source is excited from the left side, then the leaky modes propagate inside the DRW until they reach the termination and are absorbed. The electric field is sampled along the black dashed line for estimation of the α of each Bloch modes by MPM.

It is worth noting that, as illustrated in Figure 4.7, the black dashed line begins slightly offset from the start of dielectric slab and ends prior to the termination. This deliberate arrangement reduces the spurious mode effects arising from the transition between the DRW mode and the TE_1 leaky wave mode. It also minimises the impact of reflections at the termination, ensuring the excitation of each Bloch mode is captured

accurately, leading to a more precise MPM estimation.

Table 4.1. Results of extracted Bloch mode components by MPM at 250 GHz.

Mode Index	Normalized Propagation constant ($k = \alpha + j\beta$)	Magnitude of Coefficient
1	0.0011 +16.8493i	0.0817
2	-0.0081 + 0.0696i	4.6976
3	-0.0057 + 2.4705i	0.9510
4	0.0037 + 4.9101i	0.3307

Through the steps presented in Section 2.2.2, the sampled complex field data is decomposed into four Bloch-mode components. The coefficient values and normalized propagation constants of these modes are listed in Table 4.1 to demonstrate this process. The extraction results reveal that mode index 2 is the sole fast wave ($\beta < 1$), corresponding to the TE_1 mode, with a normalized leakage rate of 0.0081.

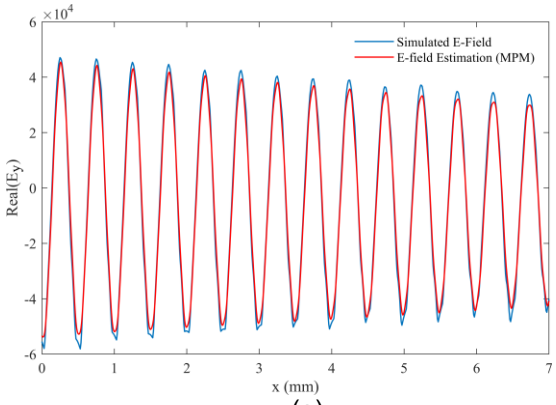

(a)

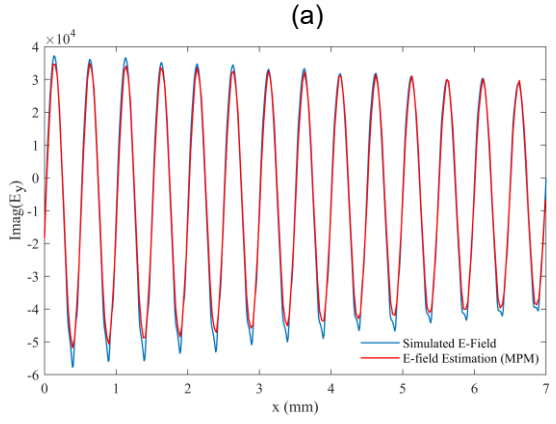

(b)

Figure 4.8. Comparison of simulated electric field (blue line) with estimations from the MPM (red line) for both (a) real part, and (b) imaginary part of the electric field y component at 250 GHz. The electric field data is sampled along the black dashed line as shown in Figure 4.7.

As shown in Figure 4.8, the y component of the simulated electric field is reconstructed based on the MPM estimated propagation constants and coefficient values listed in Table 4.1. The close agreement between the two curves demonstrates the effectiveness of the MPM in modelling the spatial variation of the sampled electric field.

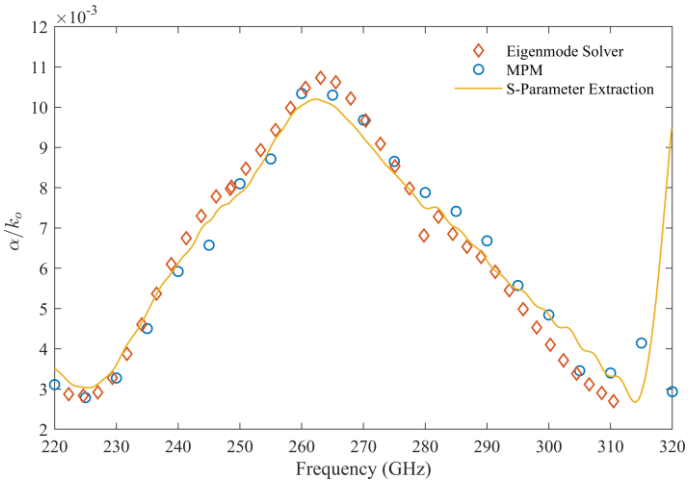

Figure 4.9. Leakage rate of the unit cell calculated by different methods.

As illustrated in Figure 4.9, the α of the unit cell calculated by these three methods has similar results, which validates the calculation method utilizing the CST eigenmode solver with open boundaries. It also confirms that the unit cell eigenmode can be readily excited by the DRW E_{11}^{y} mode.

A known disadvantage of all-dielectric LWAs is their lower leakage rate compared to conventional metal-based LWAs [20]. This requires longer antenna lengths to ensure that most of the leaky wave energy is radiated and results in narrow-beam antennas.

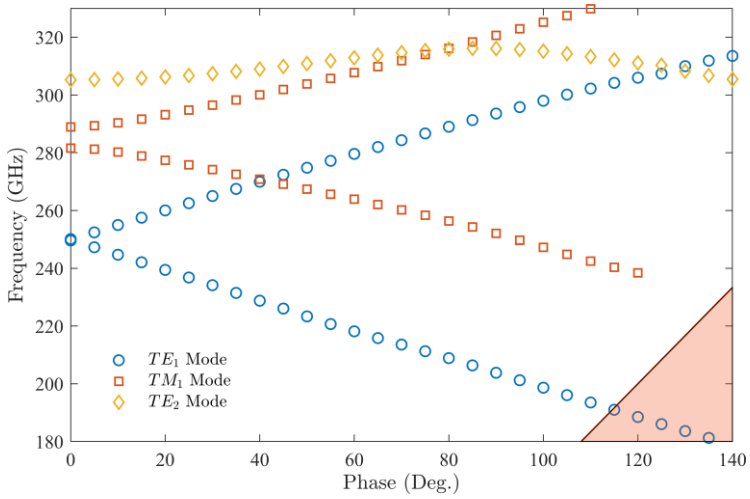

Figure 4.10: Dispersion diagram of the optimised unit cell.

The working bandwidth of the DLWA is constrained by the roll-off of the leakage rate of the unit cell at the upper and lower frequencies as shown in Figure 4.9. The ultimate constraint on the lower frequency is when the eigenmode enters the light cone, shown as the shaded region in Figure 4.10. The light cone gives the relationship between the frequency of light and its wave number. The radiating modes are above the light cone while beneath the light cone are index-guided modes that decay exponentially away from the surface of the unit cell [21]. At 305 GHz, the TE_1 and TE_2 modes become degenerate and a half of the energy (~50%) from the feeding DRW excites the TE_2 mode, which has a lower leakage rate resulting in a reduction of efficiency at this frequency. The TM_1 mode is not excited by the TE_1 DRW mode despite crossing at 270 GHz due to orthogonality.

4.3.2. Curve Fitting and Parameter Prediction

To realize the tapered aperture distribution, we require unit cells with different leakage rates while maintaining a closed bandgap. At the same time, all unit cells should have the same phase constant β to ensure all unit cells radiate at the same angle [17].

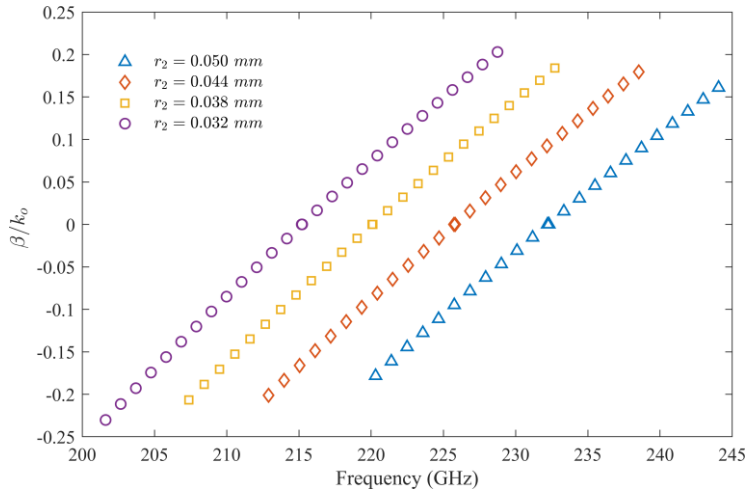

Figure 4.11. Normalized phase constant near the Γ point for different r_2.

To achieve the above two goals, we optimized the unit cell parameters using the following process. First, the value of r_2 is fixed and the above optimization process is repeated to close the band gap. As shown in Figure 4.11, these unit cells with closed band gap will have different phase constants. In addition, unit cells with larger r_2 values have higher broadside frequencies, therefore, a scale factor s, which is a function of r_2, is introduced as an extra parameter for unit cell optimization. In this work, only the parameters in the x and y dimensions are scaled by multiplying them by the scale factor s. The original cuboid dimensions a, b and h are scaled to $a \times s$, $b \times s$ and h, respectively. Similarly, r_1, r_2 and d are also scaled to $r_1 \times s$, $r_2 \times s$ and $d \times s$, respectively. In this work, all unit cells are scaled to have the same eigenmode frequency ($f_s = 250$ GHz) at the Γ point corresponding to the broadside frequency.

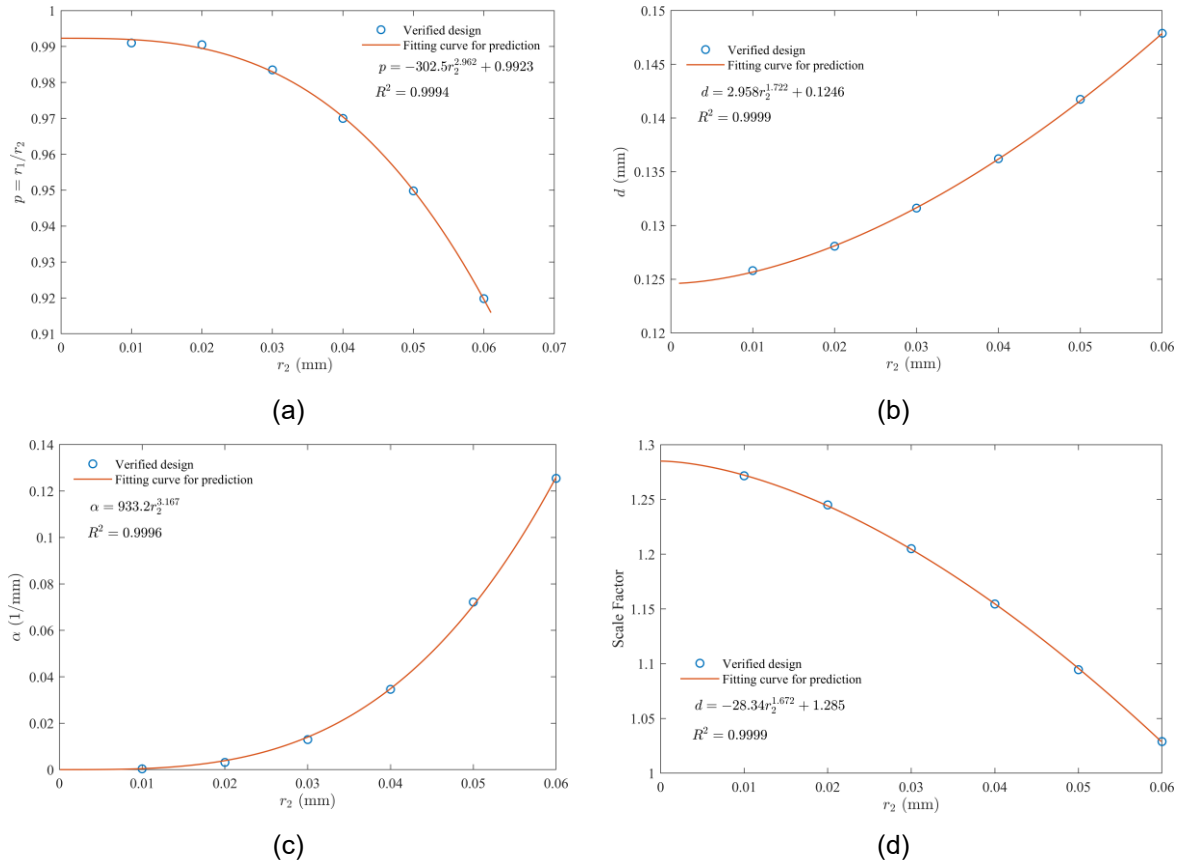

Figure 4.12. Closed bandgap design and fitting curve for parameter prediction to build the tapered aperture LWA (a) $p = r_1/r_2$ vs. r_2 (b) d vs. r_2 (c) α vs. r_2 (d) Scale factor s vs. r_2.

Each cycle of the optimization process is time-consuming and to improve the efficiency of the process, we repeat the above optimization process with different r_2 values between 0.01 and 0.06 at intervals of 0.01 to determine the relationship between all the unit cell parameters and r_2 through curve fitting. As can be seen in Figure 4.12, the relationship between the geometric parameters and α can be described by least-squares fitted power-law curves, yielding $\mathrm{R}^2 \approx 1$ in all cases.

As described in Section 4.2.1, the required α for each unit cell and the fitted curve in Figure 4.12(c) can be used to calculate the required r_2 for each unit. can be used to determine the required r_2 to achieve it. Since the remaining unit cell parameters have been expressed as functions of r_2 as shown in Figure 4.12, all unit cell parameters are

now determined.

4.3.3. Two-Dimensional Periodic Boundary Condition

Up to this point, the unit cell has been considered as infinitely periodic in the y-direction and analyzed using PBCs in both the $\pm x$ and $\pm y$ directions. In practice, the number of unit cells in the y-direction is finite and limited by the final width of the DRW taper (described in Chapter 4.3.4).

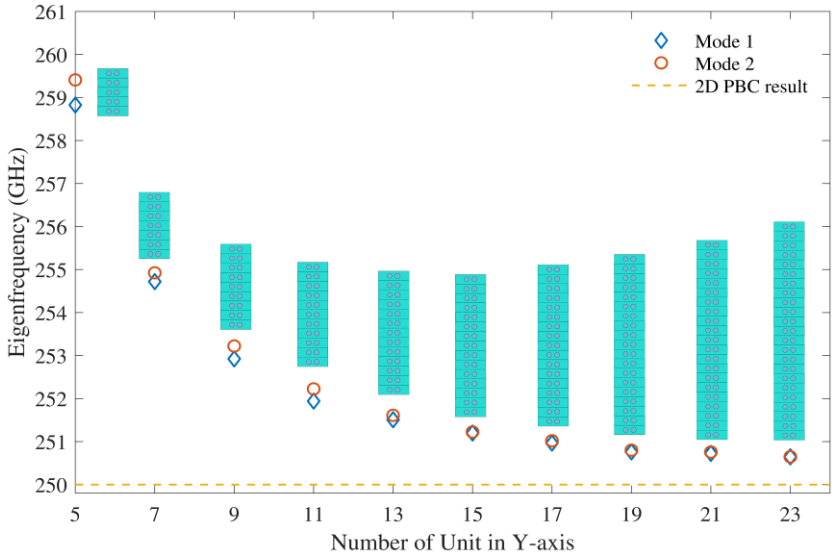

Figure 4.13. Variation trend of eigenfrequency corresponding to the number of units in the Y direction.

We now consider a new supercell that consists of N_y unit cells and OBCs in the y-direction. As can be seen in Figure 4.13, as N_y increases the corresponding eigenfrequencies at the Γ point asymptotically approaches the eigenfrequency of the unit cell with PBCs in the x- and y-directions. These simulation results confirm that for a sufficiently large number of unit cells in the y-direction the unit cell eigenmode frequency remains similar to the case of PBCs in the x- and y-directions.

4.4. Complete DLWA Design

To excite the DLWA using a WR-3 waveguide, a transition is required to efficiently convert the TE_{10} mode in the WR-3 rectangular waveguide into the E_{11}^{y} mode on the DRW over the shortest possible distance to minimize the length of the antenna. Here we use a linearly tapered DRW to realize this transition as this has previously been shown to be close to optimum [1].

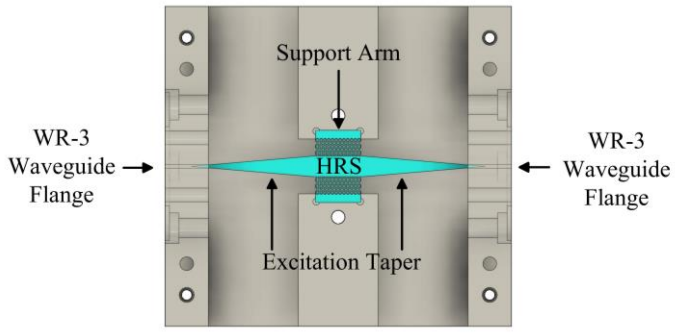

(a)

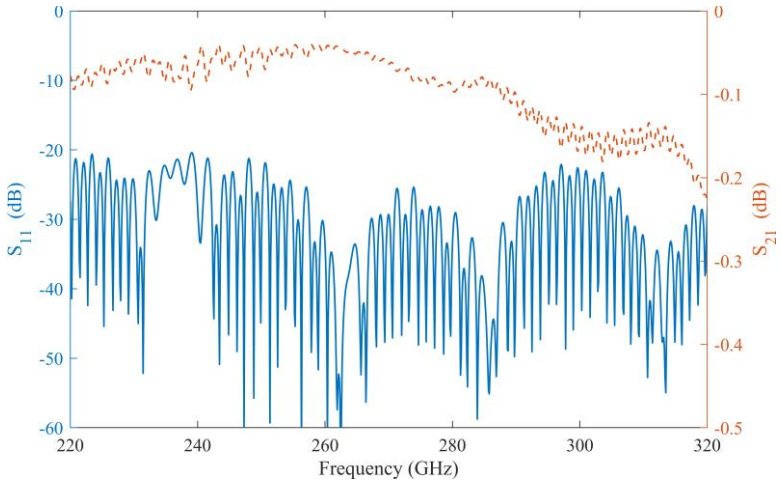

(b)

Figure 4.14. (a) Cross-sectional view of back-to-back connected tapered DRW model for simulation and evaluation. (b) Simulated *S*-parameters of the back-to-back taper.

To optimize the transition, we consider two linearly tapered DRW connected back-to-back and excited using WR-3 waveguide as shown in Figure 4.14(a). The mounting support arms (described later) are included in the simulation to quantify their effect on

transmission and reflection. The scattering parameters of this structure are shown in Figure 4.14(b). It can be seen that the loss of two tapers connected back-to-back is less than 0.2 dB from 220 GHz to 320 GHz. It is important that no higher order modes are excited at the end of the taper, otherwise the radiation properties of the antenna will be negatively affected. The higher order modes may be suppressed as long as the linearly tapered DRW is sufficiently long [22]. The length of the taper is chosen to keep the higher order mode content below -10 dB across the entire working bandwidth. Another consideration is the width of the DLWA, as increasing the number of radiating unit cells in the y-direction will form a wider radiation aperture leading to a narrower beam, however, this will require a longer taper.

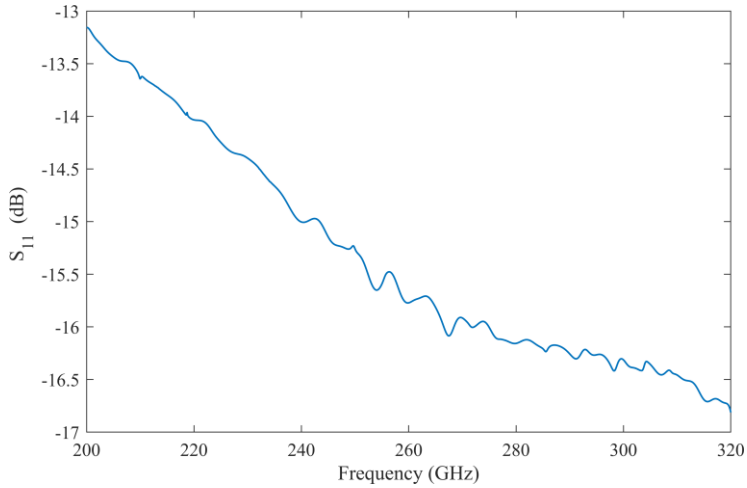

Figure 4.15. Simulated S-parameters of the antenna termination.

A termination is included at the end of the antenna to radiate the remaining energy not already radiated by the leaky wave in an end-fire direction. For a typical LWA design, the remaining energy should be less than 10% [17]. As shown in Figure 4.17, the termination used for the full antenna design includes a linearly tapered DRW and Figure 4.15 shows the simulated S_{11} of this termination. A length of 8 mm is chosen to ensure the reflection is less than -10 dB over the entire working bandwidth. To absorb the energy, the termination may be connected to a matched load using an additional

WR-3 waveguide flange, however, this was not used in this work.

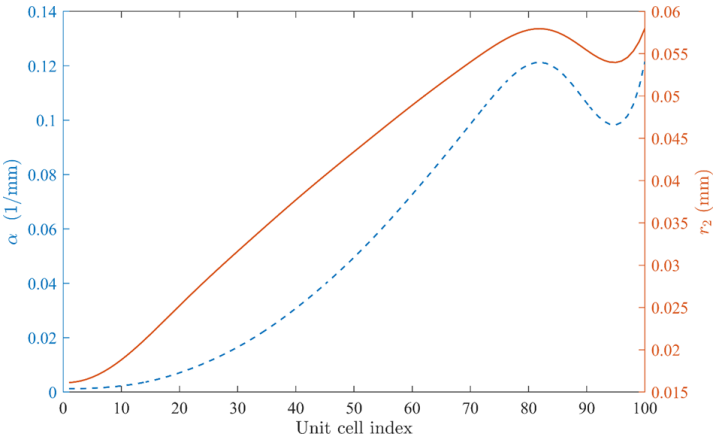

Figure 4.16. Variation of the leakage rate α and corresponding r_2 versus unit cell index defining the effective antenna aperture.

The radiation aperture of the antenna is formed from 100 units in the x-direction to achieve a high gain and to ensure that less than 10% of energy remains at the beginning of the termination. As discussed in Section 4.3.3, the final width of the taper is constrained by the length, therefore a width of $N_y = 17$ unit cells was chosen for the y-direction. The radiation aperture configuration described above has dimensions of 2.5λ by 40λ at 270 GHz. Given that the effective antenna aperture is narrower in the y-direction compared to the x-direction, this large aperture size results in a high-gain fan beam in the far-field. However, integrating this large aperture with devices that require smaller antennas can be challenging. This is attributed to the lower leakage rate of the dielectric unit cell compared to conventional metal-based unit cell designs, as previously mentioned [20].

Figure 4.16 shows the Taylor amplitude tapering of the leakage rate α and corresponding r_2 dimensions over the length of the antenna. The width of the antenna is fusiform, as shown in Figure 4.17, due to the unit cell size gradually changing with x.

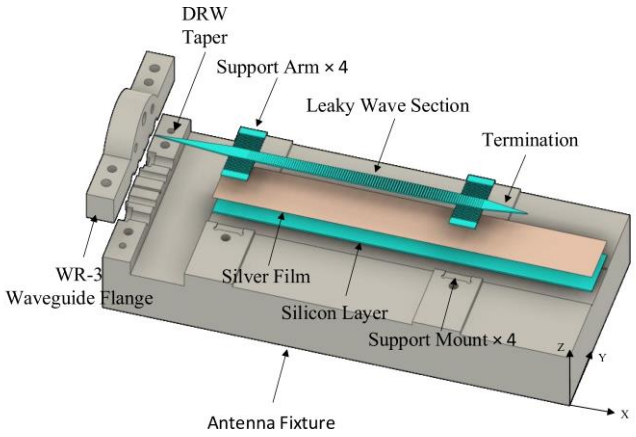

(a)

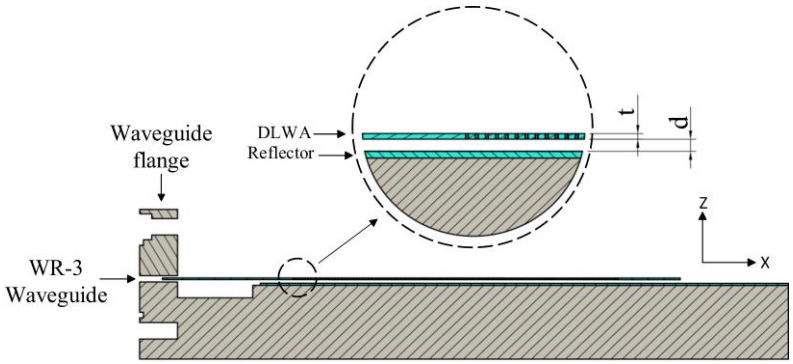

(b)

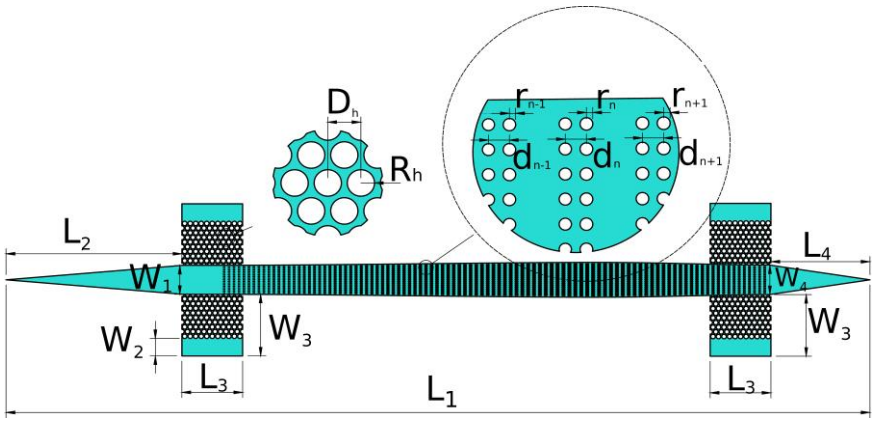

(c)

Figure 4.17. Full design of the DLWA. (a) Exploded view of the DLWA and antenna fixture. (b) Cross-section of fixture, reflector and DLWA. (c) Antenna unit cell and support arm details.

The full assembly of the DLWA is shown in Figure 4.17, which consists of the HRS DLWA, reflector and antenna fixture. The HRS DLWA comprises a linearly-tapered

DRW section, leaky wave radiating section and termination. The reflector consists of a silver thin film deposited on the surface of a silicon slab. For the convenience of measurement, a metal antenna fixture is designed with a UG387/U waveguide flange, WR-3 rectangular waveguide, and mounting points to support the HRS DLWA as shown in Figure 4.17(a).

Table 4.2. Design Parameters

Parameter	Description	Value
tan(δ)	Loss tangent of the HRS	5.18×10^{-5}
d	Distance between DLWA and reflector	0.5 mm
t	Thickness of DLWA	0.28 mm
N_x	Number of unit cells in the x-direction	100
N_y	Number of unit cells in the y-direction	17
D_h	Distance between two circles	0.437 mm
R_h	Radius of the circle	0.179 mm
ε_r	Relative permittivity of DLWA	11.67
L_1	Length of DLWA	68.4 mm
L_2	Length of tapered waveguide	14 mm
L_3	Width of support arm	4.8 mm
L_4	Length of termination	8 mm
W_1	Width at end of tapered waveguide	2.4 mm
W_2	Extra width of support arm	1.58 mm
W_3	Length of support arm	4.97 mm
W_4	Width at the start of termination	2.917 mm

Four supports arms are included on the HRS DLWA that fit into recesses in the antenna fixture. A triangular lattice of through-holes in the support arms form an electromagnetic bandgap structure (similar to in [23]) which minimizes the leakage of energy from the antenna into the support arms. A plot of the dispersion properties of this lattice of holes in Figure 4.18 shows that the bandgap covers the entire WR-3 waveguide band preventing the loss of energy. Table 4.2 summarizes the parameters of the DLWA design.

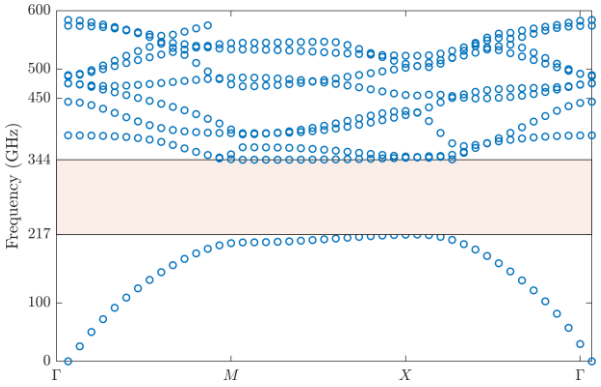

Figure 4.18. Dispersion diagram of the unit cell forming the support arms. The bandgap covers the whole WR-3 band from 217-344 GHz.

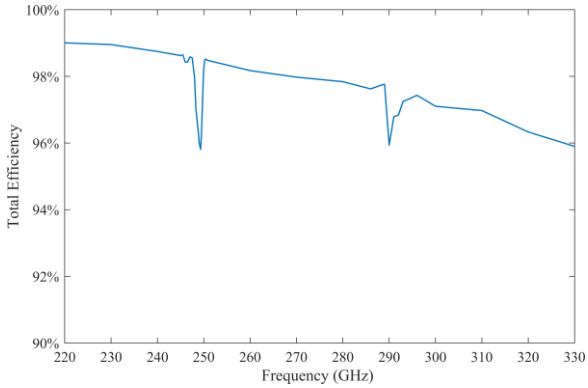

Figure 4.19. Simulated total efficiency of the DLWA.

The all-dielectric design of the DLWA, except for the reflector, significantly reduces Ohmic losses and improves antenna efficiency. The full-wave simulation indicated that the Ohmic loss attributable to the silver layer of the reflector is less than 0.1%. As illustrated in Figure 4.19, the DLWA's total efficiency remains above 95% across nearly the entire WR-3 waveguide band. Furthermore, the presence of the TE_2 mode influences the efficiency around 290 GHz.

4.5. Fabrication

This section presents the fabrication process of the DLWA, divided into two procedures: the DRIE fabrication process of HRS and the CNC machining of the

antenna fixture.

4.5.1. Deep Reactive Ion Etching of HRS

The DRIE fabrication process has several advantages over conventional CNC machining for terahertz antenna fabrication with micrometer accuracy and very low surface roughness. The Bosch process of DRIE can realize high-aspect ratio structures with near-vertical sidewalls by cycling between plasma etching with SF_6 and deposition of a C_4F_8 passivation layer [24]. Atomic force microscopy analysis of a similar etch process demonstrated a hole sidewall root mean square (RMS) roughness of less than 300 nm.

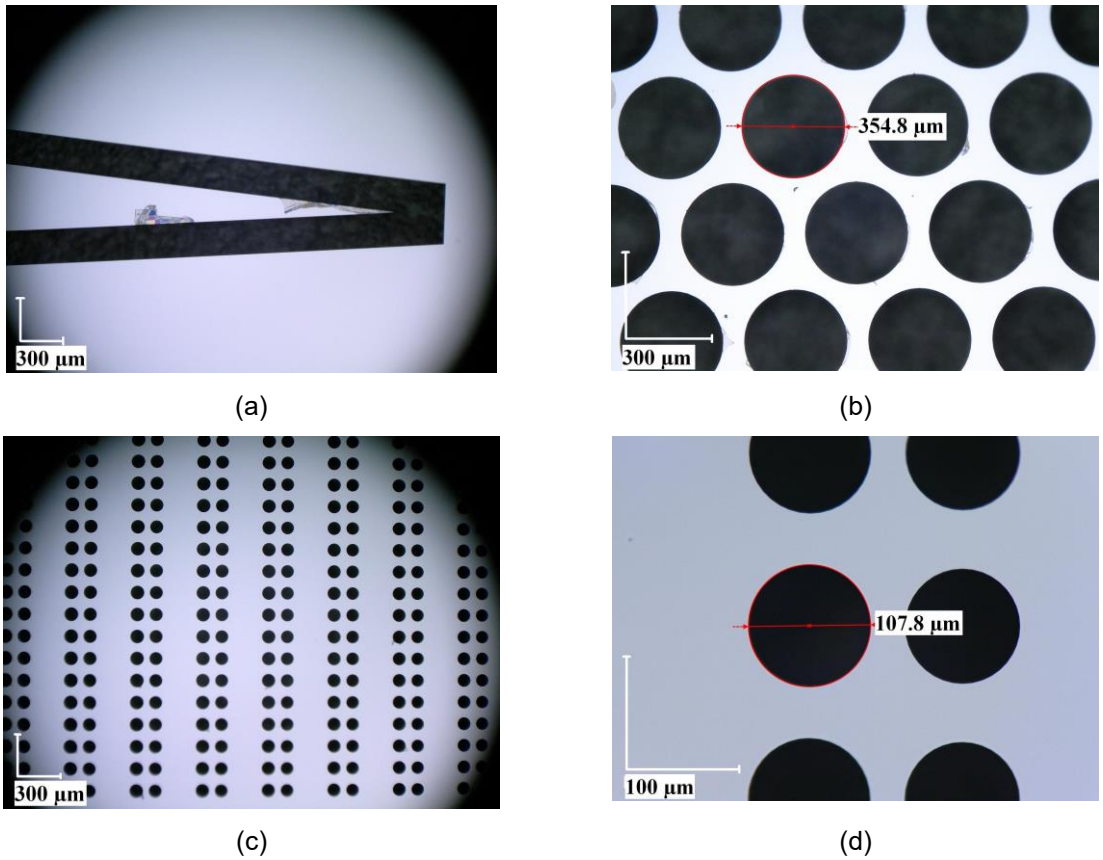

Figure 4.20. Microscope images of the HRS wafer after DRIE. (a) Waveguide taper before separation of the device from the wafer. (b) Holes in the support arm. (c) Small and (d) large holes in the leaky wave section of the antenna.

The DLWA is bulk micromachined from a four-inch diameter HRS wafer. This process employs the Bosch DRIE technique at the Vmicro SAS fabrication facility, achieving full wafer etching in a single step. The HRS wafer was 280 μm thick with a measured DC resistivity $\geq 400{,}000$ ohm.cm. The etching process was optimized to achieve uniform etching across the wafer for the different hole sizes and close to vertical sidewalls.

Figure 4.20 shows microscope images of the HRS after DRIE processing, and it can be observed that good circularity of the holes and straight edges of the taper are achieved. After microscopic measurement, over-etching of less than 5 μm in the hole diameters was observed. Near vertical sidewalls of the holes are achieved with a measured angle of less than 0.7°.

4.5.2. Antenna Fixture

The micromachined HRS DLWA was mounted in a CNC-machined brass antenna fixture which suspends it above a reflector, shown in Figure 4.20. Four nylon screws were used to fasten the micromachined HRS to the antenna fixture.

Figure 4.21. The assembled DLWA is formed from a micromachined HRS piece suspended above a reflector. A UG387/U waveguide flange (left side of the photo) is used to interface with a WR-3 rectangular metal waveguide which excites the HRS DSW.

The reflector is fabricated from a 280 μm thick rectangular piece of silicon with a 1 μm

thick sputtered silver thin film, which is significantly thicker than the skin depth of 0.135 μm at 220 GHz. The silicon wafer for the reflector was cut into the rectangular shape using laser ablation such that it sits inside a machined recess in the antenna fixture.

4.6. Measurement Results and Discussion

The DLWA S-parameters were measured using a Keysight N5247B PNA-X network analyzer equipped with WR-3 frequency extender heads. The PNA-X was calibrated using the Through-Reflect-Line (TRL) calibration technique. The radiation pattern was measured using the set-up shown in Figure 4.22.

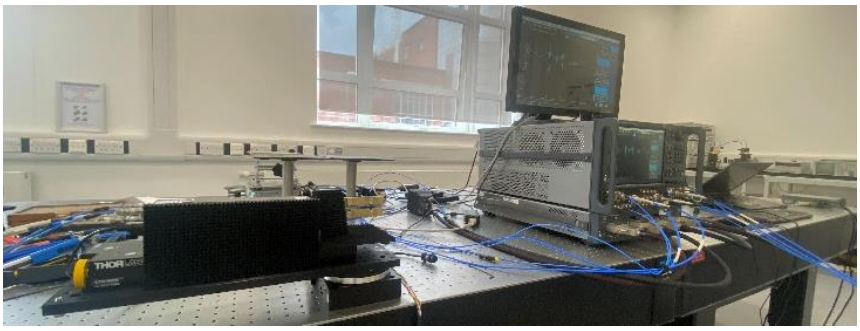

(a)

(b)

Figure 4.22. Far-field antenna measurement set-up. (a) Keysight N5247B PNA-X network analyzer and the DLWA connected to the WR-3 waveguide band frequency extender head. Note that some absorber panels have been removed for clarity. (b) Perspective view of the source frequency extender head connected to a Gaussian-beam corrugated horn antenna.

In brief, the AUT frequency extender head was mounted on a Thorlabs LTS150/M linear stage on top of a rotational stage. The linear stage was used to position the phase centre of the DLWA at broadside frequency on the rotational axis. The rotational stage was used to rotate the antenna and frequency extender head to measure the principal cuts of the radiation pattern. A Gaussian-beam corrugated horn antenna connected to a second frequency extender head was used as the source antenna. 3D-printed pyramidal absorber panels were used to mitigate the effects of reflections in the measurement set-up (see [25]). A separation distance of 4.09 m between the DLWA and corrugated horn antenna was used to satisfy the far-field measurement requirement.

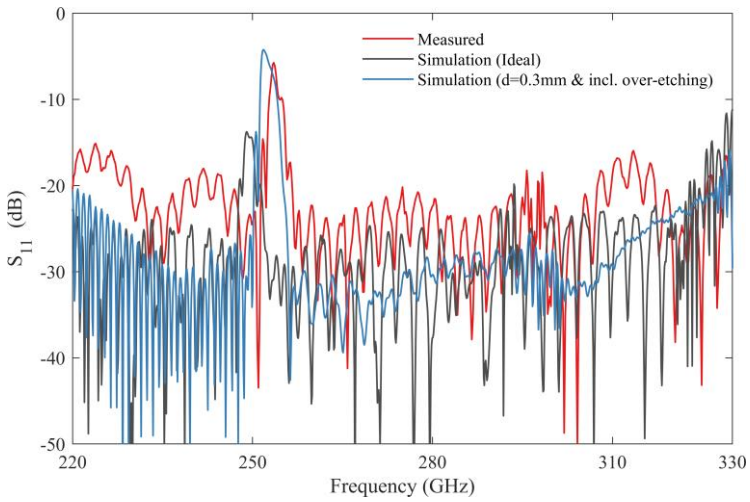

Figure 4.23. Comparison of simulated and measured S-parameter of the DLWA

As illustrated Figure 4.23, the S_{11} measurement of the DLWA demonstrates values below -15 dB across the H-band, except for a peak at approximately 253 GHz corresponding to broadside radiation. This divergence can be primarily attributed to the limitations inherent in the CNC machining process, leading to discrepancies in tolerances and subsequently, a reduced distance between the reflector and the HRS relative to the intended design. Furthermore, over-etching of the DLWA exacerbates

the disparity observed between the ideal DLWA and the simulation results. This effect can be seen in simulations which incorporates both the over-etching and the reduced distance between the reflector and HRS ($d = 0.3$ mm) as presented in Figure 4.23. The measured S_{11} aligns closely with the simulated outcomes when both the $d = 0.3$ mm deviation and over-etching are accounted for.

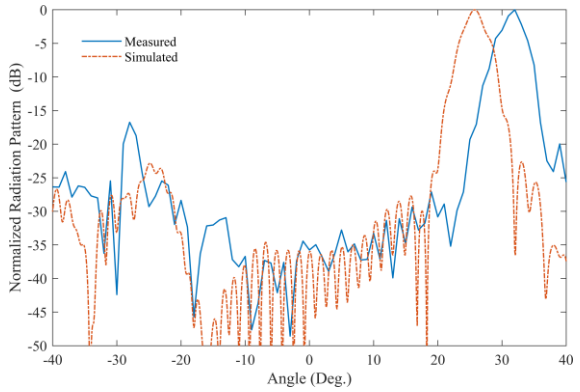

(a) 220 GHz

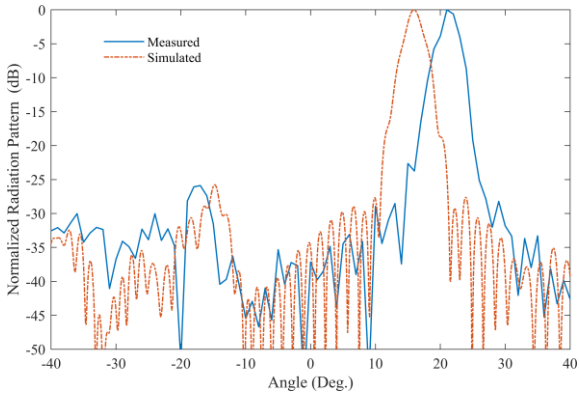

(b) 230 GHz

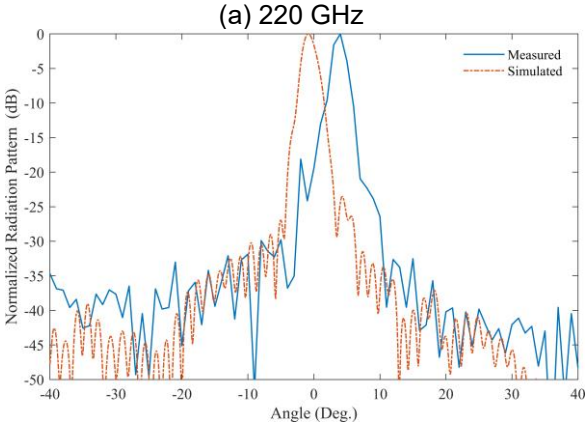

(c) 250 GHz

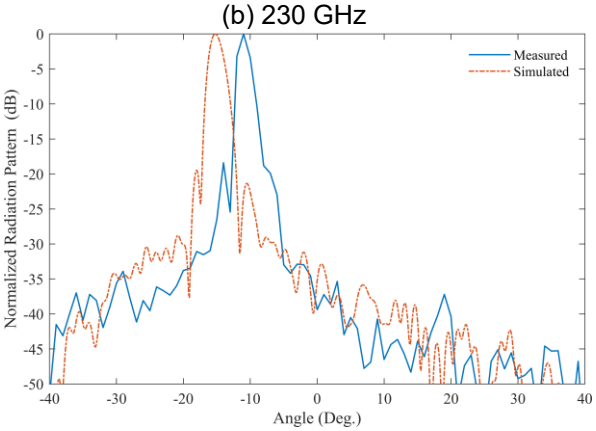

(d) 270 GHz

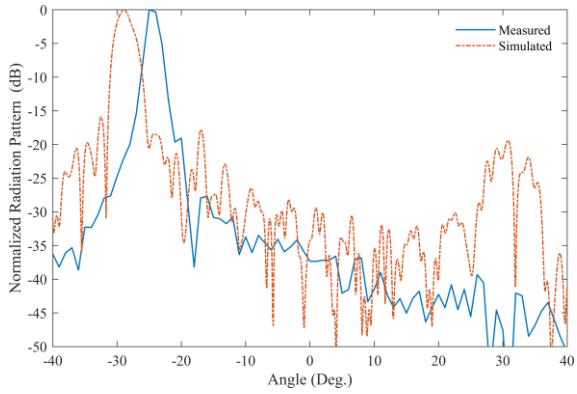

(e) 290 GHz

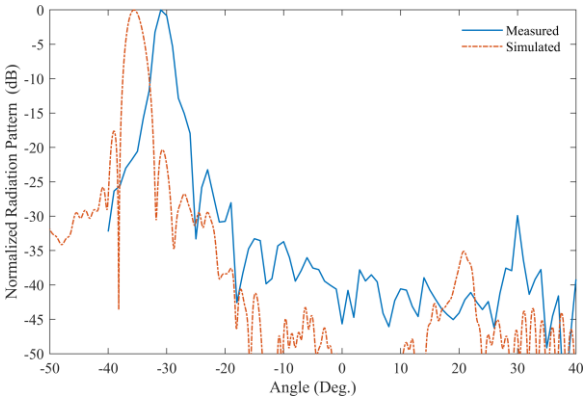

(f) 300 GHz

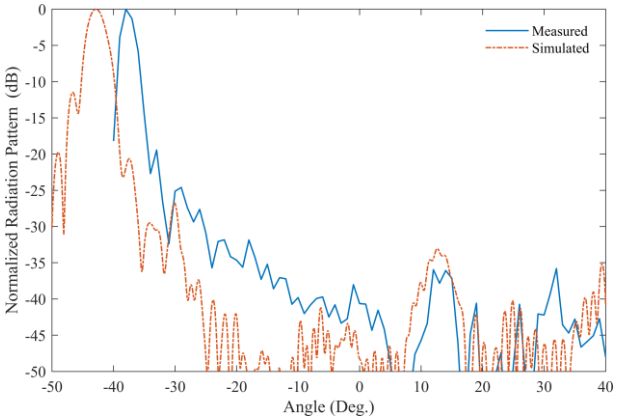

(g) 310 GHz

Figure 4.24. Measured (blue solid) and simulated (orange dashed) H-plane radiation patterns of the DLWA.

The far-field radiation pattern of the DLWA is presented in Figure 4.24 and compared with the results from full-wave simulation. It can be seen that there is a broad agreement with around 5° to 7° offset in the beam pointing angle which is attributed to limitations in the accuracy of the fabrication and packaging process. These limitations include CNC machining errors and DRIE process inaccuracies. Notably, the CNC machining error causing the reduced distance between the reflector and the HRS is not the primary reason for the beam pointing angle offset. Several rounds of simulations considering the over-etching of air holes, modelled with a normal distribution during the DRIE process, confirm that over-etching is the main cause of the beam pointing angle offset compared to the simulation results. Furthermore, given the DLWA's thickness of only 280 μm, manual packaging with fixtures and screws can cause slight deformation due to uneven pressure. Additionally, the fragility of the DLWA complicates the tuning of the assembled device.

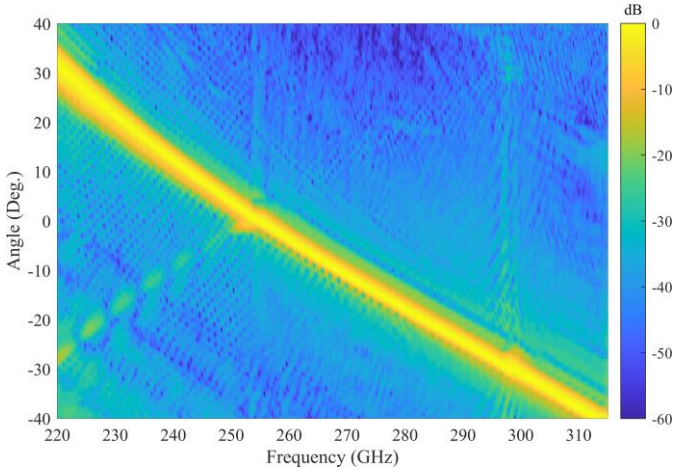

Figure 4.25. Measured normalized gain of the DLWA with frequency (x-axis) and theta angle in the H-plane (y-axis). Colour indicates the normalized gain value.

Figure 4.25 shows the measured normalized gain versus frequency and theta angle in the H-plane. It can be seen that the antenna main beam scans from -32° at 220 GHz to 40° at 313 GHz. The constraints imposed by the RF cable's length, when attached to the frequency extender, restrict the rotation angle during antenna measurements to a range of $\pm$40 degrees.

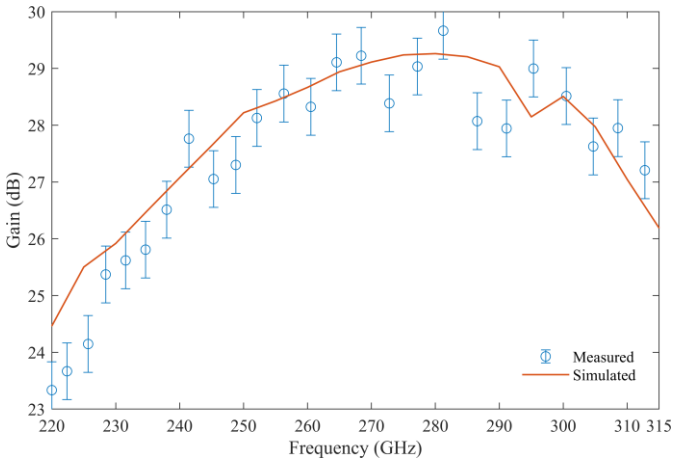

Figure 4.26. Simulated and measured antenna gain versus frequency. Error bars on the measured gain represent an uncertainty of ±0.5 dB in line with the standard gain antenna's specifications.

The gain of the DLWA is shown in Figure 4.26 and compared with the full wave simulation result. The performance of the prototype deteriorates at around 295 GHz, where the TE_1 and TE_2 modes become degenerate, as explained in Chapter 4.2.1.

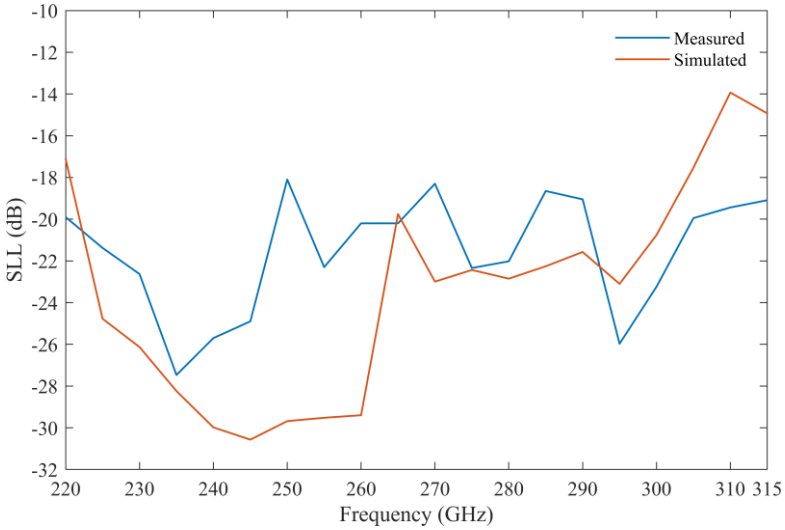

Figure 4.27. H-plane SLL of the DLWA measured and compare with the simulated result.

The far-field measured results show that the DLWA's SLL in the H-plane maintains between -17 dB and -28 dB over most of the WR-3 band, as shown in Figure 4.27.

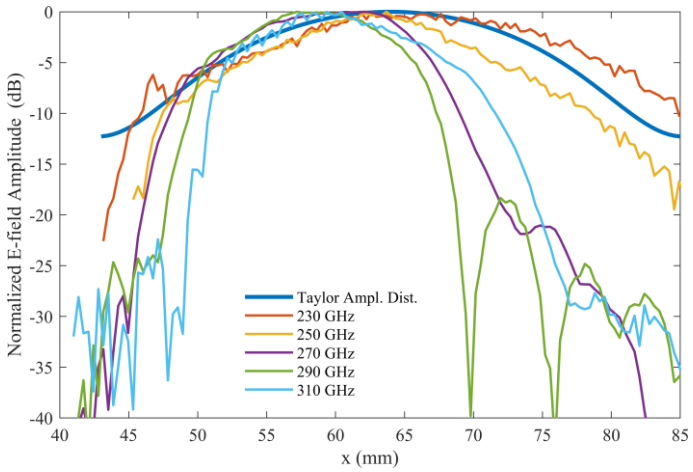

Figure 4.28. E-field amplitude measured along the length of the antenna by a near-field probe.

A near-field probe was used to measure the amplitude of the leaky wave mode along the length of the antenna. The WR-3 open-ended waveguide probe was line-scanned along the centreline in the x-direction to measure electric field strength. During the measurement, the probe maintained a distance of 3.5 mm from the HRS surface. Figure 4.28 shows the measured normalized electric field for various frequencies. It can be seen that at the design frequency of 250 GHz, there is good agreement

between the measured and the designed -30 dB Taylor amplitude distribution. However, the SLL of the measured DLWA prototype is somewhat higher than -30 dB due to the limited tolerance of the CNC machining process. It can be observed that as the frequency moves away from 250 GHz, there is increased tapering in the field distribution.

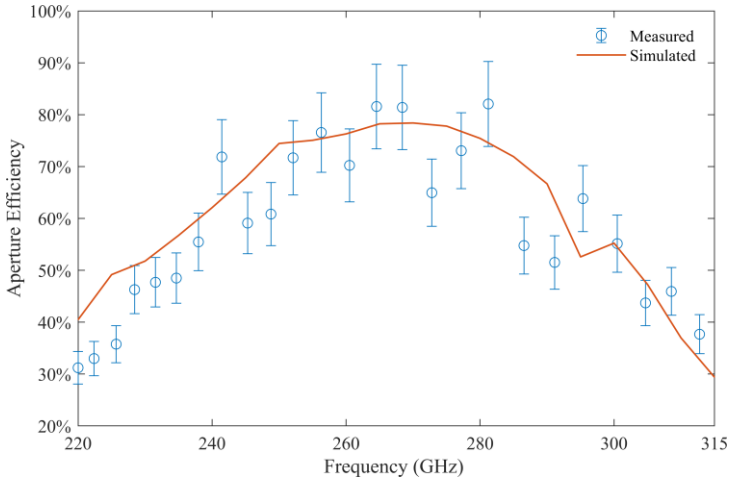

Figure 4.29: Comparison of the DLWA prototype's aperture efficiency with simulation results.

In Figure 4.29, the aperture efficiency of the DLWA is presented. The error bars indicate the measurement uncertainties related to the DLWA's gain. At 265 GHz, the aperture efficiency peaks at 81.5% for an effective radiation aperture size of 43.1 mm by 2.37 mm.

4.7. Summary

In this chapter, an all-dielectric terahertz DLWA with a fan-beam radiation pattern, low SLL and high aperture efficiency is demonstrated in the H-band (220 – 325 GHz). The periodic LWA is formed from a grating-like structure in a dielectric slab waveguide which supports a leaky slow-wave. The all-dielectric unit cell is designed to exploit accidental degeneracy (i.e. frequency-balancing) to suppress the open stopband at

broadside radiation. The radiation aperture is tapered with a Taylor amplitude distribution to achieve a SLL less than -30 dB at the centre frequency. A peak aperture efficiency of 81.5% is achieved at 265 GHz. Additionally, simulations indicate a total efficiency exceeding 95% across most of the H-band, in part, due to the minimization of Ohmic losses. The measured results confirm that the antenna achieves continuous beam-scanning from -32° to 40° with a variation in gain from 23.4 to 29 dBi when the frequency scans from 220 GHz to 313 GHz. The antenna is fabricated using through-wafer DRIE of a high resistivity silicon wafer.

Reference

[1] A. Malekabadi, S. A. Charlebois, D. Deslandes, and F. Boone, "High-Resistivity Silicon Dielectric Ribbon Waveguide for Single-Mode Low-Loss Propagation at F/G-Bands," *IEEE Trans. Terahertz Sci. Technol.,* vol. 4, no. 4, pp. 447-453, 2014.

[2] J. Dai, J. Zhang, W. Zhang, and D. Grischkowsky, "Terahertz Time-Domain Spectroscopy Characterization of the Far-Infrared Absorption and Index of Refraction of High-Resistivity, Float-Zone Silicon," *JOSA B,* vol. 21, no. 7, pp. 1379-1386, 2004.

[3] J. W. Lamb, "Miscellaneous Data on Materials for Millimetre and Submillimetre Optics," *Int. J. Infrared Millimeter Waves,* vol. 17, pp. 1997-2034, 1996.

[4] "Eigenmode Solver Overview," *CST Studio 2021 Help Files*: Dassault Systemes Deutschland GmbH., 2021.

[5] Z. Li *et al.*, "Investigation of Leaky-Wave Antenna with Stable Wide Beam-Scanning Characteristic," *IEEE Trans. Antennas Propag.,* vol. 70, no. 1, pp. 240-249, 2021.

[6] C. Hammes and A. R. Diewald, "Periodic High-Sensitive Beam-Steering Leaky-Wave Antenna with Circular Polarization," *IEEE Trans. Antennas Propag.,* vol. 68, no. 3, pp. 1937-1944, 2019.

[7] S. Otto, A. Al-Bassam, C. Zhichao, A. Rennings, K. Solbach, and C. Caloz, "Q-Balancing in Periodic Leaky-Wave Antennas to Mitigate Broadside Radiation Issues," in *2012 The 7th German Microwave Conference*, 12-14 March 2012 2012, pp. 1-4.

[8] Z.-Q. Ma, *Group Theory for Physicists*. World Scientific, 2007.

[9] A. Zee, *Group Theory in a Nutshell for Physicists*. Princeton University Press, 2016.

[10] L. Xu, H.-X. Wang, Y.-D. Xu, H.-Y. Chen, and J.-H. Jiang, "Accidental

Degeneracy in Photonic Bands and Topological Phase Transitions in Two-Dimensional Core-Shell Dielectric Photonic Crystals," *Opt. Express,* vol. 24, no. 16, pp. 18059-18071, 2016/08/08 2016.

[11] S. Otto, A. Al-Bassam, A. Rennings, K. Solbach, and C. Caloz, "Transversal Asymmetry in Periodic Leaky-Wave Antennas for Bloch Impedance and Radiation Efficiency Equalization through Broadside," *IEEE Trans. Antennas Propag.,* vol. 62, no. 10, pp. 5037-5054, 2014.

[12] S. y. Qin, B. Du, and W. j. Zhang, "Calculation of Ohm Loss Efficiency for Millimetre Wave Reflector Antennas," in *Proceedings of the 9th International Symposium on Antennas, Propagation and EM Theory*, 29 Nov.-2 Dec. 2010 2010, pp. 23-25.

[13] Y. Huang *et al.*, "Development of a Model for Evaluating Propagation Loss of Metal-Coated Dielectric Terahertz Waveguides," *J. Appl. Phys.,* vol. 130, no. 5, p. 055104, 2021.

[14] Y. V. Stebunov, D. I. Yakubovsky, D. Y. Fedyanin, A. V. Arsenin, and V. S. Volkov, "Superior Sensitivity of Copper-Based Plasmonic Biosensors," *Langmuir,* vol. 34, no. 15, pp. 4681-4687, 2018.

[15] C. S. Prasad and A. Biswas, "Dielectric Image Line-Based Leaky-Wave Antenna for Wide Range of Beam Scanning through Broadside," *IEEE Trans. Antennas Propag.,* vol. 65, no. 8, pp. 4311-4315, 2017.

[16] P. Bhartia and I. J. Bahl, "Millimeter Wave Engineering and Applications," 1984.

[17] D. R. Jackson and A. A. Oliner, "Leaky-Wave Antennas," in *Modern Antenna Handbook*, 2008, pp. 325-367.

[18] S. Jyh-Wen, L. Yu-De, and C. Tai-Lee, "A Leaky-Mode S-Parameter Extraction Technique for Efficient Design of the Microstrip Line Leaky-Wave Antenna," in *1999 IEEE MTT-S International Microwave Symposium Digest (Cat. No.99CH36282)*, 13-19 June 1999 1999, vol. 1, pp. 175-178 vol.1.

[19] A. Singh, R. Paknys, and D. R. Jackson, "Using the Matrix Pencil Method to Analyze a 3d Leaky Wave Antenna," in *2015 IEEE International Symposium on Antennas and Propagation & USNC/URSI National Radio Science Meeting*, 19-24 July 2015 2015, pp. 23-24.

[20] C. A. Balanis, *Modern Antenna Handbook*. John Wiley & Sons, 2011.

[21] J. D. Joannopoulos, S. G. Johnson, and J. N. Winn, *Photonic Crystals:Molding the Flow of Light*. Photonic crystals:molding the flow of light, 1995.

[22] P. Suchoski and R. Ramaswamy, "Design of Single-Mode Step-Tapered Waveguide Sections," *IEEE J. Quantum Electron.,* vol. 23, no. 2, pp. 205-211, 1987.

[23] D. Headland, M. Fujita, and T. Nagatsuma, "Bragg-Mirror Suppression for Enhanced Bandwidth in Terahertz Photonic Crystal Waveguides," *IEEE J. Sel. Top. Quantum Electron.,* vol. 26, no. 2, pp. 1-9, 2019.

[24] F. Laermer and A. Schilp, "Method of Anisotropically Etching Silicon," ed: Google Patents, 1996.

[25] S.-H. Shin, X. Shang, N. M. Ridler, and S. Lucyszyn, "Polymer-Based 3-D Printed 140-220 Ghz Low-Cost Quasi-Optical Components and Integrated Subsystem Assembly," *IEEE Access,* vol. 9, pp. 28020-28038, 2021.

Chapter 5

A H-Band Direct Laser Written Polymer Fabry-Perot Cavity Antenna

5.1. Introduction

In the terahertz band, the high path loss due to atmospheric absorption necessitates the use of a high gain antenna for communication, radar and imaging systems. Chapter 4 demonstrated a high-gain leaky wave antenna (LWA) using high-resistivity silicon (HRS) and deep reactive ion etching (DRIE) as a potential solution for realising such an antenna. However, the use of HRS and the DRIE process can be prohibitively expensive for many applications.

An alternate antenna commonly used in this frequency regime is the lens antenna which, as discussed in Chapter 1, can achieve moderate to high gains. However, there is a lack of inexpensive dielectrics in the terahertz band which have sufficiently low loss tangents (i.e. $\tan\delta \leq 10^{-3}$) to realise a high-efficiency lens antenna. Alternatives to HRS like crystalline quartz are still expensive when compared to polymers. In this Chapter, an alternate approach is proposed which is to use a moderately lossy polymer but engineer the antenna design to minimise the dielectric loss. An advantage of lens antennas is the (mostly) avoidance of metal guiding structures which can exhibit high ohmic loss due to the reduced skin depth with increasing frequency.

In Section 2.5 an alternative novel fabrication method: direct laser writing utilizing two-

photon polymerization (2PP) photoresin, also referred to as 2PP 3D printing, is introduced. This method offers sub-micrometre resolution at a lower cost compared to DRIE and CNC machining, and it facilitates the rapid creation of intricate and complex 3D structures. This positions it as a feasible solution for advanced terahertz antenna design.

Nevertheless, a significant challenge associated with employing 2PP 3D printing for lens antennas operating in the terahertz band is the substantial dielectric loss typically exhibited by the 2PP photoresins. However, this chapter will demonstrate an innovative antenna design that, through careful engineering, overcomes the limitations of moderately lossy commercially available photoresin, which is called IP-Q from the company Nanoscribe GmbH. This approach makes it possible to use these more affordable polymers effectively in terahertz antenna design.

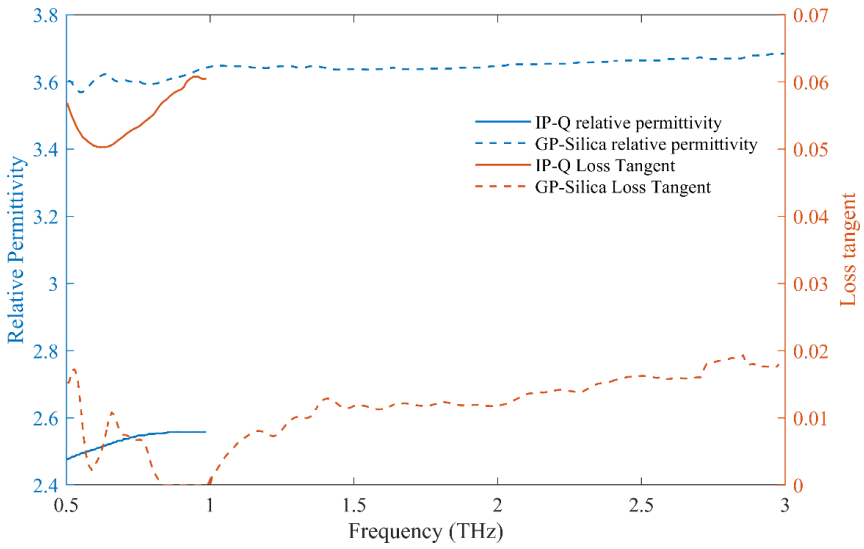

Figure 5.1. Dielectric loss tangent and permittivity of photoresins GP-Silica and IP-Q, measured by Magaway *et al.* [1].

As shown in Figure 5.1, the dielectric loss and permittivity of two photoresins suitable for millimetric scale terahertz structures, GP-Silica and IP-Q, which are available from the company NanoScribe, are measured using THz time-domain spectroscopy and

reported by Magaway et al. [1]. As shown in Figure 5.1, the relative permittivities of IP-Q and GP-Silica at 500 GHz are 2.5 and 3.6, respectively. Moreover, it can be seen that the dielectric loss tangent of GP-Silica is only 0.01 at 300 GHz, while for IP-Q it is 0.06 at the same frequency. However, 3D printed structures that utilize GP-Silica exhibit significant shrinkage after a high-temperature sintering process, thus introducing additional complexities in the design of the antenna. As a result, IP-Q is preferred for prototype antenna designs owing to its straightforward post-processing and reliable precision in creating millimetre-scale structures.

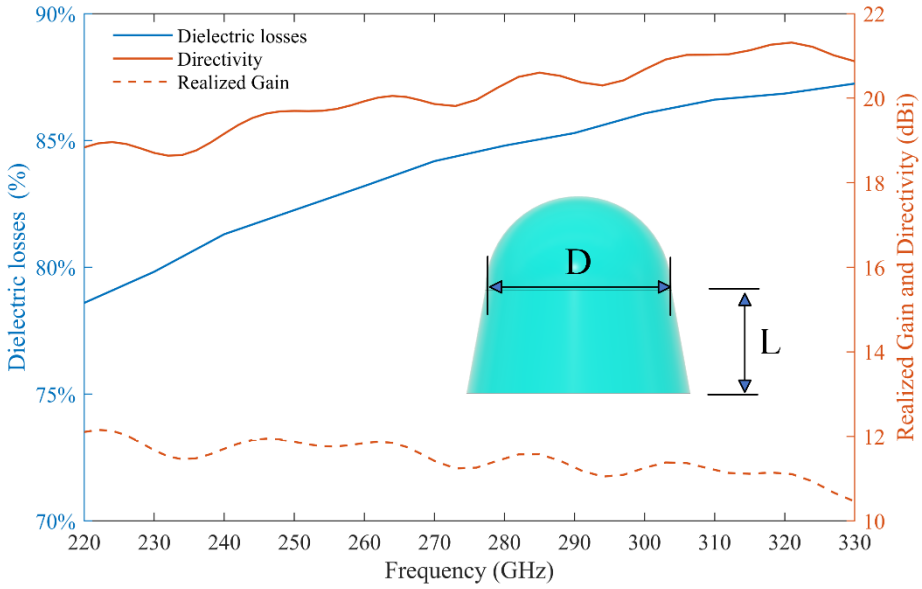

Figure 5.2. Simulated performance of a hypothetical extended hemispherical lens antenna [2] fabricated use IP-Q photon resin. $D = 5\ \mathrm{mm}$, $L = 2.75\ \mathrm{mm}$, outward tapering angle is 10.4 degrees.

To elucidate the impact of IP-Q's high dielectric loss on lens antenna gain, as depicted in Figure 5.2, a full wave simulation was conducted on an extended hemispherical lens antenna composed of IP-Q photoresin. The configuration of this extended hemispherical lens antenna follows the design reported by Konstantinidis *et al.* [2]. For an extended hemispherical lens antenna, the focal length, denoted as f, of the hemispherical lens can be calculated using the following formula [3]:

$$f = \frac{D}{2(\sqrt{\varepsilon} - 1)} \tag{5.1}$$

where D is the diameter of the sphere, and ε is the relative permittivity of the lens material. In this case, $\varepsilon = 2.4$, therefore, due to the low dielectric permittivity, for a fixed aperture size and lens diameter D, the IP-Q lens antenna will have a longer focal length. This will require a longer extension length L, leading to high dielectric loss.

As shown in Figure 5.2, the full-wave simulation results show that the dielectric loss of this lens range from 78% to 88% across the WR-3 band. Consequently, even though a directivity higher than 20 dBi is achieved in this design, the realized gain is significantly degraded to around 12 dBi across the WR-3 band. It is worth noting that in the work reported by Konstantinidis *et al*. [2], Rexolite (loss tangent = 0.008) is used for the fabrication of the extended hemispherical lens antenna, thereby avoiding high dielectric loss; however, this material is not compatible with 2PP 3D printing and requires CNC machining and polishing.

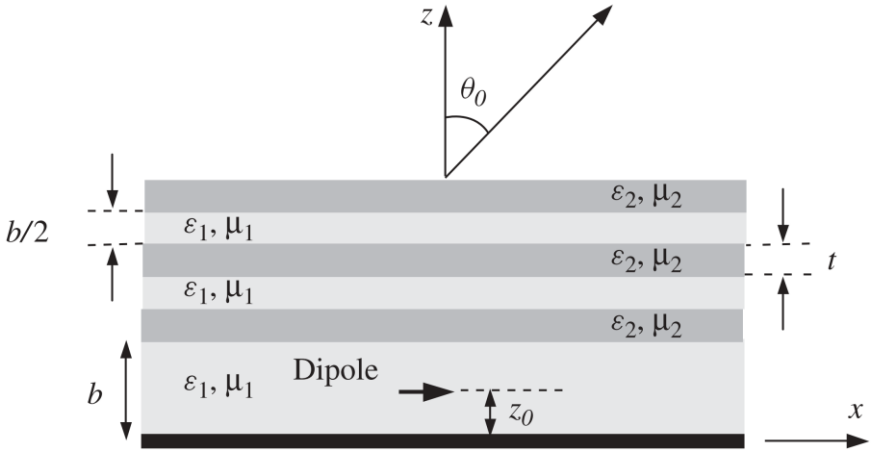

Figure 5.3. A LWA formed by multi-dielectric superstrate layers and a metal ground, excited by a horizontal electric dipole source. The figure is reproduced from [4].

The origin of the elevated dielectric loss can be attributed to substantial energy absorption by the solid dielectric volume as the wave passes through the electrically

large lens. One approach to mitigate this effect involves substituting the solid dielectric material with an alternative effective dielectric medium, and reducing the volume of the lossy dielectric material that the wave encounters. The infill factor [5] is a metric that quantifies this concept, typically defined as the ratio of the dielectric material volume within the unit cell to the total volume of the unit cell. It is expressed by the equation:

$$\text{Infill Factor} = \frac{\text{Volume of Dielectric Material within Unit Cell}}{\text{Total Volume of Unit Cell}} \tag{5.2}$$

By reducing the IP-Q infill factor within the antenna structure while preserving the wave reshaping capabilities, could lead to a viable solution.

As shown in Figure 5.3, the Fabry-Perot cavity antenna (FPCA) represents one of the antenna categories that fulfils this requirement. This chapter proposes an FPCA constructed with sub-wavelength air perforations in the partially reflective dielectric surfaces (PRDS), aiming to reduce the IP-Q infill factor and minimize dielectric loss. Additionally, the air gap between the PRDS in the FPCA decreases dielectric losses compared to a solid dielectric layer. The FPCA presented here employs 2PP direct laser writing technology, offering a balanced approach to cost, complexity, and performance. The particular 2PP 3D printer used in this work is the Nanoscribe GT+.

The fundamentals, including the background and theory of the FPCA, are discussed in Section 2.3. Details of the 2PP direct laser writing technology and comparison to other 3D printing technologies are presented in Section 2.5. A literature review of other published terahertz FPCA designs is presented in Section 3.3.

As discussed in Section 2.3, FPCAs attain high gain by reshaping the wavefront through resonance within the cavity. Nevertheless, due to its resonant nature, the FPCA's bandwidth is typically limited, especially when considering gain specifications. As a result, the 3 dB gain bandwidth product (GBWP) is used to evaluate the

performance of the FPCA.

As discussed in Section 2.3, an alternative approach to achieve higher 3 dB GBWP involves the use of a tapered PRDS, gradually modifying and compensating the PRS's reflective phase in the lateral direction to attain a broader bandwidth resonance. The FPCA proposed in this thesis employs this method, using a transverse gradient of the PRS' effective permittivity to enhance the impedance matching bandwidth. This design simplifies the feeding structure for the FPCA and achieves a higher 3 dB GBWP than other published works. Additionally, this thesis presents a novel approach to designing the FPCA. It considers each unit cell as a resonator in an attempt to maximize the unit cell's total Q-factor, thereby achieving a balance between dielectric loss and radiation.

The remainder of this chapter unfolds as follows: Section 5.2 outlines the antenna unit design; Section 5.3 describes the full FPCA design; Section 5.4 discusses the optimization of the full FPCA design. Lastly, Section 5.5 presents the fabrication and measurement results of the FPCA.

5.2. FPCA Unit Design

5.2.1. Effective Medium Theory Method

As discussed in the Introduction section, decreasing the dielectric infill factor results in lower dielectric losses. To reduce the dielectric losses induced by the 2PP photoresin, the PRS is formed using sub-wavelength perforations in cuboid units, as illustrated in Figure 5.4. The effective medium theory is employed to simplify a single-layer unit cell design, enabling further evaluation of the reflection amplitude and phase of multilayer unit cells. The effective permittivity of an individual single-layer unit cell can be determined using the Maxwell Garnett theory [6]:

$$\varepsilon_{eff} = \frac{(a^2 - b^2) \times \varepsilon_d + b^2 \times \varepsilon_{air}}{a^2} \tag{5.3}$$

where a represents the edge length of the dielectric rectangular prism unit cell, b represents the edge length of the perforated cuboid air hole, as shown in Figure 5.4. ε_d is the relative permittivity of the IP-Q, which, as discussed in the Introduction, is 2.4 at 300 GHz, ε_{air} is the relative permittivity of air. Consequently, through adjusting the unit cell configuration, the equivalent permittivity distribution of PRS can be calculated and flexibly controlled.

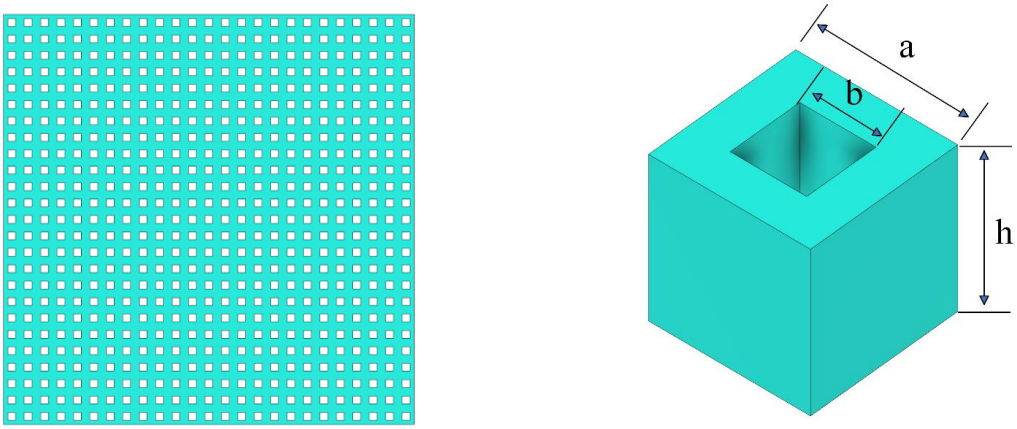

(a) (b)

Figure 5.4. PRS of the FPCA. (a) One single layer PRS. (b) PRS unit cell configuration, $a = 0.17$ mm, $b = 0.08$ mm and $h = 0.17$ mm.

As illustrated in Figure 5.5, the calculation of the effective relative permittivity of the unit cell varies with changes in the air hole edge lengths. Another aspect to consider is maintaining the structural stability of the entire FPCA; it requires that the size of the air holes not be overly large to ensure sufficient wall thickness between neighbouring unit cells. In this design, b, the maximum hole edge size is set at 0.15 mm.

From a different perspective, the FPCA proposed in this thesis essentially employs a leaky distributed Bragg reflector [7] above the WR3 waveguide aperture. The multilayer dielectric slabs, coupled with air gaps between each dielectric layer, realise a reflector

with a (weak) stopband. By managing the permittivity of each layer, both the reflection amplitude and phase distribution across the spectrum can be adjusted.

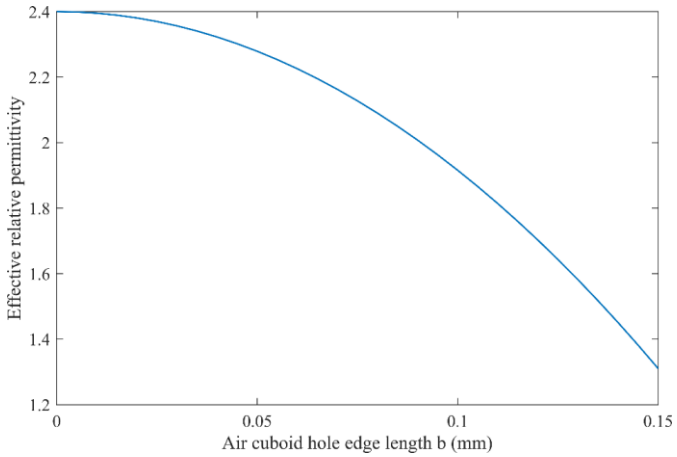

Figure 5.5. Relative permittivity of unit cell with different air cuboid hole edge length b (mm).

To further ascertain the optimal number of PRDS layers in the FPCA described in this thesis, Table 5.1 details the simulated performance of the FPCA with various number of PRDS layers. The PRDS is configured using the unit cell depicted in Figure 5.4(b). An increase in the number of layers correlates with a rise in realized gain, however, this is also accompanied by heightened dielectric loss attributable to the IP-Q. Notably, upon reaching four layers, the realized gain plateaus at 16.95 dBi. Moreover, the 3 dB gain bandwidth maintains a consistent value of approximately 10% when the layer count varies from three to seven.

Table 5.1. Comparison of simulated performance of FPCA with different number of PRDS layers.

Number of Layers	Energy Loss in IP-Q	Realized Gain	3 dB Gain Bandwidth
2	12.2%	12.8	15.1%
3	18.6%	15.5	10.3%
4	27.6%	16.95	9.65%
5	34.2%	17.3	10.53%
6	38.8%	17.8	10.25%
7	40.1%	18.35	9.11%

Based on the data shown in Table 5.1, further evaluation of the FPCA proposed in

this work involves a four-layer dielectric PRS unit cell configuration, as depicted in Figure 5.6, as this represents a good trade-off between dielectric loss and realized gain. The initial distance between each dielectric layer is 0.29 mm. This distance represents a quarter of the wavelength in the air at the designated centre frequency of 260 GHz.

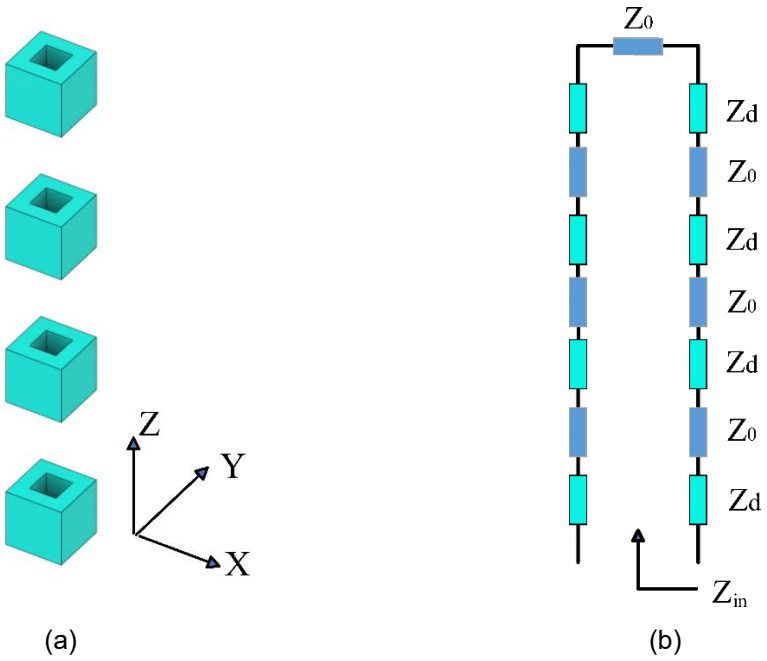

Figure 5.6. (a) Four-layer dielectric PRDS unit cell configuration. (b) TLM corresponding to the PRDS unit cell.

A common approach to calculating the properties of the FPCA is to use an equivalent transmission line model (TLM) as discussed in Section 2.4. The amplitude and phase of the reflection of the unit cell, as shown in Figure 5.6, can then be calculated with the TLM. As illustrated in Figure 5.6, the effective permittivity of each layer is represented as a section of transmission line, with the thickness of the dielectric layer corresponding to the electrical length of the respective section. The characteristic impedance of the TLM can be calculated with (2.51) and (2.52). For simplification, each layer in Figure 5.6 possesses an identical air infill factor. The evaluation process presented in this

thesis can also be extended to more complex configurations, including layers with different dielectric infill factors and distances between them. It is worth noting that the characteristic impedance of each layer is essentially frequency-dependent for both TE and TM modes. For more detailed information about the basics of TE and TM modes, please refer to Section 2.3. At this stage, the characteristic impedance for both TE and TM modes can be approximated as the same value when the antenna radiates at broadside [8]. The propagation constants for both TE and TM modes can then be calculated as follows:

$$k_{z_0} = \sqrt{{k_0}^2 - {k_\rho}^2} \tag{5.4}$$

$$k_{z_d} = \sqrt{{k_d}^2 - {k_\rho}^2} \tag{5.5}$$

Given that the radiation is only directed towards broadside, this implies:

$$k_\rho = \sqrt{{k_x}^2 + {k_y}^2} = 0 \tag{5.6}$$

Then from (5.4), (5.5) and (5.6), the following results can be derived:

$$k_{z_0} = k_0 \tag{5.7}$$

$$k_{z_d} = k_d \tag{5.8}$$

The characteristic impedance for both TE and TM modes can then be approximated as follows:

$$Z_0^{TE} = \frac{k_0}{k_{z_0}} Z_0 = Z_0 \tag{5.9}$$

$$Z_d^{TE} = \frac{k_d}{k_{z_d}} Z_d = Z_d \tag{5.10}$$

$$Z_0^{TM} = \frac{k_{z_0}}{k_0} Z_0 = Z_0 \tag{5.11}$$

$$Z_d^{TM} = \frac{k_{z_d}}{k_d} Z_d = Z_d \tag{5.12}$$

With the above approximated conditions applied, the reflection amplitude and phase of the four-layer PRDS unit cell, calculated using TLM, are shown in Figure 5.7. It can be seen from Figure 5.7 that the four-layer PRS exhibits high reflectivity from 250 GHz to 310 GHz. The analytical calculation result using TLM is further verified by full-wave simulation by setting Floquet port at both Z_{min} and Z_{max} in CST Microwave Studio. For the four-layer unit cell, unit cell boundary conditions are applied to both $\pm x$ and $\pm y$ directions, while open boundary conditions are utilized in $\pm z$ directions to allow radiation.

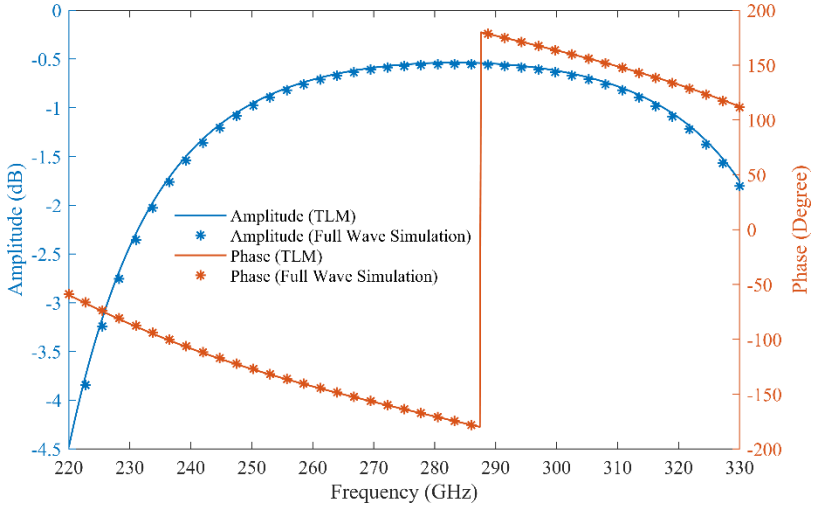

Figure 5.7. Reflection amplitude and phase of the four layers PRDS unit cell.

As observed in Figure 5.8, there is good agreement between the TLM and full-wave simulations for the four layer PRDS unit cell, confirming the accuracy of evaluating the unit cell using a TLM.

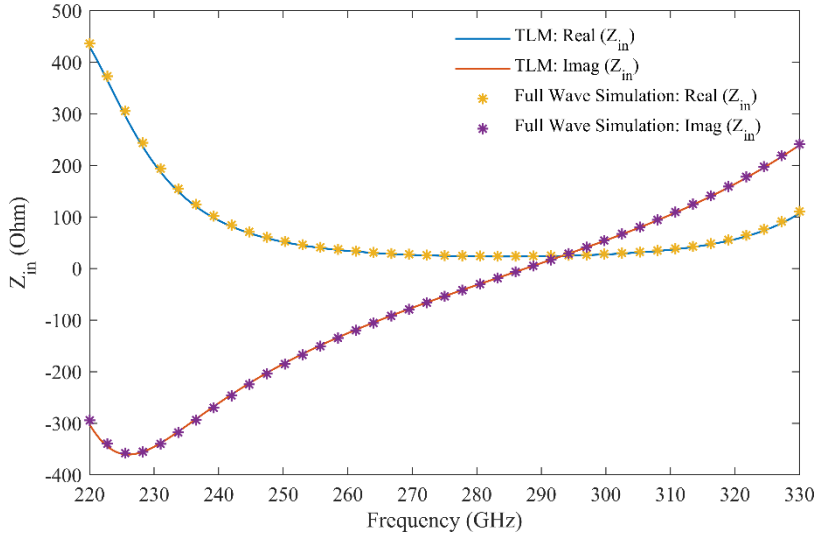

Figure 5.8. Input impedance (Z_{in}) of the four layers PRDS unit cell.

The input impedance (Z_{in}) of the four layers PRDS unit cell, as depicted in Figure 5.6(b), has been computed using the TLM. The results, presented in Figure 5.8, show a good agreement with full-wave simulation results. The analytical calculation result will be used for the dispersion analysis of the unit cell, to be discussed in the next section.

5.2.2. Dispersion Analysis

The FPCA presented in this Chapter may also be viewed as a form of 2D LWA, with the theory behind this explained in Section 2.3. The TE and TM leaky wave modes, excited by the slot open-ended waveguide, propagate radially above the metal ground surface in the air cavity [4]. Additional optimization of the unit cell design involves analysis of both TE and TM leaky wave modes using the transverse resonance method (TRM), with its fundamental theory discussed in Section 2.4.

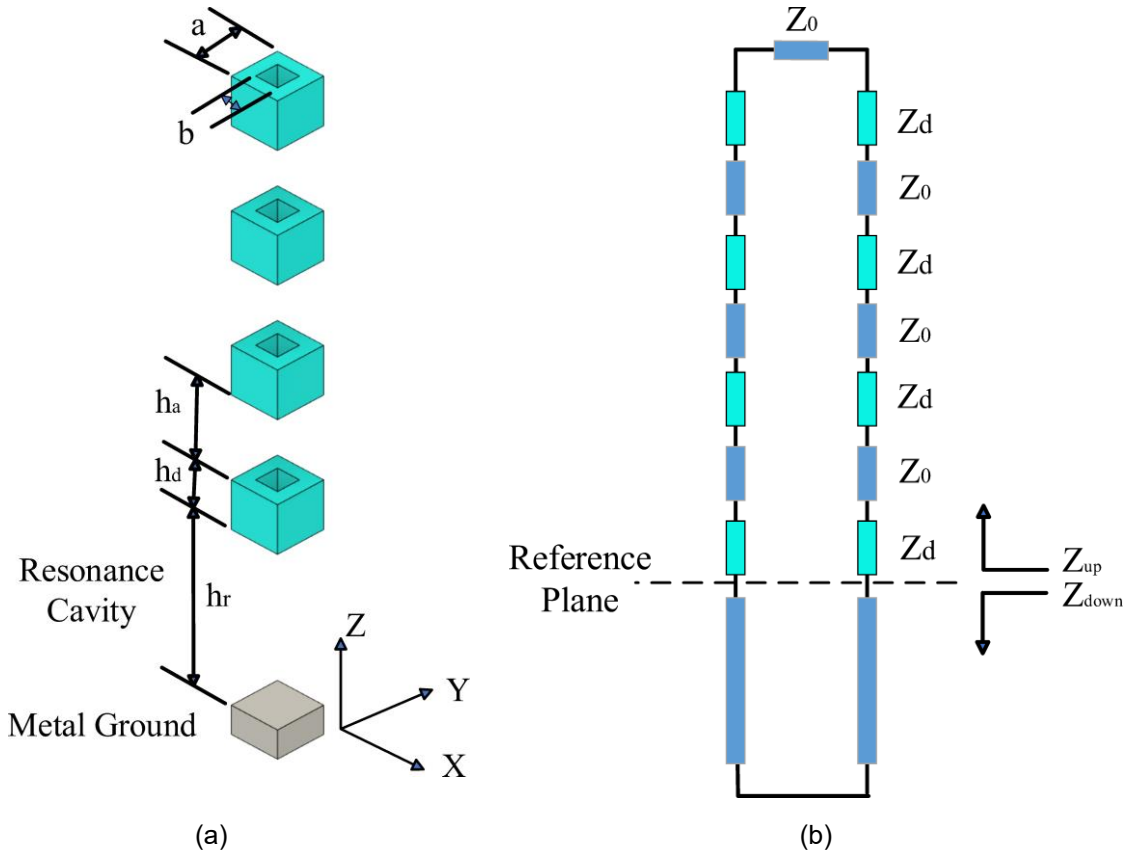

Figure 5.9. (a) Four-layer PRDS unit cell incorporating a metal ground for TRM analysis. (b) Equivalent TLM of the unit cell, the dashed line represents the reference plane for TRM analysis.

As shown in Figure 5.9(a), the four-layer PRDS unit cell is combined with an resonance cavity and metal ground, which can be electromagnetically described by the TLM shown in Figure 5.9(b), allowing computation of the input impedance on both sides of the reference plane. The chosen reference plane for TRM analysis at the top of the resonance cavity formed by the metal ground and bottom of the first dielectric unit cell, is also illustrated in Figure 5.9(b). Both the upward and downward input impedances from the reference plane are defined as Z_{up} and Z_{down}, respectively, and can be used to determine the propagation constant of the TE and TM leaky wave modes [8].

Table 5.2. Dimensions of the unit cell including metal ground, given in millimetres.

a	b	h_a	h_d	h_r
0.17	0.08	0.29	0.17	0.6

Table 5.2 provides the dimensions of the four-layer PRS unit cell, listing the uniform distance between each layer as part of the initial design for the following analysis.

The previous section approximated k_ρ as 0 for the TLM impedance calculation. However, for precise analysis of the excited TE and TM leaky wave modes in the resonance region, k_ρ is considered for the calculation of the upward input impedance Z_{up}. As Z_{up} is a function of k_ρ and frequency f for both TE and TM modes, it can be represented as follows:

$$Z_{up}^{TE/TM} = Z_{up}^{TE/TM}\left(f, k_\rho^{TE/TM}\right) \tag{5.13}$$

The transverse resonance formula can then be constructed as follows [8]:

$$Z_{down}^{TE/TM} = jZ_0^{TE/TM}\tan(k_{z_0}h_r) \tag{5.14}$$

$$Z_{down}^{TE/TM} = -Z_{up}^{TE/TM}\left(f, k_\rho^{TE/TM}\right) \tag{5.15}$$

Finally, a numerical complex root-finding technique is utilized to solve the transverse resonance formula, with the solutions for the propagation constant of the TE and TM modes represented as follows:

$$k_\rho^{TE} = \beta_{TE} + j\alpha_{TE} \tag{5.16}$$

$$k_\rho^{TM} = \beta_{TM} + j\alpha_{TM} \tag{5.17}$$

The propagation constants of TE and TM modes, solved using the TRM, are depicted in Figure 5.10. These constants are juxtaposed with the simulation results from the CST Eigenmode solver for verification. The "General (Lossy)" method [9] has been employed in the CST MWS Eigenmode solver, permitting open boundary conditions in

the simulation. With the CST MWS Eigenmode solver, periodic boundary conditions are applied in both the $\pm x$ and $\pm y$ directions. In contrast, open boundary conditions are utilized in the $\pm z$ directions, facilitating radiation. Section 2.2.3 of this thesis elaborates on the process of abstracting the leakage rates α_{TE} and α_{TM} as a function of frequency from the CST MWS Eigenmode solver solutions.

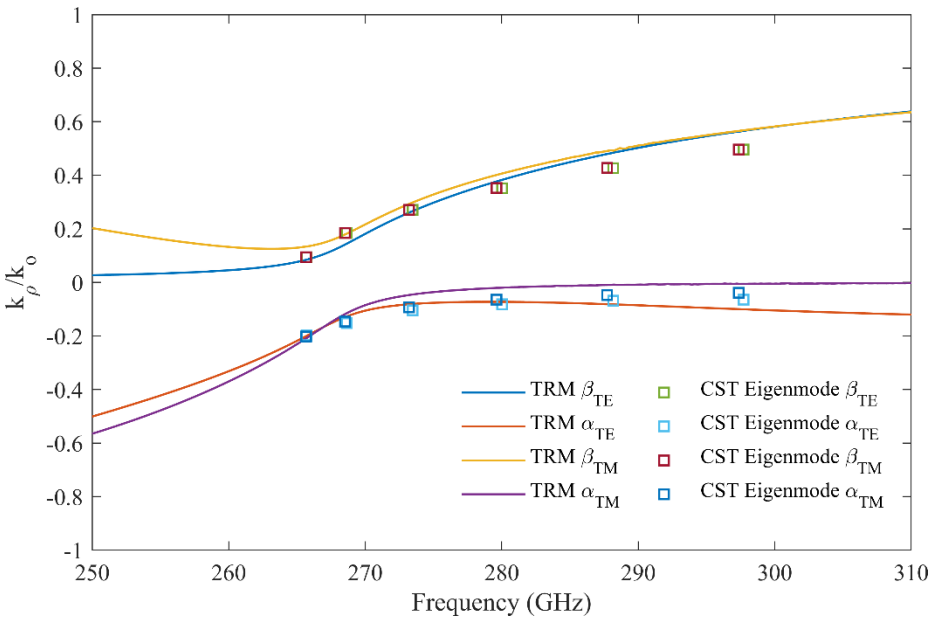

Figure 5.10. Propagation constants of the TE and TM leaky wave modes calculated using the TRM and compared with the CST Eigenmode calculations for verification.

The calculation results of propagation constants for both TE and TM modes using TRM show good agreement with the results obtained from the CST MWS Eigenmode solver, particularly when k_ρ is small. As the frequency increases, k_ρ also increases, causing the leaky mode to radiate at a larger angle away from broadside. Consequently, the TRM accuracy progressively degrades.

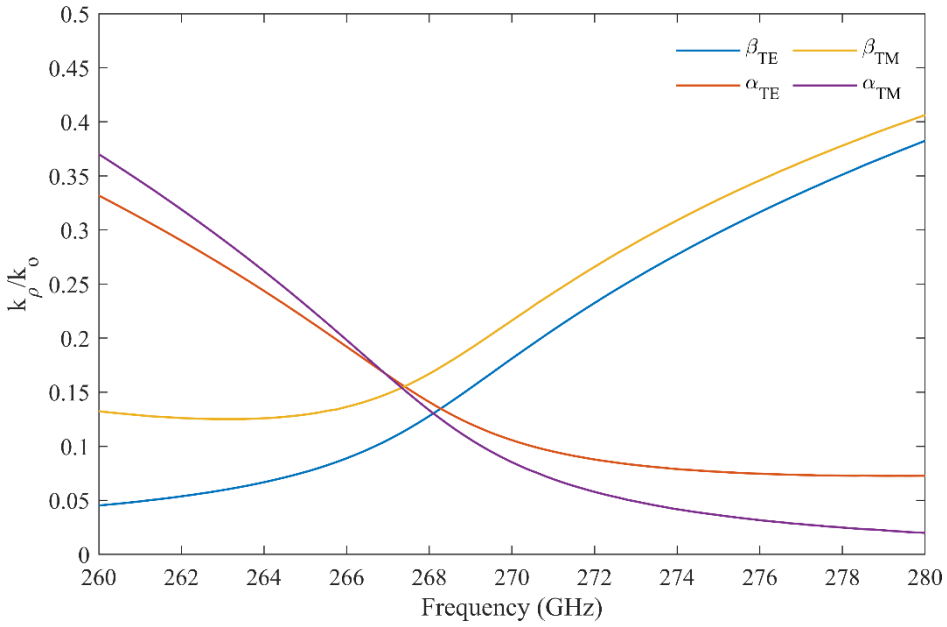

Figure 5.11. Propagation constants of the TE and TM leaky wave modes. For beam splitting evaluation, the absolute value of leakage rate α is plotted.

As discussed in Section 2.3, when TE and TM modes approach degeneracy, the beam begins to split into a scanned conical beam [7]. As illustrated in Figure 5.11, the condition for beam splitting is met at roughly 268 GHz. As the frequency increases, a higher leaky mode radiation angle leads to an elevated SLL for the FPCA. This elevation can be used to explain the radiation pattern bandwidth limitation imposed by SLL requirements, and this explanation is tied to the beam splitting condition.

5.2.3. Optimization of Unit Cell Quality Factor

As discussed in Section 2.3, a high-gain FPCA design requires a low-leakage-rate of the PRS unit cells. In this section, a novel approach to optimizing the FPCA design using the Q-factor is introduced. To prevent redundancy, only the Q-factor of TM modes are presented in this section, because the TE and TM modes exhibit near-degeneracy within the antenna working bandwidth and have similar Q-factors.

The Q-factor is an essential specification for the design of a resonator, as it quantifies the ability of the resonator to confine the electromagnetic field energy over time. For a resonator formed by a Bragg reflector and devoid of a metal structure, the total Q-factor can be represented as follows [10]:

$$Q_{total}^{-1} = Q_r^{-1} + Q_d^{-1} \tag{5.18}$$

where Q_r denotes the radiation Q-factor, and Q_d represents the dielectric Q-factor. The formula demonstrates that both dielectric loss and radiation loss contribute to the energy decay within the resonator. To further evaluate the dielectric loss, the resonator can be divided into n regions depending on the filling materials, and the dielectric Q-factor can be represented as follows [10]:

$$Q_d^{-1} = \sum_{i}^{n} p_i tan\delta_i \tag{5.19}$$

The resonator $tan\delta_i$ represents the dielectric loss tangent of the material inside the i-th region that occupies a volume V_i within the total volume V of the resonator. In (5.19), p_i is the electric filling factor for the volume V_i, which can be calculated as [10]

$$p_i = \frac{\int_{V_i} \varepsilon_i |E|^2 \, dV_i}{\int_V \varepsilon(\boldsymbol{r}) |E|^2 \, dV}. \tag{5.20}$$

In (5.20), E denotes the position dependent electric field amplitude within volume V. The term ε_i is the relative dielectric permittivity of the material in the i-th region, and $\varepsilon(\boldsymbol{r})$ is the permittivity at position $\boldsymbol{r}$. The integrals calculate the total electric energy within the i-th region and the entire resonator, respectively, allowing for the determination of the partial electric energy filling factor p_i.

Consequently, as demonstrated by (5.20), by reducing the energy density concentration within the region containing lossy dielectric material, the electric filling

factor p_i can be decreased, resulting in diminished dielectric losses Q_d^{-1}, and hence an improved total Q-factor.

This approach, first employed for optimizing resonator designs based on Bragg reflectors to minimize dielectric losses and achieve higher total Q-factor [11], is adapted in this thesis for FPCA design. In the design of an FPCA, if there's no dielectric loss, the total Q-factor will be the same as the radiation Q-factor and directly related to the FPCA's gain. If dielectric loss is significant, incorporation of the dielectric Q-factor in (5.19) becomes necessary.

Considering the FPCA as a leaky transmission line resonator and disregarding any dielectric losses, the total Q-factor of the resonator is given by [12]:

$$Q_{total} = \frac{\beta}{2\alpha} \tag{5.21}$$

By considering both (5.21) and (2.11), this approach leads to:

$$\frac{1}{\mathrm{BW}} \propto Q_{total} \tag{5.22}$$

In (5.22), BW denotes the 3 dB beamwidth, which is inversely proportional to the gain of the antenna. Equation (5.22) also indicates that the gain of the FPCA is proportional to the total Q-factor of the resonator.

In scenarios where dielectric losses are included, the dielectric Q-factor serves to quantify the extent of dielectric loss reducing the FPCA's gain. Additionally, the total Q-factor continues to be a relevant metric, being proportional to the FPCA's gain. Consequently, in the design process of the FPCA unit cell, the objective should be to maximize the unit cell's total Q-factor, while achieving a balance between dielectric loss and radiation.

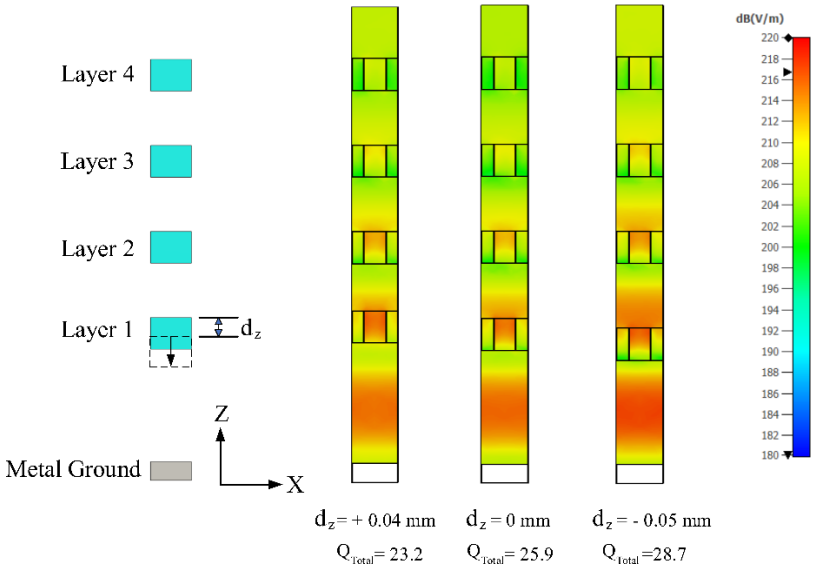

Figure 5.12. Unit cell of the FPCA. Q_{Total} is optimized through adjusting the displacement of layer 1 in z-direction.

In the case of the FPCA proposed in this thesis, the dielectric loss attributed to the lossy IP-Q can be characterized by the dielectric Q-factor Q_d. Also, the energy "dissipation" resulting from the radiation emanating from the cavity formed by the dielectric layers and metal ground, as depicted in Figure 5.12, can be represented by the radiation Q-factor Q_r, and the total-Q-factor Q_{Total} can be computed using (5.18).

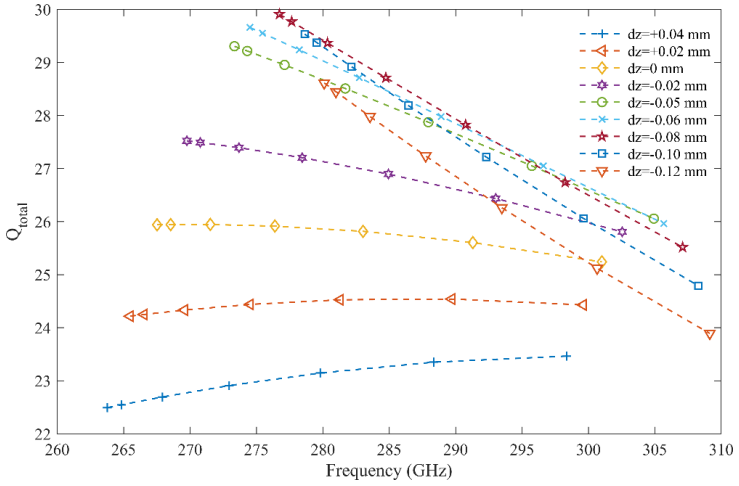

Figure 5.13. Total Q-factor of the unit cells with d_z ranging from +0.04 mm to -0.12 mm.

As shown in Figure 5.12, the electric field distribution of three different unit cells is depicted, each maintains the same configuration as previously presented in Figure 5.9,

but with variations in the parameter d_z. The electric field distribution is determined using the CST MWS Eigenmode solver. When in a resonant state, most of the electric field energy is confined within the region between layer 1 and the metal ground. As such, by modifying d_z, which is the displacement of layer 1 in the z direction, control over the penetration of the electric field within the dielectric layers can be achieved. This allows for adjustment of the electric filling factor and optimisation of dielectric losses.

As demonstrated in Figure 5.12, as d_z transitions from $+0.04\,\mathrm{mm}$ to $-0.05\,\mathrm{mm}$, Q_{Total} of the unit cell rises from 23.2 to 28.7, thereby validating the optimization methodology for the FPCA unit cell. Due to the low permittivity of the IP-Q, confinement by the dielectric layers is limited, thereby limiting Q_r and consequently resulting in a relatively small Q_{Total}.

It is important to noted that the electric field of all unit cells depicted in Figure 5.12 has been normalized to 280 GHz, and the loss tangent of the IP-Q has been considered in determining Q_{Total}.

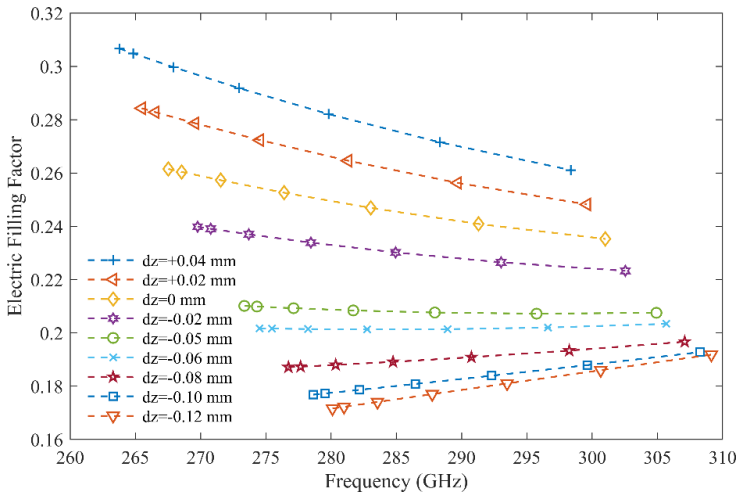

Figure 5.14. Electric filling factors of the unit cells with d_z ranging from +0.04 mm to -0.12 mm.

To further optimize the unit cell Q-factor, unit cells with d_z ranging from $+0.04\,\mathrm{mm}$ to

-0.12 mm are simulated using the CST MWS Eigenmode solver. As depicted in Figure 5.13, the Q_{Total} of unit cells with varying d_z shows a saturation increase at $d_z = -0.05$ mm. Moving layer 1 further in the negative z direction no longer achieves a higher Q_{Total} across the entire working bandwidth. Conversely, moving layer 1 further in the negative z direction begins to decrease Q_{Total}. Additionally, as d_z incrementally increases from 0 mm to $+0.04$ mm, the corresponding Q_{Total} decreases progressively, and the slope of the associated curve lessens. This indicates that FPCA will have a flatter gain bandwidth, implying that a wider 3 dB gain bandwidth can be realized by intentionally increasing the dielectric loss at the expense of overall gain.

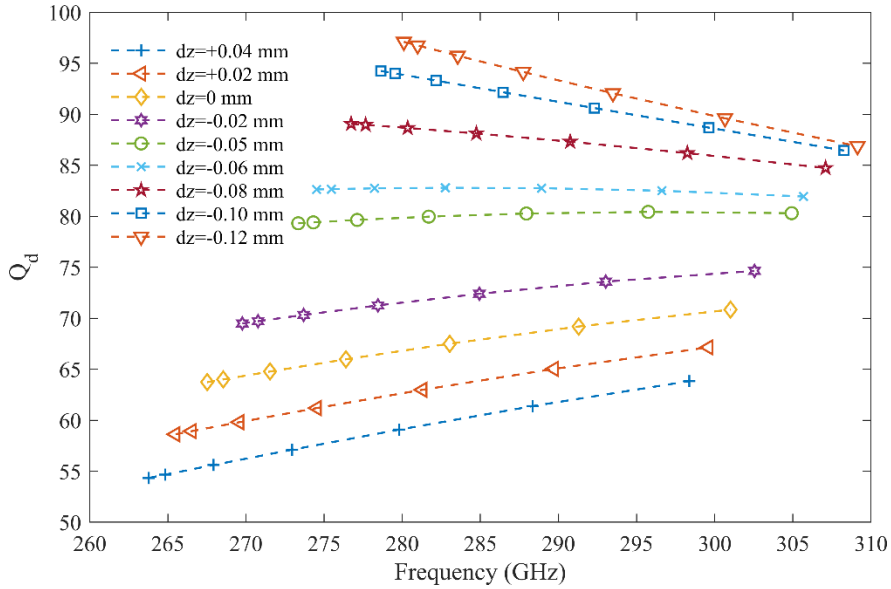

Figure 5.15. Dielectric Q-factor of the unit cells with d_z ranging from +0.04 mm to -0.12 mm

The electric filling factor of the aforementioned unit cells, simulated using the CST MWS Eigenmode solver, can be evaluated using (5.20). As demonstrated in Figure 5.14, the electric filling factor diminishes as d_z varies from $+0.04$ mm to -0.12 mm. Yet, the rate of decrease in the electric filling factor gradually slows down. Subsequently, Q_d can be ascertained using (5.19). Figure 5.15 reveals that Q_d shows an inverse trend compared to the electric filling factor. As d_z ranges from $+0.04$ mm to

-0.12 mm, Q_d gradually increases, indicating reduced dielectric losses. It should be noted that variations in d_z simultaneously affect both Q_r and Q_d. Consequently, despite the increase in Q_d as d_z diminishes, an optimal design of the unit cell must still be identified following an examination of Q_r.

Figure 5.16 shows that the Q_r of the unit cells also saturates when d_z decreases to -0.05 mm. This indicates that the leakage rate of the unit cell reaches a local minimum. Furthermore, Figure 5.13 illustrates that the curve of Q_{Total} has a gentler slope at $d_z = -0.05$ mm compared to $d_z = -0.08$ mm. This suggests that a wider 3 dB gain bandwidth is achievable at $d_z = -0.05$ mm, so that $d_z = -0.05$ mm is selected as the initial value for the FPCA design, aiming to balance radiation and dielectric losses.

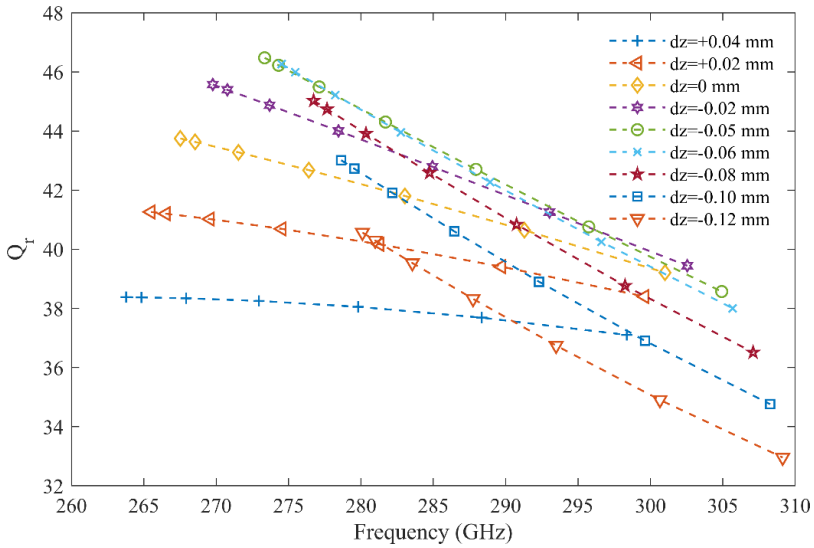

Figure 5.16. Radiation Q-factor of the unit cells with different parameter d_z.

It is important to note that the simulation results of unit cells, without considering dielectric losses, display different electric field distributions and electric filling factors. When dielectric losses are excluded, all energy dissipation within the cavity can be attributed to radiation. Comparing this with cases where dielectric losses are included results in:

$$Q_{Total}^{No\ Loss\ Tan} = Q_r^{No\ Loss\ Tan} > Q_{Total}^{Lossy} \tag{5.23}$$

Here, "No Loss Tan" refers to cases without dielectric losses, while "Lossy" represents cases where dielectric losses are considered. Equation (5.23) implies that for a cavity composed of a material with a low dielectric loss tangent, the Q_r can be approximated by $Q_{Total}^{No\ Loss\ Tan}$ abstract from the CST MWS Eigenmode solver simulation results, while disregarding the dielectric loss tangent. However, a more accurate calculation of Q_{Total}^{Lossy} is essential, along with the computation of the electric filling factor, when dealing with materials with high loss tangent, as dielectric losses cannot be disregarded.

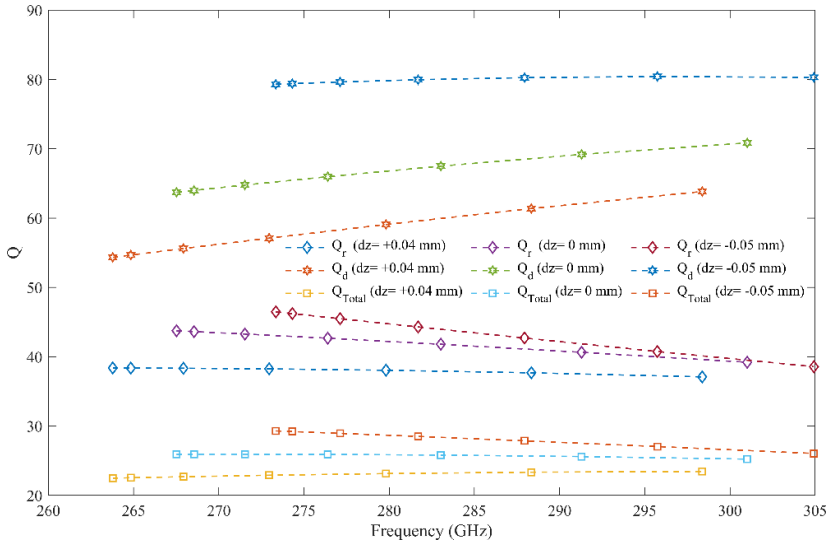

Figure 5.17. Q-factors of the unit cells with different parameter d_z.for comparison

As demonstrated in Figure 5.17, the unit cell with the optimal d_z = -0.05 mm exhibits higher Q_{Total}, Q_d and Q_r compared to other unit cells, indicating that the FPCA can achieve reduced dielectric losses and increased gain with this optimal configuration.

Adjusting the position of layer 2 can also influence the Q-factor of the unit cell. However, the energy confined inside the cavity remains predominantly between layer 1 and the metal ground, limiting the impact of adjusting layer 2.

5.3. Full Antenna Design

5.3.1. Impedance Matching Methods

The full FPCA design detailed in this section originates from the multilayer unit cell introduced in earlier sections. As depicted in Figure 5.18, the full FPCA consists of four PRDS layers, with each layer composed of unit cells having dimensions as illustrated in Figure 5.12 and $d_z = -0.05$ mm. As demonstrated in Figure 5.18(c), the full FPCA design is excited by a WR-3 band rectangular open-ended waveguide with a cross-section size of 0.864 mm $\times$ 0.432 mm.

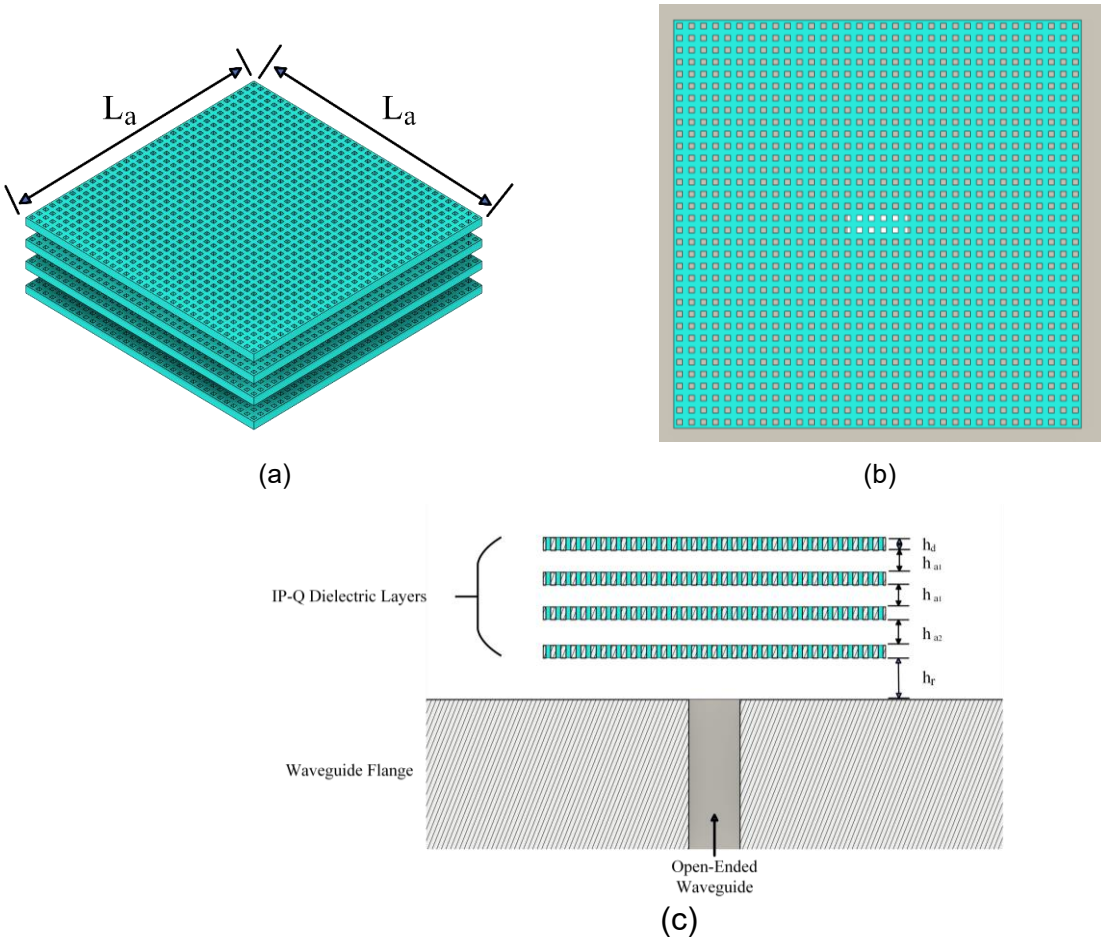

Figure 5.18. The full FPCA with PRDS formed by 34×34 unit cells. (a) Perspective view of the multilayer PRDS. (b) Top View of the full FPCA. (c) Cross-section view of the full FPCA excited by an WR-3 Open-ended Waveguide. The inner dimensions of waveguide opening are 0.864 mm $\times$ 0.432 mm.

Another consideration for the full FPCA design is the transverse size of the PRDS. As discussed in Chapter 2, to achieve high radiation efficiency and a practical antenna size, typically at the termination of a LWA less than 10% of the energy should remain within the leaky mode(s), which means at the edges of the PRDS, as shown in Figure 5.18, the energy remaining in the resonant cavity should be under 10%. As illustrated in Figure 5.19, the TM mode's normalized leakage rate of the unit cell at 280 GHz is 0.08, thus at the edge of the PRDS, which is formed by 34×34 unit cells, the energy remaining inside the cavity would be:$10 \times \log10(e^{-2\alpha k_o 0.5 L_a}) = -11.78$ dB, where $L_a = 17 \times 0.17 = 2.89$ mm. It should be noted that since the TE and TM modes cease to be degenerate after 276 GHz, as shown in Figure 5.19, and the radiation beam begins to point at a higher angle, requiring the size of the PRDS to be further optimization to achieve improved performance. This will be discussed later in this thesis and $L_a = 2.89$ mm serves as an initial value for the design process.

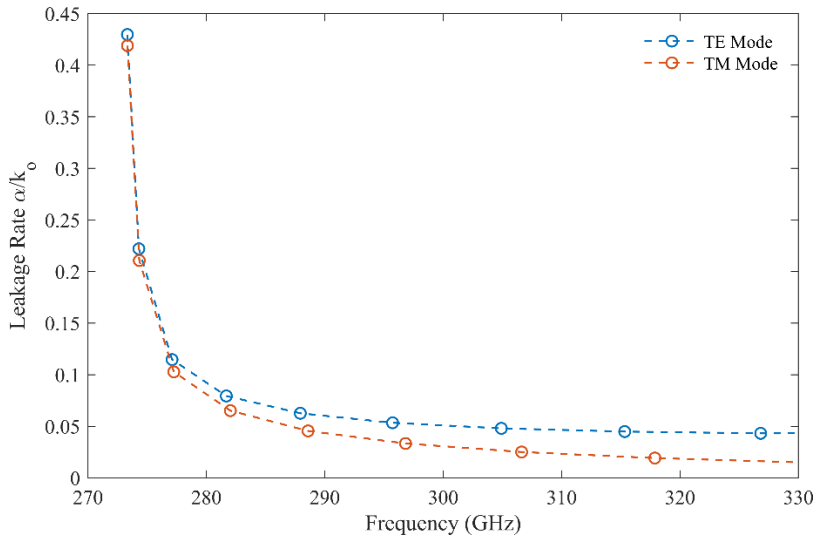

Figure 5.19. Normalized leakage rate of the unit cell deployed for the full FPCA design which is shown in Figure 5.18.

As depicted in Figure 5.21, the 3 dB gain bandwidth of the FPCA, when excited by an open-ended waveguide, ranges from 269.5 GHz to 280 GHz. However, Figure 5.20

demonstrates that the S_{11} of the FPCA, under the same conditions, is greater than -10 dB across the entire 3 dB bandwidth. Consequently, further optimization of the feeding structure is required. Typically, additional matching structures, such as a double arc slots iris [13] or double rectangular slots iris [14], are utilized for the impedance transformation between the open-ended waveguide and the FPCA, as listed in Table 3.2.

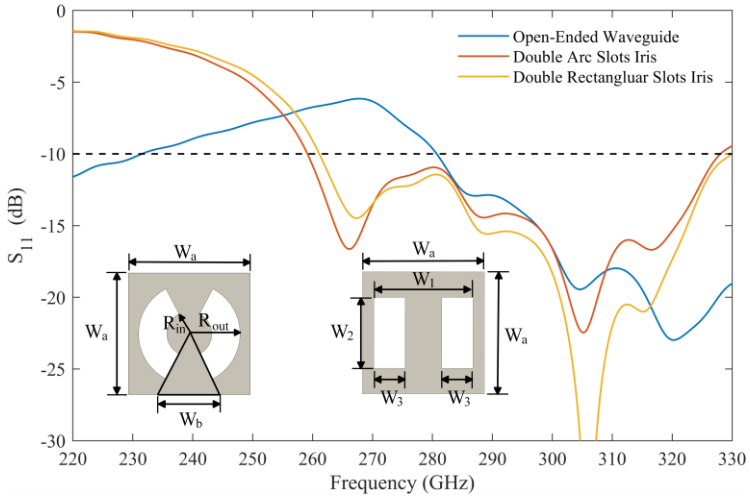

Figure 5.20. S_{11} of the full FPCA when excited by: (1) open-ended waveguide, (2) open-ended waveguide with double arc slots iris, and (3) double rectangular slots iris.

The S_{11} of the FPCA when excited by a square waveguide loaded with double arc slot irises and double rectangular slots iris, is depicted in Figure 5.20. It can be observed that, better impedance matching is attainable when an additional matching structure is utilised. Consequently, the S_{11} of the FPCA remains below -10 dB across the entire 3 dB bandwidth, which ranges from 269 GHz to 279 GHz. The dimensions of the double arc slot irises and double rectangular slots iris, as presented in the inset of Figure 5.20, are provided in Table 5.3.

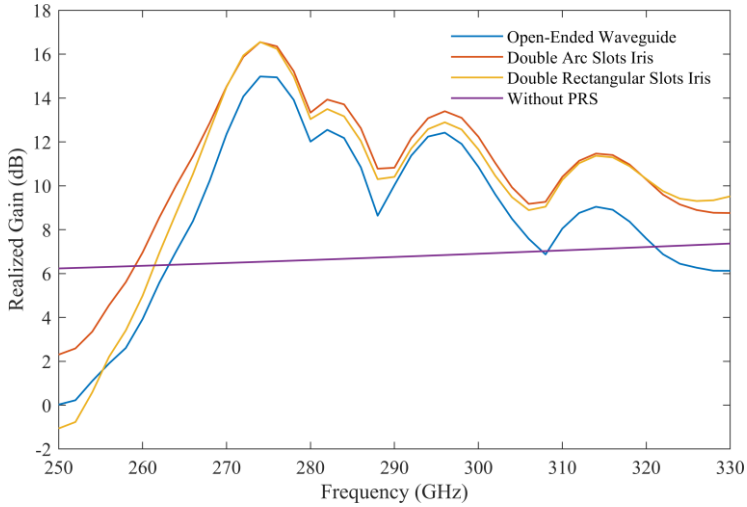

Figure 5.21. Realized gain of the FPCA excited by open-ended waveguide, waveguide port with double arc slots iris, and double rectangular slots iris.

However, implementing the aforementioned matching structures would necessitate the introduction of an additional CNC machining process step for fabrication. In the WR-3 band, the tight fabrication tolerances required leads to fabrication errors and additional costs. In addition, a step-profiled waveguide transition is required to convert the rectangular waveguide into a square waveguide. As a result, these methods are not utilized in the FPCA design proposed in this Chapter.

Table 5.3. Dimensions of the double arc slots iris and double rectangular slots, given in millimetres.

W_a	W_b	R_{out}	R_{in}	W_1	W_2	W_3
0.864	0.45	0.36	0.16	0.7	0.5	0.22

The limited 3 dB gain bandwidth of the FPCA, as shown in Figure 5.21, can be attributed to the reflection phase of the unit cell. As illustrated in Figure 5.7, it is evident that the unit cell reflection phase displays a negative gradient. As discussed in Section 2.3, the FPCA built using the PRDS based on the unit cell design proposed inherently exhibits a narrow bandwidth due to its resonant operating characteristics. This limitation can be addressed by adopting additional methods. For instance,

implementing a wedge-shaped resonance zone [15] or achieving a positive phase gradient can help broaden the bandwidth [16]. However, creating a wedge-shaped resonance zone necessitates CNC machining on the flange metal ground, which can be challenging. Further, attaining a positive phase gradient can be difficult due to the lack of metal in the PRDS unit cell, especially while maintaining the effective permittivity distribution.

Another method that can be employed to attain a wider impedance matching bandwidth involves the use of transverse permittivity gradient tapered PRDS. This method and its potential advantages over other impedance matching techniques will be thoroughly discussed in the following section.

5.3.2. Transverse Permittivity Gradient Tapering of Antenna

This section offers an in-depth explanation of the design aspects of the transverse permittivity gradient-tapered PRDS. The primary aim is to enhance the impedance matching bandwidth while concurrently expanding the 3 dB gain bandwidth. As a result, the 3 dB gain bandwidth product (GBWP) is employed as a distinct metric to assess the performance of the FPCA proposed in this thesis. This also establishes a baseline for comparison with other similar cited works.

It should be emphasized that the calculation of 3 dB GBWP in this thesis employs the following formula

$$GBWP = \left(\frac{BW}{f_c}\right) \times 100 \times 10^{G/10}, \tag{5.24}$$

where BW signifies the 3 dB gain bandwidth, f_c denotes the center frequency of the BW, and G represents the logarithmic value of the antenna's gain. Equation (5.24) is employed to compute the 3 dB GBWP for all the works referenced in Table 3.2 for an

objective analysis of similar works.

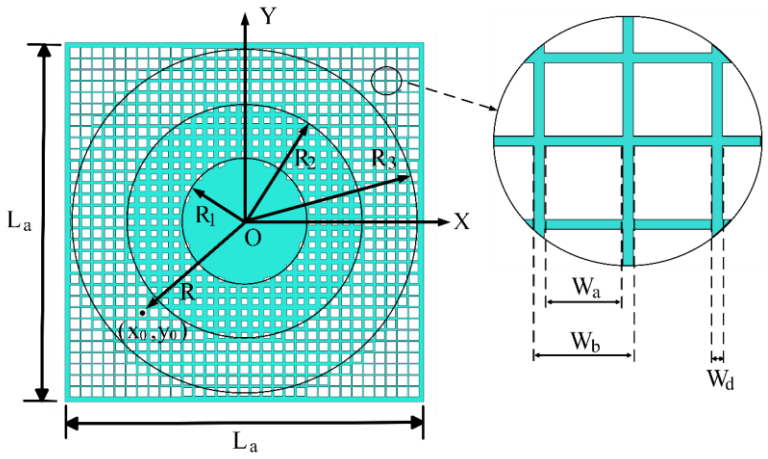

Figure 5.22. One layer of the transverse permittivity gradient-tapered PRDS of the FPCA. The effective permittivity is of each unit cell is a function of its (x, y) coordinate.

As discussed in Section 2.3, to achieve broader 3 dB gain bandwidth, a viable method is to employ a tapered PRDS, which incrementally alters the reflective phase to achieve a wider bandwidth resonance. The FPCA proposed in this thesis, adopts this method, making use of transverse gradient permittivity-distributed PRDS to accomplish an improved impedance matching bandwidth and 3 dB GBWP. The elimination of the additional impedance matching structure simplifies the fabrication process, and also reduces the overall cost of the complete FPCA design.

As shown in Figure 5.22, the single layer PRDS is constructed based on the unit cells, which has been discussed in previous sections. The target effective permittivity of each unit cell is determined by its specific coordinates. In the case of a unit cell with centre coordinates designated as (x_0, y_0), the effective permittivity, symbolized as $\varepsilon(R)$ can be depicted as a function corresponding to the unit cell's distance from the origin: $R = \sqrt{x_0^2 + y_0^2}$. For the case shown in Figure 5.22, the effective permittivity of each unit cell can be represented as follows:

$$\varepsilon(R) = \begin{cases} \varepsilon_1, & R \leq R_1 \\ \varepsilon_2, & R_1 < R \leq R_2 \\ \varepsilon_3, & R_2 < R \leq R_3 \\ \varepsilon_4, & R > R_3 \end{cases} \tag{5.25}$$

The description of the parameters in (5.25) is provided in Table 5.4. As depicted in Figure 5.22, the initial design of the PRDS is divided into a circular central region plus three annular regions with different hole sizes, shaped according to the parameters listed in Table 5.5. It is worth noting that, the effective permittivity of the cuboid unit cells positioned beyond $R > R_3$, is determined by the capabilities of the 3D printing fabrication process.

The initial design of dividing the superstrate into four distinct regions is based on the findings presented in [17]. The referenced study demonstrates that a resonate cavity antenna with a superstrate divided into three equal width sections, where the permittivity decreases in three equal steps, yields an optimal 3 dB gain bandwidth. Although this method is effective for a resonant cavity antenna, it should be noted that the PRDS shown in Figure 5.22 serves as an initial demonstration of the design process for a single layer of the PRDS. The PRDS can be further divided into additional ring areas.

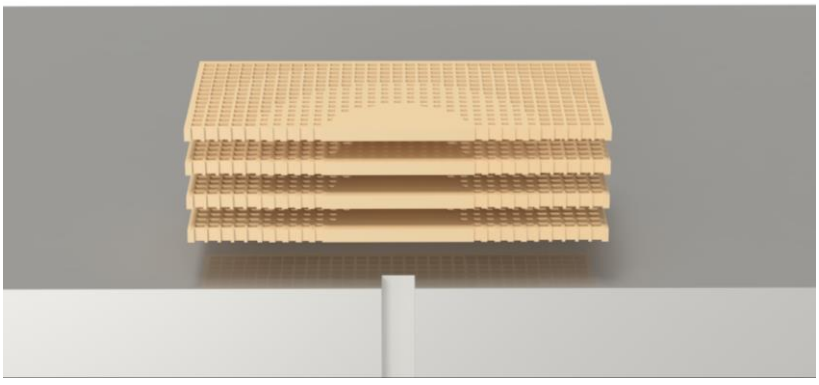

Figure 5.23. A render of the cross-sectional view of the initial FPCA design for optimization.

To prevent the high aspect ratio thin walls from bending or deforming during the 3D

printing, it is crucial to set the minimum cross-section feature size, denoted as W_d and depicted in Figure 5.22, to be $0.020\,mm$. This specific value corresponds to the effective permittivity of the unit cell of 1.31.

Table 5.4. Parameters determining the configuration of the PRDS.

Parameter	Description
ε_n	The permittivity of the ring area with index n
R_n	Radius of the ring area boundary with index n
L_a	Edge size of the square PRDS

The initial design of the full FPCA, as depicted in Figure 5.23, utilizes the same set of parameters listed in Table 5.5 for all 4 PRDS layers. In order to draw a more comprehensive comparison between the performance of the FPCA with tapered PRDS and un-tapered PRDS, simulations of both designs have been conducted using CST Microwave Studio (MWS) with the time domain solver and Open (Add Space) boundary conditions in all directions.

Table 5.5. Parameters determining the configuration of PRDS of the initial design of FPCA

ε_1	ε_2	ε_3	ε_4	R_1	R_2	R_3	L_a
2.4	2	1.6	1.31	0.9 mm	1.8 mm	2.7 mm	5.4 mm

To ensure clarity, it should be noted that the other dimensions of the FPCA are identical to the design proposed in Figure 5.18, with the exception of the PRDS, Furthermore, the simulations have taken into account the dielectric loss of the IP-Q photoresin.

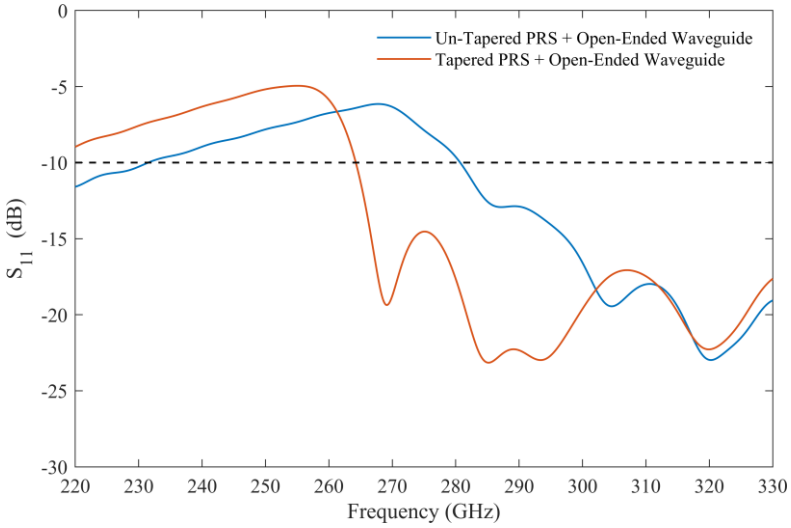

Figure 5.24. S_{11} of the full FPCA with tapered PRDS and un-tapered PRDS, excited by a WR-3 band open-ended waveguide.

As depicted in Figure 5.24, the simulation results indicate that the impedance matching bandwidth of the FPCA with a tapered PRDS is broader than that of the FPCA with an un-tapered PRDS, which is preferable when a broadside radiation beam is specifically desired. Concurrently, the realized gain of the FPCA with a tapered PRDS, as illustrated in Figure 5.25, demonstrates a wider 3 dB gain bandwidth compared to the design with an un-tapered PRDS.

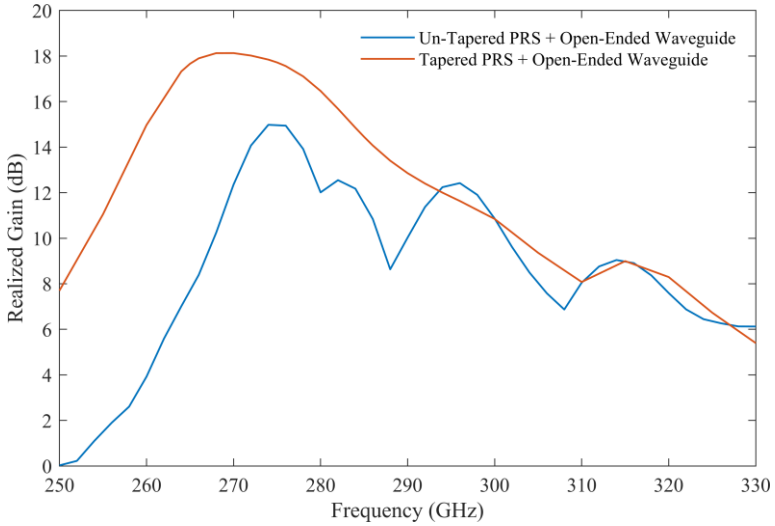

Figure 5.25. Realized gain of the full FPCA with un-tapered PRDS and tapered PRDS.

The impedance matching bandwidth of the FPCA with a tapered PRDS ranges from 264.2 GHz to 330 GHz, and the 3 dB gain bandwidth spans from 260.5 GHz to 283.2 GHz, with a maximum realized gain of 18.15 dBi. Consequently, the 3 dB GBWP of the initial design of the FPCA with a tapered PRDS, calculated using equation (5.24), is 453.4. The 3 dB GWBP value of this initial design is almost identical to the FPCA proposed in [18], which was produced using direct metal laser sintering.

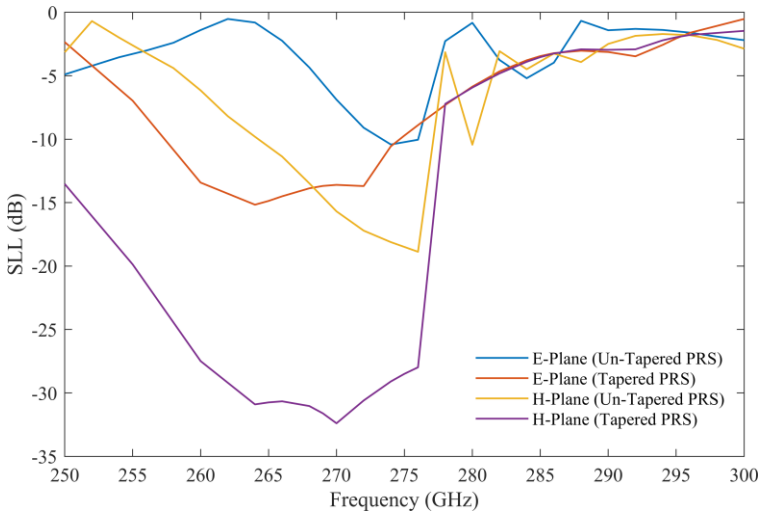

Figure 5.26. SLL of the full FPCA with un-tapered PRDS and tapered PRDS in both the E-plane and H-plane.

In Section 2.3, it was discussed that the radiation from the TM_0 mode results in higher SLL in the E-plane compared to the H-plane. Although Figure 5.26 illustrates that the full FPCA with tapered PRDS exhibits improved performance over its counterpart with un-tapered PRDS, the SLL remains high across the operating bandwidth where a broadside beam pattern is observed. Consequently, further optimization of the FPCA is warranted to enhance its performance within this frequency range, which will be covered in the next section.

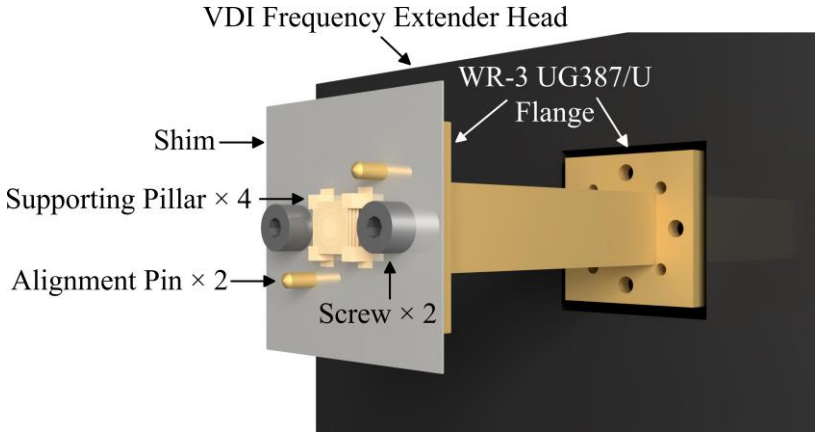

(a)

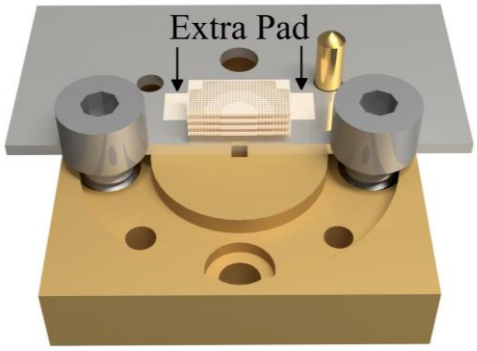

(b)

Figure 5.27. Renders of the initial FPCA design (a) Perspective view of the FPCA adhered to the shim and mounted on the WR-3 UG387/U flange. (b) Enlarged cross-sectional view of the shim and FPCA, showcasing the interface between the shim and the WR-3 UG387/U flange.

The FPCA proposed earlier was designed as a simplified model to showcase the performance of the FPCA with tapered PRDS. To create a practical FPCA design, it is necessary to mechanically support the PRDS layers and four supporting pillars should be included.

In the process of 3D printing the FPCA, supporting pillars are adhered to a shim, fabricated from laser machined silicon. This shim is designed to incorporate a waveguide along with alignment holes that are precisely positioned for attachment to a WR-3 UG387/U flange, as shown in Figure 5.27(a). Moreover, a silver layer, exceeding 0.48 um in thickness, was sputter-deposited onto both sides of this shim before the 3D printing process. This thickness is equivalent to 3 times the skin depth

of silver at the frequency of 220 GHz to minimise ohmic loss. Further details regarding the shim's fabrication process will be discussed in Section 4.4.

As depicted in Figure 5.27(b), the shim is mounted on the WR-3 UG387/U flange. To ensure the shim's secure attachment to the waveguide flange, two 4-40 UNC-2B screws are employed. Additionally, four support pillars, each extended at the base with additional pads of $0.015\ \mathrm{mm}$ thickness, are used to improve the FPCA's adherence to the shim.

5.3.3. Further Optimization and Discussion

The full FPCA design is optimized to further improve the 3 dB GBWP and reduce the SLL. The geometric parameters defining the FPCA, as detailed in Table 5.4, are considered in this optimization process.

The Non-dominated Sorting Genetic Algorithm II (NSGA-II), a multi-objective optimization algorithm, is utilized for the optimization process of the FPCA. NSGA-II is chosen for the optimization of FPCA design due to its capability to efficiently manage multiple objectives, offering a diverse set of Pareto-optimal solutions [19]. Its effectiveness in complex and non-linear search spaces, where gradient information may not be accessible or dependable, makes it exceptionally appropriate for antenna parameter optimization [20-22]. Additionally, NSGA-II's documented success in various engineering applications affirms confidence in its convergence and computational efficiency [23-25], which are essential for the simulation resource-intensive nature of antenna design optimization within predefined parameter bounds.

During the optimization process, the objective function to be maximised is defined as:

$$f_{obj} = (\sum_{n=1}^{m} SLL_n, GBWP, \max(SLL)) \tag{5.26}$$

After each round of simulation, the gain, SLL, and S_{11} are sampled at intervals of 0.5 GHz over the WR-3 band. It is worth emphasizing that the absolute value of SLL is used in the subsequent calculations. This is to align with the maximization of GBWP during the optimization process of the objective function f_{obj}. The objective function is then computed according to (5.26) based on the sampled data points within the frequency range where there's an overlap between the 3 dB gain bandwidth and S_{11} below -10 dB.

Table 5.6. Parameters determining the configuration of the PRDS of the optimized design of FPCA

ε_1	ε_2	ε_3	R_1^{L1}	R_1^{L2}	R_1^{L3}	R_1^{L4}	R_2	R_3	L_a
2.4	1.65	1.31	1.08 mm	1.43 mm	2.20 mm	1.26 mm	1.82mm	2.7 mm	5.4 mm

As evidenced in (5.26), the discrete integration of SLL data points further ensures that the optimization process yields lower SLL over a broader bandwidth. Nevertheless, it is important to note that due to the operating principles of the 2D FPCA, the beam splitting condition places limits on SLL performance. As the operating frequency increases, the SLL gradually deteriorates, so that the computed maximum SLL from the sampled results is incorporated as one element of the f_{obj}.

To enhance the efficiency of the optimization process and reduce the time required, a variance-based sensitivity analysis [26] was conducted on the parameters defining each layer of the PRDS. Sample parameters were generated by the algorithm, and after 50 simulation rounds, the first-order, second-order, and total sensitivities of each parameter were obtained. The results confirmed that in each layer of PRDS, the radius R_1 of the central circular region has the greatest impact on the objective function.

Consequently, during the optimization process, apart from R_1, the parameters of each PRDS layer share the same set of variables.

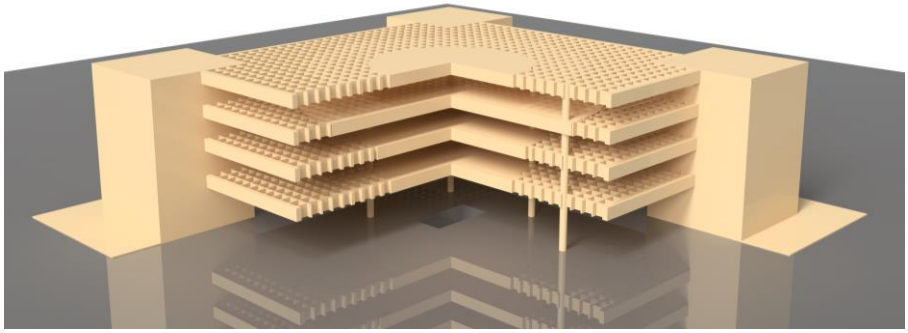

Figure 5.28. A render of the FPCA after optimization.

As shown in Figure 5.28, the FPCA design after optimization is rendered. The parameters for the PRDS configuration of the optimized FPCA across all four layers are detailed in Table 5.6. In Table 5.6, the superscript in R_1 indicates the layer index. Each PRDS layer has the same R_2, and R_3 values but differs R_1 values, with each layer's R_1 value specifying the radius of its central circle. This significantly reduces the total number of parameters to be optimized, consequently shortening the optimization process time.

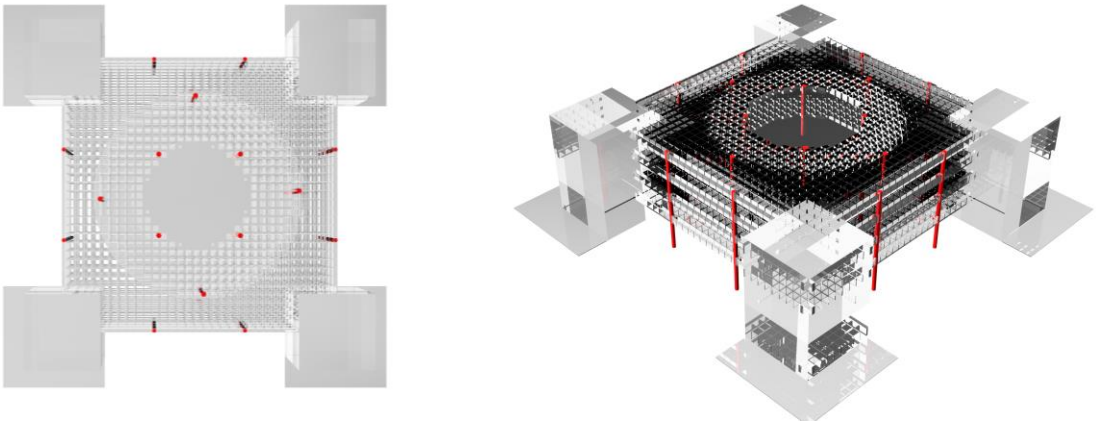

(a) (b)

Figure 5.29. Renders of the internal pillars of the FPCA. (a) Top-down view with transparent main body and red-coloured internal pillars. (b) Perspective view showcasing the arrangement of 0.1 mm diameter supporting pillars.

It is noteworthy to mention that, as listed in Table 5.6, the third layer of PRDS has a larger R_1^{L3} than R_2. This implies that in the third layer, ring area 2 is effectively supplanted by ring area 1 with an effective permittivity of 2.4. Consequently, it ceases to exist, as shown in Figure 5.30. The supporting pillars, as shown in Figure 5.30, have a width of W_p = 0.75 mm.

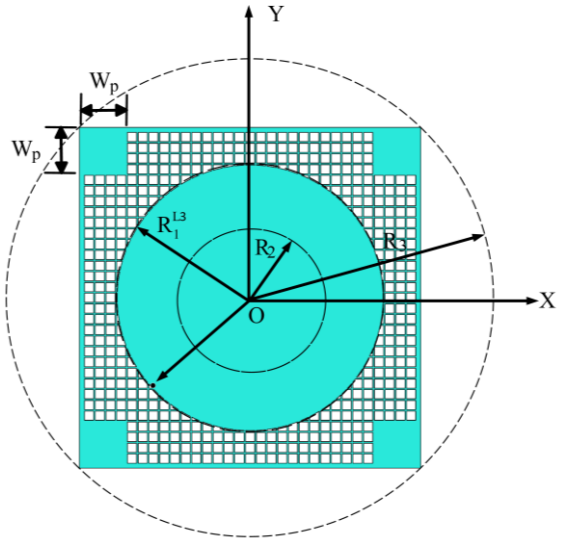

Figure 5.30. The optimized third layer of PRDS, where the value of R_1^{L3} is larger than R_2. This implies that ring area 2 is effectively overlapped by ring area 1. The supporting pillar width W_p is 0.75 mm.

As shown in Figure 5.28 and Figure 5.29, internal supporting pillars have been added between the PRDS layers and inside the cavity formed by the PRDS and the metal ground. This is to further ensure that during the 2PP 3D printing process, the FPCA is prevented from bending under the influence of gravity, thereby avoiding deformation of the PRDS.

As depicted in Figure 5.31, the maximum realized gain of the optimized FPCA retains nearly consistent values within the range of 265 GHz to 284 GHz. A notable improvement is also evident in the 3 dB gain bandwidth, which has increased from approximately 22 GHz to an impressive 32 GHz. Consequently, the 3 dB GBWP after optimization reaches a value of 700.

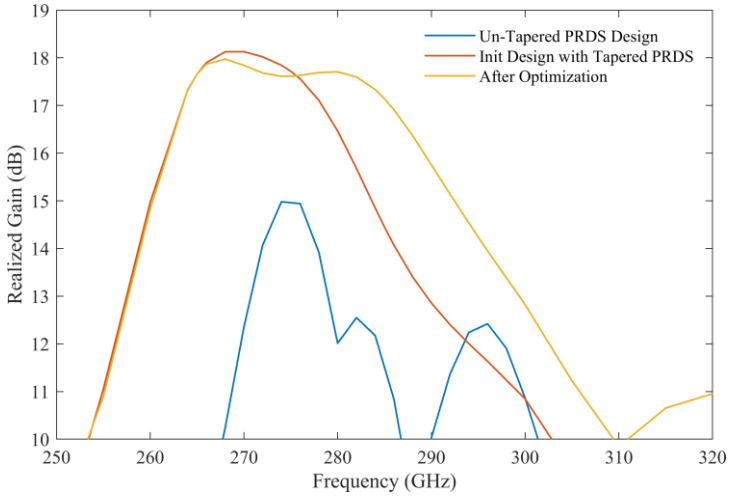

Figure 5.31. Comparison of the realized gain of the full FPCA. Notably, a broader 3 dB gain bandwidth is achieved, and the maximum gain remains more uniform as a result of the optimization process.

During the optimization process, an additional condition was incorporated into the objective function to ensure the SLL of the E-plane remained below -10 dB. This condition aimed to enhance the working bandwidth while maintaining a low SLL as much as possible. Consequently, Figure 5.32 demonstrates that the bandwidth, wherein the SLL of the optimized FPCA is less than -10 dB, surpasses its pre-optimization performance.

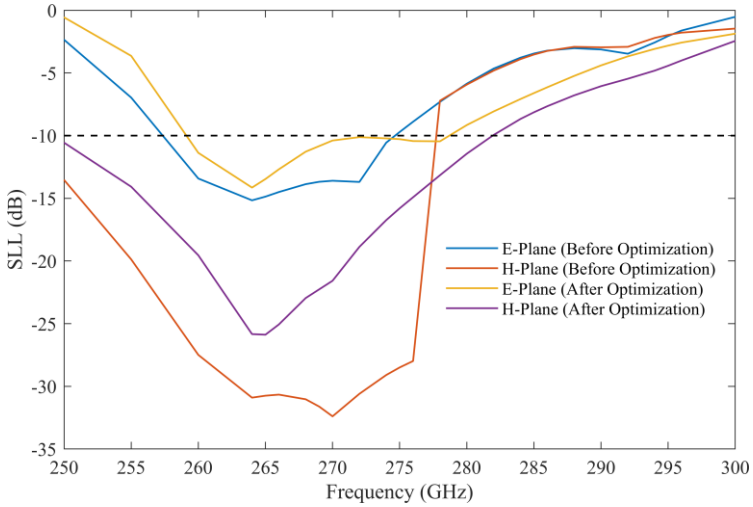

Figure 5.32: Comparison of the SLL of the full FPCA, before and after the optimization.

Another predefined condition set during the optimization process is to ensure that S_{11}

remains below -11 dB within the range of the 3 dB gain bandwidth. Figure 5.33 illustrates that after optimization, the S_{11} of the optimized FPCA peaks at -11.2 dB, near 277 GHz. Figure 5.33 also shows a broader impedance matching bandwidth is achieved compared to the pre-optimization design.

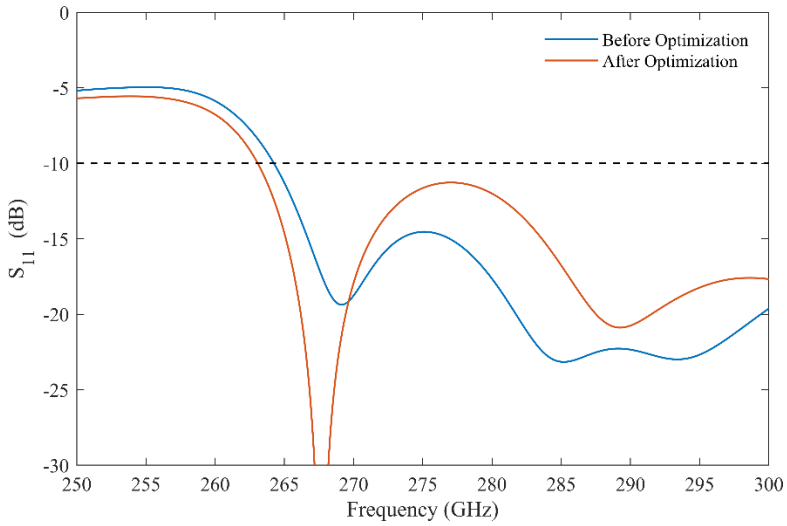

Figure 5.33: Comparison of the S_{11} of the full FPCA, before and after the optimization process.

Due to the existence of residual un-radiated energy in between the PRDS layers and the metal ground, the supporting pillars at the edge of the PRDS layers will cause minor reflections. This effect might potentially lead to a reduction in the FPCA's performance regarding gain and SLL. This also elucidates the discrepancy in SLL performance between the FPCA prior to and following the optimization, as depicted in Figure 5.32. Furthermore, as depicted in Figure 5.27, the screws and alignment pin will also potentially contribute to additional scattering. It should be noted that the optimization process previously discussed does not take into account the screws and alignment pins due to the required increase in simulation size.

One solution to minimize the impact caused by the supporting pillars, screws and the alignment pins is to deploy unit cells with higher leakage rates at the edge of the PRDS. This approach ensures that most of the energy (more than 90%) has been radiated

before reaching the support pillars.

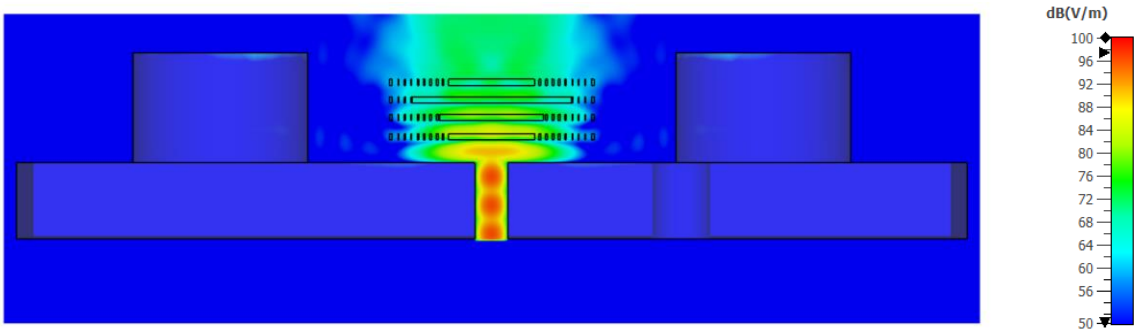

Figure 5.34. Electric field distribution of the full FPCA design in H-plane at 264 GHz. The main beam is pointing in the broadside direction and therefore, there is nearly no interaction with the screws.

Another solution to mitigate this impact involves mounting the screws solely in the H-plane, as depicted in Figure 5.27. This strategy is aimed at minimizing the reflection of the TM_0 mode. As discussed in Section 2.3, compared to the TM_1 mode and TE_1 mode, the TM_0 mode radiates towards a larger angle from broadside. This property makes it contribute more significantly to the reflection caused by the supporting pillars, screws, and alignment pins. Consequently, shorter screws are preferred to be employed to minimize this effect.

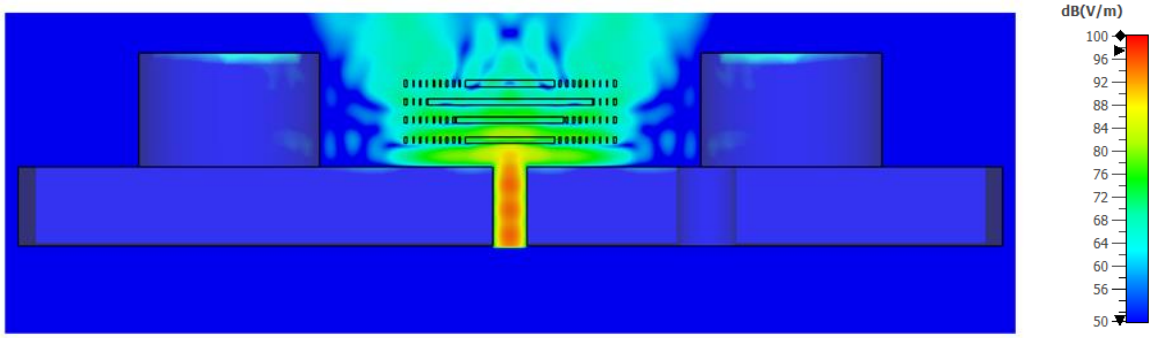

Figure 5.35. Electric field distribution of the full FPCA design in the H-plane at 292 GHz. As the frequency increases, the radiation pattern of the mainlobe starts to deviate from the broadside direction, leading to more interaction with the screws and a consequent rise in SLL.

As shown in Figure 5.34, the electric field distribution in the H-plane shows that, nearly

no reflection is caused by the screw at 264 GHz when the radiation direction of the main beam is pointing in the broadside direction. When the beam splitting condition is fulfilled as the frequency is increased, the higher radiation angle will result in more interaction with the screws, as shown in Figure 5.35.

The solutions previously proposed to alleviate the impact of reflection have demonstrated substantial effectiveness, as verified by the simulation results. The realized gain and the SLL essentially align with the simulation result acquired prior to the introduction of screws and alignment pins. It is worth noting that, in practical applications, the use of screws and alignment pins is not invariably necessary. The FPCA design could be seamlessly integrated with a MMIC chip itself, eliminating the need for any supplementary structures [27].

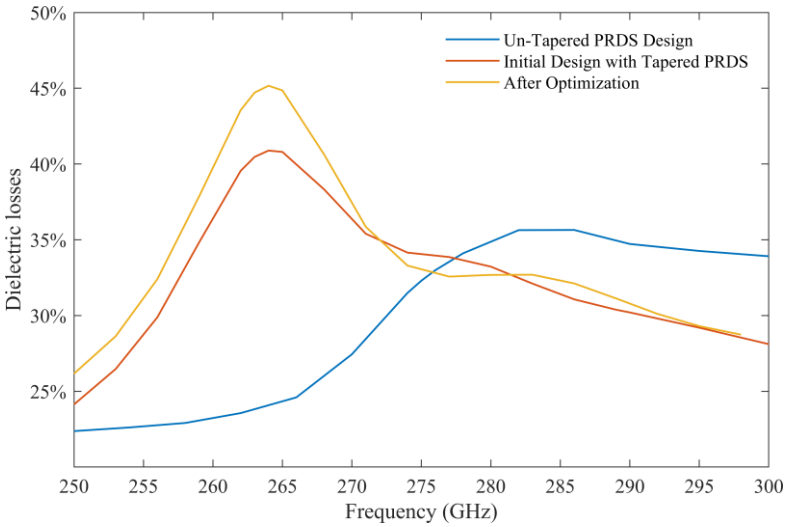

Figure 5.36. Comparison of dielectric losses in the full FPCA design, before and after optimization.

As shown in Figure 5.36, it is evident that the dielectric loss of the initial design of the FPCA with tapered PRS reach a maximum of 40.8%. This is primarily due to the high loss tangent of the IP-Q photoresin.

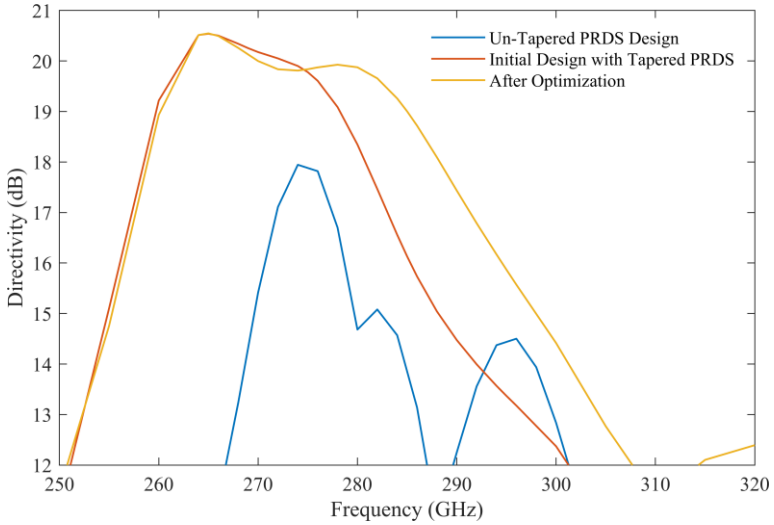

Figure 5.37. Comparison of the directivity of the full FPCA design before and after optimization.

After the optimization, the dielectric loss reaches a peak of 45% at 264 GHz as shown in Figure 5.36. As the frequency increases, starting at 270 GHz, the dielectric loss of the optimized FPCA becomes nearly equal to that of the initial design. Moreover, as shown in Figure 5.37, higher directivity is achieved after optimization of the FPCA, which means that a higher gain is attained due to this increased directivity, despite similar dielectric losses.

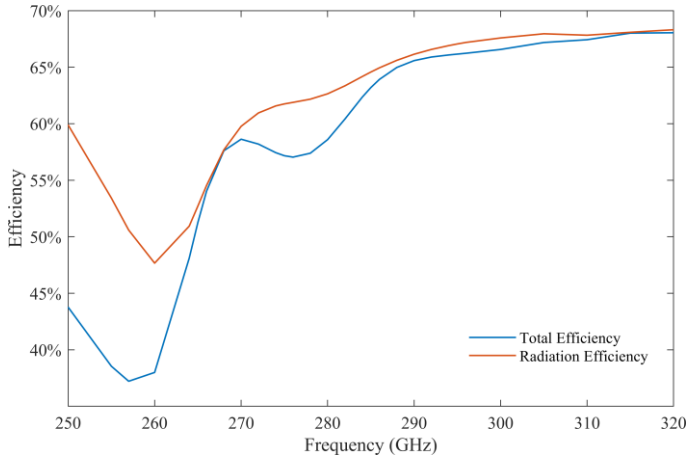

Figure 5.38. Simulated total efficiency and radiation efficiency of the FPCA after optimization.

As shown in Figure 5.38, the total efficiency of the FPCA ranges from 45% to 65% between 264 GHz and 290 GHz. The dip around 260 GHz is attributed to the high return loss, as illustrated in Figure 5.33. The radiation efficiency varies from 47% to

65% between 264 GHz and 290 GHz, with a dip around 264 GHz due to the high dielectric loss caused by the IP-Q photoresin.

It can be seen from Figure 5.31, Figure 5.36 and Figure 5.38, at 264 GHz, a 2.6 dB gain loss is caused by the dielectric loss of the IP-Q photo resin. This suggests that employing a photoresin with lower dielectric losses for the FPCA design could result in a higher realized gain.

5.4. Fabrication of Shim and FPCA

The shim, as illustrated in Figure 5.27, is manufactured through the utilization of a femtosecond pulsed laser for cutting a silicon wafer with a thickness of 300 μm. Specifically, the laser ablation system employed is the Yuja model manufactured by Amplitude.

The laser cutting systems produces an average power exceeding 10 Watts with a pulse duration below 500 femtoseconds, and the positional accuracy for 1 degree temperature stability of the system is 2 μm [28]. A primary advantage of employing femtosecond lasers for fabrication resides in their ability to ablate or alter the material while minimally dissipating heat into the adjacent material. This capability is primarily attributable to the short duration of each laser pulse, which is less than 500 femtoseconds [28]. This duration is shorter than the typical heat transfer time - typically on the order of 1 picosecond - from the impact zone to the surrounding material [29]. The above process, termed as cold ablation, curbs the formation of a heat-affected zone, thereby mitigating structural damage and defects in the processed silicon wafer. It also enables the realization of a highly precise process [30].

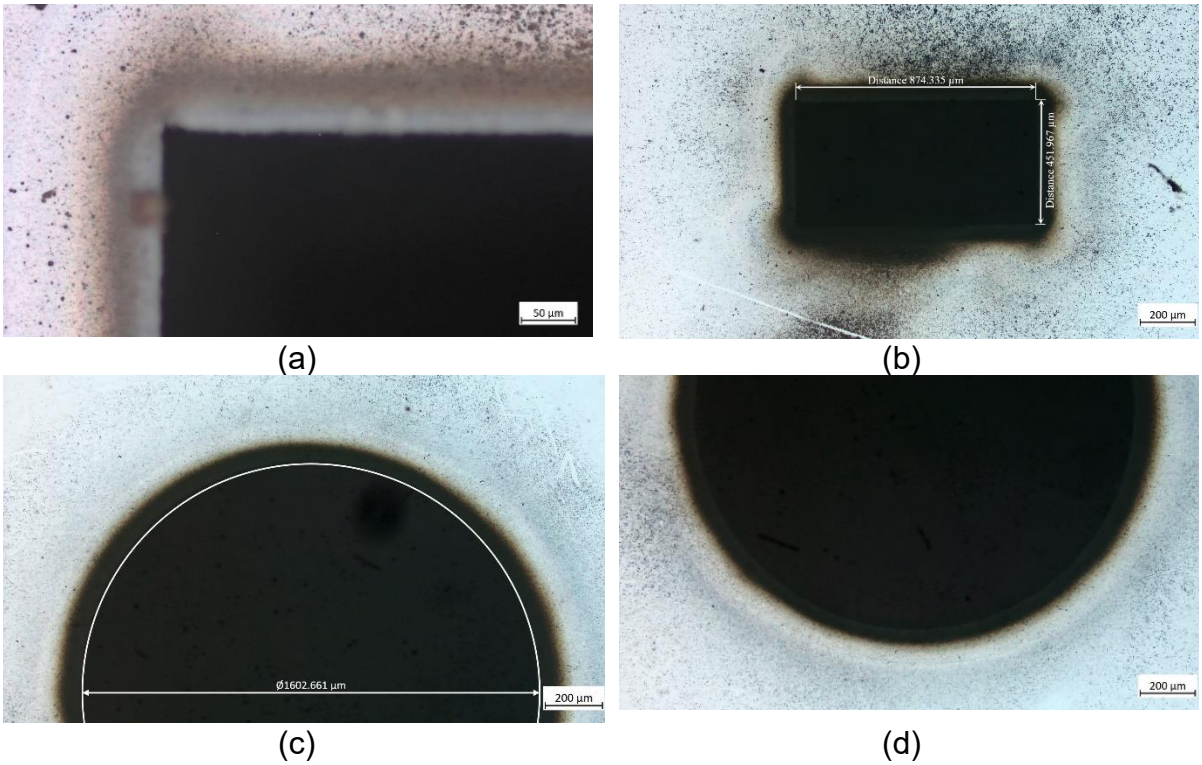

Figure 5.39. Detailed inspection of laser cut shim using microscopy. (a) and (b) close-up view of the waveguide port. (c) and (d) Close-up view of the laser cut alignment hole.

The laser cutting process begins with the designing of the shim to fit on a WR-3 band UG387/U waveguide flange using advanced computer-aided design (CAD) software. With the CAD drawing of the design ready, the laser beam is calibrated by aligning with the silicon wafer. During the laser cutting process, the laser is focused to a spot size of less than 20 µm in diameter on the silicon wafer. This precision allows for clean cuts and intricate designs, which are crucial for the accurate work involved in creating a WR-3 band waveguide flange shim.

As shown in Figure 5.39, the silicon has been slightly melted and subsequently solidified along the edges after the cutting process. The laser cut waveguide port edge size of the shim, as shown in Figure 5.39(b), is 0.875 mm × 0.452 mm, which deviates slightly from the standard WR-3 band rectangular waveguide dimensions of 0.864 mm × 0.432 mm. This discrepancy has been considered in the simulation of the full FPCA

design, given its potential influence on the waveguide's propagation characteristics and, consequently, on the overall performance of the FPCA.

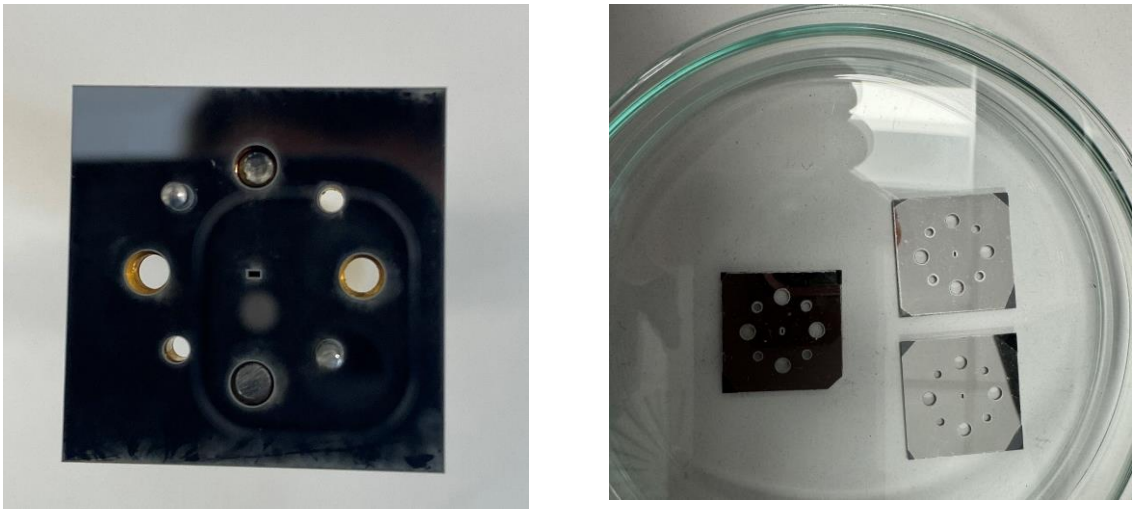

(a) (b)

Figure 5.40. (a) A shim mounted on a WR-3 UG387/U waveguide flange for fit testing. (b) A batch of shims coated with silver using magnetron sputtering.

As shown in Figure 5.40(a), the shim is mounted on a UG387 waveguide flange for fit testing to verify the accuracy of the laser cutting. The shim exhibits tight and seamless contact with the flange surface, demonstrating the effectiveness of the laser cutting process. As shown in Figure 5.40(b), the shims are coated with a silver layer using magnetron sputtering. The corners of the shims are uncoated due to the Kapton tape used to hold the pieces in place during sputtering, however, this is not expected to affect the electromagnetic performance of the antenna.

The FPCA design proposed in this study is fabricated using 2PP 3D printing. Nevertheless, due to the multi-layer PRDS inherently being a large overhanging structure, it poses a challenge during the 3D printing process. These challenges arise because the stage movement during printing can disturb the newly printed structure inside the liquid photoresin droplet, leading to drift and deformation of the overhanging

structure.

To mitigate these issues, it is crucial to pay attention to the printing order of each print block. For blocks that overhang, it is essential to ensure a connection with previously printed parts. This strategy can help avoid “flying blocks” and prevent them from being displaced due to the movement of the stage or lens. The “Avoid Flying Blocks” setting in the software provided by NanoScribe can be utilized to address this issue automatically before exporting the print job to the NanoScribe printer. Additionally, higher polymerization intensity can be achieved by either increasing the laser power or reducing the scan speed, enabling the printing of stronger and more stable overhanging structures. While the methods introduced above have proved to be effective for smaller-scale overhanging structures, they are still insufficient for printing large-scale overhanging structures.

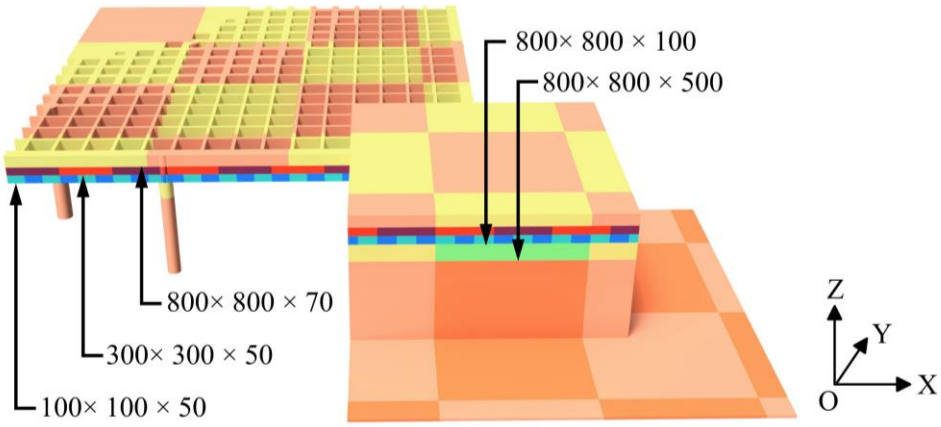

Figure 5.41. Illustrative configuration of block splitting in partial FPCA for 2PP 3D Printing. The dimensions of the blocks in each layer are specified in the order of X, Y, and Z. All values are in micrometres (μm).

The problem of printing large-scale overhanging features has been further addressed by David E. Marschner *et al.* [31]. This solution involves carefully controlling the slicing of the models to be printed, meticulously adjusting the size of the blocks that constitute

each layer, and carefully selecting the appropriate print parameters, thereby making it feasible to print structures with significant overhangs. By splitting the model into sufficiently small blocks, the movement of the stage during the printing process is minimized, which allows the production of structures with substantial overhangs. An overlap between adjacent blocks is also specified in the slicing process to ensure strong connections. However, this strategy may increase overall print time, necessitating a careful trade-off between the block size and the total time required for printing [31].

As depicted in Figure 5.41, each layer of the PRDS of the FPCA is divided into three sub-layers, with the block splitting size of each sub-layer represented in the figure. The bottom-most sub-layer possesses the smallest block size since this layer is essentially overhanging and suspended in the air. The second sub-layer is printed on top of the first sub-layer and exhibits a larger block splitting size in the *x* and *y* dimensions than the first one. However, it retains the thickness of the first sub-layer in the *z*-direction to ensure a stable base for the third sub-layer. The third sub-layer features a larger block splitting size than the second sub-layer, effectively reducing the printing time and accelerating the process of constructing the entire structure. While for the supporting pillars, the block splitting size is much larger than that of the overhanging PRDS layers, which will consume less time for printing.

The print speed of 2PP 3D printing cannot be excessively increased. When the laser scanning speed is too high, the photoresin fails to absorb a sufficient number of photons and undergo proper polymerization. This leads to instability in the printed structures. Consequently, there exists a necessary balance between print speed and structural stability in this technology.

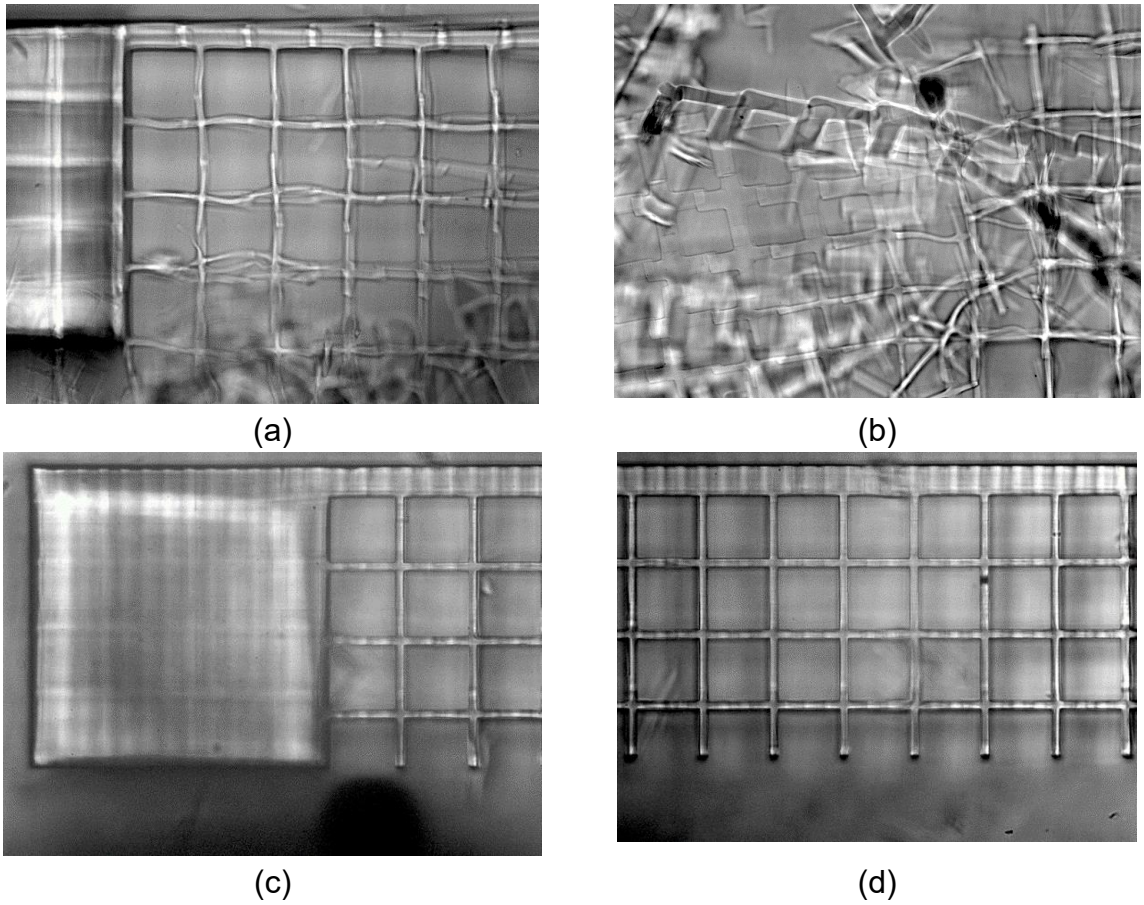

Figure 5.42: Comparison of PRDS printed using different block splitting methods. (a) and (b) print with large block splitting size, the printed overhanging structures appear deformed and detached. (c) and (d) After adopting a multi-layer and optimized block splitting plan, the PRDS layer is successfully printed.

It is worth noting that the process of splitting the FPCA CAD model into the sub-layers with different block sizes, as illustrated in Figure 5.41, is not intrinsically supported by the software. As a result, the entire block splitting process and the print job data files must be manually combined. An in-house Python code has been developed to accelerate this process.

Table 5.7. Optimal 3D print parameters for the base layer of FPCA

Base Laser Power	Base Scanning Speed	Base Slice Count
5 mW	40000 μm/s	3

Apart from the issue of printing overhanging features, another aspect that requires attention is the adhesion of 3D-printed parts to the shim. Since the FPCA is printed on

the shim's silver-coated surface layer, the laser will be reflected and interfere with the incident laser beam. This may potentially lead to the formation of bubbles during the base layer printing process, thereby affecting the pillars' adhesion to the shim. One viable solution is performing a parameter scan on the laser power and scanning speed during the base layer printing process. Suitable printing parameters can then be determined by comparing the printed structures. In this work, the optimal parameters that achieve both strong adhesion and minimal bubble formation for the base layer print are listed in Table 5.7.

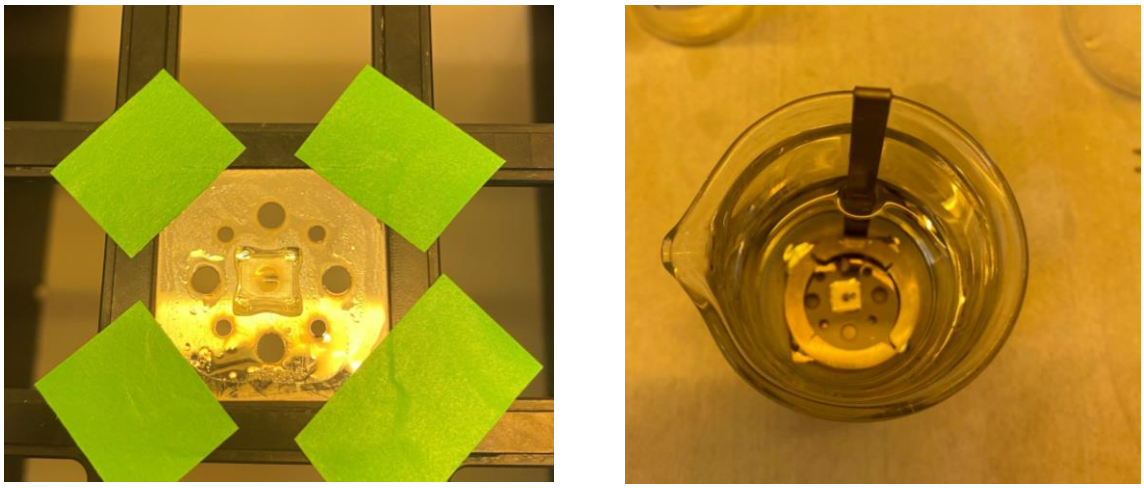

(a) (b)

Figure 5.43. FPCA printed on the shim: (a) Just after 3D printing, before being removed from the sample holder. (b) FPCA and the shim placed on the substrate holder for further development.

The total 3D printing time for the FPCA is 95 hours. As illustrated in Figure 5.43(a), the FPCA is affixed to the sample holder using adhesive tape at its four edges. As shown in Figure 5.43(b), the FPCA is then removed from the sample holder, positioned on the substrate holder and immersed in a beaker containing Propylene Glycol Methyl Ether Acetate (PGMEA) for 30 minutes. This developing step is aimed at dissolving and removing any non-polymerized photoresin. Subsequently, the FPCA is transferred from the PGMEA to a beaker filled with Isopropanol (IPA) for an additional 5 minutes

to remove any remaining PGMEA. After removal from the IPA, the FPCA is air-dried. It is crucial to emphasize that the entire procedure was carried out in a fume hood, specifically to safeguard against the health hazards posed by volatile organic solvents [32].

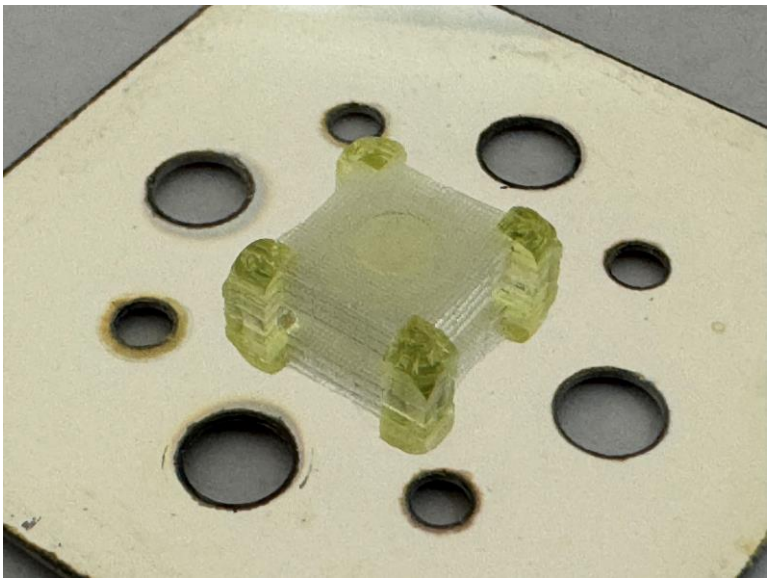

Figure 5.44. FPCA under a microscope for further inspection of the printed details.

As shown in Figure 5.44, the FPCA is further inspected under a microscope. It can be seen that the overall structure of the FPCA is nearly perfectly fabricated, with some deformation at the edge of the PRDS. This deformation is caused by the shrinkage of the photoresin. Estimating shrinkage prior to printing is challenging due to various influencing factors, including the age of the photoresin, laser power, scan rate, the geometry of the printed structure, and the post-processing procedure. Printing multiple cube samples with identical print configurations and post-processing conditions can help predict the shrinkage rate more accurately, but it is still challenging since the exact geometry of the printed structure influences the shrinkage. Future work is to simulate this shrinkage process.

The shrinkage of the photoresin will change the dimensions of the resonant cavity of

the FPCA. Consequently, the performance of the FPCA, including the resonant frequency and gain, is influenced, a topic that will be covered in the next section.

5.5. Measurement and Discussion

To further validate the performance of the FPCA proposed in this thesis, measurements of the far-field pattern and S_{11} parameter of the FPCA prototype were conducted with the configuration shown in Figure 5.45.

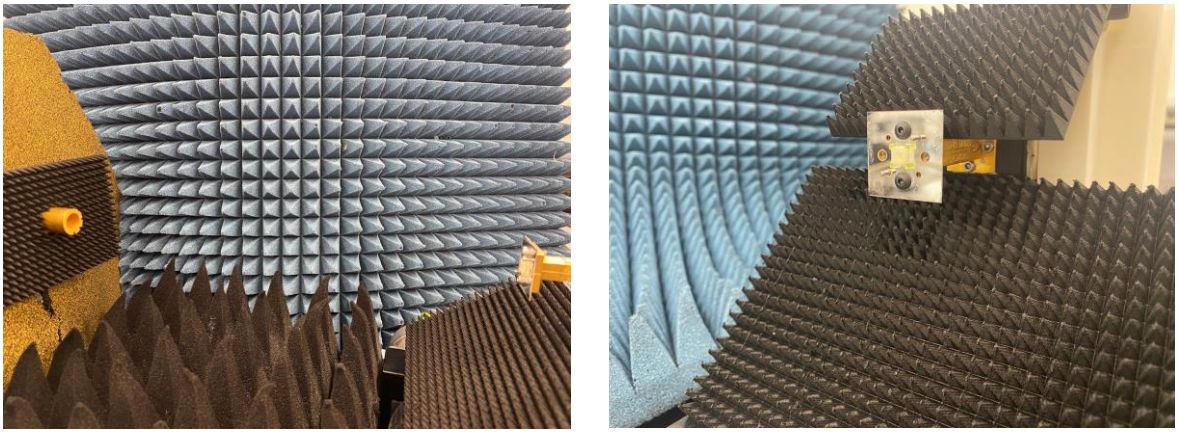

(a) (b)

Figure 5.45. Configuration of the far-field pattern measurement of the FPCA prototype: (a) A Gaussian-beam corrugated horn antenna is utilized as the source for the far-field pattern measurement of the FPCA. (b) The shim with the FPCA adhered is mounted on the WR-3 UG387/U flange.

As shown in Figure 5.45(b), the shim with the FPCA adhered is mounted on a WR-3 UG387/U flange, which is connected to the WR-3 frequency extender head of the Keysight N5247B PNA-X network analyser. As shown in Figure 5.45(a), a Gaussian-beam corrugated horn antenna is connected to the other WR-3 frequency extender head as the source for the far-field measurement of the FPCA. The separation distance between the FPCA and the Gaussian-beam corrugated horn antenna is 293 mm for the H-plane cut, and 351 mm for the E-plane cut, to fulfil the far-field measurement requirement. Terahertz band pyramid absorber panels are employed to minimize

reflections from the equipment and testbench surrounding the test field.

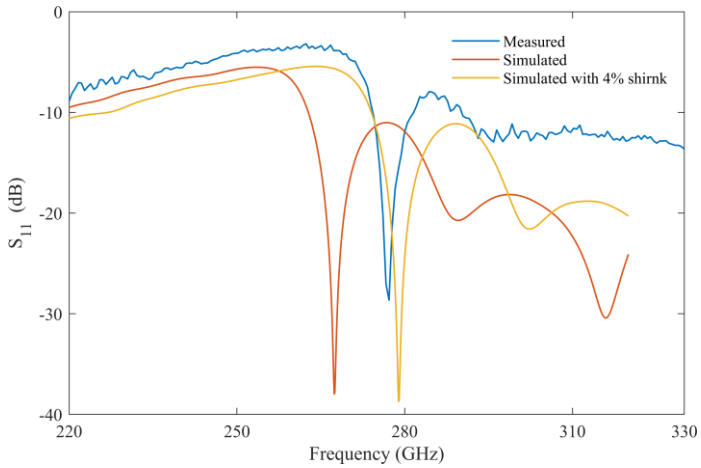

Figure 5.46. The S_{11} of the FPCA prototype, measured and compared with two simulated results: one standard and another incorporating a 4% shrinkage of the photoresin.

Figure 5.46 illustrates a discrepancy between the measured and simulated S_{11} of the FPCA, with the measured data exhibiting a frequency shift. This deviation is attributed to the shrinkage of the photoresin used in the fabrication process. To validate this, additional simulations were performed, adjusting the FPCA structure to account for a 4% shrinkage. The revised simulation results, as depicted in Figure 5.46, demonstrate a closer alignment with the actual measured S_{11}, confirming that the shrinkage of the photoresin significantly impacts the resonance frequency of the FPCA.

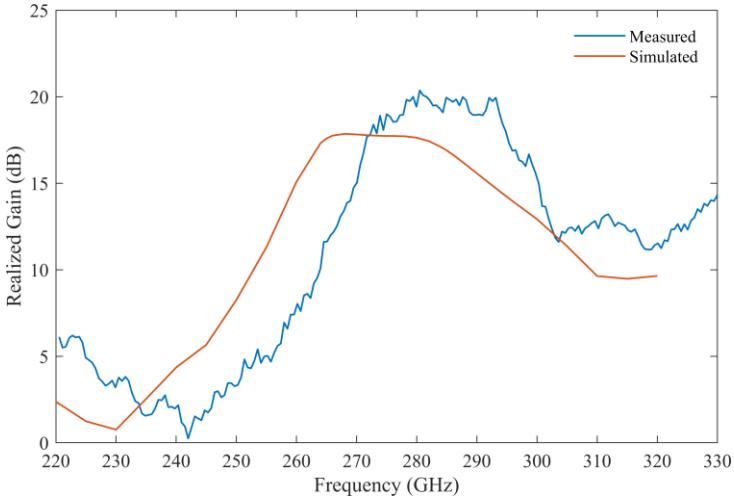

Figure 5.47. Simulated and measured realized gain of the FPCA.

As shown in Figure 5.47, the FPCA achieves a measured realized gain of 20.4 dB, with a 3 dB gain bandwidth of 23.3 GHz, ranging from 272 GHz to 295.3 GHz. This corresponds to a 3 dB GBWP of 892.4. Additionally, the frequency shift between the simulated and measured realized gains of the FPCA is attributed to the shrinkage of the IP-Q photoresin.

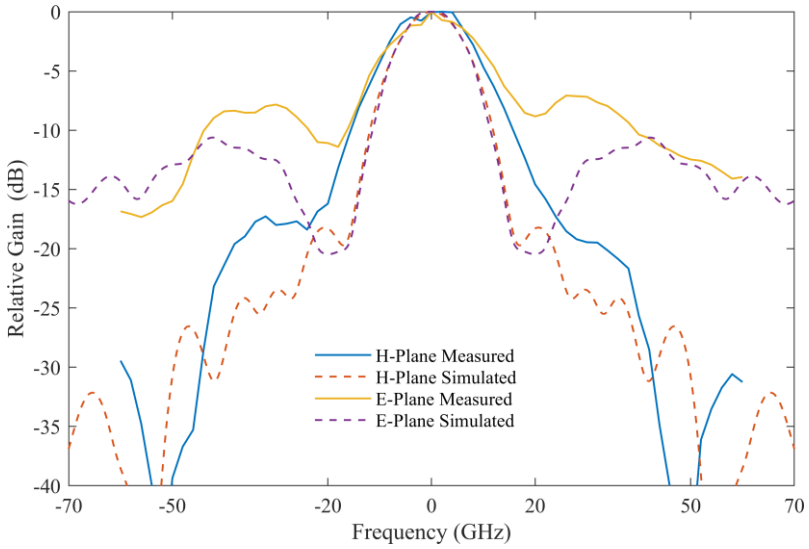

(a) 270 GHz

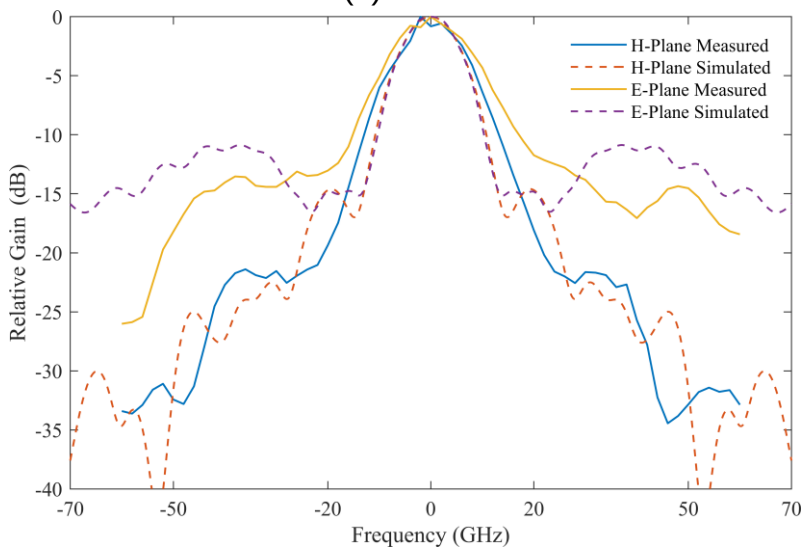

(b) 274 GHz

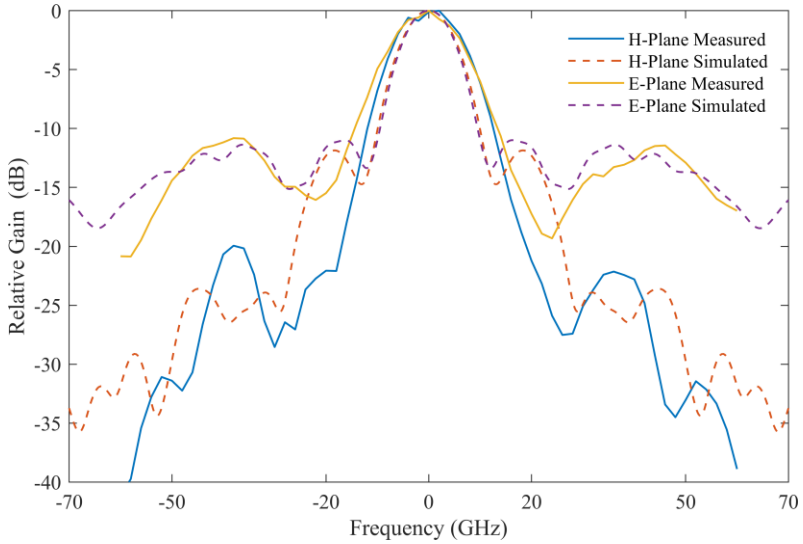

(c) 278 GHz

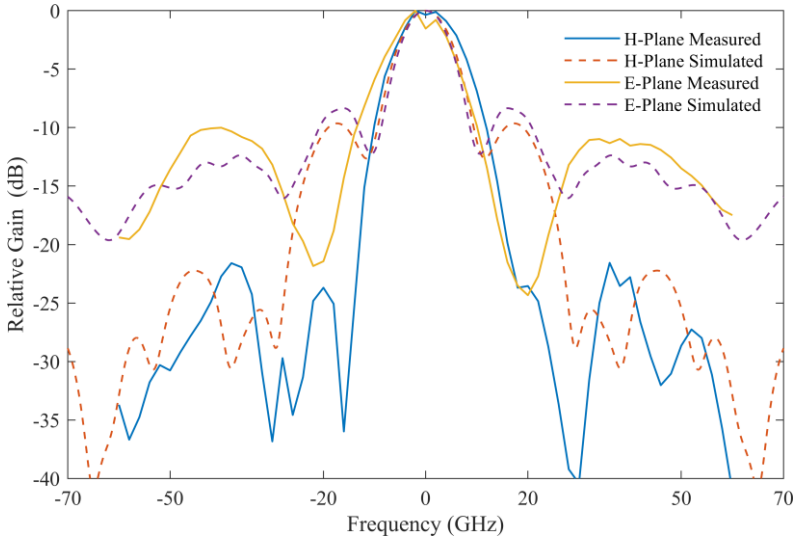

(d) 282 GHz

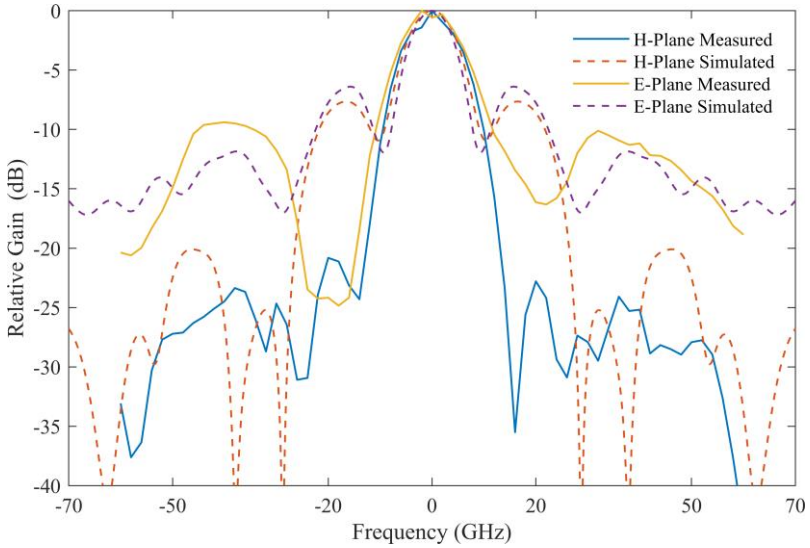

(e) 286 GHz

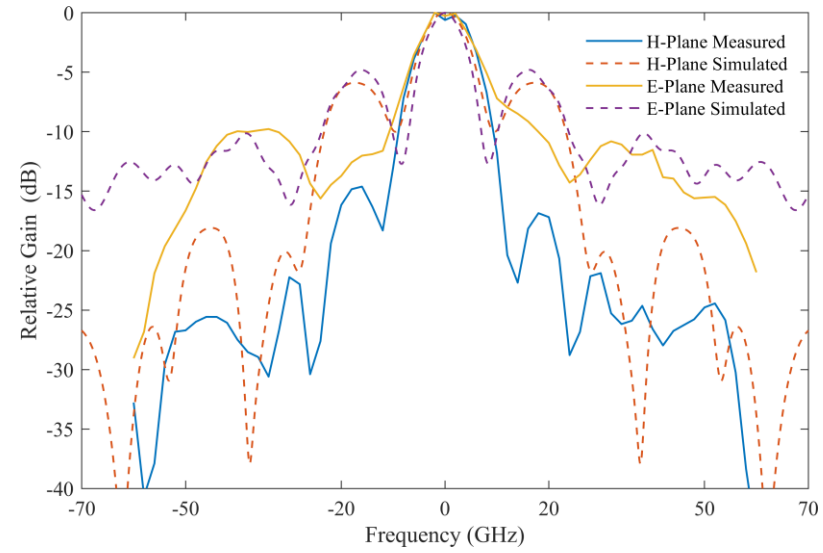

(f) 290 GHz

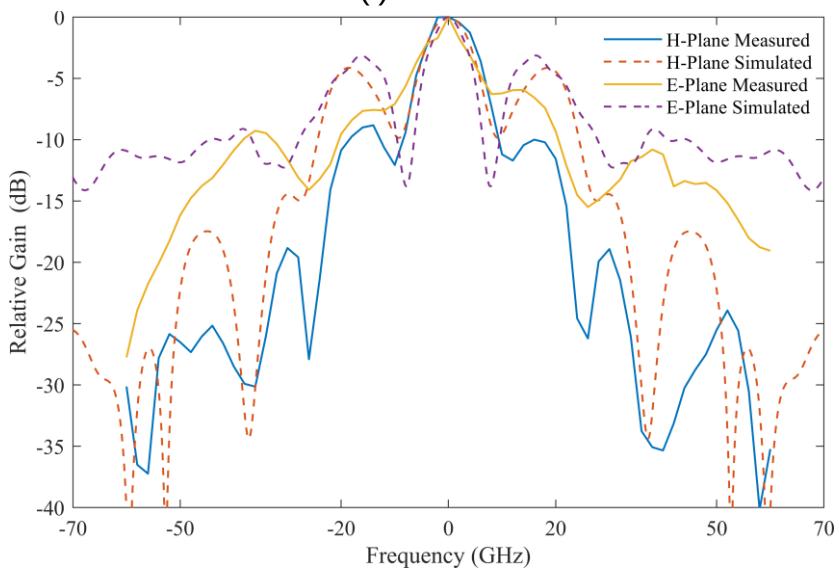

(g) 294 GHz

Figure 5.48. Far-field radiation pattern of the FPCA in both E and H-plane.

As shown in Figure 5.48, the main beam of the FPCA remains directed towards the broadside direction across the frequency bandwidth from 270 GHz to 294 GHz. It is observed that the beamwidths of the simulated and measured patterns of the FPCA match well. However, due to the frequency shift, the SLL of the measured E-plane pattern becomes higher, no longer matching the simulated results.

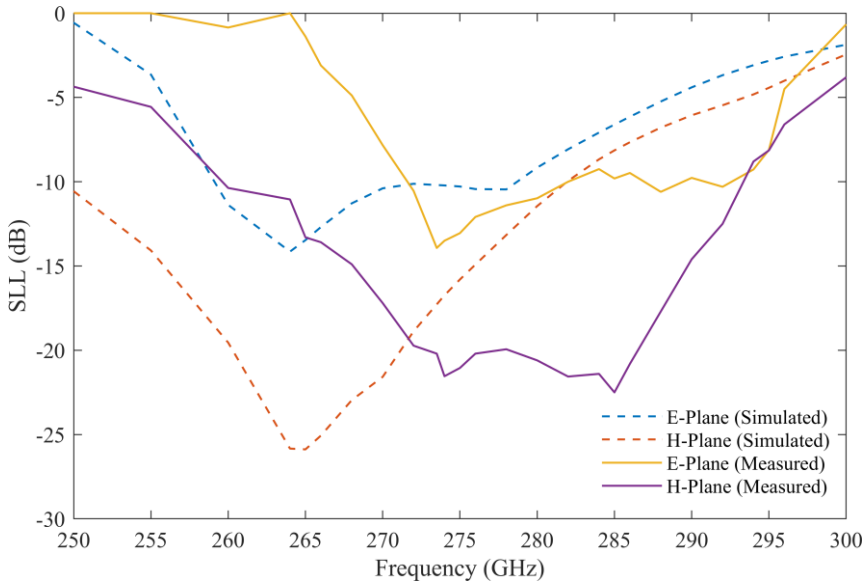

Figure 5.49. Measured and simulated SLL of the FPCA.

As shown in Figure 5.48 and Figure 5.49, the H-plane of the far-field pattern exhibits a SLL compared to the E-plane. This difference is attributed to the presence of the TM_0 mode, which contributes to the far-field radiation pattern, as previously discussed in Section 2.3. The measured SLLs of the patterns in both E and H-planes are relatively stable in the range from 274 GHz to 286 GHz. However, as the frequency increases, the SLL in both E and H-planes worsens due to the higher radiation angle of the leaky wave modes from broadside, as discussed earlier in Section 2.3.

5.6. Summary

In this chapter, a 3D-printed FPCA based on 2PP photoresin is proposed. This antenna offers a low cost, ease of integration with chips, and features a low-profile, high-gain, wide-band design with a stable radiation pattern, consistently directed broadside across varying frequencies in the H-band. Concurrently tapering the permittivity distribution of the multi-layer PRDS and optimizing the FPCA has led to achieving a 3 dB GBWP of 892.4, which is higher than those reported in similar

published works. This advancement is confirmed through experimental validation via far-field measurement. While the experimentally measured 3 dB GBWP marginally differs from the simulated value, the overall correlation is significant, especially when considering the frequency shift. Importantly, the novel design of the FPCA eliminates the need for an additional waveguide matching structure during its integration. To further optimize the agreement between the FPCA simulation and the measurement, future work will consider the shrinkage factor of the 2PP photoresin during the 3D modelling process. Additionally, GP-silica, a composite polymer-silica material, will be explored for the 3D printing of FPCA due to its lower loss tangent, while compensating for its higher shrinkage factor.

Reference

[1] E. J. Y. Magaway, Y. Farahi, S. M. Hanham, Z. J. Zhang, A. Guaidía-Moreno, and M. Navarro-Cía, "Silica Nanoparticle-Based Photoresin for Thz High-Resolution 3d Microfabrication by Two-Photon Polymerization," *IEEE Trans. Terahertz Sci. Technol.,* 2023.

[2] K. Konstantinidis *et al.*, "Low-Thz Dielectric Lens Antenna with Integrated Waveguide Feed," *IEEE Trans. Terahertz Sci. Technol.,* vol. 7, no. 5, pp. 572-581, 2017.

[3] F. Aieta, M. A. Kats, P. Genevet, and F. Capasso, "Multiwavelength Achromatic Metasurfaces by Dispersive Phase Compensation," *Science,* vol. 347, no. 6228, pp. 1342-1345, 2015.

[4] C. A. Balanis, *Modern Antenna Handbook*. John Wiley & Sons, 2011.

[5] E. Massoni *et al.*, "Characterization of 3d-Printed Dielectric Substrates with Different Infill for Microwave Applications," in *2016 IEEE MTT-S International Microwave Workshop Series on Advanced Materials and Processes for RF and THz Applications (IMWS-AMP)*, 20-22 July 2016 2016, pp. 1-4.

[6] T. C. Choy, *Effective Medium Theory: Principles and Applications*. Oxford University Press, 2015.

[7] P. Burghignoli, W. Fuscaldo, and A. Galli, "Fabry–Pérot Cavity Antennas: The Leaky-Wave Perspective [Electromagnetic Perspectives]," *IEEE Antennas Propag. Mag.,* vol. 63, no. 4, pp. 116-145, 2021.

[8] A. Neto and N. Llombart, "Wideband Localization of the Dominant Leaky Wave Poles in Dielectric Covered Antennas," *IEEE Antennas Wirel. Propag. Lett.,* vol.

5, pp. 549-551, 2006.
[9] "User Manual Version 2022," *CST Computer Simulation Technology GmbH, Darmstadt, Germany,* 2022.
[10] D. Kajfez and P. Guillon, "Dielectric Resonators," *Norwood,* 1986.
[11] J. Breeze, M. Oxborrow, and N. McN Alford, "Better Than Bragg: Optimizing the Quality Factor of Resonators with Aperiodic Dielectric Reflectors," *Appl. Phys. Lett.,* vol. 99, no. 11, p. 113515, 2011.
[12] D. M. Pozar, *Microwave Engineering*. Microwave engineering, 2004.
[13] N. Llombart, G. Chattopadhyay, A. Skalare, and I. Mehdi, "Novel Terahertz Antenna Based on a Silicon Lens Fed by a Leaky Wave Enhanced Waveguide," *IEEE Trans. Antennas Propag.,* vol. 59, no. 6, pp. 2160-2168, 2011.
[14] B. Aqlan, M. Himdi, H. Vettikalladi, and L. Le-Coq, "A 300-Ghz Low-Cost High-Gain Fully Metallic Fabry–Perot Cavity Antenna for 6g Terahertz Wireless Communications," *Sci. Rep.,* vol. 11, no. 1, pp. 1-9, 2021.
[15] L.-Y. Ji, P.-Y. Qin, and Y. J. Guo, "Wideband Fabry-Perot Cavity Antenna with a Shaped Ground Plane," *IEEE Access,* vol. 6, pp. 2291-2297, 2017.
[16] K. Konstantinidis, A. P. Feresidis, and P. S. Hall, "Multilayer Partially Reflective Surfaces for Broadband Fabry-Perot Cavity Antennas," *IEEE Trans. Antennas Propag.,* vol. 62, no. 7, pp. 3474-3481, 2014.
[17] R. M. Hashmi and K. P. Esselle, "Distribution Profiles for Transverse Permittivity Gradient Superstrates in Extremely Wideband Resonant Cavity Antennas," in *2016 IEEE International Symposium on Antennas and Propagation (APSURSI)*, 2016: IEEE, pp. 1847-1848.
[18] C. Gu *et al.*, "A D-Band 3d-Printed Antenna," *IEEE Trans. Terahertz Sci. Technol.,* vol. 10, no. 5, pp. 433-442, 2020.
[19] S. Verma, M. Pant, and V. Snasel, "A Comprehensive Review on Nsga-Ii for Multi-Objective Combinatorial Optimization Problems," *IEEE Access,* vol. 9, pp. 57757-57791, 2021.
[20] J. O. Yang, Q. R. Yuan, F. Yang, H. J. Zhou, Z. P. Nie, and Z. Q. Zhao, "Synthesis of Conformal Phased Array with Improved Nsga-Ii Algorithm," *IEEE Trans. Antennas Propag.,* vol. 57, no. 12, pp. 4006-4009, 2009.
[21] L. Liu, J. Lu, and S. Yang, "Many-Objective Optimization of Antenna Arrays Using an Improved Multiple-Single-Objective Pareto Sampling Algorithm," *IEEE Antennas Wirel. Propag. Lett.,* vol. 11, pp. 399-402, 2012.
[22] S. Jayaprakasam, S. K. A. Rahim, C. Y. Leow, T. O. Ting, and A. A. Eteng, "Multiobjective Beampattern Optimization in Collaborative Beamforming Via Nsga-Ii with Selective Distance," *IEEE Trans. Antennas Propag.,* vol. 65, no. 5, pp. 2348-2357, 2017.
[23] X. Chen, K. Li, L. Zhang, and Z. Tian, "Robust Optimization of Energy-Saving Train Trajectories under Passenger Load Uncertainty Based on P-Nsga-Ii," *IEEE Trans. Transp. Electrif.,* vol. 9, no. 1, pp. 1826-1844, 2023.
[24] Y. Liu, X. Wang, Y. Zhang, and L. Liu, "An Integrated Flow Shop Scheduling Problem of Preventive Maintenance and Degradation with an Improved Nsga-Ii Algorithm," *IEEE Access,* vol. 11, pp. 3525-3544, 2023.
[25] H. Verdejo, D. Gonzalez, J. Delpiano, and C. Becker, "Tuning of Power System Stabilizers Using Multiobjective Optimization Nsga Ii," *IEEE Lat. Am. Trans.,* vol. 13, no. 8, pp. 2653-2660, 2015.
[26] A. Saltelli, P. Annoni, I. Azzini, F. Campolongo, M. Ratto, and S. Tarantola,

"Variance Based Sensitivity Analysis of Model Output. Design and Estimator for the Total Sensitivity Index," *Comput. Phys. Commun.,* vol. 181, no. 2, pp. 259-270, 2010.

[27] J. Campion *et al.*, "Toward Industrial Exploitation of Thz Frequencies: Integration of Sige Mmics in Silicon-Micromachined Waveguide Systems," *IEEE Trans. Terahertz Sci. Technol.,* vol. 9, no. 6, pp. 624-636, 2019.

[28] Amplitude. "Product Sheet of Yuja Multi." https://amplitude-laser.com/add_ons/beam-management/yuja-multi/ (accessed 15/05, 2023).

[29] B. N. Chichkov, C. Momma, S. Nolte, F. Von Alvensleben, and A. Tünnermann, "Femtosecond, Picosecond and Nanosecond Laser Ablation of Solids," *Appl. Phys. A,* vol. 63, pp. 109-115, 1996.

[30] J. Cheng *et al.*, "A Review of Ultrafast Laser Materials Micromachining," *Optics and Laser Technology,* vol. 46, pp. 88-102, 2013.

[31] D. E. Marschner, S. Pagliano, P.-H. Huang, and F. Niklaus, "A Methodology for Two-Photon Polymerization Micro 3d Printing of Objects with Long Overhanging Structures," *Addit. Manuf.,* vol. 66, p. 103474, 2023.

[32] "Development Overview." Nanoscribe GmbH & Co. KG. https://support.nanoscribe.com/hc/en-gb/articles/360001344673-Development-Overview (accessed 2nd December, 2023).

Chapter 6

Conclusion and Future Work

6.1. Conclusions

In this thesis, two antenna designs are proposed that meet these characteristics for diverse terahertz applications: a H-band DLWA based on micromachined silicon, and a H-band direct laser-written polymer FPCA.

A DLWA based on micromachined silicon is proposed in Chapter 4. The DLWA proposed in this paper employs the novel leaky unit cell design and exhibits a Dirac-like dispersion relationship, that both addresses the common OSB problem encountered with LWA design and realizes a fan beam which scans linearly with frequency. The simulated results confirm that the bandgap of the antenna is closed and measured results show the S_{11} to be below -15 dB across the WR-3 band with the exception of a peak at 253 GHz, where reflection reaches -6.4 dB which is attributed to fabrication tolerances.

Another novel aspect of the DLWA design is the application of aperture tapering to reduce the SLL, combined with a curve fitting method for optimizing and predicting the unit cell dimensions. This method ensures the maintenance of both the same broadside radiating frequency and the closed bandgap feature of the unit cell with desired leakage rate. A SLL less than -17 dB is achieved ranging from 220 GHz to 315

GHz, covering the entire H-band. The DLWA exhibits a peak aperture efficiency of 81.5% at 265 GHz.

A further novel feature of the DLWA design is its utilization of an all-dielectric approach (except for the reflector and feeding waveguide), which minimizes Ohmic loss commonly encountered in predominantly metal structures described in prior studies. The fabrication from a single silicon wafer permits the integration of active components and future AiP implementations.

A FPCA realized through a 2PP direct laser writing process is proposed in Chapter 5. The FPCA is seamlessly integrated with a silicon shim and is connected to a WR-3 band UG387/U flange, enabling it to be fed by an open-ended waveguide. Furthermore, this thesis introduces a novel analysis method that employs Q-factor as a key design metric. This method aims to reduce the electric filling factor and minimize dielectric loss, allowing (inexpensive) polymers with moderate loss tangents, in this case IP-Q photo resin, to be employed. The ultimate goal of this approach is to achieve a higher antenna gain.

Another novel aspect of the FPCA design is the implementation of a transverse gradient permittivity-distributed PRDS in order to achieve a higher 3 dB GBWP. This approach also enables the matching of the antenna to the shim without requiring additional structures. The far-field measurement results confirm the antenna's performance, showing a gain of 20.3 dBi at 281.5 GHz, and the 3 dB GBWP reaches 892. However, shrinkage of the IP-Q photo resin after post processing leads to an increase in the FPCA's S_{11}, which raised to -8 dB at 285 GHz. Within the 3 dB gain bandwidth of the FPCA, ranging from 272 GHz to 295.3 GHz, a pencil-beam radiation pattern is maintained, and the lowest SLL reaches -14 dB.

6.2. Future Works

The future work for the DLWA proposed in this thesis includes the following:

1. Further optimise the DLWA's fabrication process to reduce fabrication errors. This can be achieved by improving CNC machine calibration, and using a more sophisticated CNC machine.
2. Experiment with alternative materials to fill the gap between the DLWA and the metal reflector. For instance, employing silica could result in a more precise distance between the DLWA and the metal ground, potentially eliminating the need for the CNC machining of the antenna mounts which control this distance.
3. Pursue further optimization of the feeding mechanism in the tapered DSW. This involves integrating reshaped photonic crystals to facilitate a broader and more uniform wave propagation. Such advancements are expected to serve as an improved source for the excitation of leaky waves, ultimately aiming to achieve a more focused pencil-beam radiation pattern.
4. Explore the integration of the DLWA with a lens antenna for advanced wavefront reshaping. This approach aims to achieve higher gain or maintain a stable beam direction despite frequency variations.
5. Investigate the substitution of HRS with more cost-effective, low-loss dielectric materials. The objective is to attain comparable performance levels while reducing costs.
6. Focus on refining the unit cell design of the DLWA to target higher leakage rates. This endeavour aims to cater to specific scenarios requiring antennas with lower gain, thereby expanding the applicability of the technology.

For the FPCA proposed in this thesis, future work and improvements would be as

follows:

1. Consider replacing the current IP-Q photo resin with a newly developed photoresin containing silica nanoparticles for the antenna's composition. Owing to silica's lower dielectric loss characteristics compared to IP-Q, such a substitution could potentially result in enhanced antenna gain.
2. Integrate piezo motors and their associated control circuits and design the FPCA's supporting pillars to flex, allowing horizontal displacement of the FPCA's layers. This addition aims to realize a steerable beam pointing functionality, enhancing the antenna's operational versatility.
3. Incorporate piezo motors beneath the shim of the FPCA. By adjusting the resonant cavity height, this modification is expected to facilitate a reconfigurable design in terms of working frequency, broadening the scope of the antenna's applications.
4. Consider replacing the current silver layer coating on the shim surface of the FPCA with corrugated ring structures. This proposed modification aims to further suppress unwanted surface wave modes, potentially resulting in a reduced SLL.
5. Optimize the printing sequence for the segmented blocks of the FPCA to achieve greater efficiency in the direct laser writing process, potentially reducing overall fabrication time.